

Proceedings of the Indian Academy of Sciences

(Earth and Planetary Sciences)

Volume 96, 1987

CONTENTS

- Gneiss-charnockite relation around Ponmudi, southern Kerala; evidences and implications of prograde charnockite formation in southern India
C Srikanthappa and G R Ravindra Kumar 1
- Analysis of gravity gradients over a thin infinite sheet
N Sundararajan, I Arun Kumar and N L Mohan 11
- Precursory swarm and its application for long range earthquake forecasting in Taiwan region
V P Singh and J Singh 15
- Results from the Indo-USSR ozonesonde intercomparison experiment
B H Subbaraya, K S Appu, K P Chatterjee, A F Chizhov, V D Grinchikov, A Jayaraman, G A Khokin, V A Kononkov, I S Moshnikov, V Narayanan, S P Perov, O V Shtrikov, Y V Somayajulu, C R Sreedharan and K S Zalpuri 25
- Satellite-observed upwelled region and prime eddy off Somali coast during Monex-79
P N Mahajan 41
- Some aspects of the 30–50 day oscillation
S V Kasture and R N Keshavamurthy 49
- Variability in the surface wind direction at a coastal site of complex terrain
Y Sadhuram 59
- Seasonal and diurnal variability of thermal structure in the coastal waters off Visakhapatnam
B Prabhakara Rao, V Ramesh Babu and P Chandramohan 69
- Variable $^{190}\text{Os}/^{184}\text{Os}$ ratio in acid residues of iron meteorites
P S Goel 81
- Gold-bearing rocks of Mangalur greenstone belt, Gulbarga District, Karnataka
S G Tenginkai and A G Ugarkar 103
- 146-day signal in the geomagnetic field—a probable association with the periodicity of the solar flare index
D R K Rao and B D Kadam 119

Geochemical studies on Kashmir loess profiles <i>G S Lodha, K J S Sawhney, H Razdan, D P Agrawal and N Juyal</i>	135
On global summer monsoonal drought mechanics <i>M Sankar-Rao and S V Sachidananda</i>	147
Characteristics of air flow over Andaman Islands including precipitation <i>Sarat C Kar and N Ramanathan</i>	169
Distribution of particulate organic carbon in the central Bay of Bengal <i>K Nandakumar, K Venkat and N B Bhosle</i>	189
North-south asymmetry in response of geomagnetic activity to different solar events <i>G K Rangarajan</i>	195
Relationship between pedogenetic manifestations in some arid soil and age of the landforms <i>J S Choudhari</i>	203
Auxiliary functions of the Hilbert transform in the study of gravity anomalies <i>G Ramadass, I Arunkumar, S M Varaprasada Rao, N L Mohan and N Sundararajan</i>	211
Petrographic criteria for establishing the copper potential in granitoid plutons <i>M S Naik and R K Trivedi</i>	221
Estimation of hypocentral parameters of local earthquakes when crustal layers have constant <i>P</i> -velocities and dipping interfaces <i>Irene Sarkar, R Chander, K N Khattri and V K Gaur</i>	229
Weathering potential index for rocks based on density and porosity measurements <i>R Pratap Singh, Vijay Kumar Upadhyay and Asok Das</i>	239
Seasonal variation of the salinity in the Zuari estuary, Goa, India <i>S R Shetye and C S Murty</i>	249
Selection of optimum frequency of a wind scatterometer <i>Abhijit Sarkar, Raj Kumar and Mannil Mohan</i>	259
Longshore grain size trends in the Kakinada-Mulapeta Beach, east coast of India <i>D Satya Prasad, G V S Sarma and M Subba Rao</i>	267
A steady state model of the Somali current <i>P K Das, S K Dube and G S Rao</i>	279
Subject Index	291
Author Index	295

Gneiss-charnockite relation around Ponmudi, southern Kerala: evidences and implications of prograde charnockite formation in southern India

C SRIKANTAPPA and G R RAVINDRA KUMAR*

Department of Geology, University of Mysore, Mysore 570 006, India

* Centre for Earth Science Studies, Akkulam, Trivandrum 695 031, India

MS received 28 September 1984; revised 7 November 1986

Abstract. Isochemical conversion of garnet-biotite bearing paragneiss to charnockite in the Precambrian Khondalite belt of southern Kerala is described from Ponmudi area. Petrographic evidences indicate the formation of hypersthene by the breakdown of biotite in the presence of quartz following the reaction: Biotite + quartz \rightarrow hypersthene + K-feldspar + vapour. The estimated pressure - temperature conditions of metamorphism are around 5-7 kbars and $750^\circ \pm 40^\circ\text{C}$. Presence of CO_2 -rich, mixed CO_2 - H_2O and H_2O -rich inclusions were noticed in gneiss as well as in charnockites. Charnockites contain abundant CO_2 -rich inclusions.

Keywords. Charnockite; khondalite; whole rock chemistry; mineral chemistry; P-T conditions; Kerala.

Introduction

The incipient charnockite formation at Kabbal reported by Pichamuthu (1960) in Karnataka, which grades on to a massive charnockite upland belt further south, opened new vistas and kindled new interest in the study of charnockites in southern Peninsular India. Several workers have suggested that the amphibole-bearing gneisses with basic enclaves are transformed to charnockite by the breakdown of amphibole to orthopyroxene at relatively low H_2O fugacities (Janardhan *et al* 1979; Friend 1981; Hansen *et al* 1984). Now there is a general consensus among petrologists that the widespread tonalitic to trondhjemitic Peninsular Gneiss in South India, which carries abundant enclaves of metasediments and basic rocks, have been metamorphosed under granulite facies conditions around 2.6 b.y. ago (Crawford 1969). So far description of arrested charnockite formation in South India is known only from southern Karnataka and in parts of Tamil Nadu (Janardhan *et al* 1979; Holt and Wightman 1983; Condie *et al* 1982). In these localities, the presence of K-rich granitic veins has been commonly noticed which may be genetically linked to charnockite-forming process (Friend 1981).

Recent field investigations in southern Kerala have brought out interesting field relations between charnockite and gneiss (Ravindra Kumar *et al* 1985; Ravindra Kumar and Chacko 1986; Srikantappa *et al* 1985). The present paper reports new data on the field relations, petrography and fluid inclusions of charnockite formation from garnet-biotite bearing para-gneiss around Ponmudi in the Precambrian 'khondalite belt' in South India. This has a bearing on the

2. Regional geology

South Kerala is predominantly composed of high-grade metapelites (khondalites) with minor amounts of charnockites (figure 1). The NW-SE trending foliation dips steeply ($55\text{--}80^\circ$) towards SW in southern and south-western part of the Kerala khondalite belt. Khondalites with minor amounts of carbonate rocks, quartzites and graphitic gneisses are interlayered with basic and ultrabasic rocks. It is generally believed that the charnockites and khondalites represent original intercalations of igneous and sedimentary suite of rocks developed in a geosynclinal environment which were later metamorphosed to granulite facies. Subsequent retrogression of these charnockites and khondalites on a regional scale lead to the development of amphibolite facies gneiss (Mahadevan 1974; Narayanaswamy 1976; Sinha Roy 1979). The prograde formation of charnockites has not been reported from this tract till recently (Ravindrakumar *et al* 1985). Crawford (1969) in his reconnaissance dating of South Indian rocks reports poorly defined Rb-Sr ages for charnockites as 2155 m.y. and 2780 m.y. and for khondalites an older age of 3070 m.y. All these dates are from a single rock collected in the vicinity of Ponmudi. These data do not seem to be reliable because of too low initial $^{87}\text{Sr}/^{86}\text{Sr}$ ratio of 0.700. Evidence for the late proterozoic age for the regional granulite facies

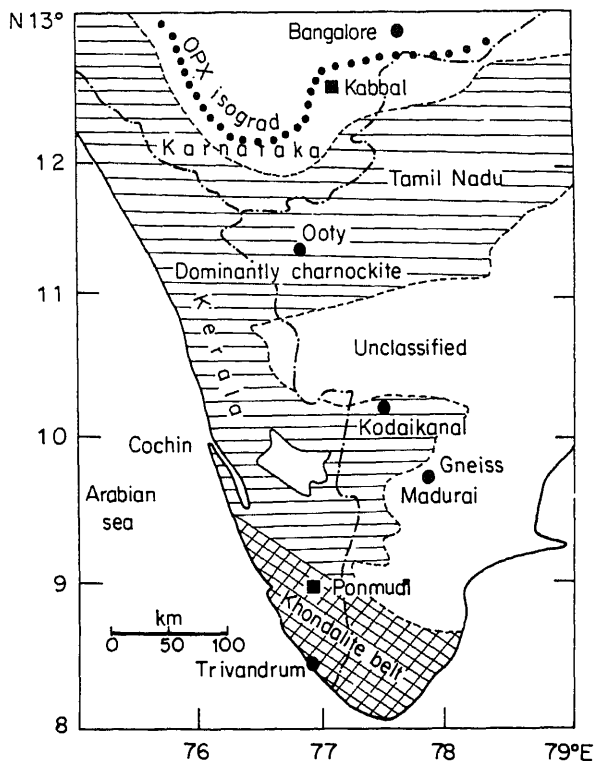


Figure 1. Generalised geological map of southern India modified after Rao (1978).

metamorphism is obtained from the U-Pb zircon data for charnockites from Ponmudi Hill which gives an age of c.540 m.y. and c.1930 m.y. (Bhul and Grauert 1985 pers. comm.).

3. Field relations and petrography

The area around Ponmudi is a hill resort situated about 60 km north of Trivandrum, at an elevation of 1074 metres above mean sea level. It is located in the northern portion of the Kerala khondalite belt (figure 1). The data presented here come from the quarries examined around Ponmudi and adjacent areas in southern Kerala. The proportion of gneiss-to-charnockite observed in these quarries can be approximated as 60:40. The gneiss is a medium-to-coarse grained leucocratic rock composed of garnet, biotite, feldspar, quartz and graphite. Mineral foliation trending N 70° W is defined by flakes of biotite and subhedral garnets. Graphite flakes are commonly noticed along the foliation planes. Thin leucocratic quartz and plagioclase-bearing acid veins in these rocks may be related to a period of migmatization preceding the formation of charnockite. Garnet, biotite and graphite are absent in these leucocratic acid veins. The garnet-biotite gneisses are interlayered with garnet-sillimanite and garnet-sillimanite-biotite-cordierite gneisses on various scales. As a result of deformation and migmatization, the metapelitic bands within the gneisses have been thinned and now occur as streaks and schlieren rich in garnet, sillimanite, biotite and cordierite. All these field evidences clearly indicate that the garnet-biotite gneisses undoubtedly represent metamorphosed pelitic sediments. This is also supported by abundance of graphite in the gneiss and their highly aluminous nature (table 1).

The garnet biotite gneiss is traversed by numerous coarse-grained, dark brownish charnockitic patches whose contacts with gneisses are diffused. These patches generally vary in size from 1 to 2 cm. Some reach to a maximum width of one metre (figures 2, 3 and 4). The development of charnockite with clots of orthopyroxene is seen concentrated in the sheared limbs and hinges of small scale folds. With the development of irregular greasy charnockitic patches there is a variable degree of obliteration of earlier foliation in the gneisses (figure 2 and 3). The distinct coarse-grained nature of charnockitic patches suggests thorough recrystallization. Quite often the gneissic foliation is bent or swerved at the borders of the charnockitic patches (figure 4). Close observation reveals the development of orthopyroxene along conjugate shears trending N 50° E and N 50° W, cross-cutting the earlier foliation. Orthopyroxene, often measuring upto 1-2 cm in size, is characteristic of the charnockite patches. Even some of the acid veins within the gneisses show development of charnockite patches suggesting that the granulite facies metamorphism followed migmatization.

A drastic reduction of biotites, the most common ferromagnesian mineral in the

Table 1. Chemical analyses of rocks and minerals from Ponnudi, Southern Kerala

	CS 35-1 wh. rock gneiss	CS 35-2 wh. rock charn.	CS 41-1 wh. rock gneiss	CS 41-2 wh. rock charn.	CS 35-1 garnet gneiss	CS 35-2 garnet charn.	CS 35-1 biotite gneiss	CS 35-2 biotite charn.	CS 35-1 opx charn.
SiO ₂	65.24	65.96	67.92	68.10	37.94	37.89	36.03	36.27	48.5
TiO ₂	0.86	0.84	0.90	0.77	0.04	0.04	4.82	3.91	0.2
Al ₂ O ₃	15.12	15.38	13.94	14.46	22.09	22.25	13.05	13.95	1.9
FeO [†]	5.98	5.51	5.80	4.94	33.88	33.65	19.10	19.61	37.1
MnO	0.05	0.06	0.08	0.04	0.45	0.67	0.02	0.02	0.2
MgO	1.89	1.36	1.06	0.95	3.95	3.62	11.32	10.85	11.0
CaO	2.95	2.73	2.39	2.62	1.63	2.06	0.02	0.04	0.2
Na ₂ O	2.44	2.16	2.45	2.81	0.46	0.05	0.0
K ₂ O	5.36	4.91	4.42	4.94	9.40	9.90	...
P ₂ O ₅	0.31	0.27	0.38	0.36
Total	100.20	99.18	99.34	99.99	99.98	100.18	94.22	94.60	99.3
FeO [†] = Total iron as FeO									
Trace elements in ppm									
Rb	251	196	190	153					
Sr	101	120	98	136					
Anorthite content of plagioclase: Charn. (35-2) = An33, Charn. (41-2) = An36									
Modal analyses	Garnet	Feldspar (plg + K-felds)	Biotite	Ortho- pyroxene	Quartz	Accessories			
Gneiss (CS 35-1)	12.20	48.85	16.40	...	22.20	0.35			
Charn. (CS 35-2)	10.10	57.50	5.20	10.50	16.28	0.42			
Gneiss (CS 41-1)	15.04	45.60	18.85	...	19.50	1.01			
Charn. (CS 41-2)	12.50	55.20	3.10	11.23	17.12	0.85			

Petrographic examination of the gneiss shows the presence of colourless inclusion-free granular garnet, pethites, dark brown biotite and quartz. The section study of charnockite shows the presence of large euhedral orthopyroxene developing after biotite (figure 5). Orthopyroxenes are generally fresh, pleochroic from pale pink to green. Occasionally pyroxenes show alteration to a brownish or pale green mineral which often follows grain boundaries or cleavage planes. The modal amount of biotite in charnockites is considerably low when compared to gneisses (table 1). Euhedral garnet crystals show a perfect equilibrium texture with pyroxene. Feldspars show a thorough recrystallization with the development of multiple twins. K-feldspar is commonly noticed. Apart from the gneiss-charnockite prograde relations noticed in many parts in southern Kerala, there are evidences particularly around Trivandrum, where retrogression of charnockites is so related to different dehydration processes (Ravindrakumar and Chacko 1986).



Figures 2-5. 2,3. Diffused dark brown charnockitic patch developing along shear planes. 4. Development of coarse-grained charnockite with clots of orthopyroxene. Note the gneissic foliation is bent at the charnockitic patches. 5. Orthopyroxenes growing at the expense of biotite polarised light ($\times 50$).

best exposure for the study of such a process is near Malayankil where charnockites show deformational features and have retrograded to biotite bearing gneiss. A detailed study of retrogression of charnockites and their age relationship will form another interesting study in southern Kerala.

4. Fluid inclusions

Fluid inclusion studies were carried out on a doubly-polished thin section using CHAIXMECA microthermometry apparatus. Heating and freezing data reported here are accurate to within $\pm 1^\circ\text{C}$.

Fluid inclusion studies in quartz grains from charnockitized portions show a presence of numerous arrays of optically dense monophase inclusions at room temperature. Fluid inclusions were also noticed in garnets. Fluid inclusions vary in size from 8 to 14 μm and some measure upto 20 μm , they occur in planar arrays in quartz grains. These inclusions are classified as pseudo-secondary, though such a term cannot be strictly applied to inclusions in metamorphic rocks. The gneisses also exhibit similar types of inclusions but the abundance of CO_2 -rich inclusions is less.

Temperature of first melting (T_m) of these monophase inclusions varies from -57.0 to -59.0°C which is below the normal CO_2 triple point of -56.6°C . This indicates the presence of CH_4 apart from CO_2 in inclusions. The amount of CH_4 estimated to be present in these inclusions (after Burrus 1981) would be 5 to 10 mol: NH_4 equivalent. Temperature of homogenization (T_h) of these monophase

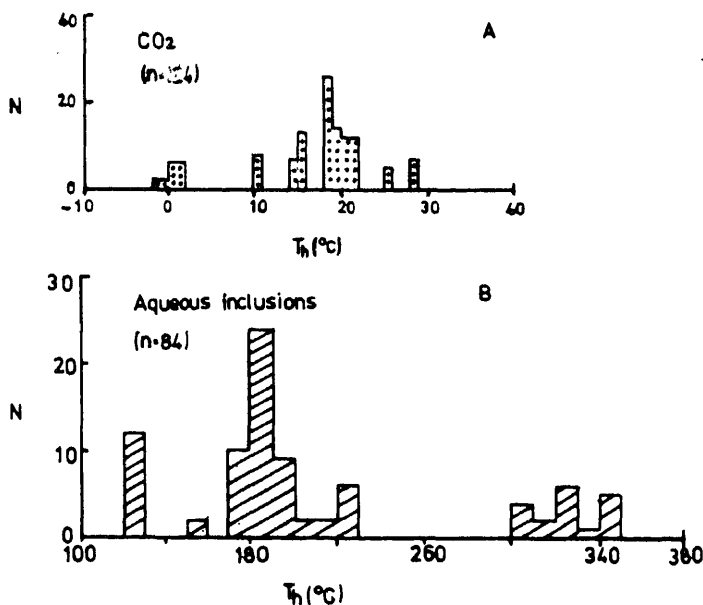


Figure 6. Homogenization temperature (T_h) of: A. Monophase CO_2 -rich inclusions and B. Aqueous inclusions.

inclusions varies from 2 to 28°C with a peak in the range of 15 to 20°C (figure 6a) corresponding to CO₂ density in the range of 0.78 to 0.81 g/cm³ (Touret and Bottinga 1979). Inclusions with two phases at room temperature which develop a third phase on cooling indicate the presence of CO₂ (liquid), CO₂ (gas) and H₂O (liquid). These inclusions range in size from 10–18 µm often reaching up to 25 µm. The CO₂ in the coexisting CO₂-H₂O inclusions homogenizes into liquid phase between 18 and 24°C with a peak around 20°C giving a density of 0.75 g/cm³ (Swanenberg 1980). CO₂ will homogenize with H₂O at a higher temperature of 200–250°C.

There is a third type of inclusion which is aqueous and seen all along rehealed microfractures. They show first melting at –2 to –5°C indicating low salinity of the order of 3 to 8 mol: NaCl equivalent (Sourirajan and Kennedy 1962). Temperature of homogenization of these inclusions varies from 120° to 380°C with a peak in the range from 160° to 180°C (figure 6b) corresponding to density in the range from 0.90 to 0.91 g/cm³ (Lemmlein and Klevtsov 1961).

5. Whole rock and mineral chemistry

The whole rock and mineral analyses are presented in table 1. Rock analysis was carried out by atomic absorption spectrometry; two sets of gneiss and the adjacent prograde charnockites were analyzed. Electron microprobe analyses of selected minerals from both the gneiss and charnockites are also reported in table 1.

The chemical composition of both gneiss and charnockite is almost identical except for slight increase of silica and alumina content in the charnockite. This points to the transformation of gneiss to charnockite under isochemical condition in conformity with a similar observation made by Ravindra Kumar *et al* (1985). The chemistry of mafic minerals shows a higher concentration of iron as against those reported from Kabbal (Janardhan *et al* 1979) and Kollegal areas (Hansen *et al* 1984). The Fe/Fe + Mg ratios of garnet, biotite and orthopyroxene are 0.82, and 0.65 respectively. Biotites are rich in TiO₂ content attesting to be a granulite facies variety stable at high temperature and low H₂O pressures (Engel and Engel 1960). Orthopyroxene is hypersthene in composition (En₃₅ Fs₆₅) with very low TiO₂, MnO and CaO content.

The PT conditions of metamorphism have been derived based on the composition of the minerals co-existing in gneiss and charnockites. The garnet-biotite K_D^{Fe-Mg} thermometry (Ferry and Spear 1978) gives a value of 700°C at 6 kbars which is somewhat lower. This has been attributed to the effect of high Al and Ti content in biotites (Ghent *et al* 1982). Garnet-orthopyroxene experimental K_D^{Fe-Mg} thermometry of Harley (1984) gives a value of 820 ± 60°C. The probable upper temperature limit may be obtained by the vapour absent melting reaction of biotite plus quartz to K-feldspar, orthopyroxene and liquid at 810°C at about 5 kbar (Luth 1967). Thus a reasonable temperature estimate would be 760 ± 40°C. The geobarometer of Perkins and Newton (1981) based on garnet-plagioclase-orthopyroxene-quartz exchange equilibrium gives a pressure estimate of 6.1 kbar at 760°C and 6 kbar at the same temperature (Bohlen *et al* 1983). These temperature and pressure estimates are in conformity with the results obtained by Ravindra Kumar *et al* (1985) and Srikantappa *et al* (1985).

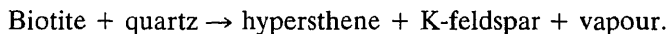
In South India, several workers have demonstrated prograde gneiss-charnockite relations (Pichamuthu 1960; Ramiengar *et al* 1978; Janardhan *et al* 1979; Friend 1981; Raith *et al* 1983). A comparison of the charnockites in the making at Kabbal and Ponmudi is attempted since such a study has regional geological implications. At Kabbal, amphibole-bearing gneiss of tonalitic to trondhjemitic composition is the predominant rock type with an assemblage of greenish brown amphibole, biotite, quartz and feldspar. The gneiss characteristically contains numerous basic inclusions with a mineralogy of greenish-brown hornblende, intermediate plagioclase, quartz and biotite. Both the gneisses and basic enclaves have been transformed to charnockite with the breakdown of amphibole to pyroxene. The process of charnockitization has been attributed to the massive influx of CO₂-rich fluids during metamorphism at low pressure of 3–5 kbar and at temperatures of 600–700°C (Janardhan *et al* 1979). Associated with charnockites at Kabbal are thin veins and sheets of K-rich granites. Generation of these K-rich granities is regarded to be pene-contemporaneous with the granulite facies metamorphism (Friend 1981). However, there are new field evidences to show that the K-rich granites (Closepet type granites) intruded only after the charnockitization of gneiss in this region (Srikantappa *et al* 1985).

The significant differences seen at Ponmudi when compared to the charnockite formation at Kabbal area are:

- (i) Garnet-biotite-feldspar-graphite bearing para-gneiss forms the precursor at Ponmudi in contrast to amphibole-bearing ortho-gneiss at Kabbal.
- (ii) There is a total absence of K-rich granitic veins or sheets at Ponmudi.
- (iii) There is a total absence of basic enclaves within the gneiss at Ponmudi.
- (iv) The formation of orthopyroxene has taken place by the breakdown of biotite at Ponmudi instead of hornblende as at Kabbal, a significant difference.
- (v) Pressure and temperature estimates indicate a somewhat higher grade for the formation of charnockite at Ponmudi as compared to the formation of charnockite in Kabbal area.
- (vi) Geochemical studies (Staele *et al* 1985; Hansen *et al* 1986) indicate that the process of charnockitization took place in an open system at Kabbal, whereas, at Ponmudi transformation of gneiss to charnockite is isochemical.

7. Discussion and conclusions

Field relations and petrography of the rock types around Ponmudi suggest that the garnet biotite bearing para gneisses have been transformed to charnockite during granulite facies metamorphism. Textural evidences indicate the formation of hypersthene by the breakdown of biotite in the presence of quartz following the reaction (Winkler 1976):



Chemical analyses of gneisses and charnockites show no change in the bulk composition of rock, except for the depletion of Rb and increase in Sr content in

the charnockite. The Rb loss may be due to the instability of biotite in charnockites. Similarity in the composition of gneiss and charnockite suggests that the process of charnockite formation at Ponmudi is essentially isochemical in contrast to the non-isochemical nature of charnockite formation at Kabbal, Karnataka.

The estimated pressure and temperature conditions of metamorphism obtained for the adjacent gneiss and charnockites in southern Kerala are almost the same: $760 \pm 40^\circ\text{C}$ and $6.0 \pm \text{kbar}$. Fluid inclusion studies suggest the presence of similar types of inclusions in both rock types but the charnockitized portions contain CO_2 -rich inclusions in greater abundance. The isochores for the three phase CO_2 - H_2O inclusions evaluated, based on the density data, ($p = 0.75 \text{ g/cm}^3$) pass through the pressure range of 5-6 kbar at temperature around 750°C . This could suggest the fluid entrapment near the peak metamorphic conditions. The density data of CO_2 -rich inclusions ($p = 0.78$ to 0.81 g/cm^3), however, indicate the significantly lower fluid pressures (2-4 kbar) of entrapment.

The present and the earlier reports of the progressive charnockitization of gneiss around Ponmudi and other parts of southern Kerala suggest that the whole of the Precambrian terrane in southern India from Kabbal and southwards has suffered granulite facies metamorphism. The crustal block, south of Achenkovil shear zone in southern Kerala appears to be entirely made up of a different lithological unit (predominantly metasedimentary) when compared to the rocks north of this shear zone (predominantly meta-igneous) as for e.g. in Idukki, northern part of Kodaikanal, Shevroy, Nilgiri and Biligirirangana Hill ranges. Further, preliminary age data of charnockites in Ponmudi suggest an younger granulite facies metamorphic event of Proterozoic age rather than Archaean. In these respects and in their lithological similarities, the crustal segment south of the Achenkovil shear zone may have similarities with Eastern Ghats. It is suggested that the crustal segment south of the Achenkovil shear zone was formed and welded to the polyphase Archaean crust in the north during the late Proterozoic times.

Acknowledgements

We thank Dr H K Gupta, Director, Centre for Earth Science Studies, Trivandrum and Prof. V Venkatachalapathy, Mysore University, for encouragement and support. Grateful thanks are due to Profs. R C Newton, M Raith and E C Hansen for helpful discussions and D Ackermund for mineral analyses presented here. One of us (C. S.) acknowledge the Volkswagen Research Foundation, Hannover, West Germany for presenting the CHAIXMECA microthermometry apparatus as gift to the Department of Geology, Mysore University and UGC (SAP) for grants.

References

- Condie K C, Allen P and Narayan B L 1982 Geochemistry of the Archaean low to high-grade transition zone, southern India; *Contrib. Mineral. Petrol.* **81** 157–167
- Crawford A R 1969 Reconnaissance Rb-Sr dating of Precambrian rocks of southern Peninsular India; *J. Geol. Soc. India* **10** 117–166
- Engel A E J and Engel C G 1960 Progressive metamorphism and granitization of the major paragneiss, northwest Adirondack mountains, New York; *Bull. Geol. Soc. Am.* **71** 1–20
- Ferry J M and Spear F S 1978 Experimental calibration of the partitioning of Fe and Mg between biotite and garnet; *Contrib. Mineral. Petrol.* **66** 113–117
- Friend C R L 1981 Charnockite and granite formation and influx of CO₂ at Kabbaldurga; *Nature (London)* **294** 550–552
- Ghent E D, Knitter C C, Raeside R P and Stout M Z 1982 Geothermometry and geobarometry of pelitic rocks, upper kyanite and sillimanite zones, Mica creek area, British Columbia; *Can. Mineral.* **20** 295–305
- Hansen E, Newton R C and Janardhan A S 1984 Pressures, temperatures and metamorphic fluids across an unbroken amphibolite facies transition in southern Karnataka, India; (eds) A Kroener, A M Goodwin and G N Hanson *Arch. Geochim.* (Berlin: Springer-Verlag) 161–181.
- Hansen E, Janardhan A S, Newton R C, Prame W K B N and Ravindrakumar G R 1986 Charnockite in the making in south India and Sri Lanka; *Contrib. Mineral. Petrol.* (submitted)
- Harley S L 1984 An experimental study of the partitioning of Fe and Mg between garnet and orthopyroxene; *Contrib. Mineral. Petrol.* **86** 359–373
- Holt R W and Wightman R I J 1983 The role of fluids in the development of granulite facies terrane of south India; *J. Geol. Soc. London* **140** 651–656
- Janardhan A S, Newton R C and Smith J V 1979 Ancient crustal metamorphism at low P_{H₂O}: charnockite formation at Kabbaldurga, South India; *Nature (London)* **278** 511–514
- Lemmlein G G and Klevtsov P V 1961 Relations among the principal thermodynamic parameters in part of the system H₂O-NaCl; *Geokhimiya* **2** 133–142
- Luth W C 1967 Studies in the system KAlSi₃O₈-Mg₂SiO₄-SiO₂-H₂O inferred phase relations and petrologic applications; *J. Petrol.* **8** 372–416
- Mahadevan T M 1974 The origin of the charnockite suite of rocks forming part of Western ghats in Kerala, India; *Inter. Geol. Congr.* **79** 130–149
- Narayana swamy S 1976 Charnockite-Khondalite and Sargur-Nellore-Khammam-Bengal-Deogarh-Pallahara-Mahagiri rock groups older than Dharwar type greenstone belts in the Peninsular Archaeans; *Indian Mineral.* **16** 16–26
- Perkins D and Newton R C 1981 Charnockite geobarometers based on coexisting garnet-pyroxene-plagioclase-quartz; *Nature (London)* **262** 144–146
- Pichamuthu C S 1960 Charnockite in the making; *Nature (London)* **188** 135–136
- Raith M, Raase P, Ackerman D and Lal R K 1983 Regional geothermobarometry in the granulite facies terrain of South India; *Trans. R. Soc. Edinburgh (Earth. Sci.)* **73** 221–244
- Ramiengar A S, Ramakrishnan M and Viswanatha M N 1978 Charnockite-gneiss-complex relationship in southern Karnataka; *J. Geol. Soc. India* **19** 411–419
- Rao P S 1978 Some aspects of structure and tectonics of Kerala region, India and related metallogeny In: *Tectonics and metallogeny of South-east Asia*; *Geol. Surv. India Misc. Publ.* **34** 61–64
- Ravindra Kumar G R, Srikanthappa C and Hansen E 1985 Charnockite formation at Ponmudi, Kerala, South India; *Nature (London)* **313** 207–209
- Ravindra Kumar G R and Chacko T 1986 Mechanisms of charnockite formation and breakdown in southern Kerala: Implications to the origin of southern Indian granulite terrain; *J. Geol. Soc. India* **28** 277–288
- Sinha Roy S 1979 Professional paper 2, Centre for Earth Science Studies, Trivandrum
- Sourirajan S and Kennedy G C 1962 The system H₂O-NaCl at elevated temperature and pressures; *Am. J. Sci.* **260** 115–141
- Srikanthappa C, Raith M and Spiering B 1985 Progressive charnockitization of a leptynite-khondalite suite in southern Kerala, India—Evidence for formation of charnockites through decrease in fluid pressure; *J. Geol. Soc. India* **26** 849–872
- Staele H J, Hoernes S and Raith M 1985 Granulitefazielle Umwandlung der Unterkruste: ein isochemischer Prozess *Annual Meeting of the German Mineralogical society Aachen Abstracts*
- Swanenberg H E C 1980 Fluid inclusions in high-grade metamorphic rocks from S W Norway; *Geologic Ultraflectina* **25** Utrecht

Analysis of gravity gradients over a thin infinite sheet

N SUNDARARAJAN, I ARUN KUMAR and N L MOHAN[†]

Centre of Exploration Geophysics, Osmania University, Hyderabad 500 007, India

[†] Present address: Al Fateh University, Tripoli, Libya.

MS received 19 April 1986; revised 9 October 1986

Abstract. A simple method to interpret gravity gradients over a thin infinite dipping sheet is discussed. The Hilbert transform is used to compute the vertical gradient from the horizontal gradient of the gravity field. The method is illustrated with a theoretical example.

Keywords. Gradients; Hilbert transform.

1. Introduction

Application of Hilbert transform to geophysical data interpretation has been gaining importance recently (Nabighian 1972; Sundararajan *et al* 1983; Sivakumar Sinha and Rambabu 1985). Nabighian discussed in detail the characteristics of the amplitude of the analytic signal and the subsequent interpretation of the body parameters, exclusively based on certain characteristic points on the amplitude curve. Sundararajan *et al* (1983) discussed a novel and simple technique to extract the body parameters. The method of Sivakumar Sinha and Rambabu (1985) is similar to that of Nabighian's but is called 'complex gradient' analysis.

All the above methods essentially make use of the Hilbert transform. We present a method for the interpretation of body parameters which also uses the Hilbert transform in a different way.

2. Theory

The geometry of the infinite thin dipping sheet is shown in figure 1 with h as the depth to the top, angle θ as the dip and σ as the density contrast.

The horizontal and vertical derivatives of the gravity field of such an infinite dipping sheet is given as (Sivakumar Sinha and Rambabu 1985)

$$g_x(x) = 2G\sigma t \left(\frac{h \cos \theta - x \sin \theta}{x^2 + h^2} \right), \quad (1)$$

$$g_h(x) = 2G\sigma t \left(\frac{x \cos \theta + h \sin \theta}{x^2 + h^2} \right), \quad (2)$$

where G is the universal gravitational constant and t is the thickness of the sheet.

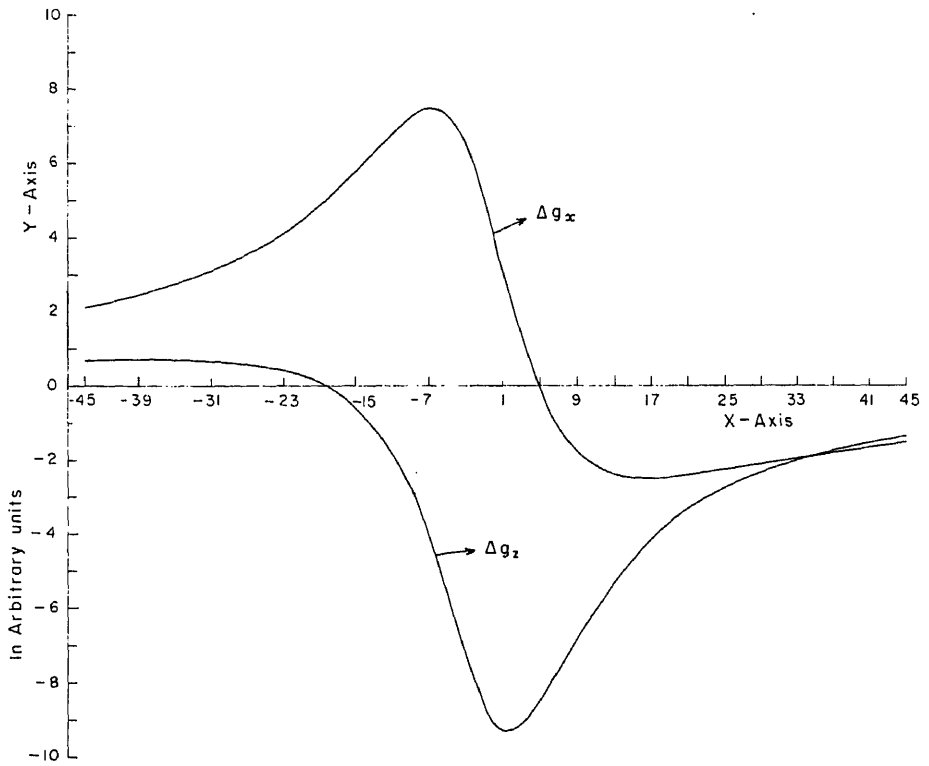


Figure 1. Computed horizontal and vertical gradients of the gravity field due to a thin infinite sheet.

According to Nabighian (1972) the horizontal and vertical derivatives form a Hilbert transform pair. That is, the vertical derivative is the Hilbert transform of the horizontal derivative and is given by

$$g_h(x) = \frac{1}{\pi x} * g_x(x) \quad (3)$$

where $*$ denotes convolution.

3. Location of origin

The analytic signal or the complex field intensity or even the complex gradient can be defined as

$$A(x) = F(x) + iH(x), \quad (4)$$

where $F(x)$ and $H(x)$ necessarily be a Hilbert transform pair. Either they can be horizontal and vertical derivatives of any order or simply the gravity/magnetic field.

4. Analysis

Equations (1) and (2) reduce to the following form at $x = 0$ as

$$g_x(0) = K \cos \theta/h, \quad (5)$$

$$g_h(0) = -K \sin \theta/h, \quad (6)$$

where $K = 2G\sigma t$.

The dip of the sheet (θ) can be evaluated from (5) and (6) as

$$\theta = \tan^{-1} [-g_h(0)/g_x(0)]. \quad (7)$$

Since (1) and (2) are of first degree in x , they ought to intersect at a point when plotted on the same scale. i.e.

$$g_x(x) = g_h(x) \text{ at } x = x_1. \quad (8)$$

Further simplification yields,

$$h = x_1 [(\sin \theta - \cos \theta)/(\sin \theta + \cos \theta)], \quad (9)$$

where x_1 is the abscissa of the point of intersection of the derivatives. As θ is known already, the depth h can easily be obtained.

At $\theta = 45^\circ$, $h = 0$ which is not true in the real sense. It is a rare theoretical concept with no practical significance.

Finally, squaring and adding (5) and (6) we get the constant term K as

$$K = [g_x(0)^2 + g_h(0)^2]^{1/2}. \quad (10)$$

From (10), either σ or t can be evaluated.

For a set of theoretical values of h , θ and K , the derivatives are computed as shown in figure 1. According to the procedure developed here, the parameters namely θ , h and K are evaluated as shown in table 1. The assumed and interpreted values closely agree with each other.

Table 1.

Parameters	θ (in degrees)	h (in meters)	K (in C G S units)
Assumed values	60.00	10.00	100.00
Present method	60.00	9.65	96.66

References

- Nabighian M N 1972 The analytic signal of two dimensional magnetic with polygenal cross section, its properties and use for automated anomaly interpretation; *Geophysics* **37** 507–512
- Sivakumar Sinha G D and Ram Babu H V 1985 Analysis of gravity gradients over a thin infinite sheet; *Proc. Indian Acad. Sci. (Earth Planet. Sci.)* **1** 71–76
- Sundararajan N, Mohan N L and Seshagiri Rao S V 1983 Interpretation of gravity anomalies due to some two-dimensional structures: A Hilbert transform technique; *Proc. Indian Acad. Sci. (Earth Planet. Sci.)* **92** 179–188

Precursory swarm and its application for long range earthquake forecasting in Taiwan region

V P SINGH and J SINGH

Department of Geophysics, Banaras Hindu University, Varanasi 221 005, India

MS received 27 April 1985; revised 5 August 1986

Abstract. At trenches a few earthquake swarms of low magnitude have been observed before the medium size earthquake swarms. The first swarm was designated as precursory swarm and the second as mainshocks. Seismicity fluctuations before six such mainshocks events of medium size earthquakes of magnitudes ranging from 5.3 to 6.1 occurring in the east belt of Taiwan region have been discussed. A precursory gap between the precursory swarm and mainshock events has been observed. The duration of the gaps increases with magnitudes of the mainshocks suggesting a causal relationship between the two. Regression equations between the largest magnitude in the precursory swarms, the largest mainshock magnitude and the precursory gaps have been given.

Keywords. Seismicity fluctuation; precursory swarm; regression equation; precursory gap.

1. Introduction

It has been observed that some earthquakes are preceded by a decrease in *P*-wave velocity (Scholz *et al* 1973; Robinson *et al* 1974; Dung Sung-Sheng *et al* 1977; Johnston 1978) and seismicity (Brady 1974, 1977; Rikitake 1975; Evison 1977a, b; Singh *et al* 1982; Singh and Singh 1984). The extent of such decrease depends on the magnitude of the ensuing earthquakes in the region. Scholz *et al* (1973) gave a relation between the length of the time for which the velocity decreases and the magnitude of the corresponding earthquake. Seismicity fluctuation studies may also be used to derive a mathematical relationship with the magnitude and time of occurrence of the mainshock and therefore may be used for long-range earthquake forecasting.

Evison (1977a) and Singh *et al* (1982) identified possible precursory swarms before a few earthquakes of New Zealand, Burma and Szechwan regions, analyzed the seismicity fluctuations of the region and recognized the following four episodes: the normal seismicity, the precursory swarm, the precursory gap and the major event. The occurrence of the four episodes was explained by a hypothesis known as swarm hypothesis. It is well known that at trenches, earthquakes occur due to plate movement. In these regions rocks may be assumed to be at different state of stresses as is obvious from the occurrence of the earthquakes. During plate movement some regions become active showing redistribution of stresses which increases the stresses in some localities beyond the strength of the material resulting in smaller earthquakes known as swarm. After the occurrence of the

swarm the stress in the region becomes homogeneous. The generated stress is due to the plate movement which continues for a longer period and the mainshock sequences result. The magnitude level in the precursory swarms is always less than the magnitudes level of the mainshock. Therefore, the largest magnitude in the precursory swarm can be correlated with the length of the gap period and the largest mainshock magnitude.

Evison (1977b) and Singh and Singh (1984) identified precursory swarms before a number of earthquakes of different regions. They established two statistical relations for the concerned regions between the precursory swarm magnitude, mainshock magnitude and the precursory time in days. The present analysis considers six moderate earthquakes from Taiwan region, all of which were preceded by identifiable swarm activity and precursory gaps. Expressions relating the magnitude of the largest event in the precursory swarm to the logarithm of the length of precursory gap in days and to the largest mainshock magnitude have been derived.

2. Seismicity of Taiwan and the surrounding areas

The seismicity of the Taiwan region is quite diffuse. Earthquake activity is believed to result largely from the subduction of the Pacific Plate beneath the Taiwan and the Ryukyu-Islands. On the basis of the distribution of the epicentres in the region, Hsu (1971) delineated three seismic zones namely the west, the east and the Ryutai seismic zones. These three zones and the earthquake epicentres considered in the present study are shown in figure 1. The west and east seismic zones run NNE–SSW. The Ryutai seismic zone has a WSW trend, and terminates in central Taiwan. The area common to the east seismic zone and Ryutai seismic zone is more active than the rest.

3. Data

The ISC regional catalogue of earthquakes for 1968–76 for the Taiwan region has been used to identify six earthquakes with magnitude ≥ 5.3 . These events were preceded by identifiable precursory swarms followed by a precursory gap as listed in table 1. The location of the epicentres and the precursory areas is shown in figure 1.

Seismicity fluctuation data for six events are discussed in the present analysis. Body wave magnitudes, focal depths and epicentres used are ISC estimates. In the regional catalogues, magnitudes and focal depths for a few earthquakes are not reported even by the local agencies. For such events, the body wave magnitude has been assumed to be a minimum of 4.0 and a shallow focal depth. The assumption of 4.0 magnitude may be valid, firstly, because the ISC and the other agencies have not reported body wave magnitude less than 4.0 for any earthquake of this region and, secondly, some of the events have been observed at about 10° epicentral distance. Shallow focal depths have been assumed for some of the swarm events because only about 5% of the earthquakes of the Taiwan regions occur below

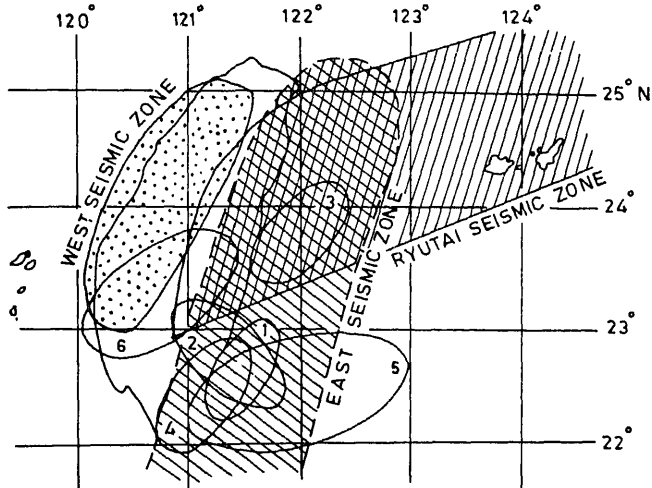


Figure 1. Different seismic belts of Taiwan region and the surrounding areas. The symbol ▨ denotes west seismic zones, ▩ Ryutai seismic zones, ▩ east seismic zones, and ▩ the common areas of Ryutai and east seismic zones (after Hsu 1971). The elliptical boundaries from 1 to 6 denote the approximate precursory areas for the considered medium size earthquakes.

Table 1. Major events with date, epicentre, focal depth and magnitudes. t_p is the time of precursory gap between swarm onset and the main shock (ISC data from the Regional Catalogue of Earthquakes).

Date	Lat. (°N)	Long. (°E)	Focal depth h (km)	Largest mainshock magnitude m_m	Largest magnitude in the pre- cursory swarm m_p	Approx. precursory area (km ²)	Time in days between swarm onset and largest mainshock magnitude t_p
26.02.68	22.76	121.47	8	6.0	5.4	4.2×10^3	530
14.11.70	22.82	121.36	26	5.7	4.8	7.77×10^3	380
16.02.71	24.03	122.18	46	5.7	5.0	8.66×10^3	408
22.09.72	22.37	121.15	8	5.7	4.3	5.60×10^3	261
23.03.75	22.68	122.84	29	6.1	5.5	2.47×10^4	412
14.04.76	23.29	120.76	37	5.3	4.5	1.75×10^4	287

60 km depth and, secondly, when a group of earthquakes occurring in the epicentral region are of shallow origin, the remaining one or two earthquakes of the same epicentral region occurring at the same time may be assumed to be shallow. For the sake of uniformity and availability of data, priority is given to the ISC data. The ISC estimates for any earthquake might vary with those given by other agencies. However, we feel that such variation in earthquake parameters would not change the nature of the regression equation.

A swarm has been described as a series of events which occur in an area over an interval of time and may extend to several months without any outstanding principal event (Bullen 1965). Therefore, earthquake magnitude is considered as a critical parameter in identifying the precursory swarms. In earlier studies the difference between the largest and the second largest magnitude of the events in precursory swarm ranged from 0 to 0.3 (Evison 1977b). For the Gulf of California region Evison (1977b) considered the magnitude difference upto 0.5 in identifying the swarm. In the present analysis, for uniformity, ISC body wave magnitudes have been selected from the Regional Catalogue of Earthquakes. In this case, the magnitude difference between the largest and second largest event of the precursory events is ≤ 0.3 except for events 1 and 6 for which the differences are 0.4 and 0.5 respectively. Bath (1973) pointed out that even in the best cases, errors of 0.2–0.3 units can be expected in calculated magnitudes. No event of the precursory swarm can therefore be considered as an outstanding principal event and hence all the precursory events may be collectively classified as a swarm. In major event sequences, earthquakes of magnitude ≥ 5.0 have been considered as they are recorded at teleseismic distances. In some cases only one major event connected with the local tectonic environment occurred.

5. The precursory swarm and regression equations

Precursory swarms and gaps have been identified for six intermediate magnitude earthquakes belonging to the same tectonic regions. Their magnitude varied from 5.3 to 6.1 (table 1). The epicentres of the precursory swarm, mainshock sequence and aftershocks for the six main events are shown in figure 2. Seismicity data for 6 months from the time of occurrence of the mainshock have been considered as aftershocks of the main event sequences. The representative source regions for the occurrence of the mainshocks have been approximated using epicentres of precursory swarms, main event sequences and after-shocks. The representative source regions have been demarcated by elliptical boundaries for all the six main events. For event no. 3 the position of elliptical boundaries may vary due to paucity of aftershocks in the regions. These areas are shown in table 1. In some cases, the epicentre of the main event is at the corner of the precursory elliptical areas. The occurrence of mainshock near the boundary of the precursory area was reported by Mogi (1968). In some cases the main events are surrounded by precursory swarm events. The four episodes for the six earthquakes have been shown in figure 3(a). Figure 3(b) shows the relationship between swarm and mainshock magnitudes. Table 1 shows that the difference between the mainshock magnitude (m_m) and the largest swarm magnitude (m_p) ranges from 0.6 to 1.4 units.

To draw regression lines, it is assumed that linear relationships exist between m_m and m_p as well as between the logarithm of precursory time in days ($\log_{10} t_p$) and m_p . The distributions of m_m and $\log_{10} t_p$ are assumed to be normal. Figure 4(a) shows the plot of m_m versus m_p and figure 4(b) shows precursor time t_p on logarithmic scale versus m_p along with the regression lines. These regression equations are

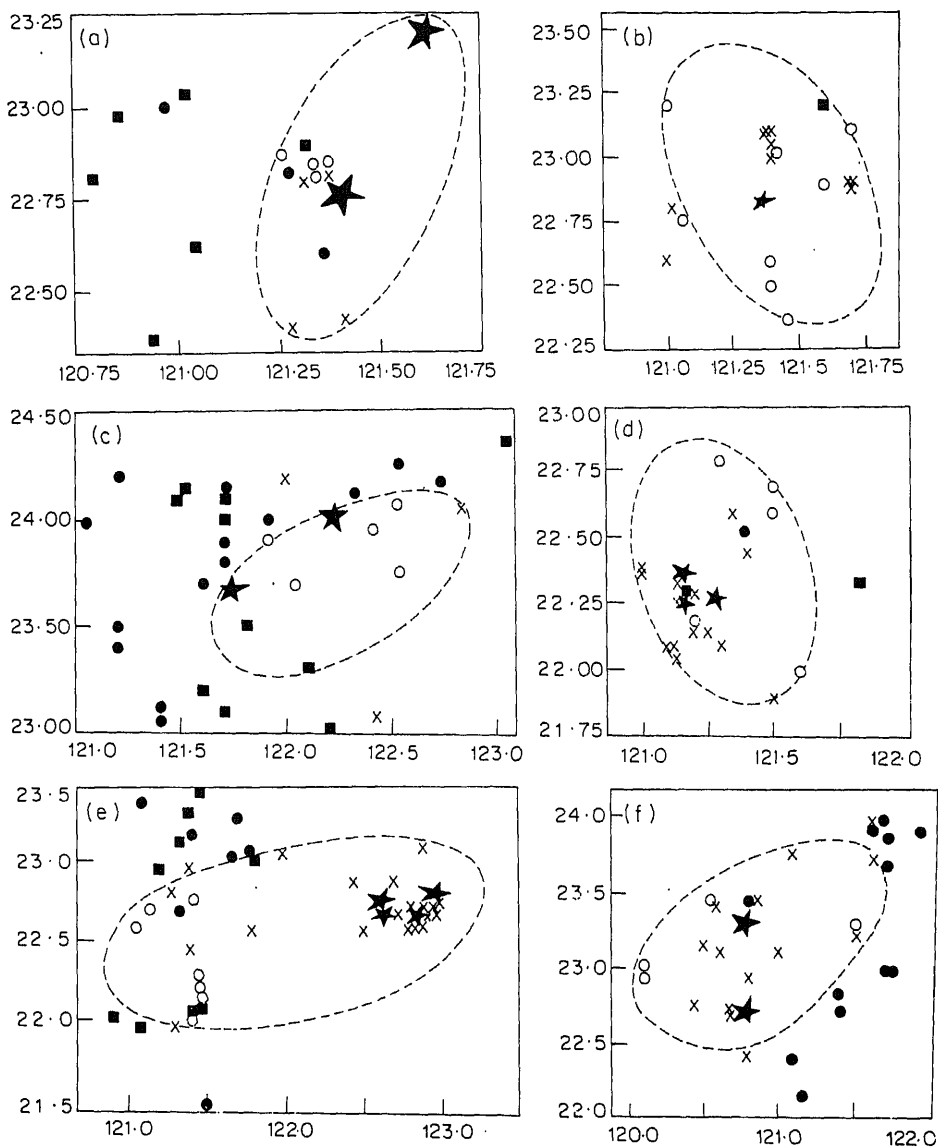


Figure 2. Epicentral maps for the six earthquakes along with precursory swarms. The precursory areas have been approximated by precursory swarm, mainshocks and aftershock sequences. In aftershocks six months seismicity data of the region from the time of the occurrence of the mainshock have been plotted. All the events show elliptical precursory area. The symbol ■ denotes normal seismicity (i.e. the seismicity pattern of the region before the precursory swarm). ○ denotes precursory swarm, ● denotes precursory gap event (i.e. the seismicity pattern of the region between precursory swarm and main event sequences), * denotes major event with magnitude ≥ 5.0 and × denotes aftershocks which continues upto six months in the region.

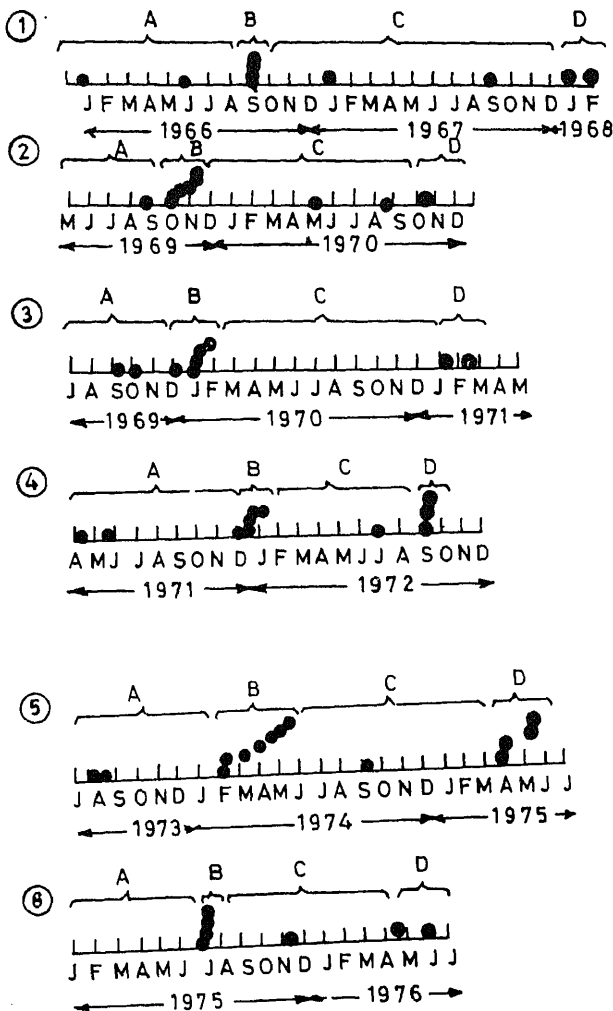


Figure 3a. Fluctuation of seismicity within the precursory areas. A denotes normal seismicity, B the precursory swarms, C the precursory gap events and D the major event sequences. Solid circles indicate the number of earthquakes in the months. They have been kept one over the other to show that the events have occurred in short intervals. In major events, earthquakes of magnitude ≥ 5.0 only have been considered.

$$m_m = 0.47 m_p + 3.44, \quad (1)$$

and

$$\log_{10} t_p = 0.21 m_p + 1.52. \quad (2)$$

The regression lines represent the least square fits. The upper and lower regression lines show 95% tolerance limits for six degrees of freedom to estimate m_m and t_p respectively. The standard error of estimates for (1) and (2) are 0.18 and 0.057 respectively. Both regression lines are significant as the square root of correlation

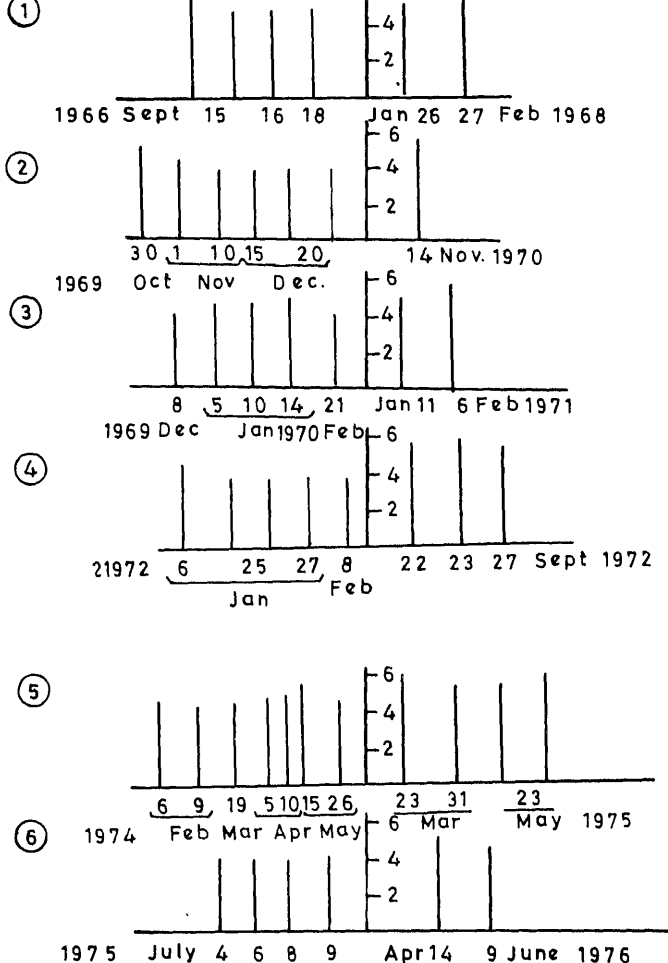


Figure 3b. Magnitude relationships in precursory swarm and major events. A magnitude of 4.0 has been assumed for the earthquakes whose magnitude is not mentioned in the Bulletin. It is quite possible that the magnitude of some earthquakes may be < 4.0. However, the magnitude of these earthquakes has been assumed to be 4.0 just to draw magnitude relationships. The magnitude of these small earthquakes does not change the analysis and the interpretation.

coefficient $R = 0.81$ for m_m and $R = 0.9$ for $\log_{10} t_p$. If m_p is known, m_m and t_p can be estimated. Similar regression equations have been reported by Evison (1977b) and Singh and Singh (1984) for other regions. The values of the constants differ from region to region suggesting different tectonic environments.

5. Discussion

In the present study, nine years of seismicity data (1968–76) of Taiwan region have been considered. The data were taken from the Bulletin of the Regional

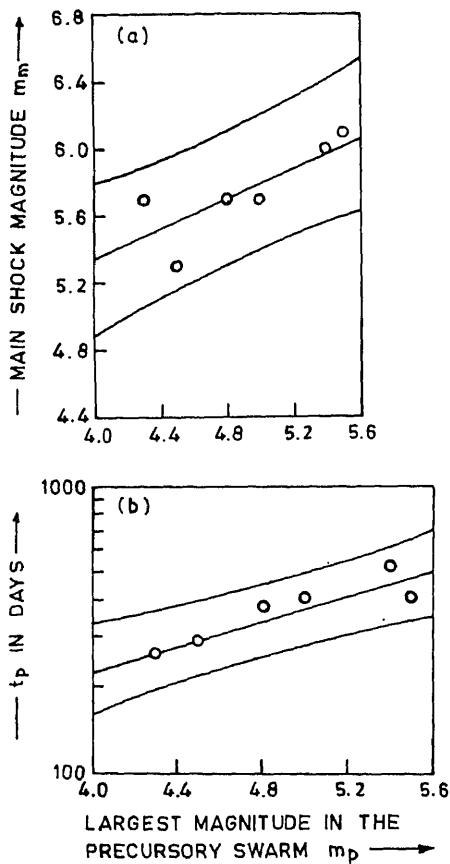


Figure 4. Variation of (a) mainshock magnitude m_m with largest magnitude in the precursory swarm m_p , (b) precursor time t_p in days with the largest magnitude in the precursory swarm. Here t_p is the time from the day on which the precursory swarm begins to the occurrence of the major event.

Catalogues of Earthquakes. A total of 52 earthquakes with body wave magnitudes ≥ 5.3 occurred during the considered period. Of these, 16 earthquakes (i.e. about 33% of the total earthquakes of $m_b \geq 5.3$) are related with six sets of precursory swarms and mainshock sequences which have been studied here. The remaining 36 earthquakes are not preceded by swarm activity in the epicentral region. In each set the largest magnitude of the former swarm is always much less than its largest mainshock magnitude. Therefore, the former swarms may be considered as precursory swarms to the latter ones.

Results obtained by Evison (1977b), Singh and Singh (1984) and the present study indicate that swarm activities in a tectonically active region can be used as a predictive parameter to estimate the magnitude and time of occurrence of future earthquakes. Figures 4(a,b) demonstrate a relationship between the largest magnitude and the precursor time. If data for lower magnitude earthquakes were included in the analysis, the value of the constants would have changed by a small

amount and the tolerance limites might have been further reduced. However, the change would not have been significant as the slope of the lines is gentle. It seems therefore that the magnitude and the time of occurrence of medium size earthquakes ($5.3 \leq m_m \leq 6.1$) can be estimated for the east seismic zone of Taiwan, if the swarm activity could be identified.

The difference between the main event magnitude and the largest magnitude in the precursory swarm for the region decreases from 1.4 to 0.6 as the mainshock magnitude increases from 5.3 to 6.1. The regression equations cannot be used to estimate earthquakes of magnitude > 6.1 since the difference between m_m and m_p decreases considerably at higher magnitudes.

7. Conclusions

The study for Taiwan region reveals that: (a) Precursory swarm is a possible precursor for earthquakes (b) The largest magnitude in the precursory swarms is related to the magnitude and the time of occurrence of the mainshock (c) Earthquakes of magnitude ≥ 5.3 and ≤ 6.1 could be predicted if swarm activity can be identified in the region.

Acknowledgements

The authors thank to Dr H K Gupta, Director, CESS, Trivandrum and Prof. N Toksoz of MIT for offering many valuable suggestions.

References

- Bath M 1973 *Introduction to seismology* (Basel and Stuttgart: Birkhauser Verlag) p. 111
- Brady B T 1974 Seismic precursors before rock failures in mines: *Nature (London)* **252** 549–552
- Brady B T 1977 Anomalous seismicity prior to rock burst: Implications for earthquake prediction; *Pure Appl. Geophys.* **115** 357–374
- Bullen K E 1965 *An introduction to the theory of seismology* (Cambridge: University Press) p. 287
- Dungsung-Sheng, Ce Huan-Chan Lo Yong-Lian and Hsu Chaoyong Wang Feng-Chi 1977 Prediction of earthquakes on the basis of velocity ratio—A case history (Abstract): Joint Assemblies IASPEI and INVCEI, Durham
- Evison F F 1977a Fluctuations of seismicity before major earthquakes: *Nature (London)* **266** 710–712
- Evison F F 1977b The precursory earthquake swarm: *Phys. Earth Planet. Interiors.* **15** 19–23
- Hsu M T 1971 Seismicity of Taiwan and some related problems: *Bull. Int. Inst. Seismol. Earthquake Eng.* **8** 41–140
- Johnston A C 1978 Localized compressional velocity decrease precursory to the Kalapana Hawaii earthquake: *Science* **199** 882–885
- Mogi K 1968 Development of aftershock areas of great earthquake: *Bull. Earthquake Res. Inst.* **46** 175–203
- Regional Catalogue of Earthquakes (Edinburgh): 1968–1976
- Rikitake T 1975 Earthquake precursors; *Bull. Seismol. Soc. Am.* **65** 1133–1162
- Robinson R, Wesson R L and Ellsworth W L 1974 Variation of *P*-wave velocity before the Bear Valley California earthquake of 24 February 1972; *Science* **184** 1281–1283
- Scholz C H, Sykes L R and Aggarwal Y P 1973 Earthquake prediction: a physical basis: *Science* **181** 802–805

Results from the Indo-USSR ozonesonde intercomparison experiment

B H SUBBARAYA^{1*}, K S APPU², K P CHATTERJEE³, A F CHIZHOV⁶, V D GRINCHINKOV⁶, A JAYARAMAN¹, G A KHOKIN⁶, V A KONONKOV⁶, I S MOSHNIKOV⁶, V NARAYANAN², S P PEROV⁶, O V SHTRIKOV⁶, Y V SOMAYAJULU⁵, C R SREEDHARAN⁴ and K S ZALPURI⁵

1. Physical Research Laboratory, Ahmedabad 380 009, India
2. Vikram Sarabhai Space Centre, Trivandrum 695 022, India
3. India Meteorological Department, New Delhi 110 003, India
4. India Meteorological Department, Pune 411 005, India
5. National Physical Laboratory, New Delhi 110 012, India
6. Central Aerological Observatory, State Committee for Hydro-meteorology and Control of Natural Environment, USSR.

MS received 30 June 1986; revised 18 October 1986

Abstract. A total of seventeen vertical profiles of ozone were obtained during an Indo-USSR collaborative experiment on ozonesonde intercomparison conducted at Thumba during March 1983. The vertical distribution of ozone was measured using rocket-borne, balloon-borne as well as ground-based instruments. Four different rocket ozonesondes from India and USSR and the balloon ozonesonde were used to make *in situ* observations of ozone concentrations in addition to the Dobson spectrophotometric observations of total ozone and Umkehr. The rocket and the balloon launchings were effected in three salvos and measurements were made at different times of the day as well as during night. The results of all these measurements are used to obtain a mean ozone vertical distribution over Thumba for the spring equinoctial period. The mean profile shows the maximum ozone concentration at 27 km with a value of $(3.86 \pm 0.52) \times 10^{12}$ molecules per cc. Comparison of this mean profile with available satellite data for the equatorial regions shows that, in general, the Thumba values are lower by 10–15% at altitudes below 40 km and larger at altitudes above 50 km compared to the satellite results. The data also show evidence for a day-to-day variability and a possible day-to-night variability in the ozone vertical distribution with the night-time values higher than the daytime values at all altitudes above 35 km and the difference is found to increase with the increasing altitude.

Keywords. Ozone; intercomparison; vertical distribution; variability.

1. Introduction

A systematic programme of monitoring atmospheric ozone in the Indian zone has been in progress for quite some time with a Dobson spectrophotometer network of five stations at Kodaikanal (10°13' N), Pune (18°31' N), Varanasi (25°19' N), New Delhi (28°35' N) and Srinagar (34°08' N) maintained by the India Meteorological Department and at Mt Abu (24°30' N) that is being maintained by the Physical Research Laboratory, Ahmedabad. Regular balloon soundings for the measurement of ozone vertical profile are being conducted by the India Meteorological

* To whom all correspondence should be addressed.

Department from Trivandrum (8°31' N), Pune (18°31' N) and New Delhi (28°35' N) for more than a decade. The data from these programmes have been used in several studies of the low latitude ozone morphology as well as studies of short-term and long-term changes in ozone, their association with climatological features, solar and geophysical parameters etc. The balloon and the Umkehr data have recently been used to construct a reference ozonosphere for the Indian zone (Kundu 1982).

Vertical distribution of ozone, especially at altitudes above 30 km, is important for understanding the stratospheric chemistry as well as the ozone depletion problem. The Umkehr data is model-dependent, has poor vertical resolution and assumes that there are no temporal variations shorter than a few hours. This can give rise to some uncertainties in the upper levels where the photochemical time constants are small. Balloons used for regular ozone soundings rarely reach altitudes more than 30 km. *In situ* measurements with rockets and the satellite-borne sensors provide information on the vertical distribution of ozone at upper stratospheric and mesospheric levels. There are a few measurements available for mid-latitudes, especially from Wallops Island. These have been used to construct a model for the mid-latitude ozone distribution (Krueger and Minzner 1976). The vertical distribution in the tropics is expected to be different and there is not much of observational data from the tropical sites. With the advent of satellites, there has been a significant improvement and now there is a certain amount of data available even for the equatorial regions (McPeters *et al* 1984). While the satellite sensors give a large amount of data and provide a global coverage with better statistics, the vertical resolution is still poor, being of the order of 8 km and the satellite data reduction techniques depend largely on ground truth provided by Dobson and Umkehr data. *In situ* measurements with rockets have the disadvantage that they cannot provide a continuous data and the spatial and temporal frequency of soundings is limited. But they give height profiles with good vertical resolution. A resolution of 1 km or better can be achieved with most sensors. However, there is a need for an intercomparison of different rocket sensors if data from different sensors are to be used in morphological studies and to construct a global model. This need has been well appreciated and there have been several intercomparison experiments conducted in recent years.

A solar MUV photometer has been developed at the Physical Research Laboratory, Ahmedabad to measure the ozone concentrations at stratospheric and mesospheric levels and a few experiments have been conducted at the tropical site, Thumba, to study the vertical distribution of ozone in the tropics (Subbaraya and Shyam Lal 1981) and the transient changes produced during a solar eclipse (Lal and Subbaraya 1983). An instrument has also been developed at the National Physical Laboratory (NPL), New Delhi and flown from Thumba (Somayajulu *et al* 1981). The instrumentation for the IMD balloon ozonesonde has undergone significant improvements in recent years and the measurements made since 1980 are believed to be much more reliable than those made in earlier years. Further, there have been some shipboard rocket launches by the Soviet Union off the coast of South India for measurements of ozone concentration profiles over low latitudes. An Indo-USSR collaborative ozonesonde intercomparison experiment was conducted at Thumba during March 1983 with a view to intercompare these instruments. The experiment included all the rocket ozonesondes currently in use in India and the

photometric observations, surface ozone measurements and filter photometer observations.

2. The ozonesonde intercomparison experiment at Thumba

The experiment involved the launching of thirteen rocket ozonesondes, six contributed by the Central Aerological Observatory of USSR including three optical ozonometers for day-time measurements and three chemiluminescent ozonesondes for night-time measurements. India contributed seven ozonesondes, three photometers for day-time measurements and one for night-time measurements from Physical Research Laboratory (PRL) Ahmedabad and three optical ozonesondes from the National Physical Laboratory, New Delhi for day-time measurements. In addition to these rocket flights, three meteorological rockets and eleven balloon ozonesondes from IMD were also launched during the programme. The rocket and balloon launchings were supported by onsite Dobson spectrometer observations of both total ozone and Umkehr by IMD, filter photometer observations made by the Indian Institute of Tropical Meteorology, Pune, as well as surface ozone observations made by IMD. The rocket and balloon launchings were effected in three salvos on 23 March 1983, 28/29 March 1983 and 31 March 1983. Near simultaneous measurements were made by different rocket and balloon sensors during morning hours, afternoon hours as well as night-time periods. The details of the measurement programme and the results of a study on intercomparison of different sensors are reported by Acharya *et al* (1984). However, the experiment yielded a data set of eleven rocket profiles, five balloon profiles in addition to the Umkehr data, all collected within a reasonably short time of eight days. In this study an attempt has been made to delineate from the data collected during the intercomparison experiment, the basic features of the vertical distribution of ozone and construct a reference ozone profile for the tropical site, Thumba.

3. Experimental results

Rocket data

Figure 1 shows the data obtained from three day-time flights of the PRL optical ozonesonde flown on 23 March at 9.15 hr and 15.45 hr IST and on 28 March at 15.30 hr IST respectively. The night-time launch of the PRL lunar MUV photometer made at 23.35 hr IST on 28 March failed to give any data due to a malfunction of the onboard electronics. The day-time optical ozonesonde was a four-channel instrument working at 250 nm, 280 nm, 310 nm and 450 nm respectively and yielded data typically in the altitude region of 16 km to 60 km. The inset in figure 1 illustrates the accuracy of measurements. The uncertainties which are mostly due to random errors are partly due to errors in the measurement of the sensor current and partly due to uncertainties in the estimation of the rocket attitude and the consequent correction factors to be applied. The net uncertainty in

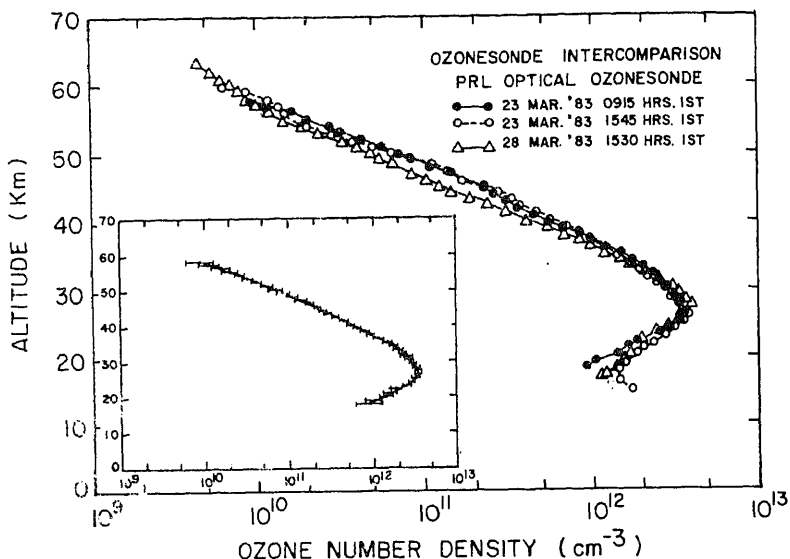


Figure 1. Ozone concentration profiles from the three PRL rocket ozonesondes flown on 23 and 28 March 1983. The inset shows typical uncertainties in the ozone concentration estimates.

the estimation of ozone concentration is of the order of $\pm 25\%$ at 20 km, decreases to $\pm 10\%$ in the altitude range of 30 to 35 km and $\pm 5\%$ in the altitude range of 35 to 45 km. At altitudes above 45 km the errors increase rapidly with the increasing altitude reaching a value of $\pm 20\%$ at 50 km and $\pm 50\%$ at 60 km. The larger uncertainties in the altitude region above 50 km are mostly due to the change in the rocket attitude in this region and the resulting uncertainties in the aspect correction employed. The instrument in principle is capable of measuring the ozone concentrations of the order of 1×10^{10} molecules per cm^3 with an uncertainty of $\pm 20\%$ or less. The data of figure 1 show that the ozone concentration peak is attained at an altitude of 27 km with number densities ranging between 3.2 and 3.6×10^{12} per cc. The ozone concentration values are, in general, lower by about 30% on 28 March 1983 than on 23 March 1983 in the entire altitude region of 30 to 60 km. This will be discussed in greater detail later.

Measurements are available from two of the three flights that were conducted with the NPL optical ozonesonde. The measurements were made in the afternoon hours, at 16.10 hr IST on 29 March 1983 and 15.53 hr IST on 31 March 1983 respectively. The data are shown in figure 2. The instrument was a two-channel photometer operating at wavelengths of 255 and 290 nm and was expected to yield ozone concentrations in the altitude range of 30 to 60 km. Since the instrument suffered from a delayed door ejection on both the flights, the data collected during the descending portion of the rocket trajectory had to be used for analysis. The rocket executes a large coning motion during its descent and the aspect corrections that have to be applied are generally large. The data shown in figure 2 are the result of smoothing the original data and the error bars amounting to $\pm 20\%$ on the flight of 29 March 1983 and $\pm 30\%$ on the flight of 31 March 1983 represent the spread

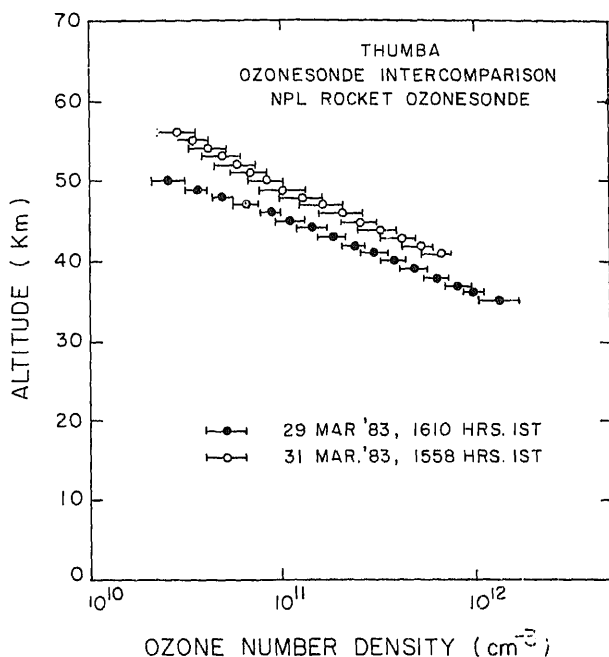


Figure 2. Ozone profiles from the two NPL ozonesonde rocket ozone-flights on 29 and 31 March 1983.

around this smoothed line. The data show that the ozone concentrations were, in general, lower on 29 March 1983 than on 31 March 1983 and the differences in the region of overlap amounting to 50–60% are qualitatively similar to the result from the PRL instrument.

Figure 3 shows the three profiles obtained by the Soviet optical ozonometer, two on 23 March at 08.20 hr IST and 16.50 hr IST respectively and the third on 31 March at 17.20 hr IST. The instrument was a two-channel photometer working at 260 nm and 300 nm respectively and the measurement errors are typically of the order of 25% at 20 km and are much smaller in the 30 to 45 km altitude region (Brezhgin 1982). Maximum ozone concentrations are in the range of $3.2\text{--}4.2 \times 10^{12}$ molecules per cc. While the three profiles show very good agreement in the range of 35 to 50 km, at lower altitudes they show a larger spread. The profile obtained at 08.20 hr on 23 March 1983 shows a double-peaked structure. The afternoon profile of 23 March 1983 shows maximum ozone at 22 km which is quite unusual. None of the previous measurements at Thumba show an ozone maximum at such a low altitude. This could be due to the large slant optical path that solar rays had to traverse before reaching the detector and the consequent uncertainties/inaccuracies in the air mass correction used. The solar zenith angle at the time of launch was 61° .

Figure 4 shows the data obtained from the three Soviet chemiluminescent

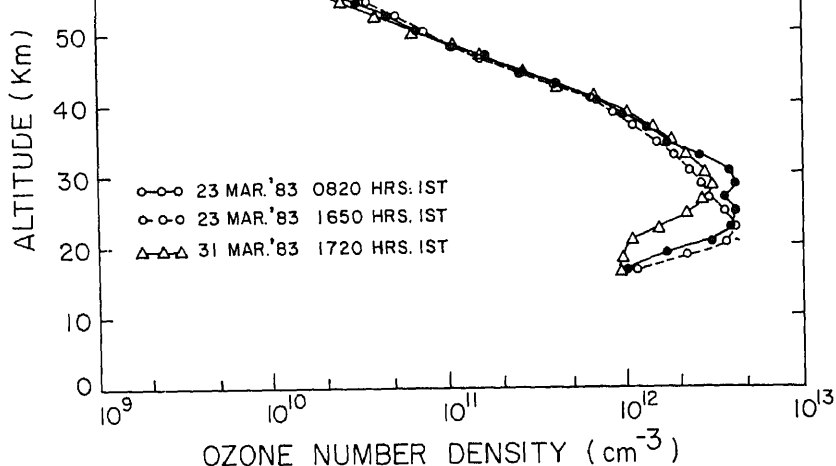


Figure 3. Ozone concentration profiles obtained from the three Soviet optical rocket ozonometers flown on 23 and 31 March 1983.

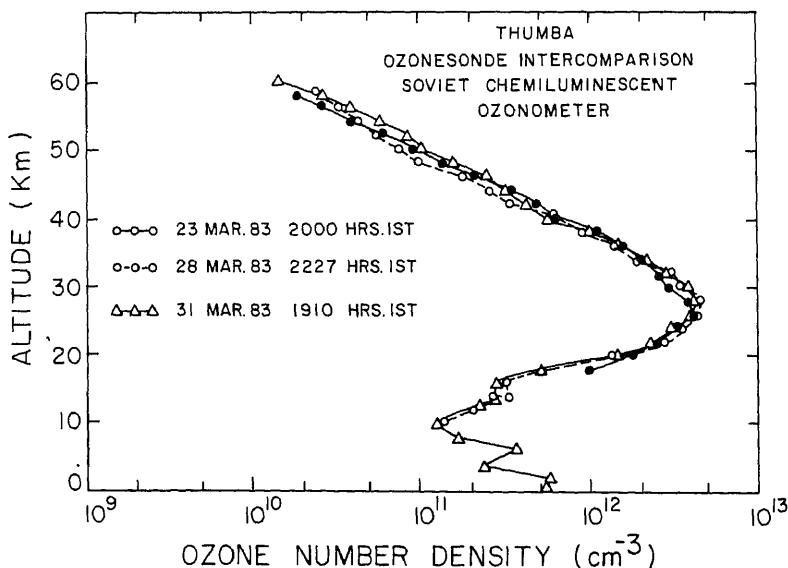


Figure 4. Ozone concentration profiles obtained from the three Soviet chemiluminescent rocket ozonesondes flown on 23, 28 and 31 March 1983.

the ground as illustrated by the data of 31 March 1983. On the flights of 23 and 28 March 1983 data could be obtained down to 18 km and 10 km respectively. The ozone number densities are obtained by first integrating the rocket profile and comparing the integrated ozone amount with the total ozone content for that day as given by the Dobson spectrophotometer. A height-independent correction factor is

current into ambient ozone mixing ratios and random errors in measurement of photometer currents. Absolute errors in the calibrating factor due to possible day-night variations in total ozone are likely to be small. These errors are in the range of 7–15% upto about 40 km and increase to much higher values at altitudes above 40 km (Kononkov *et al* 1982). The data of figure 4 show that the maximum ozone level is situated in the 26–28 km region with peak values ranging between 4.1 and 4.7×10^{12} molecules/cc. These values are larger than the maximum ozone concentrations of $3.2 - 4.2 \times 10^{12}$ molecules/cc estimated by the day-time optical ozonesondes. Further, the 31 March 1983 profile shows marked structures in the troposphere. This is an unusual feature, not generally seen on the balloon profiles. This particular rocket flight took place under thunderstorm conditions and there is evidence that the rocket trajectory intercepted the region of thunderclouds and lightning. It is believed that lightning produces NO_x in the tropical troposphere which enhances the ozone concentration (Ko *et al* 1986).

3.2 Balloon data

Eight successful balloon ascents were made with the IMD electrochemical-ozonesondes from Trivandrum during the period 4 March 1983 to 5 April 1983. The data from these flights are shown in figure 5. The balloon reached a peak altitude of 25–26 km or less on many of the flights and only in a few cases did the balloon penetrate the peak of the ozone layer which has been revealed to lie in the altitude range of 26–28 km from the rocket data. The procedure for obtaining absolute values of ozone concentrations involves converting the instrument signals into ozone mixing ratios using laboratory calibration of the instrument and obtaining a

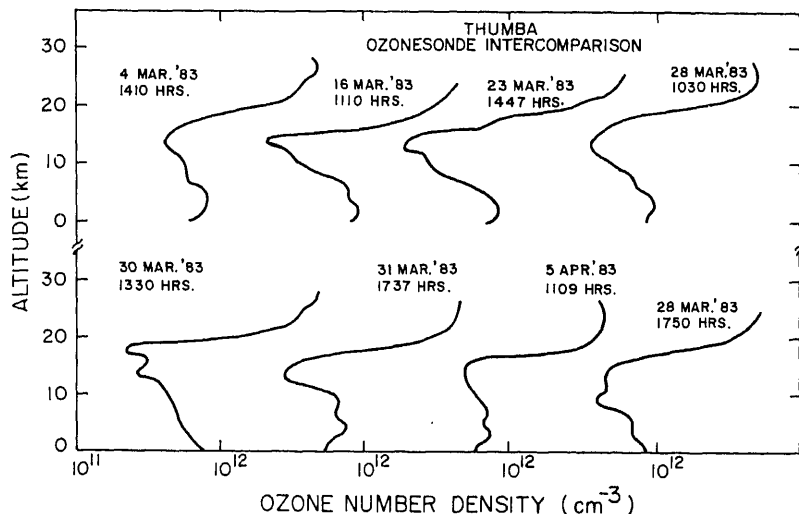


Figure 5. Balloon ozonesonde data obtained at Thumba during the intercomparison experiment.

first order ozone profile which is integrated to obtain the total ozone content. It is assumed that ozone maintains a constant mixing ratio above the peak. The resulting total ozone content is then compared with the Dobson spectrophotometer data for total ozone and a blanket height-independent correction factor is applied to give the final ozone profile. If the balloon does not penetrate the peak ozone level and ascend at least a few kilometers higher, this procedure can give rise to significant errors in the estimation of ozone concentrations. A significant fraction of the total ozone amount is contained in the region ± 5 km around the peak. Ozone chemistry in this region is quite complex and ozone concentrations in the first 5 to 10 kms above the peak level do not maintain a constant mixing ratio. The situation becomes critical at tropical/equatorial stations where the peak of the ozone concentration profile is higher than at middle or higher latitudes. The anomalies that can arise are illustrated in table 1 which shows the maximum height attained by the balloon, the maximum ozone level as detected by the balloon ozonesonde and the maximum ozone concentration value for the eight balloon ascents conducted during the intercomparison period.

A careful examination of the data of table 1 shows that when the balloon measurements are available beyond the ozone maximum, the detected level of maximum ozone nearly coincides with that obtained by rocket ozonesondes. However, when the balloon does not penetrate the ozone maximum and the measured profile is extrapolated upwards on the assumption of a constant mixing ratio above the balloon burst level the recorded value of the peak ozone density becomes larger than the actual values. At a tropical site like Trivandrum, unless the balloon reaches a peak altitude of about 30 km, it is not possible to make a proper assessment not only of the level of maximum ozone but also of the absolute values of the ozone concentrations from the balloon data. The Umkehr data for Trivandrum always shows maximum ozone in layer 5 which corresponds roughly to the altitude region of 24 to 28 km and never at lower levels. The maximum ozone concentrations obtained from the Umkehr analysis (figure 6) are in agreement with

Table 1. Balloon ozonesonde data—peak level and maximum ozone number densities.

Launch date in 1983	Time IST (hr)	Maximum		Detected ozone peak		
		Level reached (mb)	Height attained (km)	Level (mb)	Height (km)	No. density $n(\text{O}_3)\text{cm}^{-3}$
4 March	1410	16	27.8	18	27.2	4.49 (12)
16 March	1110	22	25.8	≤ 24	≥ 25.4	5.09 (12)*
23 March	1447	24	25.4	≤ 24	≥ 25.4	5.37 (12)*
28 March	1030	15	28.5	20	26.4	4.29 (12)
28 March	1750	26	24.8	≤ 26	≥ 24.8	5.15 (12)*
30 March	1330	15	28.5	18	27.2	4.75 (12)
31 March	1737	19	26.8	≤ 26	≥ 24.8	4.59 (12)*
5 April	1109	16	27.8	≤ 24	≥ 25.4	4.13 (12)*

* The values of the peak number density are estimated using the standard procedure recommended by WMO for analysis of the ozonesonde data. Since the balloon did not penetrate the peak of the ozone layer, these values are uncertain (refer discussions in §3.2).

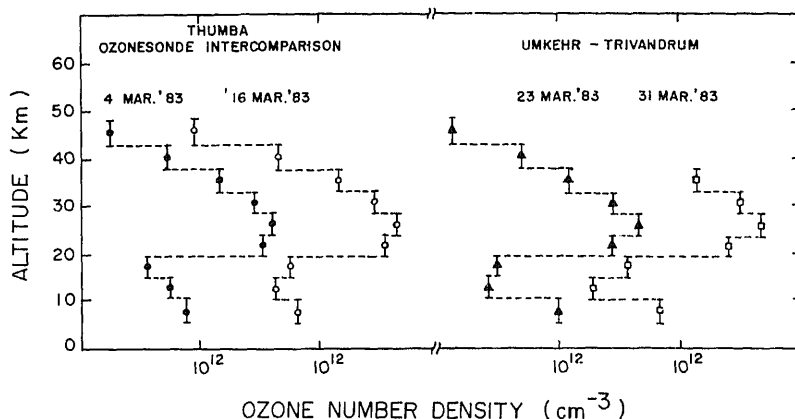


Figure 6. Umkehr data obtained at Thumba during the inter-comparison experiment.

the rocket ozonesonde values within 10%. This shows much better agreement than between the rocket and the balloon ozonesondes.

4. Mean distribution for the intercomparison period

A preliminary study of the data from the March 1983 experiment aimed at an intercomparison of the different sensors was published earlier (Acharya *et al* 1984) where all sensors were given equal weightage and no single sensor was considered to be more standard than the others. Since a number of different sensors have been used, it is realized that the present data set of seventeen ozone profiles consisting of 11 profiles from rocket ozonesondes which includes 8 optical ozonesonde data and 3 chemiluminescent ozonesonde data, 4 balloon profiles and 2 Umkehr profiles represents a significant amount of data, all collected in three salvos within a reasonably short period of eight days from one location and should give an average picture of the vertical distribution of ozone over Thumba accurately and unaffected by individual instrument biases. Further, such a large amount of data from a tropical site has been obtained for the first time. This data set is used to obtain a mean ozone distribution for the Thumba site representing the tropical reference profile. Although this mean distribution cannot represent all seasons of the year, it can be considered as a reference profile for the spring equinox.

The mean vertical distribution of ozone number density is obtained by taking the average of all 17 measurements made on 23 March, 28/29 March and 31 March respectively. The mean ozone number density and the standard deviation ($\pm \sigma$) are shown in figure 7 and the values tabulated in table 2. The tropospheric ozone values are mainly the mean of balloon and rocket chemiluminescent measurements and Umkehr observations since the optical ozonesonde data become available only above 16 km. The distribution shows a minimum in the troposphere in the 12–14 km region with number density of 2.8×10^{11} molecules/cc and the ozone maximum is obtained at an altitude of 27 ± 1 km with a concentration of $3.86 \times 10^{12} \pm 0.52 \times 10^{12}$ molecules/cc. Above the peak the ozone concentrations decrease steadily and at altitudes above 40 km the profile can be represented by a scale

Table 2. The mean vertical distribution of ozone over Thumba for the spring equinox period of March 1983.

Altitude (km.)	Ozone con- centration molecules/cm ³	Standard deviation	Ozone mix- ing ratio PPMV	Standard deviation
0	0.6825E+12	0.1121E+12	0.2834E-01	0.4653E-02
1	0.7600E+12	0.1541E+12	0.3454E-01	0.7000E-02
2	0.7675E+12	0.1011E+12	0.3838E-01	0.5056E-02
3	0.7775E+12	0.9323E+11	0.4286E-01	0.5137E-02
4	0.7450E+12	0.7141E+11	0.4546E-01	0.4356E-02
5	0.7125E+12	0.8539E+11	0.4824E-01	0.5782E-02
6	0.6300E+12	0.1042E+12	0.4748E-01	0.7856E-02
7	0.5625E+12	0.1464E+12	0.4719E-01	0.1228E-01
8	0.6215E+12	0.2698E+12	0.5802E-01	0.2518E-01
9	0.5083E+12	0.1787E+12	0.5283E-01	0.1857E-01
10	0.3769E+12	0.1878E+12	0.4367E-01	0.2176E-01
11	0.3294E+12	0.1318E+12	0.4259E-01	0.1705E-01
12	0.2894E+12	0.9829E+11	0.4242E-01	0.1442E-01
13	0.2811E+12	0.7499E+11	0.4587E-01	0.1217E-01
14	0.2794E+12	0.6417E+11	0.5101E-01	0.1156E-01
15	0.3300E+12	0.8864E+11	0.6942E-01	0.1886E-01
16	0.7108E+12	0.4432E+12	0.1696E+00	0.1087E+00
17	0.8424E+12	0.4669E+12	0.2410E+00	0.1355E+00
18	0.1159E+13	0.5738E+12	0.3941E+00	0.1993E+00
19	0.1631E+13	0.6988E+12	0.6750E+00	0.2920E+00
20	0.2207E+13	0.9104E+12	0.1134E+01	0.4825E+00
21	0.2725E+13	0.9041E+12	0.1681E+01	0.5801E+00
22	0.3173E+13	0.9915E+12	0.2318E+01	0.7516E+00
23	0.3473E+13	0.9487E+12	0.3005E+01	0.8608E+00
24	0.3597E+13	0.8772E+12	0.3696E+01	0.9630E+00
25	0.3757E+13	0.6861E+12	0.4537E+01	0.8989E+00
26	0.3834E+13	0.5264E+12	0.5419E+01	0.7174E+00
27	0.3858E+13	0.5196E+12	0.6393E+01	0.7983E+00
28	0.3783E+13	0.5817E+12	0.7422E+01	0.1072E+01
29	0.3477E+13	0.5556E+12	0.7904E+01	0.1174E+01
30	0.3168E+13	0.5081E+12	0.8481E+01	0.1245E+01
31	0.2820E+13	0.4364E+12	0.8740E+01	0.1255E+01
32	0.2427E+13	0.3907E+12	0.8774E+01	0.1384E+01
33	0.2082E+13	0.3242E+12	0.8738E+01	0.1309E+01
34	0.1755E+13	0.2583E+12	0.8667E+01	0.1230E+01
35	0.1468E+13	0.2290E+12	0.8398E+01	0.1295E+01
36	0.1232E+13	0.2003E+12	0.8210E+01	0.1270E+01
37	0.1034E+13	0.1810E+12	0.7950E+01	0.1348E+01
38	0.8577E+12	0.1532E+12	0.7602E+01	0.1371E+01
39	0.7000E+12	0.1308E+12	0.7263E+01	0.1386E+01
40	0.5568E+12	0.9951E+11	0.6758E+01	0.1301E+01
41	0.4675E+12	0.1080E+12	0.6491E+01	0.1417E+01
42	0.3742E+12	0.8918E+11	0.6032E+01	0.1385E+01
43	0.3096E+12	0.7650E+11	0.5723E+01	0.1439E+01
44	0.2508E+12	0.6445E+11	0.5329E+01	0.1419E+01
45	0.2056E+12	0.5496E+11	0.4953E+01	0.1362E+01
46	0.1632E+12	0.4616E+11	0.4421E+01	0.1234E+01
47	0.1348E+12	0.3953E+11	0.4131E+01	0.1189E+01

Table 2. (Contd.)

Altitude (km.)	Ozone con- centration molecules/cm ³	Standard deviation	Ozone mix- ing ratio PPMV	Standard deviation
48	0.1053E+12	0.3099E+11	0.3624E+01	0.1039E+01
49	0.8577E+11	0.2591E+11	0.3322E+01	0.9796E+00
50	0.6900E+11	0.2052E+11	0.3052E+01	0.8798E+00
51	0.5764E+11	0.1938E+11	0.2856E+01	0.9097E+00
52	0.5050E+11	0.1565E+11	0.2806E+01	0.7693E+00
53	0.4167E+11	0.1438E+11	0.2596E+01	0.7977E+00
54	0.3365E+11	0.1243E+11	0.2371E+01	0.7874E+00
55	0.2775E+11	0.1110E+11	0.2212E+01	0.8061E+00
56	0.2260E+11	0.9395E+10	0.2037E+01	0.7760E+00
57	0.1925E+11	0.1048E+11	0.1965E+01	0.9811E+00
58	0.1572E+11	0.8725E+10	0.1823E+01	0.9355E+00
59	0.1650E+11	0.7365E+10	0.2066E+01	0.9115E+00
60	0.1300E+11	0.5292E+10	0.1858E+01	0.7539E+00

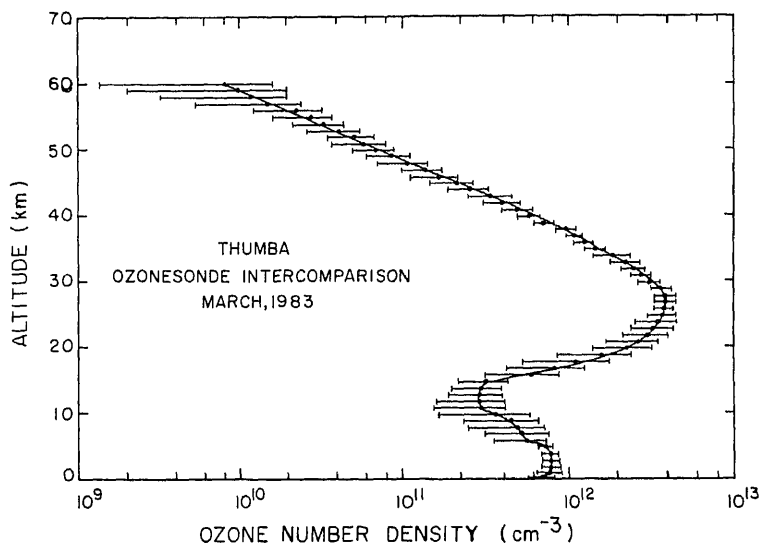


Figure 7. Mean ozone concentration profile obtained from the March 1983 ozone intercomparison experiment at Thumba. The bars denote the \pm one σ standard deviations from the mean.

height of about 5 km. The distribution above the peak is dominated by the rocket data and upto 56 km they represent the mean of 10 profiles and are statistically

standard deviation of ± 2.6 DU. Hence the mean profile of figure 7 gives a total ozone amount which is less than the Dobson value by 3.1%. While the difference is within the uncertainties of the Dobson estimates, it is noted that there have been earlier studies dealing with a comparison of Dobson data with satellite data (Lovill and Ellis 1983) suggesting that the Dobson instrument overestimates the total ozone content by a few per cent. This is considered by some researchers to be due to contamination by other absorbing gases in the atmosphere (e.g. Komhyr and Evans 1980). Further, Klenk *et al* (1985) show that the revised ozone absorption coefficient data of Bass and Paur (1985) would give 4% less total ozone. Hence the above discrepancy might be due to the incorrect use of ozone absorption coefficient for the Dobson data.

The ozone number density profiles observed over Thumba are converted into mixing ratio profiles and the mean of all is compared with other measurements. In order to obtain mixing ratios, air density values obtained from the meteorological rocket flights on 23, 28 and 31 March are used and the individual ozone concentration profiles are converted into mixing ratio profiles. These data are plotted in figure 8 along with other published values for the equatorial region, viz (1) the SBUV measurement of NIMBUS-7 for March 1979 by McPeters *et al* (1984), (2) the ozone number density values from the solar maximum mission (SMM) by Aikin *et al* (1984) for the fall equinoctial period of 1980 converted into mixing ratios using the mean of the above meteorological data and (3) the UV measurement on the Atmospheric Explorer-E (AE-E) satellite reported by Frederick *et al* (1978) for the March 1976 period.

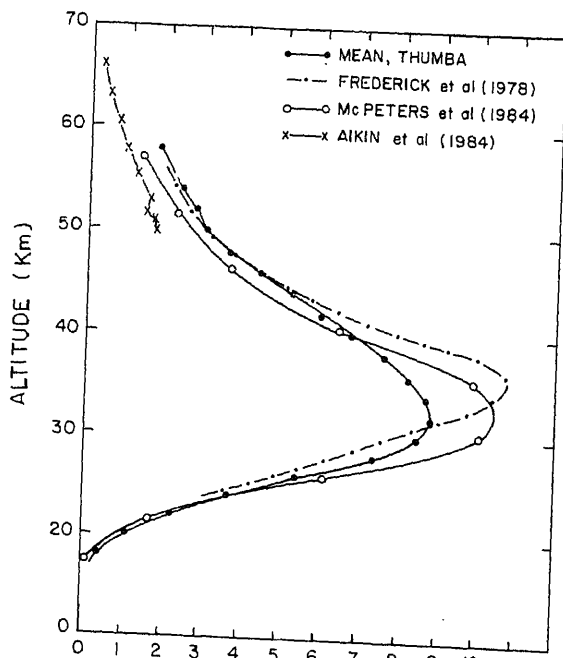


Figure 8 shows that at altitudes below 20 km the present rocket values are larger than the NIMBUS-7 data, the difference being of the order of 15%. The mean Thumba profile crosses the NIMBUS-7 profile at 24 km and at higher altitudes the NIMBUS-7 values are larger than the Thumba mean values. In the entire region of 25 km to 35 km the NIMBUS-7 profile shows values larger by about 15%. The Thumba profile crosses the NIMBUS-7 profile again around 40 km and above this altitude the Thumba values are consistently larger than the NIMBUS-7 values. The discrepancy lies in the range of 20% to 30% in the 45–55 km altitude region. The AE-E satellite data for the March equinox period of 1976, reported by Frederick *et al* (1978) show lower values for altitudes below 30 km and higher values in the altitude region of 30 to 45 km. This is also seen as a difference in the peak levels with the AE-E data showing the peak about 4 km above the rocket data. However, at altitudes above 45 km the two sets of data agree within a few per cent. The data from the SMM satellite show lower ozone values in the limited region of data overlap and the difference is about 40%. The possibility of a systematic bias in the satellite data depending on the altitude and length of the integration time has been considered by some workers earlier (e.g. Herman 1979) due to the fact that the satellite instruments look through different local times and altitudes. Further, the satellite data represent global averages for a given latitude belt whereas the present data refers to one location. This aspect needs special consideration at mesospheric altitudes where the ozone concentrations are sensitive to water vapour and temperature.

5. Day-to-day and day-night variations

The mean vertical distribution of ozone obtained for the three individual salvos on 23, 28/29 and 31 March shows existence of a day-to-day variability at different altitudes. This is demonstrated in figure 9 which shows percentage deviation of mean ozone concentration at different altitudes from one salvo to another. The percentage deviation lies within 10% in the altitude region of 25 to 35 km, but it is larger at other heights. The differences below 25 km are random in nature and are considered to be the manifestation of the dynamical process. Such short-term variations in this height region are well known (Dutsch 1980). At altitudes above 35 km, the ozone concentration values obtained from the 28/29 March salvo are systematically lower than those obtained on the other two days. The difference is 25–30% around 40 km and is of the order of 40–50% in the altitude region of 40 to 55 km. This feature is shown not only in the mean distribution, but also in the data from individual instruments. From figure 1 it can be seen that the ozone values obtained from PRL ozonesonde on 28 March are lower than those of 23 March. Figure 2 shows that the NPL ozone values for 29 March are lower than those for 31 March. The night-time chemiluminescent ozonesonde values are also lower on 28 March when compared to the values of 23 and 31 March in this altitude region. Hence it does appear that ozone concentration in the 30–50 km altitude were really lower on 28/29 March when compared to 23 and 31 March. This altitude region is photochemically dominated. The solar and geophysical data reported for this period show no anomalies. But the temperature data for three days obtained from

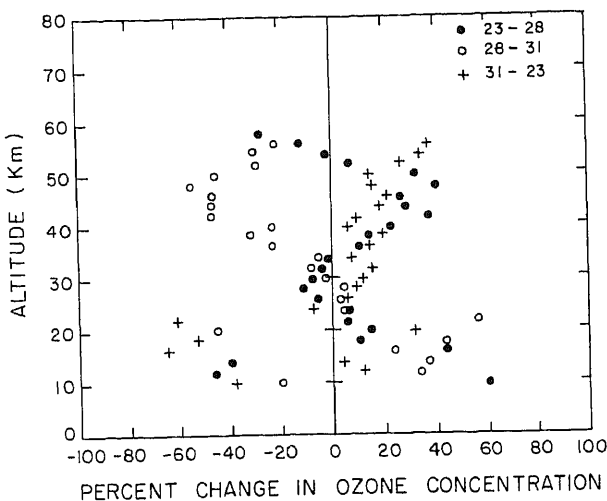


Figure 9. Day-to-day variability in the vertical distribution of ozone indicated by the rocket data of the inter-comparison experiment.

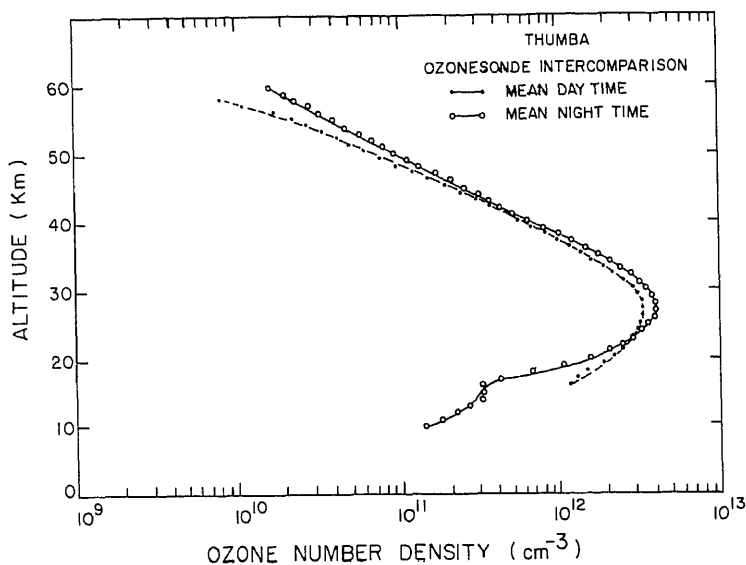


Figure 10. Day-night variations in ozone concentrations at different altitudes from the data of the Thumba March 1983 experiment.

and 31 March. Also, the temperature maximum around stratopause is broader on this day. Since temperature and ozone concentrations are anti-correlated in this height region, the observed decrease in ozone concentration on 28 March can be qualitatively attributed to this temperature increase.

The data from the March 1985 experiment gave an opportunity to see the variations in the ozone concentration values from day to night since there was one successful night-time flight in each of the three salvos. The mean of the three Soviet chemiluminescent rocket flights conducted during night-time is compared with the mean of the daytime values in figure 10. The night-time values are higher than daytime values at all altitudes above 22 km, but are lower at altitudes below. The differences between the night-time and daytime values are within the standard deviations upto 42 km. However, above this altitude, the differences are more than the standard deviation limit showing a statistically significant day to night increase in the ozone concentration. The increase in night-time is by an amount of 28% at 45 km, 32% at 50 km, 45% at 55 km and 56% at 60 km. The same feature is apparent when the data for the same day and same night is compared. Although this is qualitatively in agreement with the earlier rocket data from Thumba (Subbaraya *et al* 1985) and theoretical predictions, quantitatively the observed increases are much larger. Whether this increase is partly or wholly due to a systematic bias between the two sets of instrumentation, since all the three night-time profiles are from chemiluminescent sonde and all the daytime data in this altitude region come from optical ozonesondes or the differences represent a genuine day-night variations, needs to be established.

Acknowledgements

The experimental programme was organised and conducted under an Indo-Soviet collaborative agreement between the State Committee for Hydrometeorology and Control of Natural Environment (SCHCNE) of USSR, the Indian Space Research Organisation and the India Meteorological Department. It was made possible by the encouragement and support of a number of senior scientists and administrators from both sides. Special mention is made of Prof. Israel, Chairman, SCHCNE, Prof. N P Kozlov, Deputy Chairman, SCHCNE and Dr Chernikov, Director, Central Aerological Observatory of SCHCNE from the Soviet side and of Prof. R R Daniel, Chairman, ADCOS, Shri S K Das, the then Director General, India Meteorological Department and Shri P N Jayaraman of the ISRO Headquarters. The successful completion of the experiment was due to the enthusiastic co-operation of a large number of scientists and engineers of ISRO, IMD and CAO. Special mention is made of the efforts of the personnel at the Thumba rocket range under the leadership of Mr R Jayamani, Director, IREX, Mr N P Raghavendra Rao and Mr A C Bahl. One of us (BHS) would like to express his personal gratitude to his colleague, Dr Shyam Lal who went through the draft of the paper and made several suggestions for improvement and to Mr. N. P. M. Nair in the preparation of this manuscript.

References

- Acharya Y B *et al* 1984 The ozonesonde intercomparison experiment at Thumba; *Adv. Space Res.* **4** 59-68
- Aikin A C, Woodgate R and Smith H J P 1984 Equatorial ozone profiles from the solar maximum mission—A comparison with theory; *Planet. Space Sci.* **32** 503-513

- Bass A M and Paur R J 1985 The ultraviolet cross sections of ozone: I The measurements; in *Atmospheric ozone* (eds) by C S Zerefos and A Ghazi, (Dordrecht: D Reidel) pp. 606–610
- Brezgin N I 1982 Technique of measuring the vertical ozone distribution by optical methods using meteorological rockets; *Meiorol. Hydrol. (Moscow)* **4** 100–105
- Dutch H W 1980 Vertical ozone distribution and tropospheric ozone; *Proc. NATO Advance Study Institute* (ed) A C Aikin pp. 7–30 (Washington: US Dept. of Transportation)
- Frederick J E, Guenther B W, Hays P B and Heath D F 1978 Ozone profiles and chemical loss rates in the tropical stratosphere deduced from back-scatter ultraviolet measurements; *J. Geophys. Res.* **83** 953–958
- Herman J R 1979 The response of stratospheric constituents to a solar eclipse, sunrise and sunset; *J. Geophys. Res.* **84** 3307–3310
- Klenk K F, Monosmith B and Bhartia P K 1985 Absorption coefficients of ozone for the back-scattered UV instruments-SBUV, TOMS and BUUV and for the Dobson instrument; *Atmospheric ozone* (eds) C S Zerefos and A Ghazi (Dordrecht: D Reidel) pp 625–629
- Ko M K W, McElroy M B, Weisenstein D K and Sze N D 1986 Lightning: a possible source of stratospheric odd nitrogen; *J. Geophys. Res.* **91** 5395–5404
- Komhyr W D and Evans R D 1980 Dobson spectrophotometer total ozone measurement errors caused by interfering absorbing species such as SO₂, NO₂ and photochemically produced O₃ in polluted air; *Geophys. Res. Lett.* **7** 157–160
- Kononkov V A, Kononkov V I and Perov S P 1982 Experiment employing chemiluminescent method for measurement of atmospheric ozone onboard M-100B meteorological rockets; *Proc. symposium on investigations of atmospheric ozone, TBILIS*, p. 78–82
- Krueger A J and Minzner R A 1976 A mid-latitude ozone model for the 1976 US Standard Atmosphere; *J. Geophys. Res.* **81** 4477–4481
- Kundu N 1982 Reference ozonosphere over India; ISRO-IMAP-SR-09-82 ISRO Bangalore India
- Lal S and Subbaraya B H 1983 Solar eclipse induced variations in mesospheric ozone concentrations; *Adv. Space Res.* **2** 205–208
- Lovill J E and Ellis J S 1983 Correlative studies of satellite ozone sensor measurements; *Geophys. Res. Lett.* **10** 447–450
- McPeters R D, Heath D F and Bhartia P K 1984 Average ozone profiles for 1979 from the NIMBUS 7 SBUV instrument; *J. Geophys. Res.* **89** 5199–5214
- Somayajulu Y V, Zalpuri K S and Sampath S 1981 Rocket measurement of ozone density distribution in the equatorial stratosphere and mesosphere; *Indian J. Radio Space Phys.* **10** 197–200
- Subbaraya B H and Lal S 1981 Rocket measurements of ozone concentrations in the stratosphere and mesosphere over Thumba; *Proc. Indian Acad. Sci. (Earth. Planet. Sci.)* **90** 173–187
- Subbaraya B H, Jayaraman A and Shyam Lal 1985 Rocket measurements of the vertical structure of the ozone field in the tropics; in *Atmospheric Ozone* (eds) C S Zerefos and A Ghazi (Dordrecht: D. Reidel) pp 295–299.

Satellite-observed upwelled region and prime eddy off Somali coast during Monex-79

P N MAHAJAN

Indian Institute of Tropical Meteorology, Pune 411 005, India

MS received 15 May 1986; revised 11 August 1986

Abstract. An upwelled region as seen through satellite imagery off the Somali coast is compared with sea surface temperature during summer Monex-79. The relationship between satellite-derived low-level cloud drift winds and the sea-surface temperature is studied. Cloudiness associated with a prime eddy off the Somali coast is also studied. It is observed that the upwelled region has a unique crescent shape and reflects the sea-surface temperature that is driven by low-level strong winds. The prime eddy, as observed through a satellite imagery, shows that low cloud convection tends to be greater over the warm waters of the prime eddy, and the upwelled cold water tends to encircle the eddy leading to the identification of its outer boundary.

Keywords. Prime eddy; crescent-shaped upwelled region; satellite-derived low-level winds; Somali current; Monex.

1. Introduction

During the months of northern summer, the Somali current commences south of equator by late April and flows along the east African coast (Leetmaa 1972, 1973). It then progresses northward during May and reaches its full strength during July and August (Swallow and Bruce 1966). Large anticyclonic eddies (diameter 400–600 km) are formed off the Somali coast during monsoon season and is termed as prime eddies (Bruce 1979). Generally, these eddies are formed between 4 and 12°N and between the Somali coast and 58°E. In some years, an eddy of small size forms adjacent to and south of the prime eddy. Using SST reports from ships and satellite-sensed SST data Evans and Brown (1981) showed that prime eddy occurred each year with some variation in the location of the southern eddy. A cloud-free area is seen off the Somali coast during each monsoon season, and it remains prominent during the established phase of the monsoon season. During the summer Monex-79, a crescent-shaped cloud-free area and the prime eddy were seen through satellite imagery off the Somali coast. In this paper an attempt has been made to investigate the oceanic features and the cloudiness patterns associated with these phenomena.

2. Data

2.1 Satellite data

During FGGE year 1979, Indian ocean geostationary satellite (GOES-IO) was specially brought to a new location of 60°E to observe the atmospheric activity.

This gave investigators their first opportunity to view the monsoon circulation over the Indian ocean. At the same time, the TIROS-N polar orbiting satellite provided useful information over the Indian ocean. Satellite-derived low-cloud drift winds were obtained from GOES satellite during May–July 79 (Crozal 1979). GOES measurements were ideal because they possessed both high spatial and high temporal resolution (1 km in visible, 8 km in infrared and half hour sampling frequency). GOES-IO produced images of the earth and its cloud cover in the spectral bands $0.5\text{--}0.9\ \mu\text{m}$ (visible) and $11\text{--}12\ \mu\text{m}$ (infrared) respectively. Based on the sequence of cloud photographs, wind vectors at two levels in the troposphere were determined by several groups in USA and France. Satellite-derived wind vectors along the sea lane (figure 1) were averaged for each day to show its relation with the sea surface temperature (SST).

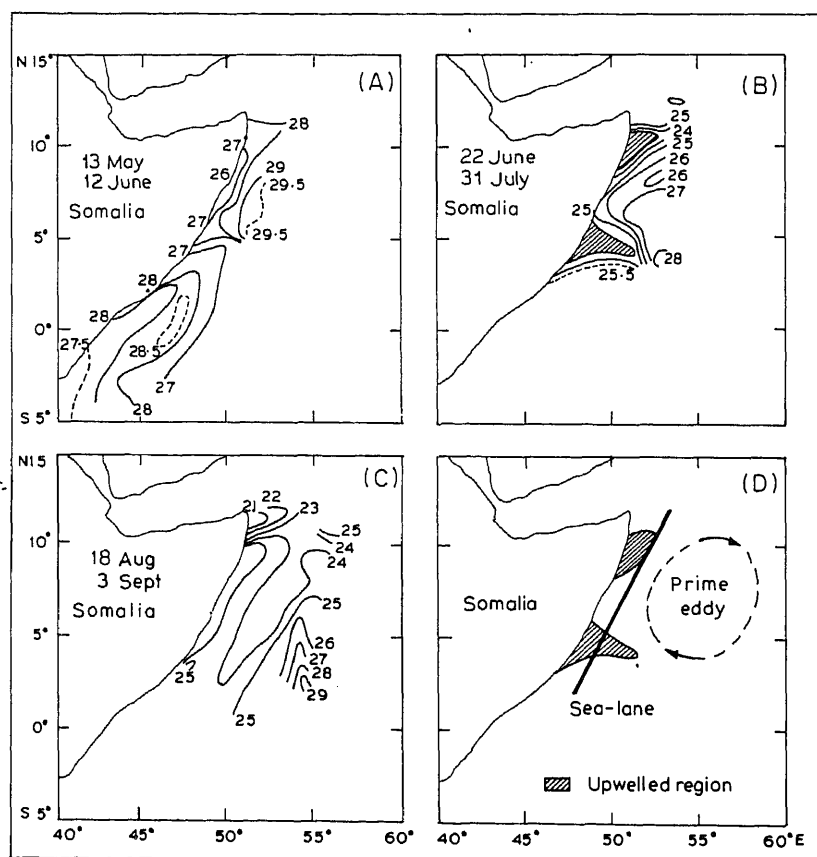


Figure 1. Time sequence of ship-observed SST fields for oceanic response to the monsoon.

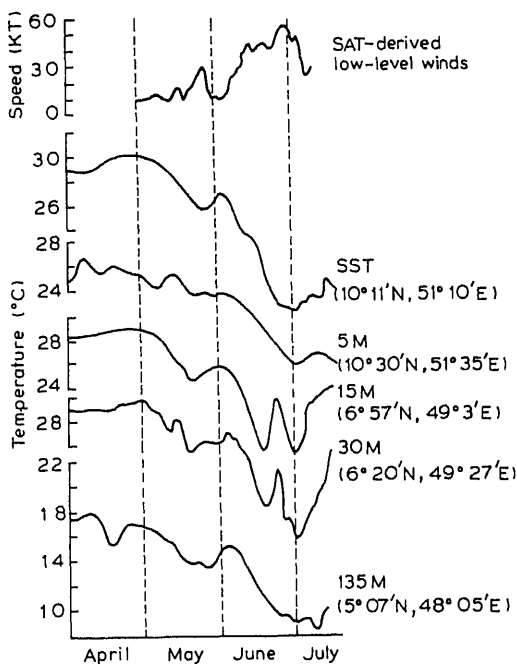


Figure 2. Time series of satellite-derived low-level cloud drift winds and temperature records at different locations off Somalia; sensor depths as indicated.

2.2 Moored station data

During Monex-79 a plan was designed to investigate the spatial and the temporal development of the Somali current and its associated cloudiness, upwelling and eddy fields. Moored stations were deployed off the Somali coast with instruments recording currents and temperatures at several locations. Shipboard observations of the vertical profiles of temperatures were made by several research ships taking part in the FGGE experiment. Temperatures and satellite-derived low-level cloud drift winds at different locations off the Somali coast are shown in figure 2.

3. Sea temperature and satellite-derived winds

Time series of coastal temperatures and satellite-derived low-level cloud drift winds at different locations off Somalia (figure 2) reflect the immediate near coastal surface response during different phases of monsoon. With the onset of the southwest monsoon and the development of strong southerly surface winds, the offshore transport of water increases, compensating upwelling increases and significant SST drops occur off Somalia. Intercomparison of ship wind estimates and satellite-derived low-level winds showed that both methods agreed reasonably well in describing the large-scale monsoon wind changes off east Africa (Schott and

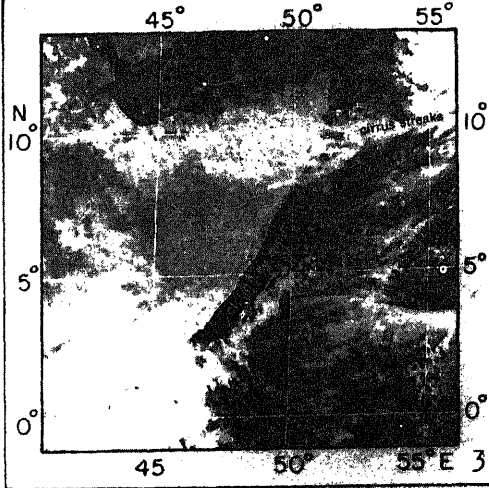
Fernandez-Partagas 1981). However, there seemed to be a noteworthy effect of cold water upwelling areas on the cloud level wind data. It is significant to note that the number of cloud level vectors off northern Somalia decreased drastically at the monsoon onset. This was caused due to the reduced convection over the cold water areas. Onset of summer monsoon 1979 was of a multiple type (Sikka 1980) with a temporary onset in early May accompanied by moderate southerly winds off Somalia. This temporary onset resulted in an inphase cooling at the coastal weather stations. Abrupt increase in wind intensity and drastic decrease in sea temperature during mid-June followed the regular onset (Brown and Schott 1981).

Figure 1A depicts the time sequence of ship observed sea surface temperature fields. During late May and early June, light to moderate winds off Somalia produced upwelling and resulted in the coastal cooling northward from near the equator to near 10°N . During late June and the whole of July (figure 1 B), the configuration of wedge-shaped regions of cold upwelled water and crescent shape of the ocean thermal front resulted from the advection of large oceanic anticyclonic eddies.

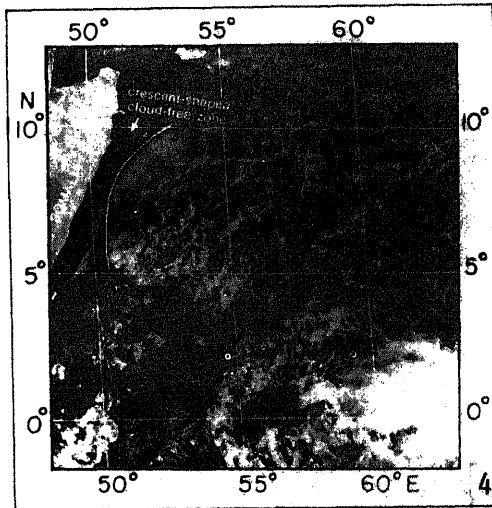
4. Crescent-shaped upwelled region and prime eddy

Figure 3 depicts the visible picture of 18 June 1979. Low cloud-free zone extends from 2°N to 8°N . Some portion of the north Somali coast is obscured by cirrus clouds. This period represents the early stage of the southwest monsoon. Figures 4 and 5 depict the visible and IR pictures of 5 July 1979 and illustrate the continuation of a cloud-free zone from mid-June to early July. Figure 6 depicts the cloud-free zone with a more pronounced crescent shape than in June. The visible picture once again gives an indication of inhibited low cloud development in the upwelled region. Figures 4 and 5 show the upwelling and thermal pattern off Somalia. The crescent-shaped region in the thermal pattern correlates directly with SST (figure 1B). It is significant to note that the thermal pattern, which resembles upwelling and advection pattern in the infrared picture, is largely free of low clouds in the visible picture. This indicates that the temperature pattern of the infrared image is in fact that of the ocean surface and not of the clouds. There is an indication to suggest that the development of low clouds is inhibited by cold-upwelled water. Therefore, an upwelled crescent-shape is observed in the visible picture.

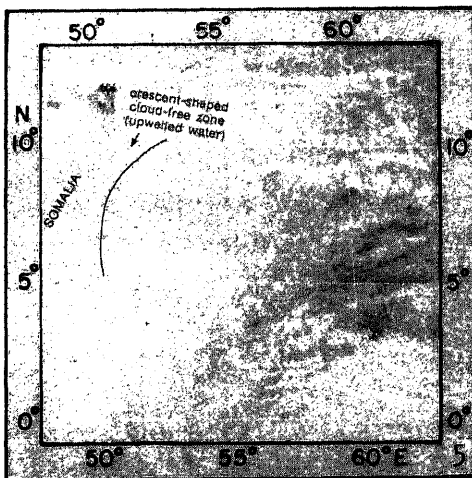
A northward flowing alongshore Somali current is a part of an eddy field formed during each southwest monsoon season off the Somali coast (Swallow and Bruce 1966; Bruce 1968, 1973). The current diverges from the coast turning eastward around 9°N to 10°N each year. In some years it turns eastward around 3°N to 5°N to form a southern eddy. It turns southward at about 55° – 58°E and then back toward the shore. Past measurements indicate that during the southwest monsoon a clockwise 'warm' eddy (prime eddy) of this general description occurs within the Somali basin. Figure 7 depicts the IR photograph of a TIROS-N satellite showing the prime eddy on 18 August 1979. We observe that the Somali current prime eddy is warm and anticyclonic. Low cloud convection tends to be greater over the waters of the prime eddy. Upwelled cold water tends to encircle the eddy leading



(3)



(4)

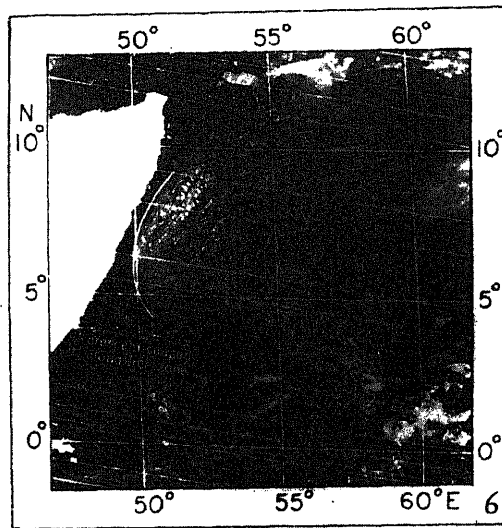


(5)

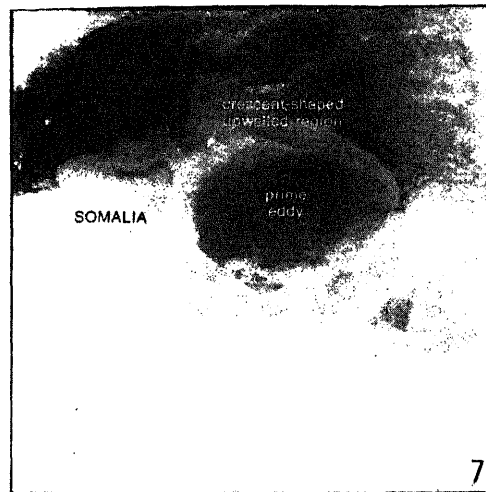
Figures 3-5. DMSP visible picture 3. 18 June 1979.

4. 5 July 1979.

5. DMSP infrared picture of 5 July 1979.



(6)



(7)

Figures 6 and 7. 6. DMSP visible picture of 14 July 1979. 7. TIROS-N infrared picture of 18 August 1979. (Photo Courtesy R. Whritner, Scripps Institution of Oceanography)

the identification of its outer boundary. Cloud formation is inhibited in the upwelled region, creating a crescent-shaped clear area as depicted in satellite visible imagery.

5. Conclusions

In this paper the relationship between a crescent-shaped upwelled region and satellite-derived low-level cloud drift winds and SST has been illustrated. Similar

anic features and cloudiness patterns associated with a prime eddy off the Somali coast has been illustrated. The following are the main conclusions of the study. (i) Satellite-observed cloud-free area off the Somali coast persists throughout the monsoon season. (ii) The upwelled region has a crescent shape and reflects cold SST pattern that is driven by strong low-level winds. (iii) Air and sea temperatures are markedly lower in cloud free area. (iv) Low-cloud convection is present over warm waters of the prime eddy. (v) Upwelled cold water tends to encircle the eddy to mark its outer boundary.

References

- Bryden J G 1968 Comparison of near surface dynamic topography during the two monsoons in the western Indian ocean; *Deep Sea Res.* **15** 665-667
- Bryden J G 1973 Large scale variations of the Somali current during the southwest monsoon 1970; *Deep Sea Res.* **20** 837-846
- Bryden J G 1979 Eddies of the Somali coast during the southwest monsoon; *J. Geophys. Res.* **84** 7742-7748
- Desbet P, Desbois M, Semery A and Sitbon P 1979 Champs de vent déduits des déplacements des nuages mesurés à partir d'images successives du satellite géostationnaire GOES I.O. au-dessus de l'Océan Indien du 16 Mai au 7 Juillet 1979; Note LMD n°97, Lab. de Meteorol. Dyn. Paris
- Evans R H and Brown O B 1981 Propagation of thermal fronts in the Somali current system; *Deep Sea Res.* **28** 521-527
- Matsumura A 1972 The response of the Somali current to the southwest monsoon 1970; *Deep Sea Res.* **19** 319-325
- Matsumura A 1973 The response of the Somali Current at 2°S to the Southwest monsoon of 1971; *Deep Sea Res.* **20** 355-374
- Robinson W A and Fernandez-Partagas 1981 The onset of the summer monsoon during the FGGE 1979 experiment off the East African coast: A comparison of wind data collected by different means; *J. Geophys. Res.* **86** 4173-4180
- Sankaran D R 1980 An appraisal of the onset of Summer Monsoon over India in the light of Monex 79 data; *FGGE Operations, Rep.* **B9** 87-95
- Stewart J C and Bruce J G 1966 Current measurements off the Somali coast during the southwest monsoon of 1964; *Deep sea Res.* **13** 861-888
- Wang J A, Virji H, Wylie D P and Lo C 1980 Summer monsoon windsets from geostationary satellite data: Summer MONEX; 1 May-31 July 1979; Space Sci. and Eng. Centre and Dept. of Meteorol., Univ. of Wisconsin. Madison

Some aspects of the 30–50 day oscillation

S V KASTURE and R N KESHAVAMURTY

Physical Research Laboratory, Navrangpura, Ahmedabad 380 009, India

MS received 13 March 1986; revised 13 August 1986

Abstract. The structure and interannual variability of the 30–50 day oscillation over the Indian region have been studied during the monsoon season. The power spectra of the zonal component of wind show large power in the 30–50 day time scale. The oscillation has a meridional wavelength of about 25° latitude and a slow northward phase speed of about 0.7° latitude per day. The oscillation also has some interannual variability. The periods are somewhat longer during the drought years.

Keywords. Oscillation; subseasonal oscillation; active break monsoon cycle; interannual variability.

1. Introduction

There is considerable variation of the monsoon on the subseasonal time scale i.e. during a monsoon season. There are spells of active and break monsoon which are well known to Indian synoptic meteorologists. Keshavamurty (1973) carried out power spectrum analysis of the zonal component of wind and found large power in the period around 30 days. When he plotted the phase difference of stations at different latitude pairs against their latitude difference a northward propagation of this mode was found. The wavelength was about 25° latitude and the phase speed was about 0.8° latitude per day. Dakshinamurti and Keshavamurty (1976) extended the analysis to five monsoon season and found large power in the 30–day time scale. Yasunari (1979) found a similar northward propagating mode in the 30–50 day time scale using satellite cloud pictures. Alexander *et al* (1978) composited six cases of active monsoon and six cases of break monsoon and found that there is a slow northward progression of the shear zone-cyclonic in the case of active monsoon and anticyclonic in the case of break monsoon. Krishnamurti and Subramanyam (1982) found an eastward propagating global scale mode on this time scale. They also found a northward progressing regional mode in the Indian monsoon region and suggested an interaction between these two modes. Murakami *et al* (1983) found modes in the 40–50 day time scale in the monsoon region using FGGE data. Krishnamurti *et al* (1985) found 30–50 day oscillations in the 200 mb divergent component of wind. Lorenc (1984) found an eastward propagating wave number one on this time scale. There is however a need to study the year-to-year variation of this oscillation. We have been investigating the three-dimensional structure of this oscillation in the Indian region. We have also studied the interannual variability of this oscillation.

2. Structure of the 30-50 day oscillation

Power spectrum analysis of the U-component of wind at 7 Indian stations viz Hyderabad, Nagpur, New Delhi, Lucknow, Bombay, Ahmedabad and Jodhpur were conducted. The analysis was done at all standard levels during the monsoon seasons of 1972, 1973, 1975 and 1979. Of these 1973 and 1975 were years of good monsoon rainfall and 1972 and 1979 were years of drought. The idea is to see whether 30-50 day oscillation exists in these years and to study the interannual variability of this oscillation. The power spectrum was analyzed by the standard method given in WMO Tech. Note 79. The spectral density was calculated by taking the cosine transform of the lagged auto-covariance. There are 240 data

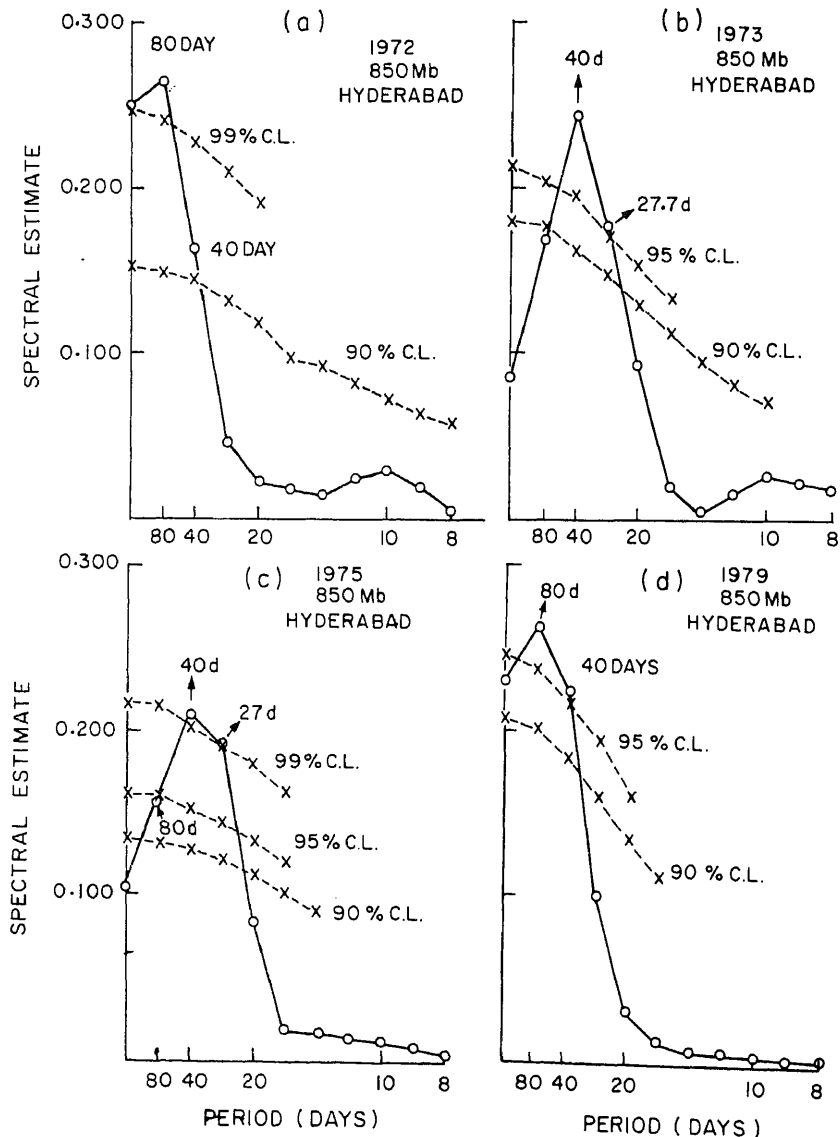


Figure 1. Power spectra of U component of wind at Hyderabad—850 mb.

as follows. From the value of lag one (and also lags 2 and 3) serial correlation coefficients the null continuum is found to be either of the white noise or of the Markov red noise type. Then from the ratio of actual spectral density and local magnitude of the null continuum, the confidence level is determined.

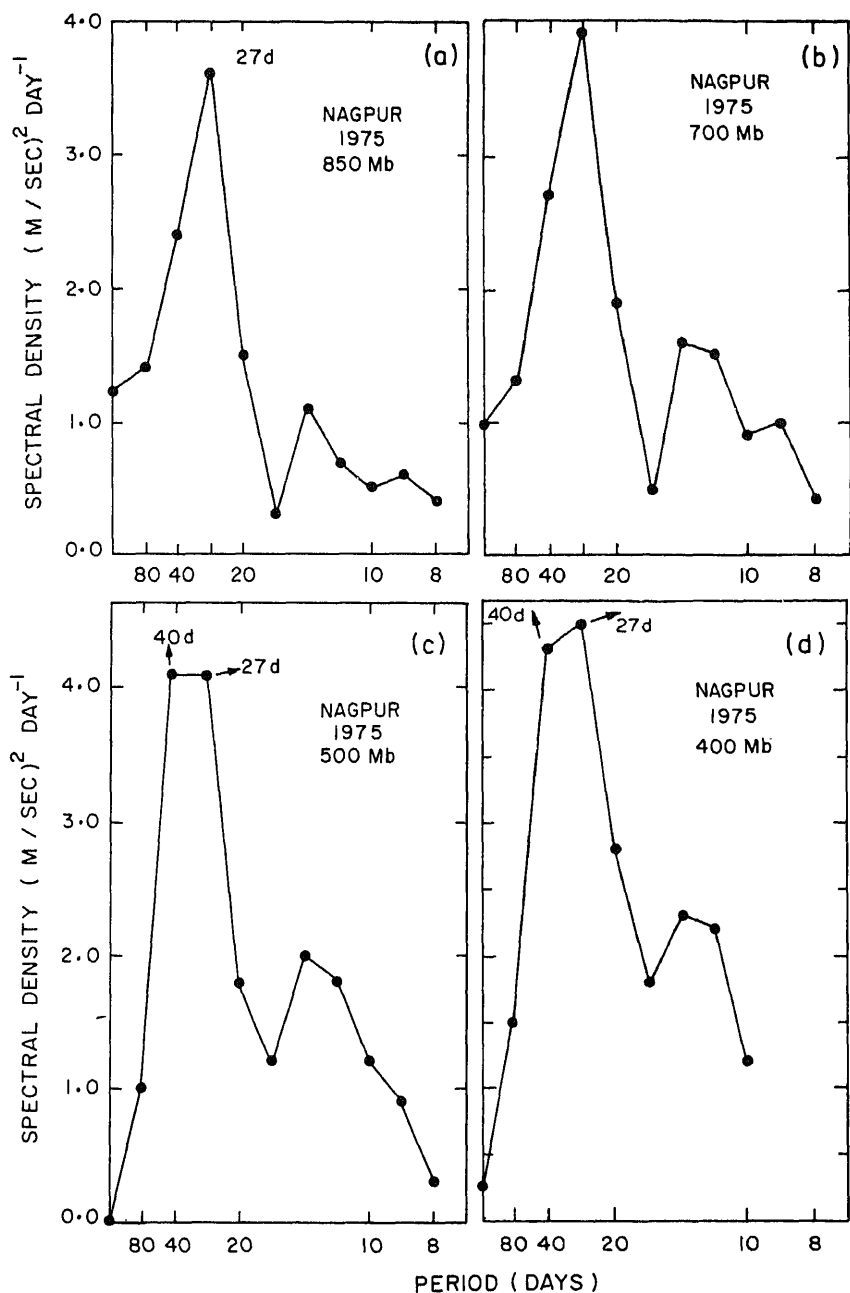


Figure 2 (a-d). For caption see page 52.

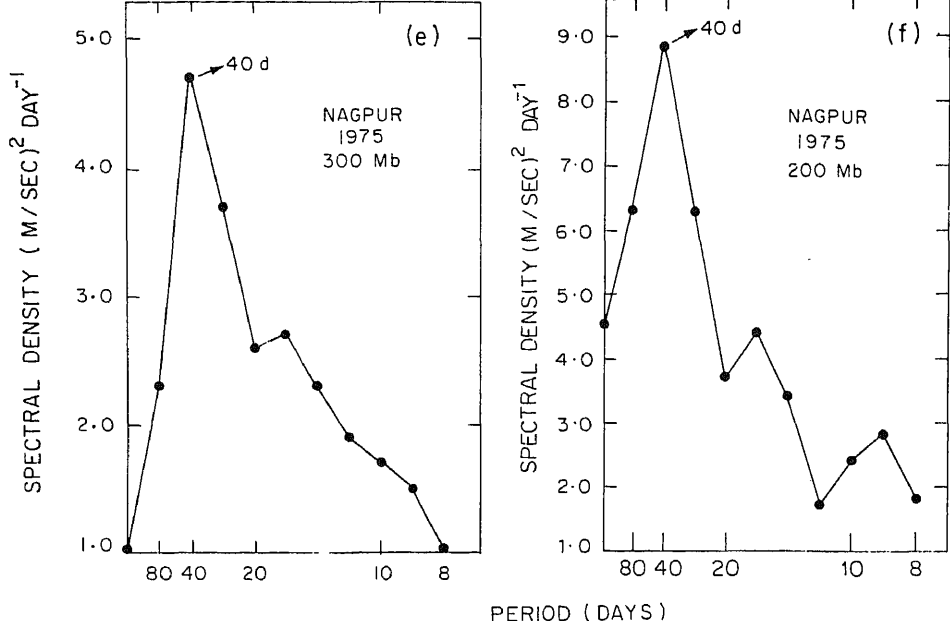


Figure 2. Power spectra of U component of wind at Nagpur—1975.

Figures 1(a, b, c, d) show the power spectra of the U-component at Hyderabad at 850 mb during 1972, 1973, 1975 and 1979. It is seen that there is large power in the periods 27, 40 and 80 days which are statistically significant at 95% significance level. Tables 1 and 2 show the peak spectral density significant at the 90% level at 850 mb and 700 mb respectively for all the stations and for the four years. The tables clearly show that the 30–40 day period is significant during all the years at both the levels.

Figures 2(a, b, c, d, e, f) show the power spectra of U-component of wind at Nagpur at different levels during 1975. It is seen that the 30–40 day peak stands out clearly at all the levels in the troposphere.

The phase difference of this oscillation between different pairs of stations was calculated from cospectrum and quadrature spectrum of the time-series. The plots of phase difference vs latitude difference are presented in figure 3. Figures 3(a, b, c, d) show such diagrams for 850 mb for the different years. It is seen that there is a reasonable straight line fit and from the slope of the line the wavelength is obtained. This is the latitude difference corresponding to a phase difference of 360° . The phase speed is obtained by dividing the wavelength by the period. We get a wavelength of about 24° latitude and a northward phase speed of about 0.7° per day. Table 3 shows the wavelength and phase speed at different levels (850, 700 and 500 mb) for the four years. It is seen that 30–50 day oscillation is a dominant feature in all the years. A regular northward progression is seen in the lower and middle tropospheres (850, 700 and 500 mb). However such a progression was not seen in the upper troposphere.

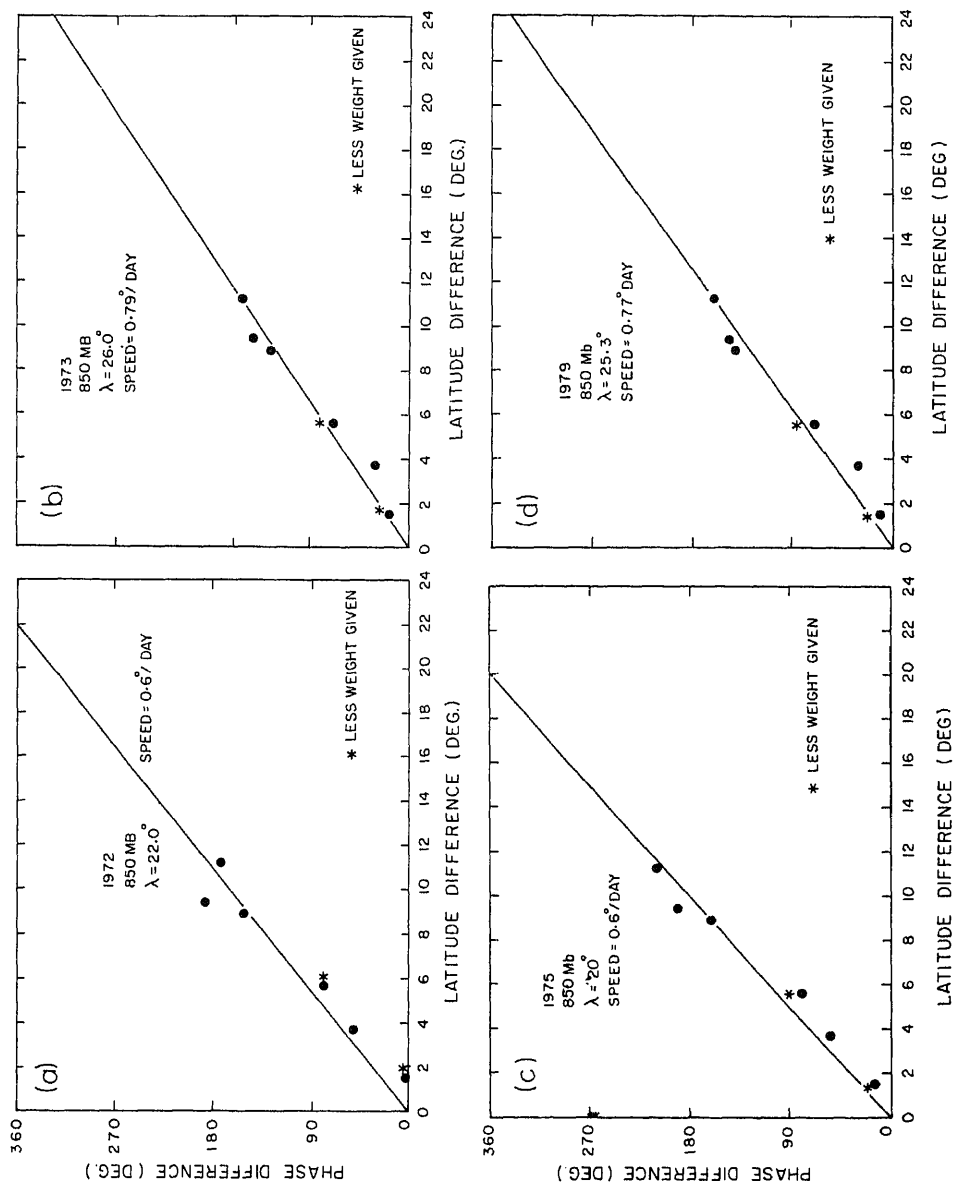


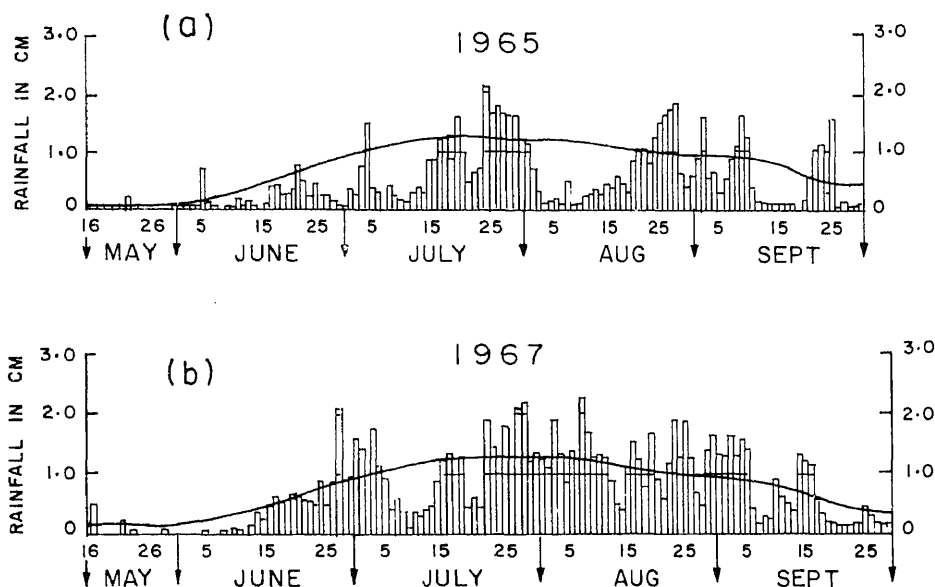
Figure 3. A plot of phase difference versus latitude difference—850 mb.

3. Interannual variability

Tables 1 and 2 show the peaks with large amplitude (in the low frequency) at different stations at different levels during the four years 1972, 1973, 1975 and 1979. It can be seen that during the drought years 1972 and 1979 significant peaks at 40 and 80 days are more common. During the normal monsoon years 1973 and 1975, on the other hand, the peaks at 27 and 40 days are more common. Thus it is likely that the period of this oscillation is somewhat longer during the drought years as compared to the normal years.

Figures 4(a) and 4(b) show the time series of rainfall over central India during the monsoon seasons of 1965 and 1967*. 1967 was a normal monsoon year with no long breaks; 1965 was a drought year. The long period of (break) below normal rainfall during August 1965 can be seen. Figures 5(a) and 5(b) show the time series of vorticity over east-central India at 900 and 850 mb taken from Keshavamurty (1973). It is seen that there is a very good correspondence between the lower tropospheric vorticity and rainfall. In particular the long break in August 1965 is seen to be a period of negative or small vorticity. This is when the monsoon trough shifted north to the foot of the Himalayas. There was no such long break during 1967.

Figures 6(a, b, c, d) show the power in different frequencies at different levels for New Delhi for the years 1972, 1973, 1975, 1979. It can be seen that the power (u'^2) in the low frequency part of the spectrum is much larger in the upper troposphere during the drought years 1972 and 1979 compared to the normal years



DAILY AVERAGE RAINFALL OVER CENTRAL INDIA

Figure 4. Time series of rainfall over Central India during 1965 and 1967.*

Table 1. Periods (days) at which spectral values are significant at 90% level or more are shown. Underlined values are significant at 95% level.
(850 MB)

Station	Year			
	1972	1973	1975	1979
New Delhi	<u>40,80</u>	–	<u>27</u>	27
Lucknow	–	40	27	–
Jodhpur	40	40	27	<u>40,80</u>
Ahmedabad	40,80	27,40	<u>27,40</u>	–
Nagpur	–	27,40	<u>27,40</u>	40
Bombay	<u>40,80</u>	<u>27</u>	–	80
Hyderabad	<u>40,80</u>	27,40	<u>27,40,80</u>	<u>40,80</u>

Periods (days) at which spectral values are significant at 90% level or more are shown.

Underlined values are significant at 95% level.

Table 2. Periods (days) at which spectral values are significant at 90% level or more are shown. Underlined values are significant at 95% level.
MD denotes missing data.
(700 MB)

Station	Year			
	1972	1973	1975	1979
New Delhi	40,80	–	–	27
Lucknow	–	–	<u>40</u>	–
Jodhpur	<u>27,40</u>	27,40	<u>40</u>	MD
Ahmedabad	40,80	27	27,40	–
Nagpur	80	27	27	27,40
Bombay	<u>40,80</u>	MD	–	MD
Hyderabad	<u>40,80</u>	<u>27,40</u>	<u>27,40</u>	40,80

Periods (days) at which spectral values are significant at 90% level or more are shown.

Underlined values are significant at 95% level.

MD denotes missing data.

Table 3. Wavelength and speed of the oscillation at different levels.

Pressure (MB)	1972		1973		1975		1979	
	Wavelength (Degree latitude)	Speed (Degree latitude per day)	Wavelength (Degree latitude)	Speed (Degree latitude per day)	Wavelength (Degree latitude)	Speed (Degree latitude per day)	Wavelength (Degree latitude)	Speed (Degree latitude per day)
850	22	0.7	26	0.8	20	0.6	25	0.8
700	23	0.7	25	0.8	20	0.6	23	0.7
500	29	0.9	28	0.8	21	0.6	21	0.6

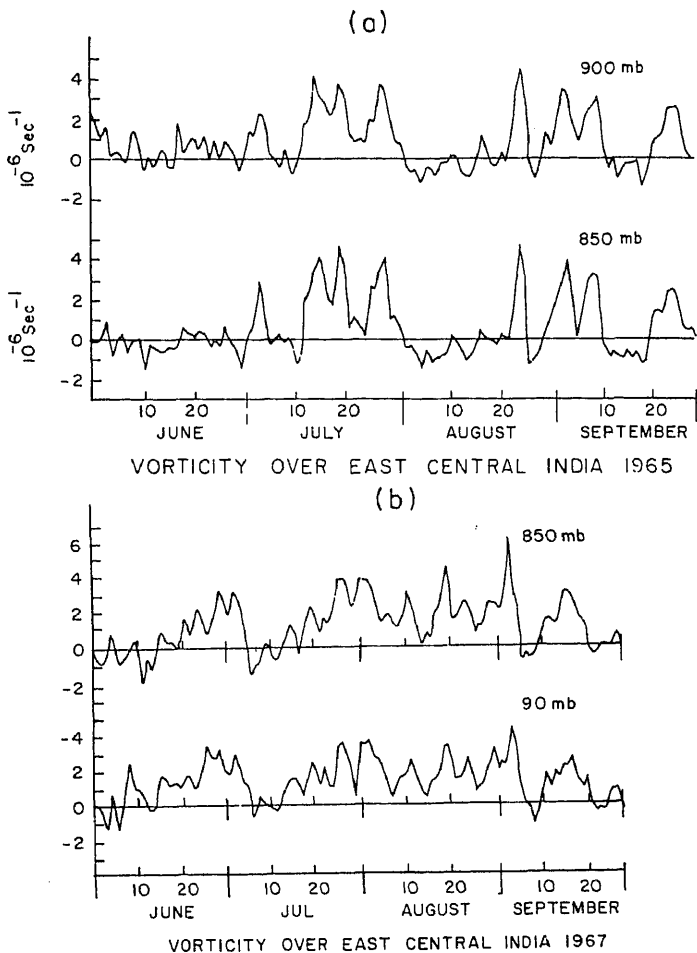


Figure 5. Time series of vorticity over East Central India during 1965 and 1967.

1973 and 1975. Jodhpur, Ahmedabad and Lucknow stations show similar results. This is perhaps due to the north-south oscillation of the upper tropospheric ridge in association with large amplitude westerly troughs.

4. Summary and conclusions

We have identified the 30–50 day mode during a few monsoon seasons. It has a wavelength of about 25° latitude and a slow northward phase speed of about 0.7° latitude per day.

There is also some interannual variability of this oscillation. The periods are somewhat longer (40–80 days) during drought years as compared to (30–40 days) normal years. There are long periods of negative vorticity over central India during the drought years.

In the upper troposphere over northwest India, the fluctuation on this time scale is larger during the drought years.

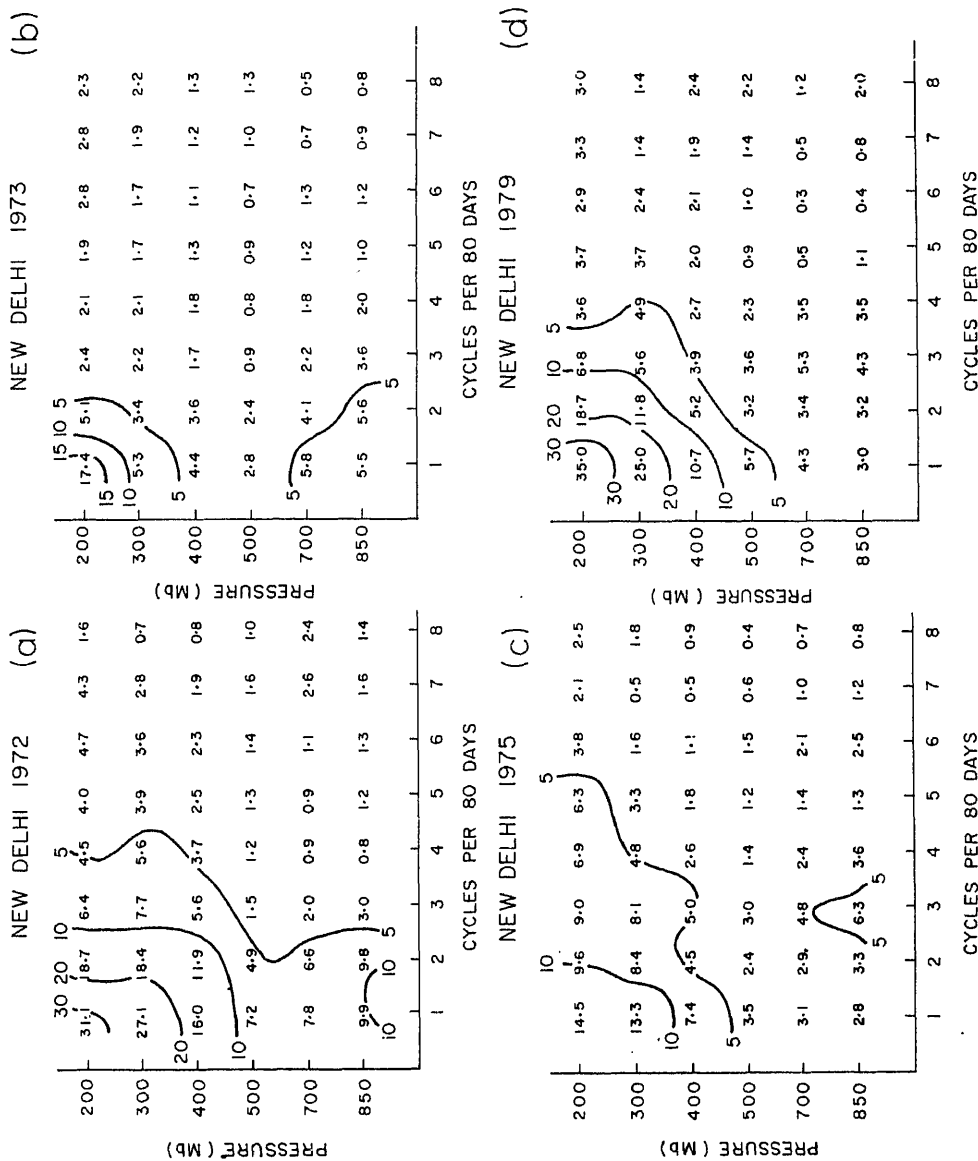


Figure 6. Spectral density as a function of pressure level and frequency—New Delhi.

References

- Anderson G, Keshavamurty R N, De U S, Chellapa R, Das S K and Pillai P V 1978 Fluctuations of monsoon activity; *Indian J. Meteorol. Hydrol. Geophys.* **29** 76-87
- Chinamurti J and Keshavamurty R N 1978 On oscillation of period around one month in the Indian summer monsoon; *Indian J. Meteorol. Hydrol. Geophys.* **27** 201-208
- Keshavamurty R N 1973 *On the maintenance of the mean Indian southwest monsoon circulation and the structure and energetics of monsoon disturbances*; Ph.D. thesis, Mysore University, India
- Keshavamurty T N, Jayakumar P K, Sheng J, Surgi N and Kumar A 1985 Divergent circulations on the 30-50 day time scale; *J. Atmos. Sci.* **42** 364-375
- Keshavamurty T N and Subramanyam D 1982 The 30-50 day mode at 850 mb during MONEX; *J. Atmos. Sci.* **39** 2088-2095
- Kumar A C 1984 The evolution of planetary scale 200 mb divergent flow during the FGGE year; *Q.J.R. Meteorol. Soc.* **110** 427-441
- Nakamura T, Nakawa and He J H 1983 40-50 day oscillations during the 1979 northern hemispheric summer; Tech. Rep. No. UHMET 83-02. Department of Meteorology, University of Hawaii, Honolulu, Hawaii
- NOAA Tech. Note No. 79 (1966)
- Nakamura T 1979 Cloudiness fluctuations associated with the northern hemisphere summer monsoon over India; *J. Meteorol. Soc. Jpn.* **58** 225-229

Variability in the surface wind direction at a coastal site of complex terrain

Y SADHURAM

National Institute of Oceanography, Dona Paula 403 004, India

MS received 12 May 1986; revised 28 November 1986

Abstract. Variability in the standard deviation of surface wind direction (σ_θ), under different Pasquill stability regimes on diurnal, seasonal and interannual scales has been investigated making use of a 10-year data set collected at Visakhapatnam (17°42' N., 82°18' E) during January, April, August and October for winter, pre-monsoon, monsoon and post-monsoon seasons respectively. The diurnal scale variability in σ_θ is more pronounced during day time than in night. The seasonal variability in σ_θ is only moderate around noon while relatively large fluctuations are noticed on inter-annual scale only during day time in January and August. The seasonal dispersion in σ_θ decreased from most unstable regime to most stable regime.

Keywords. Inter-annual variability; wind direction fluctuation; gravity waves; meso-scale eddies; Pasquill stability; turbulence.

1. Introduction

Standard deviation of surface wind direction (σ_θ) is drawing the attention of the environmental scientists owing to its significance in dispersion studies, especially over a complex terrain. The standard deviation of the horizontal distribution of concentration (σ_y) may be obtained from σ_θ using the relation

$$\sigma_y = \sigma_\theta \cdot x \cdot f(x),$$

where x is the downwind distance from the source and $f(x)$ is a function of distance which varies between 1.0 and 0.33 from the source to a distance of 10 km (Pasquill 1976). An excellent review of diffusion schemes was presented by Hanna *et al* (1977). The study of σ_θ is also useful to characterize the atmospheric turbulence in terms of Pasquill (A-G) stabilities to give σ_y and σ_z (standard deviation of vertical distribution of concentration) values indirectly (Sedefian and Bennett 1980). Several studies have appeared in the literature showing relations between σ_θ and Pasquill stability classes (Singer and Smith 1953; Slade 1968; McElroy 1969; Shirvaikar 1975; Panchal and Chandrasekharan 1978; Padmanabhamurthy and Gupta 1979; Sadhuram and Vittal Murthy 1983).

σ_θ is known to be influenced by several factors which should be considered while using σ_θ values in diffusion models. Munn (1964) showed the dependence of σ_θ on the sampling interval, wind speed and roughness elements. The influence of meandering air flow, roll vortices and gravity waves on wind direction has been described exhaustively (Metcalf 1975; Sethuraman 1977; Sethuraman *et al* 1982; Hanna 1983; Raynor and Hayes 1984). Sethuraman (1977) demonstrated that during breaking of a gravity wave the turbulent energy would be about 100 times

stability and its seasonal variability utilizing a 10-year data set and concluded that a climatological value of σ_θ is not a good choice for diffusion models. From the above discussion it is apparent that σ_σ has to be derived from the measurements for use in diffusion models particularly over a complex terrain. In this context the following questions are relevant; what would be the error of estimation in the pollution concentration if we use climatological (seasonal or annual) values? Do the values of σ_θ considerably vary from year to year? If so, what would be the order of magnitude in the variation of σ_θ ? The present study attempts to address these questions and the results are expected to be useful for environmental studies. The temporal variation of σ_θ under different Pasquill stability regimes for typical seasons is discussed.

2. Data and methodology

Verrall and Williams (1982) reviewed some commonly used methods for the computation of σ_θ and proposed a new method based on sines and cosines of direction angles. Here, the computations of σ_θ are made from wind direction range, a method proposed by Slade (1968) which is quite simple and widely used by several workers. The method is as follows:

σ_θ is computed utilizing the continuous wind direction traces. The accuracies in the wind speed and direction are approximately ± 0.2 m/sec and $\pm 2.0^\circ$ respectively. Depending upon the fluctuations the trace in any hour could be divided into 10, 15 or 20 min periods. If the trace is smooth and uniform, longer averaging periods would suffice. If the fluctuations are large, a shorter averaging period is to be chosen. Here, a 20-min interval for smooth and uniform traces and a 15-min interval for large fluctuations have been selected. The range of wind direction during the sampling period has to be estimated and all such ranges during a one-hour period are averaged and considered as the mean range of wind direction for the hour. Approximate values of σ_θ are obtained by dividing the direction range values by 6.0 as proposed by Slade (1968).

This method is simple and it would be possible to compare these results with those reported for other sites. The details of data, description of the roughness elements near the experimental site, climate of the city had been reported earlier (Sadhuram and Vittal Murthy 1983, 1984a; Sadhuram 1986).

Here, the interannual variability of σ_θ , σ_σ vs Pasquill stability regimes and diurnal variation of σ_θ during different seasons have been presented diagrammatically for the period 1958–67.

3. Results and discussion

3.1 *Climatology of σ_θ*

The mean values of σ_θ for different Pasquill stability regimes were compared with the values reported for a flat terrain and for a coastal station (Sadhuram and Vittal

deviation values in σ_θ are higher in unstable regimes (A,B&C) and lower in stable regimes (E&F). Mean wind speeds are lower in stable and unstable regimes and higher in neutral regimes which is quite obvious. Weaker winds and strong insolation at noon favours free convection and with the strengthening of the wind speed the mechanical turbulence dominates the thermal turbulence. Similarly during night weaker winds discourage vertical diffusion and turbulence. However, the horizontal eddies are not totally suppressed by vertical stability processes but could be produced by gravity waves, terrain interactions with the flow or surface inhomogeneities etc (Hanna 1983).

The diurnal variation in σ_θ , wind speed and Pasquill stability frequencies is shown in figure 1. The value of σ_θ showed a progressive increase from dawn reaching the maximum at local noon (= 1200 hr) and a decrease thereafter during all the seasons. The wind speed also showed a similar trend but the maximum occurring during afternoon (= 1500 hr). In general, the speeds are weaker during night in all the seasons. The winds are stronger during afternoon in January and April compared with those in August and October which could be due to the influence of land sea breeze circulation. But in August and October which are typical months for the SW and NE monsoon seasons respectively conditions may not favour the generation of local circulation. The dominance of unstable conditions during day and stable conditions during night is quite obvious. Neutral conditions (D) predominant at 0700 hr and 1700 hr (Sadhuram 1982) are not discernible due to coarse time interval considered here. More details on Pasquill stability classes and their percentage frequencies are presented elsewhere (Sadhuram and Vittal Murthy 1986).

3.2 Day-to-day variation

The mean σ_θ values also show day-to-day variation and the variability is significant around noon than in night (figure 2a). The values of σ_θ are higher in January at

Table 1. Mean wind speed and σ_θ values with Pasquill stability regimes.

Month/stability		A	B	C	D	E	F
Jan	I	5.2	17.6	10.7	5.0	12.0	49.5
	II	1.9	2.5	3.8	4.4	3.2	1.0
	III	16.0±2.7	12.0±2.2	8.0±3.2	6.0±2.3	6.0±0.9	4.0±0.8
Apr	I	1.0	10.0	16.3	14.0	20.3	38.4
	II	2.1	3.5	4.7	5.5	3.5	1.7
	III	17.0±1.2	13.0±2.1	9.0±1.2	8.0±0.8	6.0±1.3	6.0±0.5
Aug	I	3.6	13.6	13.3	12.0	23.5	34.0
	II	2.2	2.4	3.6	3.4	3.4	1.4
	III	12.0±2.2	10.0±2.0	7.0±1.3	7.0±1.3	5.0±1.3	4.0±0.6
Oct	I	7.1	20.8	8.7	4.1	11.7	48.4
	II	2.2	2.4	2.8	2.7	3.3	1.2
	III	14.0±2.3	10.0±1.5	8.0±1.6	7.0±1.9	6.0±1.4	4.0±0.8

I-percentage frequency of stability; II-wind speed (m/sec); III- σ_θ (Deg)

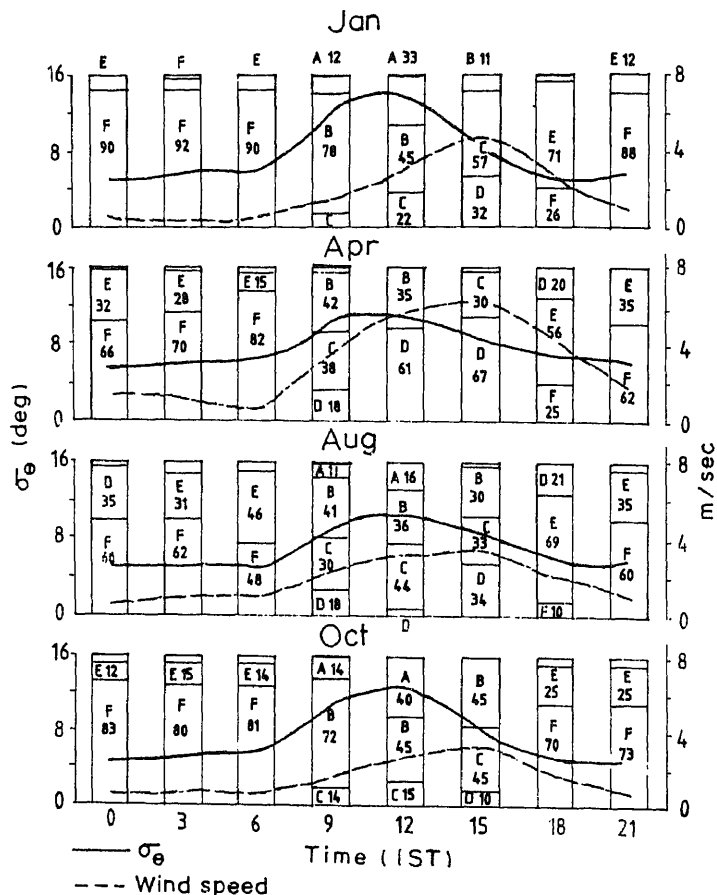


Figure 1. Diurnal variation of mean wind speed, σ_θ , Pasquill stability and the percentage frequency during typical months of the respective seasons.

0900 and 1200 hr and lower at 1800 hr compared with those in April. Similarly 1500 and 1800 hr the values of σ_θ are found to be higher in August whereas lower at 1200 hr compared with those in October. Observing figures 2a, b carefully it can be inferred that the trends in σ_θ in January and October as well as April and August are similar because the city (Visakhapatnam) is under the influence of SW winds during April and August and NE winds in January and October (Sadhuram and Vittal Murthy 1984a). The higher values in January and October are due to the lower wind speeds. At 1800 hr the mean values of σ_θ are higher in April compared with those in August although the wind direction and the roughness elements are the same (see figures 2a, b). The mean wind speed in April and August at 1800 hr are about 4.0 and 2.0 m/sec respectively whereas the values of σ_θ are 8.0 and 6.0. Normally one would expect a decrease of σ_θ with the increase of wind speed which is not seen here. Therefore, obviously there must be some other mechanism responsible for the enhancement of σ_θ such as meandering, roll vortices and gravity waves. It is already mentioned that the stronger wind during afternoons in April

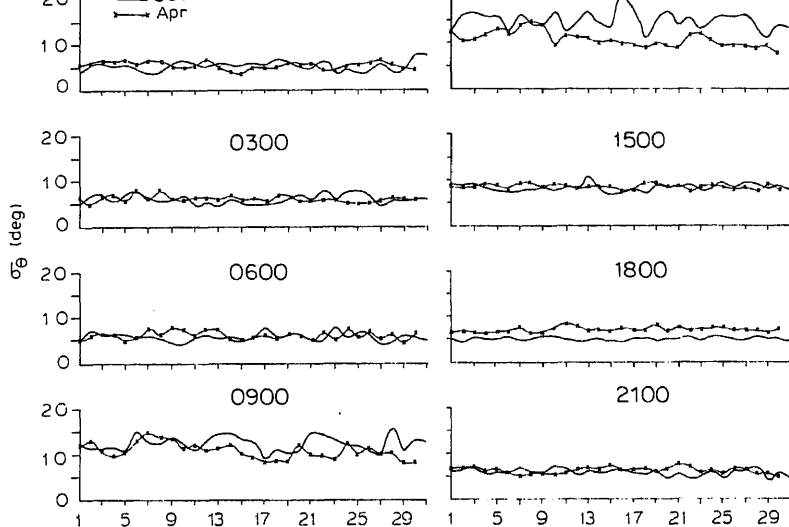


Figure 2a. Daily variation of mean σ_θ during January and April (10 year means).

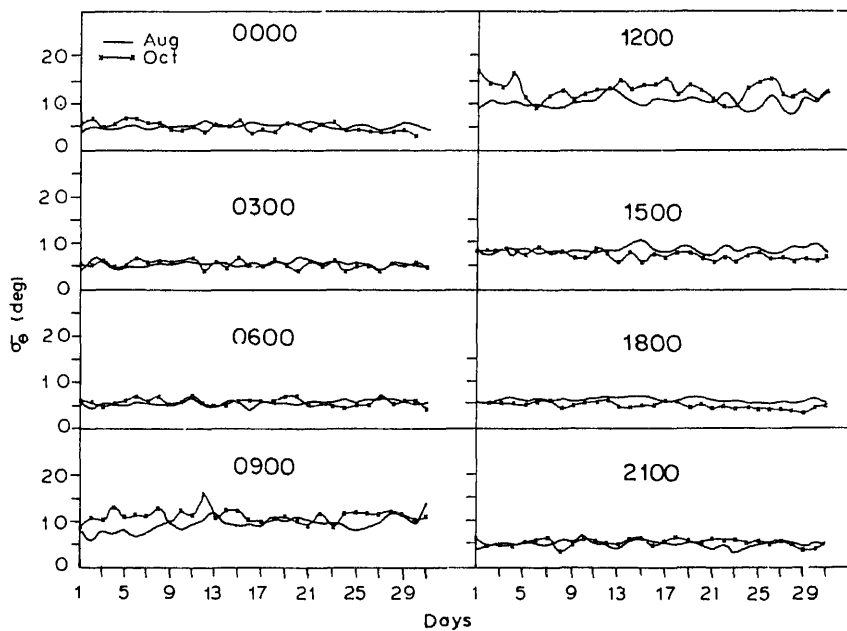


Figure 2b. Same as figure 2a but for August and October.

due to the superposition of the local land-sea breeze circulation on general synoptic flow. It is also observed that the percentage frequency of stable layers is maximum in April and almost nil in August during afternoon hours (Sadhuram and Vittal Murthy 1984b). Formation of stable layers often leads to the generation and propagation of gravity waves (Sethuraman *et al* 1982). The stability wind roses also show a considerable SSW and S directions during April and August in D&E Pasquill stability regimes and the wind speed classes 3–6 and > 6 m/sec are present in those directions (Sadhuram and Vittal Murthy 1986). Sethuraman *et al* (1982) found that the frequency of occurrence of gravity waves is more pronounced in the wind speed range 3–8 m/sec during spring and summer at a coastal site. The above points suggest that the enhancement of σ_θ in April may be due to the generation and propagation of gravity waves towards the observational site while in August the conditions are not favourable for the generation of gravity waves. Unfortunately studies on gravity waves are not available for Indian conditions to confirm the above view.

3.3 Interannual variability

Figures 3a, b show the year-to-year variations of σ_θ and wind speed with time 1800–0600 hr (night time) 0600–1800 hr (day time) corresponding to typical seasons. For the sake of clarity, the variability is shown for four years viz 1958, 1960, 1964 and 1967 instead of all the 10 years starting from 1958 to 1967. It is clearly seen from the figures that both σ_θ and wind speed gradually increase from 0000 to 1200 hr and decrease further in all the years. Figure 3a shows that in January σ_θ varies significantly from year to year during day time whereas such a trend is not significant in wind speed. Year-to-year fluctuations are also higher around 0300 hr which could be attributed to the variability in the frequency and intensity of ground inversions. In general, the variability in σ_θ is less in April and October compared with January and August. But in the case of wind speed the scatter is larger in April and August compared with January and October. It is interesting to see that in August the entire curve of σ_θ deviates from year to year. The highest values are seen in 1958 and the lowest in 1967. The deviation is mainly due to the activity of the monsoon which shows fluctuation from year to year. Therefore, during August the synoptic scale circulation seems to be the dominating factor. But the fluctuations in σ_θ in January may not be due to the above mechanism since the wind speeds are more or less uniform in all the years. The higher fluctuations in σ_θ during 0900 to 1500 hr are mainly due to the variability in thermal turbulence. The winds are very weak in January during early hours which favours the formation of strong ground inversions. From the selected years the general variability in σ_θ and wind speed at 1200 hr is as follows: The σ_θ value varied from 12–18, 10–12, 8–14 and 12–15 during January, April, August and October respectively. The corresponding ranges in the wind speed are \approx 4, 6–7, 3–6 and 3–4 m/sec respectively. From this it could be pointed out that the variability in σ_θ is higher than that of wind speed. This suggests that wind speed alone cannot control the behaviour of σ_θ .

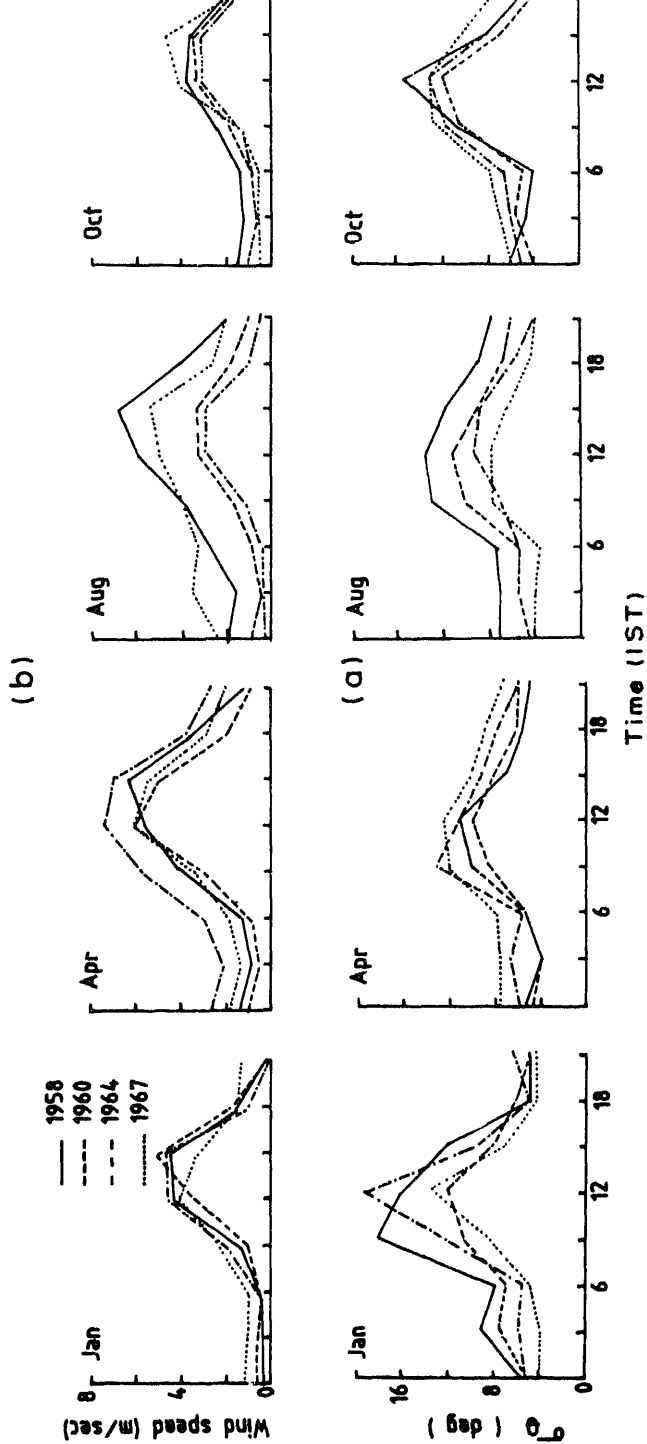


Figure 3. Inter-annual variability of (a) σ_θ and (b) wind speed with time during representative months of the respective seasons.

4. Conclusions

The present study reveals that day-to-day variability in mean σ_θ is significant during the day as compared to night. Seasonal variability in σ_θ could be attributed to variability in the predominant wind direction and insolation. Year-to-year fluctuations are noticed in σ_θ which are greater pronounced during day in January and August. It appears that in August the synoptic scale circulation is more important than the local factors. In general, the scatter in σ_θ is higher in unstable conditions and lower in stable conditions. In April at 1800 hr the climatological values of σ_θ are higher compared to those in August although the roughness elements and the wind direction are the same. This is not seen in the individual years.

Acknowledgements

The author wishes to express his thanks to Dr J S Sastry and Dr H N Siddiquie for their encouragement. He is grateful to Prof. H A Panofsky, Dept. of Meteorology, The Pennsylvania State University, U.S.A. for his suggestions which helped improve the original version of this manuscript. The author is also thankful to referees for their helpful comments.

References

- Hanna S R 1983 Lateral turbulence intensity and plume meandering during stable conditions; *J. Clim. Appl. Meteorol.* **22** 1424-1430
- Hanna S R, Briggs G A, Deardorff J, Egan B A, Gifford F A and Pasquill F 1977 AMS workshop on stability classification schemes and Sigma curves—summary of recommendations; *Bull. Meteorol. Soc.* **59** 1305-1309
- Mc Elroy J L 1969 A comparative study of urban and rural dispersion; *J. Appl. Meteorol.* **8** 19
- Metcalf J I 1975 Gravity waves in a low level inversion; *J. Atmos. Sci.* **32** 351-361
- Munn R E 1964 Turbulence statistics at Douglas point; *J. Appl. Meteorol.* **3** 771-779
- Padmanabhamurthy B and Gupta R N 1979 Stability classification in micrometeorology; *Mausam* **28** 526-527
- Panchal N S and Chandrasekharen E 1978 Examination of Pasquill stability classification for a coastal site; *Meteorol. Rundsch.* **31** 84-86
- Panofsky H A, Egolf C A and Lipschutz R 1978 On characteristics of wind direction fluctuations in the surface layer; *Boundary Layer Meteorol.* **15** 439-446
- Pasquill F 1976 Atmospheric dispersion parameters in Gaussian plume modelling. Part II. Possible requirements for changes in the Turner work book values. EPA 600, USEPA, RTP, NC 271
- Raynor G S and Heyes J V 1984 Wind direction meander at a coastal site during onshore flow; *Climate. Appl. Meteorol.* **23** 967-978
- Sadhuram Y 1982 A study of dispersion of pollutants over complex terrain with special reference to Visakhapatnam city. Ph.D. thesis submitted to Andhra University, Waltair
- Sadhuram Y 1986 Seasonal variation of σ_θ with wind speed, direction and stability; *Boundary-Layer Meteorol.* **34** 99-101
- Sadhuram Y and Vittal Murthy K P R 1983 Seasonal variation of wind direction fluctuations vs Pasquill stability in complex terrain; *Boundary-Layer Meteorol.* **26** 197-202
- Sadhuram Y and Vittal Murthy K P R 1984a Correlation between mixing height and surface turbulence; *Environ. Pollut. (Series B)* **8** 17-21

- Sadhuram Y and Vittal Murthy K P R 1984b A study of pollution potential of Visakhapatnam *Boundary-Layer Meteorol.* **29** 397-407
- Sadhuram Y and Vittal Murthy K P R 1986 Diurnal variation of Pasquill stability classes at a coastal station; *Mausam* **37** 187-192
- Sedefian L and Bennett E 1980 A comparison of turbulence classification schemes; *Atmos. Environ.* **14** 741-750
- Sethuraman S 1977 The observed generation and breaking of atmospheric internal gravity waves over the Ocean; *Boundary-layer Meteorol.* **12** 331-349
- Sethuraman S, Nagle C and Raynor G S 1982 Seasonal variations in the formation of internal gravity waves at a coastal site; *J. Appl. Meteorol.* **21** 237-244
- Shirvaikar V V 1975 Recommended code of practice for micrometeorological techniques in air pollution. ISI. Doc. CDC53 (6358)
- Singer I A and Smith M E 1953 Relation of gustiness to other meteorological parameters; *J. Meteorol.* **10** 121-126
- Slade D H 1968 *Meteorology and atmospheric energy*; USEAC, TID 24490, Division of technical information extension.
- Verrall K A and Williams R L 1982 A method for estimating the standard deviation of wind direction; *J. Climate. Appl. Meteorol.* **21** 1922-1925

Seasonal and diurnal variability of thermal structure in the coastal waters off Visakhapatnam

B PRABHAKARA RAO, V RAMESH BABU* and
P CHANDRAMOHAN*

National Institute of Oceanography, Regional Centre, Andhra University Campus,
Waltair 530 003, India

* National Institute of Oceanography, Dona Paula, Goa 403 004, India

MS received 21 December 1985; revised 4 October 1986

Abstract. Seasonal and diurnal variability of thermal structure in the coastal waters off Visakhapatnam has been examined in relation to the flow field and surface winds utilizing the hourly data of temperature and currents taken at a fixed location over a tidal cycle at monthly intervals. The coastal currents in the pre-monsoon period and strong near-surface winter cooling processes affect the thermal structure of the coastal sea. Upwelling which is predominant during March to May with an intermittent relaxing event helps in the development of a strong layered thermal structure while convective mixing due to winter inversions during November to February causes weak thermal gradients in the water column.

Keywords. Thermal structure; upwelling; sinking; coastal currents; Visakhapatnam coast.

1. Introduction

The changes in the thermal structure of the coastal sea are generally attributed to the coastal current patterns. Earlier studies on the variability of water characteristics off Visakhapatnam coast mainly dealt with the temperature and salinity data (La Fond 1954; La Fond and Rao 1954; Varadachari 1958; Murthy and Varadachari 1968 and Rao *et al* 1986). A few studies have been attempted to describe the coastal circulation off Visakhapatnam based on the information derived indirectly either from density field (Rao 1956; Murthy and Sastry 1957) or by drift methods (Ramanatham *et al* 1967). These studies have indicated two different regimes of upwelling and sinking off the coast during pre-monsoon and autumn periods respectively under the influence of seasonally varying wind and current systems. On the shorter time scales, the oscillations in the thermal structure are related to surface tidal forces. Though Shetye (1984) investigated the thermal variability in the coastal waters off Kerala, studies relating to the actual observed flow field with the thermal variability off the Visakhapatnam coast are not generally available. We present here the seasonal and diurnal variabilities of the thermal structure of waters off Visakhapatnam coast which are discussed in relation to the observed current and surface wind fields.

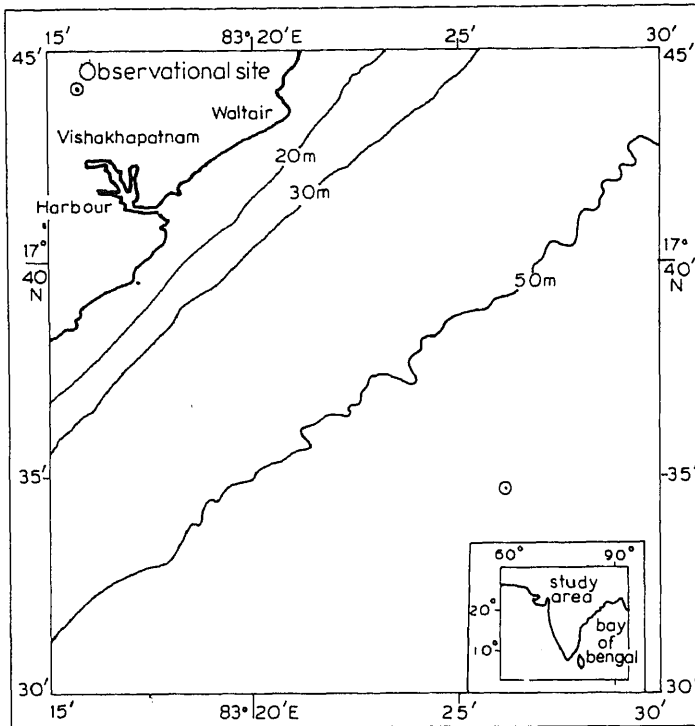


Figure 1. Observational location map.

was selected to represent every calendar month. The observational site (figure 1) was located at a depth of 62 m. The mechanical bathythermograph (MBT) and a direct reading current meter (DRCM) (Model: DNC 3; accuracy: ± 5 cm/sec; $\pm 10^\circ$) were deployed from an anchored boat for collecting the temperature and current data respectively at every 10 m depth interval of water column. While the temperature data were obtained by digitizing continuous depth-temperature profile and thereafter by applying the necessary corrections, the currents were obtained by reading the display of the current meter which was held for a short time at every 10 m depth. Simultaneously, the wind data were obtained using an anemometer and a portable magnetic compass. The temperature data were collected over a semi-diurnal tidal cycle for every month from February 1980 to January 1981. During the monsoon season (July-August) the observations could not be carried out fully due to the prevailing rough sea conditions and limited MBT and the surface meteorological data were then collected. The current data were available upto June only and for subsequent period, no information on currents was obtained due to the failure of the current meter.

Table 1. (I) Wind speed (m/sec) and (II) Direction (degrees true north).

Month/Time	0600	0700	0800	0900	1000	1100	1200	1300	1400	1500	1600	1700	1800	1900	2000	IST	Average
Feb	I	-	-	-	4.3	-	4.3	4.3	5.0	5.3	4.3	4.0	5.2	5.5	5.2	200	4.8
	II	-	-	-	225	-	210	210	200	180	200	180	200	230	200		205
Mar	I	-	-	1.9	2.0	2.6	1.8	-	1.0	2.7	2.9	3.3	5.3	5.0	-	-	2.9
	II	-	-	10	10	20	80	-	150	150	150	160	180	185	-	-	110
Apr	I	-	6.7	7.5	8.0	8.0	8.3	8.3	-	-	-	-	-	-	-	-	7.8
	II	-	220	220	220	220	220	220	-	-	-	-	-	-	-	-	220
May	I	-	4.3	3.7	3.8	5.0	5.0	6.0	5.0	5.0	5.0	-	-	-	-	-	4.8
	II	-	210	210	210	210	170	210	180	200	200	-	-	-	-	-	201
Jun	I	-	2.2	2.8	4.0	3.0	2.0	2.3	4.0	2.7	2.7	1.9	-	-	-	-	2.8
	II	-	180	180	200	160	170	180	200	200	200	200	-	-	-	-	187
Jul	I	-	10.8	-	-	-	-	-	-	-	-	-	-	-	-	-	10.8
	II	-	200	-	-	-	-	-	-	-	-	-	-	-	-	-	200
Aug	I	-	-	4.3	5.5	5.6	-	-	-	-	-	-	-	-	-	-	5.1
	II	-	-	180	180	180	-	-	-	-	-	-	-	-	-	-	180
Sep	I	-	2.6	3.3	2.5	2.6	-	2.6	3.6	3.8	4.5	3.3	4.6	-	-	-	3.3
	II	-	45	45	45	45	-	180	180	180	180	180	160	-	-	-	126
Oct	I	-	6.3	6.3	6.7	6.7	6.0	6.0	6.0	5.0	5.0	4.2	-	-	-	-	5.8
	II	-	45	45	45	45	45	45	45	45	45	45	-	-	-	-	45
Nov	I	-	2.8	4.0	4.0	5.0	5.0	5.2	5.0	5.3	5.3	5.0	-	-	-	-	4.7
	II	-	40	40	40	40	40	40	40	40	40	40	-	-	-	-	40
Dec	I	3.0	3.0	4.8	4.3	5.0	5.0	4.2	4.2	2.5	2.2	2.0	3.6	-	-	-	3.7
	II	45	45	45	45	45	45	45	45	45	45	45	45	-	-	-	45
Jan	I	3.4	5.0	5.0	3.0	3.9	2.5	2.5	3.4	3.4	3.4	3.4	-	-	-	-	3.5
	II	50	50	50	50	60	60	40	40	50	50	70	-	-	-	-	52

Table 3. Surface meteorological conditions.

Calender period	Diurnal variation of winds Speed	Direction	Air temperature and SST	Diurnal SST range (°C)
Feb	Small	Small	Mean air temp. < Mean SST	0.4
Mar	High	High	Mean air temp. \approx Mean SST	1.7
Apr	Small	Nil	—	0.2
May	Small	Small	Mean air temp. > Mean SST	0.5
Jun	Small	Small	Mean air temp. > Mean SST	1.0
Jul	—	—	—	—
Aug	—	—	Mean air temp. > Mean SST	—
Sep	Small	High	Mean air temp. \approx Mean SST	0.7
Oct	Small	Nil	Mean air temp. > Mean SST	1.5
Nov	Small	Nil	Mean air temp. > Mean SST	1.2
Dec	High	Nil	Mean air temp. \approx Mean SST	0.5
Jan	Small	Small	Mean air temp. > Mean SST	0.8

observational site. In February, the winds vary little diurnally and they are mainly from southwest and south directions with a speed of around 5 m/sec. In March, the wind data show a diurnal instability in both direction and speed. They are weak blowing from north-northeast and east directions before noon and are strong in the evenings blowing from southeast and south directions. In April, very steady and strong southwest winds with typical speeds around 8 m/sec prevail, while in May, the winds become weak again with moderate speeds around 5 m/sec and directed from south-southwest. In June, the winds are further lowered reaching an average value of 2.8 m/sec and are seen to rotate anti-clockwise. During July, the winds are strengthened (11 m/sec) with the onset of summer monsoon whereas in August, the wind speeds decrease to around 5 m/sec. The wind speeds weaken further (3 m/sec) during September and show a marked diurnal instability, especially in the direction as in March. From October to January, the wind speeds are mainly between 2 and 7 m/sec and the wind direction is predominantly from northeast. The diurnal stability in the wind field, especially the wind direction, is well pronounced during this period.

3.1b Air and sea surface temperature: The hourly values and the diurnal averages of both air (dry bulb) and sea surface temperatures (SST) at the observational site are presented in table 2. The air temperature is on an average lower than SST in February whereas during March, the difference between the averages of these two temperatures is considerably reduced. During the rest of the year, the air temperature in general is higher than SST. However, there is a tendency for the air temperature to be lower than SST at certain morning hours during post-monsoon and winter periods with an exception in January. These results are further summarized in table 3.

3.2 Temperature variation

3.2a Diurnal time scales: Figure 2 shows the diurnal variations of thermal structure depicted for every month except July. During February, the diurnal SST range (maximum minus minimum) for the observational period is 0.4°C. A positive

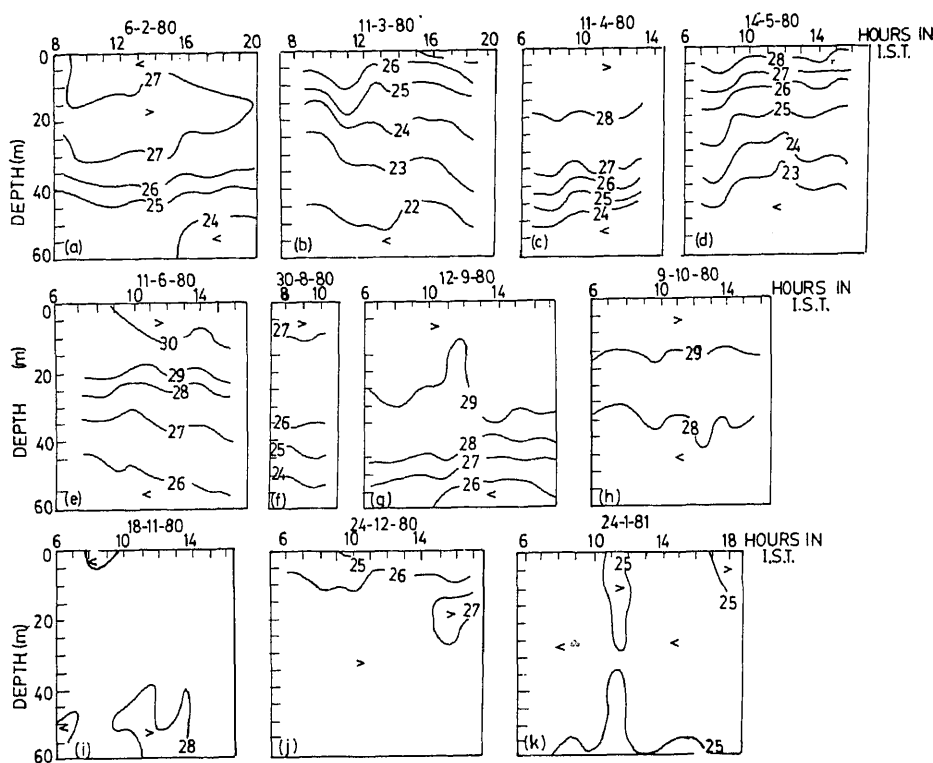


Figure 2. Diurnal variation of temperature($^{\circ}\text{C}$) in the coastal waters off Visakhapatnam for different months.

temperature gradient found in the depth range of 10–30 m continues to be present throughout the day (figure 2a). However, near the bottom, pockets of warm and cold waters are seen. During March, the diurnal SST range is well pronounced (1.7°C) and the positive temperature gradient as observed in the previous month completely disappears (figure 2b). The isotherms further exhibit the same mode of diurnal variation throughout the water column. In April, the mixed layer is conspicuously well developed (~ 35 m thickness) with an increase in temperature at all depths (figure 2c) while in May, the rising of isotherms is again seen throughout the water column (figure 2d) as in March. The mode of diurnal variation of isotherms in April is uniform depthwise whereas during May, its nature in the upper 20 m layer is in contrast to that in the near bottom layer where a dome in isotherms is seen around 1200 IST. During June, the surface layer gains heat and the diurnal SST range is about 1°C (figure 2e). The temperature of the water column lowers in July (diurnal SST range not presented here due to limited data) and August (figure 2f) with a simultaneous increase in the depth of thermocline. The diurnal SST range in September is more or less the same as that in the pre-monsoon period and the entire water column gains heat as seen from a general increase in temperature at all depths (figure 2g). In October, the temperature of water column further rises along with an increase in the diurnal SST range (1.5°C) (figure 2h). It is also to be noted that the thermal gradients are low in the water

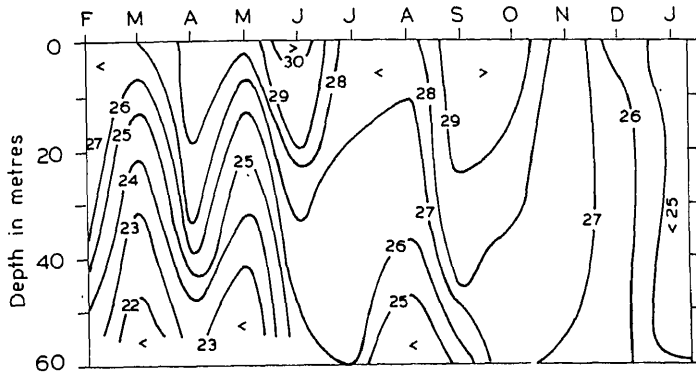


Figure 3. Seasonal variation of temperature(°C) in the coastal waters off Visakhapatnam.

of inversion layers near the surface (figures 2i and 2j) and the SST diurnal range is 1.2°C in November and it is 0.5°C in December (figure 2k). In January, the temperature of the water column reaches a minimum (around 24.8°C) and the inversions continue to be present.

3.2b Seasonal time scales: The temperatures observed at an hourly interval are averaged over each day to obtain daily averages which in turn represent the monthly values. The seasonal variation of thermal structure is presented in figure 3 which clearly shows the layered structure from February to September with a general weakening of thermal gradients with time. During November to January, the layered structure completely disappears leading to a strong mixed layer as seen from the vertical orientation of isotherms. In general, the thermal structure shows a very shallow thermocline during March and May with a conspicuous development of a strong intermittent mixed layer in April. A general lowering of isotherms takes place in the water column from May to June. During the summer monsoon season (July to August) again isotherms rise resulting in a zone of relatively cold waters (< 25°C) near the bottom. The seasonal cooling in the surface layer is found to be more than 1°C. A rapid increase in the temperature especially in the surface layers is observed during the post-monsoon season (September to October) and from November onwards, the temperature generally falls with time throughout the water column reaching a minimum value in January.

3.3 Currents

In February (figure 4a), the currents in the upper 30 m layer are steady and directed northward and northeastward while at deeper depths, currents vary considerably with time. During March (figure 4b) the flow is mainly between northeast and east with some off-shore drift in the upper layers in contrast to the longshore flow in February. From the data available in April (figure 4c), one could see that the flow is strengthened suddenly in the entire water column and is directed towards northeast with speeds around 1 m/sec. In May (figure 4d) the currents show a predominant off-shore direction in 0–10 m depth range as in March while below it, the currents are found oscillating. During June (figure 4e), the currents in

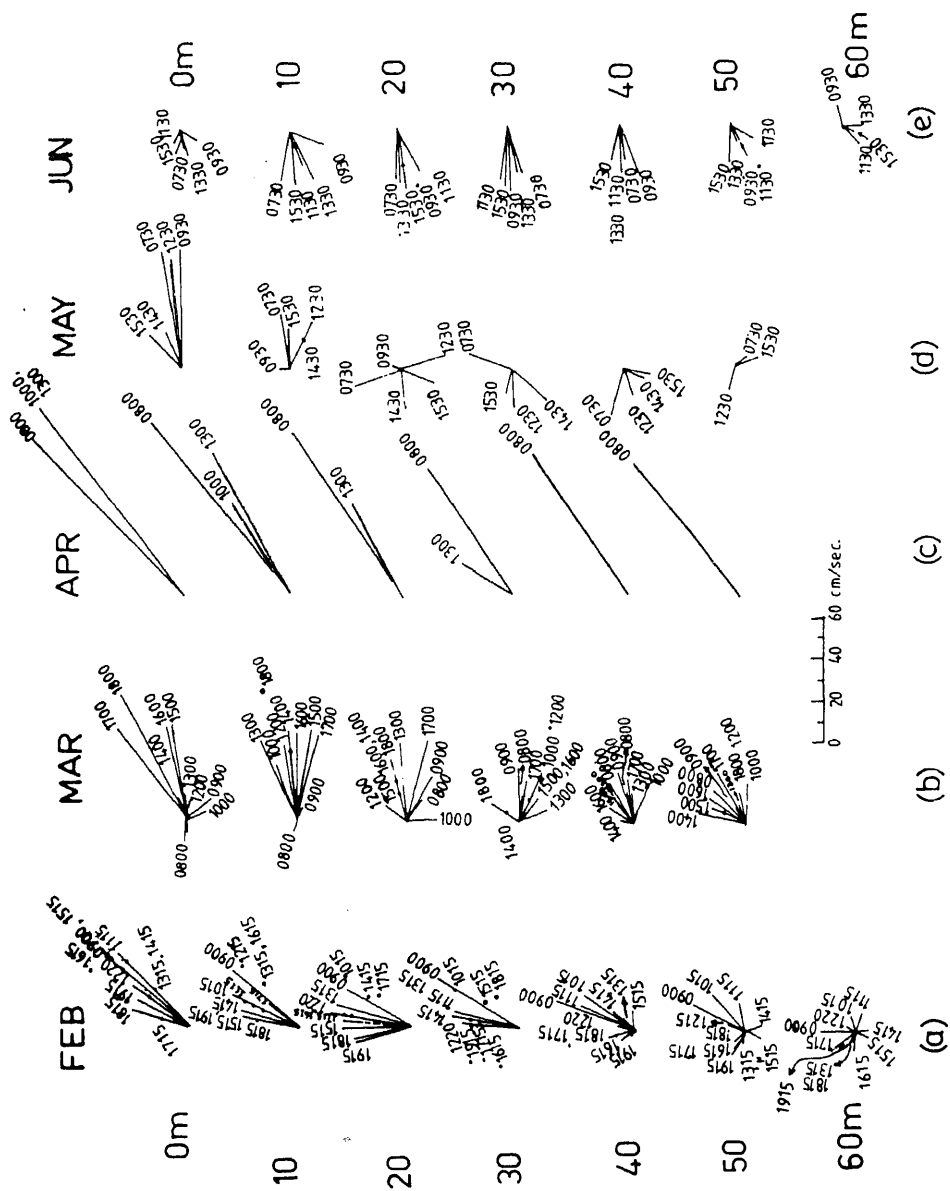


Figure 4. Coastal currents off Visakhapatnam.

general reverse in direction as seen from the presence of steady on-shore components in the upper 40 m water column while near the bottom they are slightly variable in direction.

4. Discussion

The maximum diurnal SST variation (range = 1.7°C) in March could be attributed to the stronger development of land-sea breeze system under which a high diurnal variation in wind field is seen (table 3). As the winds during the day time change their direction from north to south with a simultaneous increase in the speed (table 1) a wind drift is set up bringing more inshore warm waters into the observational location. The dry cold winds (table 2) during February cool the surface layer through an increase in both sensible and evaporative heat fluxes from sea to the atmosphere. This cooling in the surface layer as seen from the presence of inversions (figure 2a) leads to the formation of denser waters. The resultant convective mixing due to the sinking of denser waters is responsible for the development of weak gradients in the depth range of 0–15 m. Near the bottom (> 40 m), the presence of low and high temperature regimes indicates the effect of tides which can be inferred from the oscillatory nature of observed flow field.

The consistent occurrence of very cold waters ($< 22^{\circ}\text{C}$) near the bottom in March (figure 2b) is due to the upwelling of waters in the coastal region as a result of increase in the off-shore components of currents compared to those in February. Although the near bottom currents do not show any on-shore flow tendency in this month, upwelling occurs in response to the presence of a vertical shear flow (stronger off-shore flow above the weaker one). It is not possible to examine the influence of the currents on the thermal structure in April due to limited current data. However, the strong surface winds (8 m/sec) which are conspicuously set during this month increase turbulent mixing in the upper layers resulting in weaker thermal gradients. Relatively, weaker off-shore components in the near surface flow field (figure 4c) during this month would also help in weakening the upwelling processes. When wind force is relaxed in May, the near surface currents (figure 4d) have become weak and are directed off-shore while below 10 m depth, they show some tendency of on-shore flow. This flow field revives upwelling in the water column.

It might be surprising to notice sinking under stronger winds blowing parallel to the coast situated on their left side and revival of upwelling accompanied by relaxation of winds. In shallow coastal regions where the angle of deflection between winds and the Ekman drift becomes smaller than 90° , upwelling is not expected to be intensive though winds are favourably blowing parallel to the coast. Moreover, some deviations from the Ekman theory are expected and the present set of observations need not follow the classical theory since the assumptions made in the theory cannot be approximated in a shallow coastal area. For the present study, the mean Ekman layer (depth of frictional resistance) is found to be about 40 m and the Rossby's radius of deformation is around 30 km. The reversal of surface currents in June from predominant off-shore components to on-shore components causes a cessation of upwelling and initiates sinking of waters which further helps in the development of surface layer and an increase in the

Table 4. Departures of dew point temperature from SST (°C).

Month	Mean dew point temperature	Departure from SST
Feb	25.2	-1.7
Mar	26.0	-1.0
Apr	-	-
May	28.3	-0.1
Jun	28.6	-1.7
Jul	-	-
Aug	27.7	+0.2
Sep	28.8	-0.9
Oct	28.5	-1.1
Nov	25.8	-1.3
Dec	22.0	-3.4
Jan	22.0	-2.9

temperature by about 3°C near the bottom from May to June. Thus, the upward motions in the water column seem to be mainly controlled by the off-shore/on-shore currents which are driven by factors other than wind. There is also a possibility of transient effects on sinking/upwelling processes caused by propagation of long period boundary waves which are trapped in the coastal regions. When a wave trough(ridge) passes over the area of study, it suppresses the upward (downward) motion of the thermocline intensifying the sinking (upwelling) processes in the water column.

The strong monsoon winds in July and August enhance the mixing processes resulting in a general cooling of water column (1°C). It is not possible to examine the influence of currents on the cooling processes in this period as there is no current data available after June. The absence of thermal gradients in the upper layer during September indicates the persistence of monsoonal wind effect. The homogeneous nature of the entire water column during November to January shows the influence of strong convective mixing as a result of inversions in the water column. The presence of thermal inversions could be related to net heat exchange between the sea and the atmosphere. Though sensible heat transport is directed towards the sea during November and January by virtue of higher air temperatures as compared to SST (table 3), the winter cooling is mainly effected through latent heat losses as seen from larger departures of dew point temperature from SST (higher evaporation rates) (table 4).

5. Conclusion

The present study gives some general characteristics of thermal variability in the coastal waters off Visakhapatnam based on a single year data. It is seen that the water column off Visakhapatnam coast is normally characterized by a layered thermal structure during spring and pre-monsoon (March to June) whereas during the later part of the year, this layered structure becomes weak and is absent by

winter (November to February) due to an increase in the convective mixing. The seasonal variations in the depth of thermocline are rather controlled by current structure than by wind field alone.

Acknowledgements

The authors wish to express their sincere thanks to the late Dr H N Siddiquie and to Dr T C S Rao for their keen interest.

References

- La Fond E C 1954 On upwelling and sinking off the east coast of India *Andhra Univ. Mem. Oceanogr.* **1** 117-121
- La Fond E C and Moore A T 1972 Sea temperature variations off the east coast of India *Indian J. Mar. Sci.* **1** 63-65
- La Fond E C and Rao C P 1954 Vertical oscillations of tidal periods in the temperature structure of the sea *Andhra Univ. Mem. Oceanogr.* **1** 109-116
- Murthy C B and Sastry A A R 1957 Distribution of density and the associated currents at the sea surface in the Bay of Bengal *Indian J. Meteor. Geophys.* **8** 88-92
- Murthy C S and Varadachari V V R 1968 Upwelling along the east coast of India *Bull. Natl. Inst. Sci. India* **38** 80-86
- Ramanatham R, Murthy A V S, Varadarajulu R and Reddy B S R 1967 Coastal currents near Waltair by double theodolite method *J. Indian Geophys. Union* **4** 107-112
- Rao C P 1956 Ocean currents off Visakhapatnam *Indian J. Meteor. Geophys.* **7** 377-379
- Rao T V N, Rao D P, Rao B P and Ramaraju V S 1986 Upwelling and sinking along Visakhapatnam coast *Indian J. Mar. Sci.* **15** 84-87
- Shetye S R 1984 Seasonal variability of the temperature field off the south-west coast of India *Proc. Indian Acad. Sci. (Earth Planet. Sci.)* **93** 399-411
- Varadachari V V R 1958 *On some meteorological and oceanographic studies of the coastal waters off Waltair in relation to upwelling and sinking* DSc thesis, Andhra University, Waltair

STATEMENT ABOUT OWNERSHIP AND OTHER PARTICULARS ABOUT
PROCEEDINGS OF THE INDIAN ACADEMY OF SCIENCES
(EARTH AND PLANETARY SCIENCES)

Place of Publication	.. Bangalore
Periodicity of Publication	.. Minimum of Four numbers in each volume
Printer's Name	.. C. N. R. Rao Indian Academy of Sciences Bangalore 560 080
and 5. Publisher and Editor	.. C. N. R. Rao
Nationality	.. Indian
Address	.. Indian Academy of Sciences P B No. 8005 Bangalore 560 080
Name and Address of the Owner	.. Indian Academy of Sciences Bangalore 560 080

C. N. R. Rao, hereby declare that the particulars given above are true to the best of
my knowledge.

Dated 1st April 1987

C. N. R. Rao
Signature of Publisher

Variable $^{190}\text{Os}/^{184}\text{Os}$ ratio in acid residues of iron meteorites

P S GOEL

Department of Chemistry, Indian Institute of Technology, Kanpur 208 016, India

MS received 18 June 1985; revised 6 April 1986.

Abstract. In residual materials obtained on dissolution of iron meteorites in $2\text{M H}_2\text{SO}_4$, the ratio of $^{190}\text{Os}/^{184}\text{Os}$ has been measured by radiochemical neutron activation analysis. Most residues have a normal isotopic ratio (to within $\pm 2\%$). However, in some residues both positive and negative deviations in the isotopic ratio are seen. The most spectacular deviations are in the insoluble fragments (nuggets) from Sikhote Alin iron meteorite where the $^{190}\text{Os}/^{184}\text{Os}$ ratio is about 50% of the normal value. The new results confirm our earlier observations that iron meteorites contain pre-solar grains.

Keywords. Iron meteorites; osmium isotopes; isotopic anomalies; pre-solar grains; origin of iron meteorites.

1. Introduction

In two recent papers from this laboratory experimental evidence was presented that iron meteorites contain pre-solar grains which are apparently associated with the residues obtained on dissolving the metal in 1 to 2 M H_2SO_4 (Goel and Murty 1983; Murty *et al* 1983). The acid-insoluble residues are found to have isotopically anomalous osmium and xenon. In the present paper a number of experiments are described giving additional results to establish that the ratio of $^{190}\text{Os}/^{184}\text{Os}$ in some of the acid-residues of iron meteorites is indeed variable and anomalous. A number of control experiments are to show that our results are not due to experimental artifacts introduced during neutron irradiation or during radiochemical processing and counting of the osmium activities. In view of the startling nature of these results, experimental details on all aspects of the work are presented.

While neutron activation analysis technique has been extensively used for reliable measurements of trace elements in cosmic matter, its application to isotope ratio determination has been rather limited. In meteorites, isotopic ratios have been measured by RNA for Hg (Reed and Jovanovic 1969), Os (Takahashi *et al* 1976; Goel and Murty 1983) and Te (Oliver *et al* 1981). With the availability of high resolution gamma spectrometry systems, the RNA method stands to be developed into a powerful technique for isotopic ratio measurements.

The basis for the determination of isotopic ratio for the Os isotopes can be seen from the relevant nuclear data presented in table 1. In most samples we did not see the gammas from ^{193}Os because of the cooling time of more than one week. The gamma lines of 646.1 keV and 129.4 keV were spectrum-analysed. The samples, particularly those showing anomalous ratios were repeatedly counted over long period of time so that the identification of the nuclide could be confirmed from their characteristic half-lives.

2. Experiments and results

Acid-insoluble residues were obtained by dissolving pieces of iron meteorites slowly in 2M H₂SO₄ (Murty *et al* 1982, 1983; Goel and Murty 1983). The insoluble residues were often found to contain millimeter size brittle pieces and thin metallic flakes. Most of the material was black powder of sub-metallic luster. A low density fraction, (*L*) could be separated in the form of slurry with water. The high density fraction, (*H*) was more lustrous. We further separated the residues into magnetic and non-magnetic fractions with the help of a hand magnet. From Sikhote Alin, several large size (few mm) pieces (inclusions) were obtained which had a specific gravity of about 6.5. They were submetallic in luster, magnetic and brittle. Further characterization could not be done.

Samples from residues, masses varying from about 10 to 200 mg, were sealed in quartz capsules and packed for irradiation along with the monitors. Few milligrams of a standard solution of ammonium hexachlorosmate were weighed on MgO or Al₂O₃ matrices for use as monitors. Nine different irradiations, listed in table 2, were carried out for Os isotopic work. There were some variations in the detection systems for some of the runs. These are described in each case.

2.1 The NBS-run

Several acid residues were sealed in quartz tubes. Some of the residues were spiked with osmium salt, freeze-dried and sealed. Irradiation was carried out at the U.S.

Table 1. Nuclear parameters for Os isotopic ratio measurements.

Mass number (A)	Abundance (%)	$\sigma_{n, \gamma}$ (barns)	Daughter nuclide.		
			A	$t_{1/2}$	$E\gamma(\text{keV})$
¹⁸⁴ Os	0.018	3000	¹⁸⁵ Os	93.6d	646.1
¹⁹⁰ Os	26.38	12	¹⁹¹ Os ^g	15.4d	129.4
¹⁹² Os	40.96	1.6	¹⁹³ Os	30.5h	138.9
					460.5

Table 2. Different irradiations for ¹⁹⁰Os/¹⁸⁴Os measurements.

Experiment number	Date	Reactor	Flux (cm ⁻² sec ⁻¹)	Duration of irradiation	Target material
NBS	June '82	NBS	1.5×10^{14}	32 hr	Residues
No 21	Oct '82	CIRUS	1×10^{13}	24 hr	Osmate on different matrices
J-1, J-2	Oct '82	CIRUS	1×10^{13}	1 week	Residues
J-4	Jan '83	CIRUS	1×10^{13}	1 week	Residues and Os salt
Q-1	Feb '83	CIRUS	1×10^{13}	4 hr	Osmium metal and salts
P-1	Feb '83	APSARA	1×10^{12}	4 hr	Osmium metal and salts
1/84	Nov '84	CIRUS	1×10^{13}	1 week	Residues (Canyon Diablo)
1/85	Jan '85	CIRUS	1×10^{13}	1 week	Residues (Bear Creek)
2/85	Feb '85	CIRUS	1×10^{13}	1 week	Residues (Sikhote Alin)

National Bureau of Standards (Washington, D.C.) reactor in position G2 where the cadmium ratio is given as 55 (Becker and La Fleur 1974). The samples were cooled for 24 hr before radiochemical processing.

After adding osmate carrier (1.4 mg Os), a sample was dissolved in conc. HNO_3 . Os was distilled with additional 2 ml HNO_3 as OsO_4 by heating the solution. The Sikhote Alin sample did not dissolve completely. The distillate (OsO_4) was collected in 5% solution of thiourea in 6N HCl. The Os-thiourea complex was made alkaline with NaOH. H_2S was passed and OsS_2 was precipitated from the solution after it had been acidified with HCl. It was necessary to purify the OsS_2 thus obtained by one more cycle of distillation and sulphide precipitation steps. The most prominent and troublesome interference was from Br isotopes. Os from several samples was lost during chemical processing. Only two residues (Odessa, m-H, spiked and Sikhote Alin inclusion) could be successfully prepared for counting. Solid OsS_2 was counted in contact geometry on a high purity Gamma-X detector. Resolution at 1332 keV was 1.65 keV (FWHM). The sensitivity was 0.208 keV per channel. The data analysis programme had ^{191}Os in the memory card. For ^{185}Os , the 646 keV peak area, taken from the print-outs was corrected for decay. The counting was done over a period of one week so as to obtain 3 points on the decay curve for each nuclide. The activities decayed with the expected half-lives. The activity ratios of three nuclides ^{185}Os , ^{191}Os and ^{193}Os were measured. The results, presented in figure 1, which show that (i) the $^{191}\text{Os}/^{193}\text{Os}$ ratios in the residues and standard are identical and (ii) spiked Odessa is about 7% enriched in ^{184}Os similar to the results of Goel and Murty (1983).

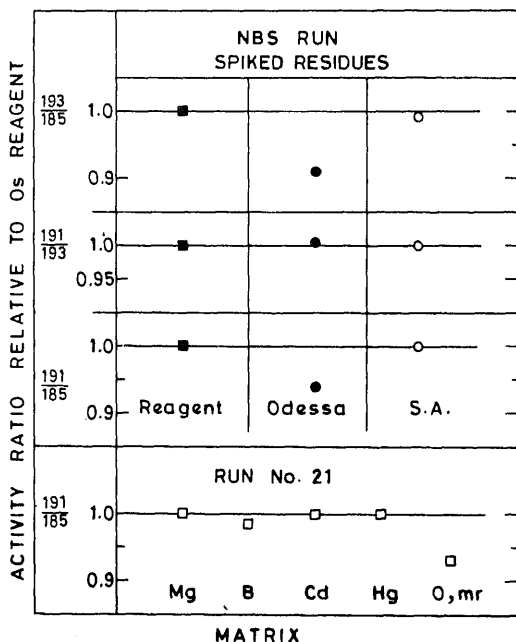


Figure 1. Osmium isotopic ratios from the NBS run and vial no. 21. The $^{190}\text{Os}/^{184}\text{Os}$ ratio in residues from Odessa is lower than the value for reagent Os in both runs.

Table 3. Contents of irradiation vial no. 21.

Matrix compound	Al ₂ O ₃	H ₃ BO ₃	CdCl ₂	HgO	Odessa, m-H
Weight (mg)	5.0	11.0	14.0	12.0	160
Os added (μg)	14.5	16.8	13.1	13.1	0.5

2.2 BARC bombardment: run no. 21

A solution of ammonium hexachlorosmate was loaded on matrices of different reagents in quartz capsules which were dried and sealed. The Odessa magnetic residue was an aliquot from the high density fraction of the residue used earlier. It was spiked with 0.5 μg Os. The details are given in table 3.

The vial was irradiated in CIRUS reactor at Bombay for 24 hr to a thermal neutron flux of 1×10^{13} n cm⁻² sec⁻¹. In the CIRUS reactor, in the position in which our samples are normally irradiated, the fast ($E > 1$ MeV) to the thermal neutron ratio is < 0.01 and the epithermal ($E > 100$ keV) to the thermal ratio is < 0.1 . Radiochemical processing was done after 4 weeks of bombardment. Os carrier was added and OsO₄ from each sample was distilled. The Os-thiourea complex was made to 5 ml volume in each case and counted in liquid form. It was necessary to purify the Odessa sample by adding 5 ml conc. HNO₃ to the thiourea complex and distilling OsO₄ again in fresh thiourea solution. The detector used was a coaxial high purity germanium crystal (ORTEC; Gamma-X). At 1332 keV, the resolution (FWHM) was 2 keV. Since, only a 1024 channel MCA was available, the gain was kept low (1.5 keV/channel). No other gamma lines were seen. Area of the peaks under three channels was taken after proper background subtraction. No shoulders were noted in the gamma-ray-peaks of the samples. The results are shown in figure 1. Only one sample, Odessa residue (m-H), is anomalous.

2.3 Vial nos J-1 and J-2

Acid-insoluble residues from different iron meteorites were sealed in quartz capsules as listed in table 4. The sample capsules were placed in an aluminium irradiation can to its full capacity, along with the monitors. The two cans were irradiated in the self-service tray of the reactor concurrently. Osmium from the samples was distilled and, when needed, was purified by redistillation as described for vial no. 21. Gamma ray intensities were measured using the Gamma-X (ORTEC) detector and the Canberra MCA (1024 channels).

The decay-corrected ¹⁹¹Os/¹⁸⁵Os ratios for reagent osmium samples in J-1 and J-2, on November 25, 1982 were 15.21 ± 0.15 and 15.53 ± 0.15 . Since the reproducibility of the replicate measurements on aliquots was within statistical errors, the difference of 2% in the two numbers might as well be a reflection of the variation in neutron energy spectrum over a distance of about 10 cm (a likely separation between capsules of the two different vials). Within one vial such an effect should be negligible since the capsules were all stacked within a lateral distance of about 2 cm.

The decay-corrected ¹⁹¹Os/¹⁸⁵Os activity ratios for vials J-1 and J-2 are given in table 4. The results, given for three different days, show good reproducibility. We

Table 4. Results from vial numbers J-1 and J-2.

Acid residue	Mass (mg)	Os (ppm)	$(^{191}\text{Os}/^{185}\text{Os})_s / (^{191}\text{Os}/^{185}\text{Os})_{\text{std}}^*$		
			Nov. 9	Nov. 13	Nov. 25
Sikhote Alin, nm	10	9	0.98	1.00	1.00
Sikhote Alin, m	100	0.8	0.98	1.00	0.99
Sikhote Alin, flakes	40	0.03	1.04 \pm 0.04	1.00 \pm 0.04	0.97 \pm 0.05
Sikhote Alin, inclusion	100	0.004	0.9 \pm 0.1	0.8 \pm 0.2	0.8 \pm 0.2
Henbury, nm(1)	4.0	17	1.00	1.00	1.00
Henbury, nm(2)	4.5	500	1.01	1.02	1.00
Henbury, m	119	45	1.00	1.01	1.00
Henbury, flakes	47	9	0.98	0.99	0.98
Toluca, nm	4.5	430	0.99	1.01	1.00
Toluca, m	58	56	0.99	1.00	1.00
Toluca, flakes	31	40	1.01	1.01	1.00
Canyon Diablo, nm(1)	10	160	1.02	1.00	0.99
Canyon Diablo, nm(2)	10	234	1.04	1.02	1.01
Canyon Diablo, nm(3)	6	314	1.01	1.01	1.00
Canyon Diablo, m(H)	175	5	1.03	1.00	0.99
Canyon Diablo, M(L)	42	155	1.00	0.99	0.98
Canyon Diablo, flakes	16	13	1.04	0.98	1.00
Odessa, m(H)	104	1.4	1.01	0.98	0.98
Odessa, m(L)	38	5	1.02	1.00	0.99
Campo del Cielo, nm	17	1000	0.98	0.96	1.00
Campo del Cielo, m(H)	118	520	1.00	1.00	1.00
Campo del Cielo, m(L)	50	120	0.98	0.99	1.00

* Statistical errors are \pm 1% unless specified.

find that the Os isotopic ratio in all the samples of J-1 and J-2 is remarkably constant to within 2%. This is clearly seen from the plot of data for November 25 in figure 2. The possibility that the Sikhote Alin inclusion has a 20% lower value of the isotopic ratio, is not ruled out. Unfortunately, due to low counting rates in these samples, the measurement error could not be reduced. The osmium contents of the iron meteorite residues were calculated assuming that the distillation step is quantitative. If the recovery is $< 100\%$, the Os contents may be higher than the values given in table 4.

These results may appear to negate the large variations that we found earlier (Goel and Murty 1983) and also in the subsequent runs that are reported in this work. A significant heterogeneity in the $^{190}\text{Os}/^{184}\text{Os}$ isotopic ratio must be present in some minor phase which shows up only when the normal osmium is low and the presolar component is not overshadowed by the homogenized component which is present in widely variable concentrations in all fractions of the acid insoluble residue. It is intriguing to note that Os varies from 4×10^{-3} to 1×10^3 ppm in residues of iron meteorites. The negative results of these vials may be taken to provide further support to the reliability of our measurements.

2.4 Run no. J-4

This vial contained acid-insoluble residue (magnetic, heavy) from Odessa iron meteorite and osmate salt on different matrices as listed in table 5. The matrix

enhanced. The irradiation was carried out using the CIRUS reactor. Os from samples was distilled and its gamma activities measured as described for samples vial no. 21. The values of the $^{191}\text{Os}/^{185}\text{Os}$ ratio are shown in figure 3. Acid residue Odessa (m, H), is anomalous.

2.5 Vial no. P-1

Samples of natural osmium (table 6) in the form of osmate salt and metal powder were packed in a polythene tube and were bombarded in Apsara reactor at Trombay for 4 hr. The neutron flux was about $10^{12} \text{ cm}^{-2} \text{ sec}^{-1}$ with a fast-to-thermal ratio < 0.20 and the epithermal-to-thermal ratio of 0.40 to 0.45. The irradiated samples were subjected to gamma counting on Gamma-X detector connected to a Canberra MCA. The decay of the radio-nuclides was followed for two weeks and it was found to be consistent with the respective half-life. Since the activities were quite high, no radiochemical separation was done. The results given in figure 2 show no abnormal behaviour and an absence of self-shielding effects.

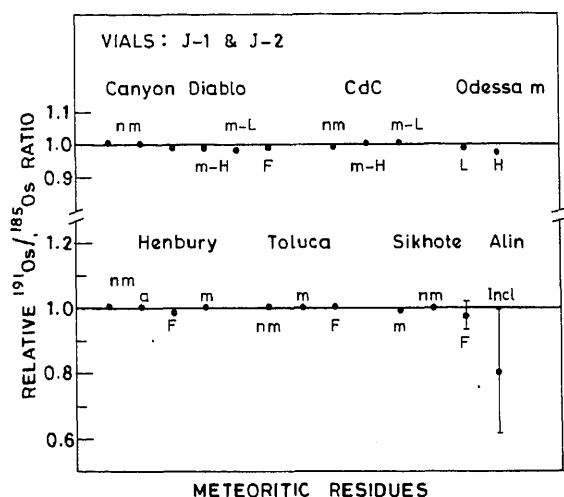


Figure 2. Results from vials J-1 and J-2.

Table 5. Contents of vial no. J-4.

Sample (matrix)	Mass (mg)	Os(μg)
Odessa m-H	96.4	0.65 ⁺
Al ₂ O ₃	10	1.44
Odessa, m+H	88	nil ⁺
CdCO ₃	5.9(Cd)	11.6
H ₃ BO ₄	1.7(B)	18.7
AgNO ₃	8.6(Ag)	13.5
Al ₂ O ₃	3 mg	16.8

⁺ plus natural osmium contents (about 0.2 μg)

Table 7 describes the samples packed for this run in a quartz vial for irradiation in CIRUS reactor. Additional information is given in table 2. The quantities packed were sufficiently large and pure so that the Os activities could be easily measured without radiochemical processing. It was also possible to measure the 2-day ^{193}Os in samples from this run. No variations were seen. However the measurement errors for ^{193}Os were large (about 5%).

The samples of Os metal powder after the bombardment were found smeared over the inner walls of the sample capsules which posed a serious problem in keeping the geometry of counting the same for all samples. This was overcome by

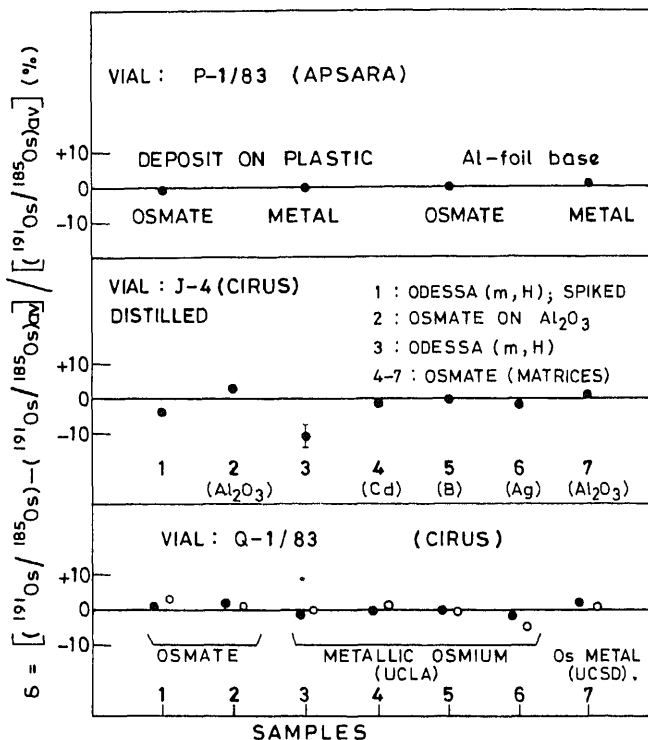


Figure 3. Osmium isotopic ratios (δ values in per cent) for samples of Os metal and Os salts on different matrices. Only Odessa, m-H is anomalous.

Table 6. Packing of vial P-1.

Number	Description
49 μg Os	Osmate on plastic
77 μg Os	Osmate on aluminium foil
460 μg Os	Osmium metal* powder on plastic
790 μg Os	Osmium metal* powder on aluminium foil

* Kindly provided by Professor J T Wasson (UCLA).

crushing each quartz sample capsule, along with osmium, into powder which was transferred to a 1 cm dia round bottom glass tube for counting. The counting was done on Gamma X detector connected to the Canberra MCA. The results are presented in figure 3. All samples gave identical values for the activity ratio of $^{191}\text{Os}/^{185}\text{Os}$, showing again an absence of self-shielding effects on isotopic ratio measurements.

2.7 Vial no. 1/84

Magnetic residue from Canyon Diablo iron meteorite was subjected to sieving by Sonic sifter into various size fractions with the hope that some of these would show enhanced anomalous component. The packing pattern and irradiation conditions were similar to the other vials, as listed in table 2. Aliquots of irradiated residues were dissolved in aqua regia and OsO_4 was distilled at 90°C , after adding 2 ml conc. HNO_3 . The aliquots were labelled as A and B. Some samples were distilled twice. In most cases, the second distillation (labelled II) of the once-distilled (labelled I) residue gave much lower activity. Some data on repetitive distillations are given in table 8. Counting was done on the Canberra detector connected to the ND-65 multi-channel analyser. The net counts were summed up in the 10 and 4 channels (1 channel = 0.5 eV) in the two gamma-ray energy peaks of the Os isotopes. The decay-corrected gamma ray activity ratios were calculated for both the 10-channel peak areas (R_{10}) and the 4-channel peak areas (R_4). This was done to guard against

Table 7. Packing on vial Q-1

11 μg Os (osmate)
40 μg Osmate Os
680 μg osmium metal (UCLA)
60 μg osmium metal (UCLA)
330 μg osmium metal (UCLA)
810 μg osmium metal (UCLA)
550 μg osmium metal sponge (La Jolla)*

* Kindly sent by Dr S V S Murty.

Table 8. Os activity ratios for successive distillations.

Residue	$^{191}\text{Os}(\text{c/s})$	R_{10}
Canyon Diablo, m-HI	3.9	21.9 ± 0.2
No. 5 II	3.6	22.0 ± 0.2
Canyon Diablo, m-HI	18.6	22.1 ± 0.2
No. 7 II	20	21.4 ± 0.2
Canyon Diablo, m-HI	14	22.8 ± 0.2
Nos. 8 and 9 II	13	22.5 ± 0.2
Toluca, m I	55	22.2 ± 0.2
No. 14 II	8	22.1 ± 0.2
Toluca, nm I	279	22.4 ± 0.2
No. 15 II	75	22.2 ± 0.2
III	13	21.9 ± 0.2

the influence of any spurious neighbouring gamma rays on the measured activity ratios and their intercomparisons. No inconsistencies were found. The results are given in table 9. The major aliquots of Canyon Diablo residues 8 and 9 happened to get accidentally mixed. These are given as '8 and 9' collectively. Comparisons of aliquots A and B are made in table 10. The agreement is good taking into consideration the possibility of heterogeneous distribution. In table 9 the data on aliquots A only are presented.

In vial 1/84, several samples show an enhancement of ^{190}Os over ^{184}Os . The maximum variation is + 8% (see table 9, figure 4) and is noted in both R_{10} and R_4 . Since the measurement errors are within 1% (or 2%, conservative) this variation is significant. In order to ensure that the variation is not due to such factors as drift of gain and instability of the counting system, or the variations in counting geometry etc many replicate countings were made of several standard samples and also of the sample (8 and 9). These results are given in the form of histograms for R_4 and R_{10} in figures 5 and 6. The results clearly show that the two sets of samples have different gamma activity ratios. The gamma ray spectra of (8 and 9) I and 2D3 (diluted standard no. 2) are shown in figures 7 and 8. In these two samples, the counting rates are comparable and the spectra shapes are similar, yet the activity

Table 9. Results on vial no. 1/84

Meteorite residue	Code	Mass (mg)	Os (ppm)	R^*	
				10 ch	6 ch
Canyon Diablo m-H					
< 30 μm	5	35	23	22.0	24.4
30-45 μm	6	37	19	22.3	24.7
45-75 μm	7	34	20	21.9	24.2
75-105 μm	8	36	5	22.0	23.6
105-125 μm	9	35	6	22.0	24.2
75-125 μm	8 and 9	70	5.7	22.53	24.78
125-150 μm	10	37	7.8	21.8	23.8
> 150 μm	11	36	5	21.9	24.4
Sikhote Alin, nm	12	30	2.7	22.7	25.0
Bear Creek, m	13	31	0.1	22 \pm 3	—
Toluca, m	14	20	140	22.0	24.4
Toluca, nm	15	18	210	22.0	23.8
Standards	1 and 2	—	—	21.42	23.65

* Error: less than 2% unless specified.

Table 10. Measurements on aliquots A and B of some residues (vial no. 1/84).

Sample	Code	R_{10}	
		A	B
Canyon Diablo, m-H			
< 30 μm	5	22.0 \pm 0.2	21.7 \pm 0.2
30-45 μm	6	22.3 \pm 0.2	21.5 \pm 0.3
45-75 μm	7	21.9 \pm 0.2	21.4 \pm 0.2
125-150 μm	10	21.8 \pm 0.2	22.6 \pm 0.4

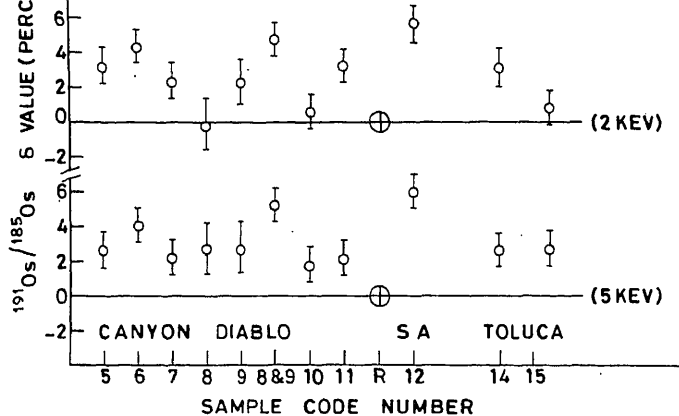


Figure 4. δ values for $^{190}\text{Os}/^{184}\text{Os}$ ratio for samples from vial no. 1/84 in 4 channels (upper line) and in 10 channels (lower line). The anomalous samples are (8 and 9) and 12.

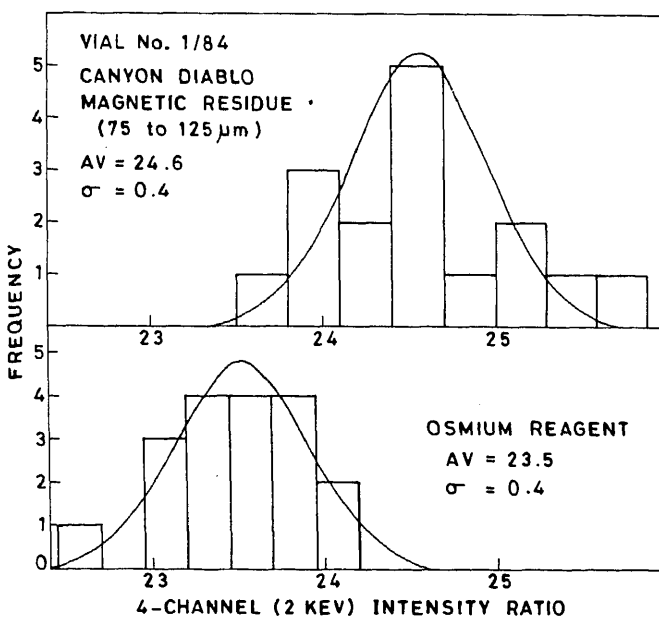


Figure 5. Frequency distributions of measured values (decay corrected) of $^{191}\text{Os}/^{185}\text{Os}$ ratios in 4 channels of the peak area for samples (8 and 9) and the reagent standard. The averages in the two cases are different.

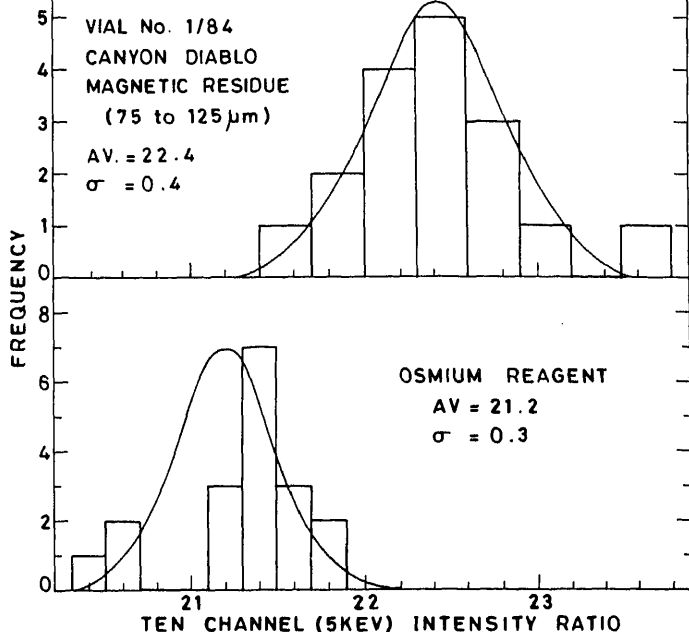


Figure 6. Frequency distribution of measured values (decay corrected) of $^{190}\text{Os}/^{185}\text{Os}$ ratios in 10 channels of the peak area for samples (8 and 9) and the reagent.

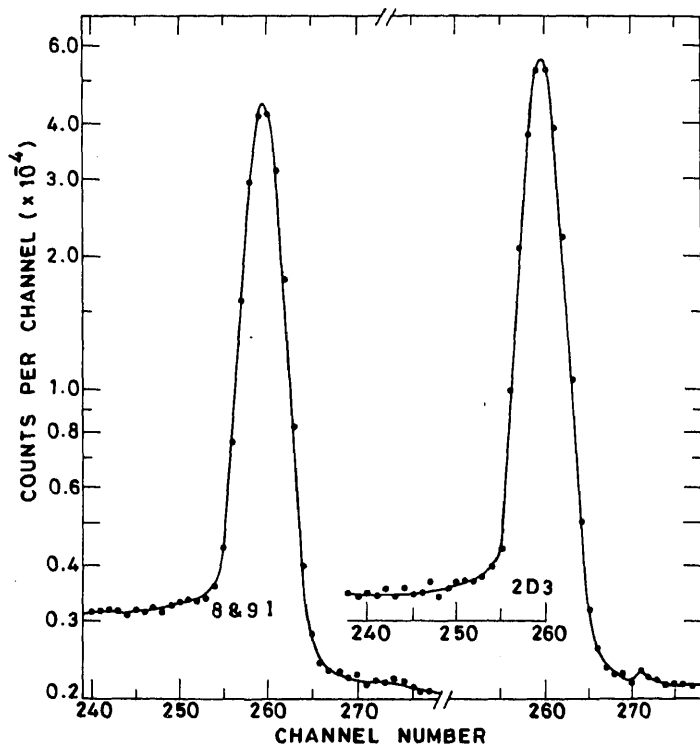


Figure 7. Comparison of the 129.4 keV gamma-ray spectra for Canyon Diablo residue (nos 8 and 9 I) and osmate standard.

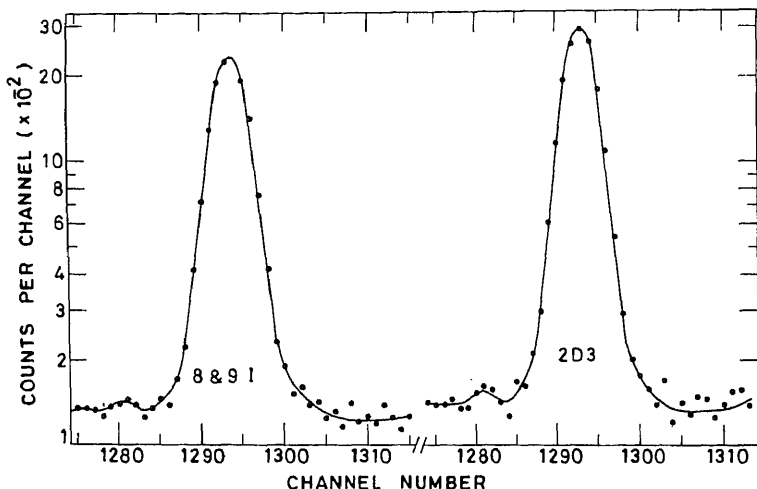


Figure 8. Comparison of the 646.1 keV gamma-ray spectra from residue of Canyon Diablo (nos 8 and 9 I) and the reagent osmium (2D3).

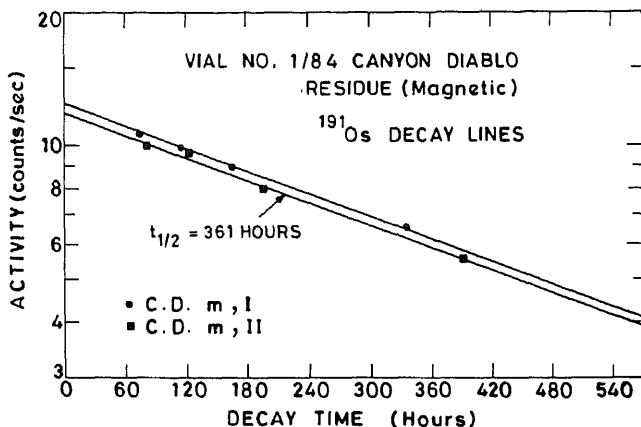


Figure 9. Decay curve for ^{191}Os gamma rays from a residue of Canyon Diablo of anomalous isotopic composition.

ratios in sample (8 and 9) are about 6 to 7% higher. A final check on reliability of our radiochemical measurement was done by following the decay of sample (8 and 9). The ^{191}Os peak decreased with the expected half-life (figure 9). Also the $^{191}\text{Os}/^{185}\text{Os}$ ratio decreased as expected and in parallel with the ratio for a standard osmium sample. This is shown in figure 10. It may be noted that all the data points on the sample (8 and 9) in figure 10 are above the line for the standard sample.

2.8 Vial no. 1/85

The preceding results suggested that perhaps a sieving of the residues could provide some clues to the nature of the anomalous osmium bearing phase in a sample. The magnetic residues of some iron meteorites were sieved through a $32\text{ }\mu\text{m}$ size hand sieve, to yield coarse and fine fractions. The coarse fraction was grounded in an

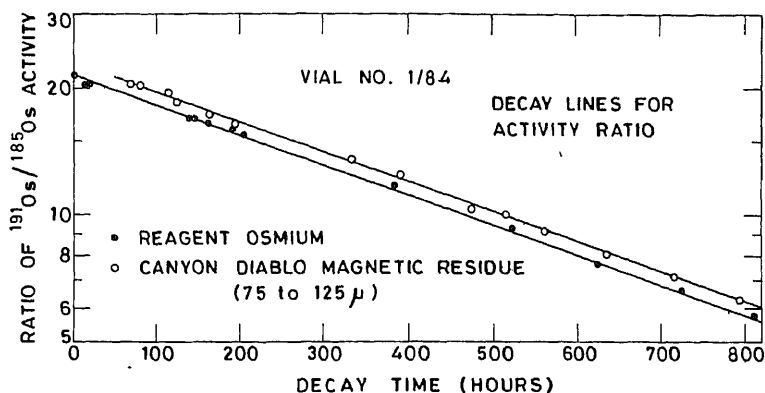


Figure 10. Decay curve for the activity ratio of $^{191}\text{Os}/^{185}\text{Os}$ for anomalous sample is identical to that for the reagent osmium. However, the data on sample (8 and 9) are always higher.

Table 11. $^{191}\text{Os}/^{185}\text{Os}$ activity ratio in vial no. 1/85.

Meteorite residue	Code	Mass (mg)	Os (ppm)	Activity ratio*	
				10 ch	5 ch
Bear Creek, magnetic					
< 32 μm	1	160	0.3	29.4	31.0
Crushed, < 32 μm	2	170	0.5	29.7	31.3
Crushed, > 32 μm	3	230	0.2	28.8	30.8
Campo del Cielo, magnetic					
H, < 32 μm	4	143	84	30.5	31.5
H, crushed, < 32 μm	5	76	145	31.4	33.2
H, crushed, > 32 μm	6	16	690	29.4	31.0
L, < 32 μm	7	84	261	30.5	32.5
L, > 32 μm	8	22	267	30.2	31.9
Bulk < 32 μm	9	21	308	30.0	31.9
Osmate salt on Fe_2O_3				29.22	30.85
Osmate salt on Al_2O_3				29.05	30.61

Error is ± 0.3

agate mortar to further yield, after sieving, two crushed fractions of < 32 μm and > 32 μm sizes. These were packed and processed for measurement of $^{191}\text{Os}/^{185}\text{Os}$ activity ratios. The details, along with the results on this vial, are given in table 11. Only one sample in this vial (sample number 5) showed an anomalous osmium isotopic ratio. The activity ratio of $^{191}\text{Os}/^{185}\text{Os}$ was about 8% greater than the standard value. To ensure that this small but significant difference is not due to any shortcomings of the analysis and detection technique the following measures were undertaken: (i) Aliquots of the anomalous sample were counted repeatedly over a period of several weeks along with samples of the aliquots of the two standards. The values of R for sample no. 5 were always higher than those for the standards. Both sets of the activity ratios decreased exponentially with the expected slope as shown in figure 11. (ii) The distribution pattern of decay-corrected R_5 and R_{10}

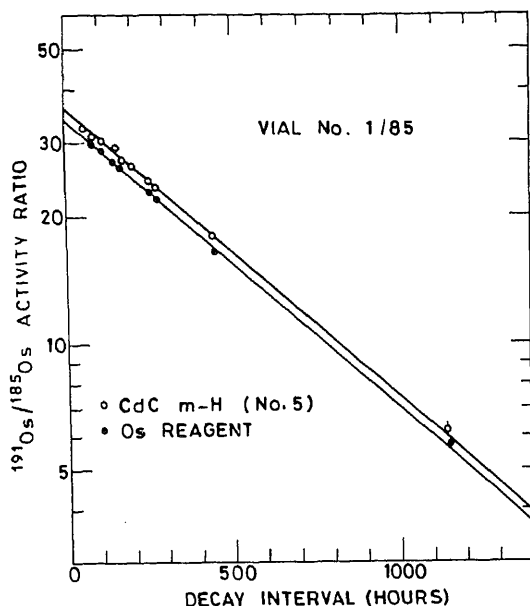


Figure 11. Decay lines for the activity ratios for reagent and CdC-m-H from vial no. 1/85. The slopes are the same but the value of the ratio for the meteoritic residue is consistently higher than the reagent value.

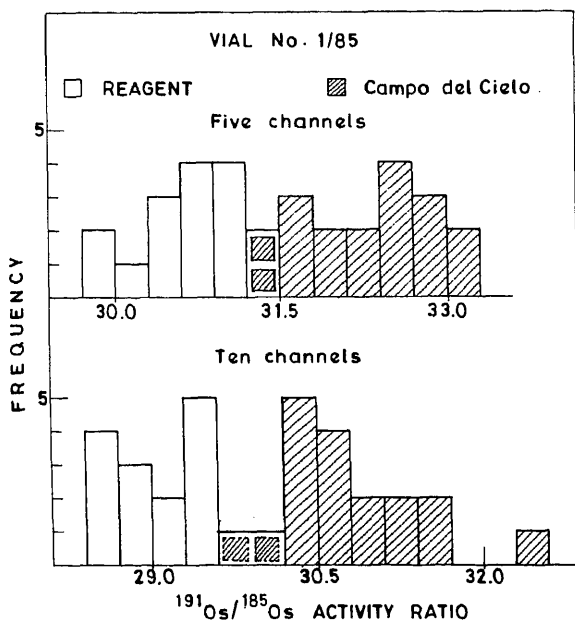


Figure 12. Frequency distribution of measured values of $^{191}\text{Os}/^{185}\text{Os}$ ratios (decay-corrected) for osmate reagent and CdC, m-H (no. 5) from vial no. 1/85.

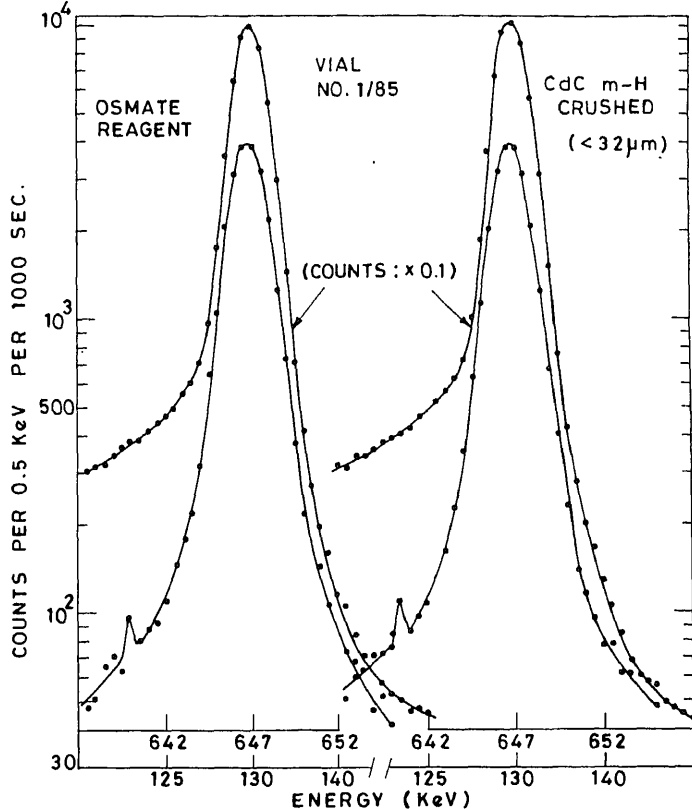


Figure 13. Comparison of the gamma-ray spectra from osmium samples of reagent osmate and CdC-m-H. In both cases the upper curves refer to the lower energy peak. Its relative area is greater for CdC-m-H.

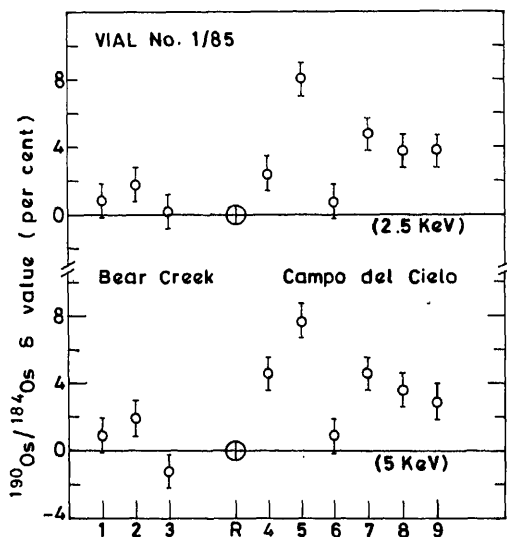


Figure 14. Results on $^{190}\text{Os}/^{184}\text{Os}$ δ values for samples from vial no. 1/85. Sample no. 5 is clearly anomalous.

values for no. 5 and standards showed distinctly different average values for the two sets (figure 12). (iii) The gamma ray spectra of no. 5 and standard (both aliquots of comparable activity) are quite similar and show no abnormal shape (figure 13). The δ values are shown in figure 14.

2.9 Vial no. 2/85

Since the Os anomaly was most pronounced in the inclusions of Sikhote Alin meteorite, this run was planned to investigate these residues more carefully and with larger sample sizes. During the dissolution of Sikhote Alin iron meteorite many large size (few mm) inclusions were obtained with a density of about $6 \cdot 5 \text{ cm}^{-3}$. These could be easily crushed into a powder. During this process, tiny fragments of magnetic material were found that did not crush, and these malleable pieces were examined for Os isotopic anomaly. For lack of any proper identification and better name, these are called "nuggets". The nuggets were irradiated in capsules containing powdered masses of the inclusions to optimize space in the vial. Thus the no. 9 nugget was sealed in the capsule containing powder of the inclusion no. 9 and the no. 4 nugget was irradiated with 160 mg of the inclusion powder in capsule no. 4. The three sets of powders 9, 4 and 5 were from different inclusions. The densities of the samples were estimated from the length that each weighed sample occupied in the capsules and are only crude estimates.

Realizing that the Os contents of Sikhote Alin inclusions are very low, the decomposition sequence of the samples was adopted in the order listed in table 12. This avoided the possibility of memory effects. The results are also given in table 12. The δ values are shown in figure 15. These measurements confirm the large

Table 12. Results from vial no. 2/85.

Sample	Code	Mass (mg)	Density* (g/cc)	Os (ppm)	$^{191}\text{Os}/^{185}\text{Os}$	δ (%)
Sikhote Alin residues						
nugget	9N	8.2	8.0	0.22	14.0 ± 2	-53
nugget	4N	7.2	8.0	0.22	13.0 ± 2	-56
inclusion	4	160	6.5	0.07	25.2 ± 1.2	-16
inclusion	5	240	6.5	0.04	26.5 ± 0.5	-11
inclusion	9	61	6.5	0.13	24.4 ± 1.0	-18
m, 32 μm	1	55	2.0	1.8	29.8 ± 0.4	n
m, crushed, 32 μm	2	18	2.0	5.6	29.8 ± 0.3	n
m, crushed, 32 μm	3	55	2.5	6.5	30.0 ± 0.3	n
nm, crushed, 32 μm	6	29	2.0	4.0	—	n
nm, crushed, 32 μm	7	11	1.5	10.7	28.8 ± 0.3	-3.4
nm, 32 μm	8	6.8	1.5	6.5	30.0 ± 0.5	n
Toluca, residues						
m, 32 μm	11	27	1.5	504	30.0 ± 0.2	n
m, crushed, 32 μm	12	51	2.0	12	30.0 ± 0.2	n
m, crushed, 32 μm	13	83	4.0	35	29.2 ± 0.2	n
Osmate on Fe_2O_3	14	—	—	25 μg	29.7 ± 0.2	—
Osmate on Al_2O_3	15	—	—	20 μg	29.9 ± 0.2	—

* Approximate values only. Normal δ values are indicated by n.

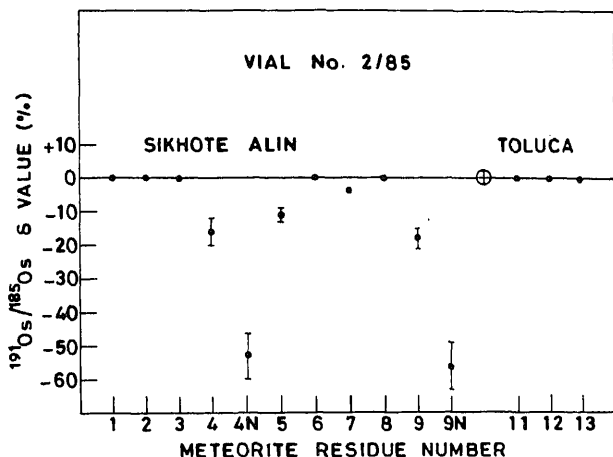


Figure 15. Results on $^{190}\text{Os}/^{184}\text{Os}$ values for samples from vial no. 2/85. Several Sikhote Alin residues are abnormally low.

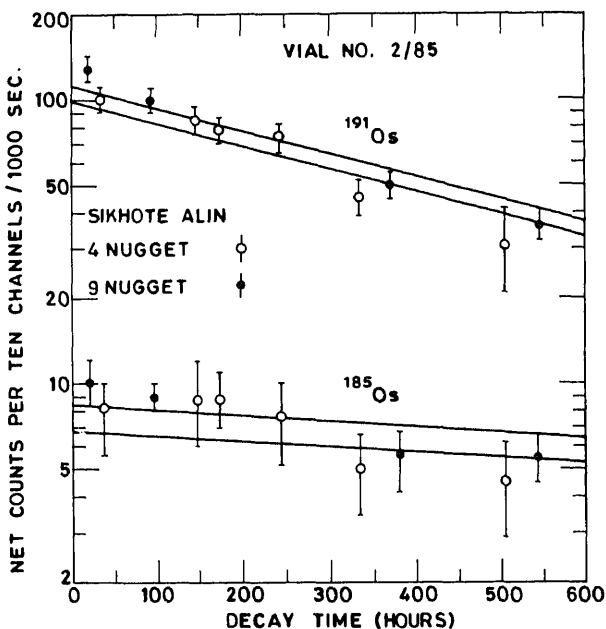


Figure 16. Spectrum of the 129.4 keV gamma rays from ^{191}Os (upper scale) and the 646.1 keV gamma rays from ^{185}Os (lower scale) from a sample of Sikhote Alin nugget having highly anomalous isotopic ratio.

anomaly reported by Goel and Murty (1983). A gamma ray spectrum of S.A. nugget no. 4 is shown in figure 16. The decay curves for Os isotopes for the two nuggets are shown in figure 17. Even though the scatter in the points is large, the decay curves are consistent with the half-lives of ^{191}Os and ^{185}Os , keeping in view the large statistical error of counting for these samples.

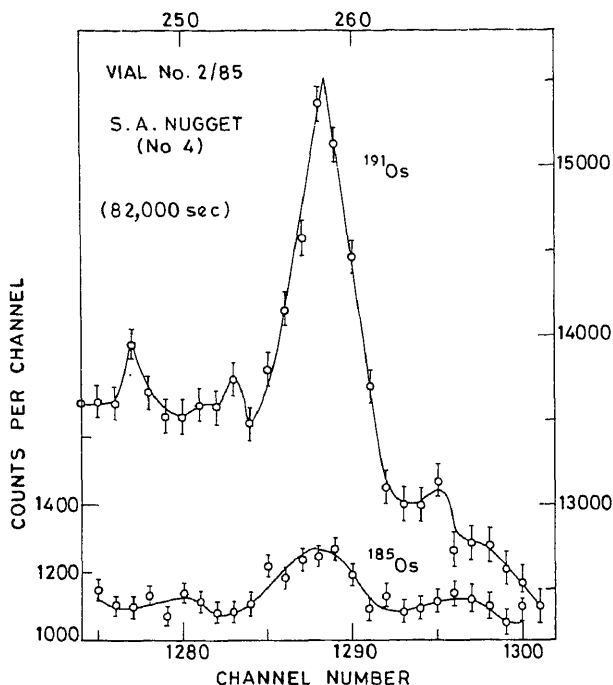


Figure 17. Decay lines for ^{191}Os and ^{185}Os from nuggets of Sikhote Alin. Due to counting rates the scatter is rather large.

3. Discussions

In view of the profound implications of the existence of isotopic anomalies of this kind found by Goel and Murty (1983) in iron meteorites, it is necessary that a thorough scrutiny of various steps involved in the experiments is carried out to ensure that the observed abnormal activity ratios that we have sporadically found are not due to experimental artifacts which might have arisen either during the irradiation step or during the subsequent radio-chemical purification and counting steps.

It may be plausible that the anomaly is caused during neutron irradiation due to such causes as (i) variations in the composition of the residues, (ii) modification of neutron energy spectra at different sample sites and (iii) generation of secondary neutrons at some specific positions. These are inter-related factors and, if present, would be responsible for significant self-shielding effects. The high absorption cross-section for ^{184}Os (table 1) implies a low-lying resonance level for this nuclide. Its activation may therefore be prone to local fluctuations in neutron energy spectrum. It is conceivable that the Os-bearing phase in some samples has an element which has a neutron capture resonance at the same energy as ^{184}Os . This would, however, give only a higher value for the activity ratio of $^{191}\text{Os}/^{185}\text{Os}$ and would not be able to explain the larger number of cases where we have found low ratios.

The residue, Odessa-m-H, that had a δ value of -10% (Goel and Murty 19

gave similar anomaly when studied at the NBS reactor. A 160 mg sample of this with natural Os as 0.23 μg (or so), spiked with 0.5 μg Os, showed - 7% anomaly (figure 1). Another residue of Odessa (m-H, spiked and unspiked) also showed a -ve anomaly (figure 3, run no. J-4). Since the anomaly persists in three different irradiations and in two different reactors it cannot be explained due to perturbation in the energy spectrum of the neutrons. In two control runs (P-1 and Q-1) we kept Os contents variable from 50 to 800 μg , yet the activity ratios remained invariant. In these two runs the reactors were different and the bombarding neutrons had different energy spectra. Results of run no. 21 show that the presence of neutron absorbers like Cd and B, also does not affect the osmium activity ratio. Normal ratio in the Sikhote Alin inclusion in the NBS run may be either due to memory from preceding high Os sample or it may be that the inclusion had normal Os.

Mass fractionation of Os isotopes during distillation is insignificant as supported from the data on Os activity ratios recovered from successive distillation of some samples (table 8). During sample counting, errors may arise from (i) variations in counting geometry, (ii) variations in counting rates, (iii) presence of contamination near any of the gamma lines and (iv) drift in the instrument gain. We have made enough checks as given below to ensure that none of these is responsible for the observed osmium isotopic anomaly.

In order to investigate the effect of geometry on R we took equal aliquots of distilled osmate from a high activity sample and diluted these to volumes ranging from 4 to 7 ml. Two sets of such experiments were done. The measured activity ratios are shown in figure 18. In spite of large changes in the volume, the R values remain unchanged. In practice we did not allow the counting volume to change by more than ± 0.1 ml and kept it generally as 5 ml.

Since the osmium contents of samples in some vials varied by several orders of magnitude, the counting rates were also widely different. Even though the resolution of the detector became poor at high counting rates, it was experimentally demonstrated (figure 19) that the value of R did not change. However the samples of very high counting rates were diluted to maintain good resolution. Diluted aliquots are labelled as D1, D2, D3, etc.

Evidence that the two gamma lines do not have any contaminant in their vicinity has been presented for measurements on vial nos. 1/84 and 1/85 where it was seen that (i) the values of R_{10} and R_4 (or R_5) were consistent with each other and

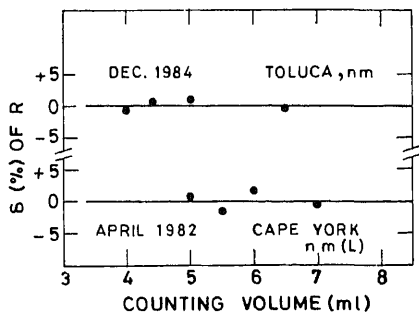


Figure 18. δ values of R for a sample of Cape York nm (L) show no variations when the volume is changed from 4 ml to 7 ml.

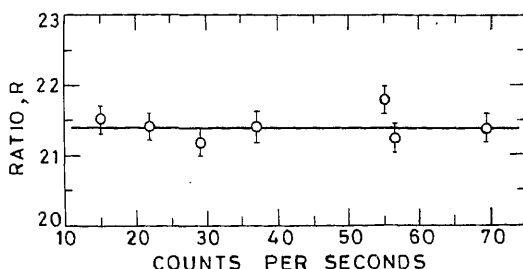


Figure 19. Activity ratio (decay-corrected) of $^{191}\text{Os}/^{185}\text{Os}$ for residue of He meteorite (with normal ratio) shows no variation in R with counting rate.

Table 13. Summary of all anomalous residues with δ values $\geq 5\%$.

Insoluble residue	Vial no. and code no.	δ (%)
<i>Negative values</i>		
Sikhote Alin, nugget	2/85 9N	53 ± 7
nugget	2/85 4N	56 ± 7
incl.	Goel and Murty, 1983	44 ± 6
m, I	Goel and Murty, 1983	36 ± 7
m, II	Goel and Murty, 1983	24 ± 9
incl.	2/85 9	18 ± 3
incl.	J-1 and J-2	20 ± 20
incl.	2/85 4	16 ± 4
incl.	2/85 5	11 ± 2
Odessa, m-H	NBS Run	> 6
m-H	J-4	10 ± 2
m	Goel and Murty, 1983	10 ± 2
Sikhote Alin, nm	Goel and Murty, 1983	6 ± 2
Cape York, mag	Goel and Murty, 1983	5 ± 2
Canyon Diablo, nm	Goel and Murty, 1983	6 ± 2
<i>Positive values</i>		
Campo del Cielo, nm	Goel and Murty, 1983	13 ± 2
Campo del Cielo, m-H	1/85 5	8 ± 2
Sikhote Alin, nm	1/84 12	6 ± 2
Canyon Diablo m-H	1/84 8 and 9	5 ± 2

(ii) the activity of ^{191}Os and the activity ratio $^{191}\text{Os}/^{185}\text{Os}$ decayed as expected pure pairs. That line drift and gain shift etc. are not responsible for the abnormal ratios is clear from the patterns of frequency distributions for R values present in figures 5, 6 and 12.

4. Cosmochemical implications

In table 13 the results on $^{190}\text{Os}/^{184}\text{Os}$ ratio are summarized for samples whose δ values are 5% or greater in magnitude. Not included in this table are a number of residues which give normal ratio. Positive anomalies of upto 10% negative anomalies of upto 50% are noted. It seems that the component of anomalous osmium is found to be present in iron meteorites of different classes.

is not possible from our studies to identify the phase which contains the anomalous Os. The anomaly in osmium isotopic composition is well outside the range for known or plausible solar system processes and must be attributed to the presence of some presolar matter in iron meteorites. Apparently Os in iron meteorites has been derived from several source materials of widely different isotopic composition. The terrestrial and most meteoritical samples represent Os from a well-mixed reservoir, while iron meteorites contain some matter which has escaped homogenization. This would place iron meteorites as the most primitive objects available to mankind.

Results of other experimental works supporting the idea that iron meteorites contain presolar grains have been discussed in our earlier papers (Goel and Murty 1983; Murty *et al* 1983). Since then it has been reported by Becker and Pepin (1984) that Washington County iron meteorite contains trapped noble gases of unfractionated solar composition strengthening the idea that iron meteorites have been produced by an accretion process, entrapping some presolar grains which have been preserved essentially unaltered to retain isotopic anomalies of Os and Xe, and retain the solar flare rare gases implanted on the surface of the grains. It may also be pointed out that Prombo and Clayton (1985) have recently found large isotopic anomalies in nitrogen in the metal phase of Bencubbin mesosiderite. More recent work in our laboratory has shown that the acid-residues of Sikhote Alin iron meteorite often contain anomalously low ratio of $^{196}\text{Hg}/^{202}\text{Hg}$ (Thakur and Goel 1985; Goel and Thakur 1987).

Acknowledgements

Financial support for this work from the Indian Space Research Organization is deeply appreciated. The author is most grateful to Dr Richard Lindstrom and Dr Lloyd Currie of National Bureau of Standards, Washington D.C. (U.S.A.) for extensive help and hospitality during the work carried out at NBS. Dr S V S Murty is thanked for the chemistry of samples from Vials J-1 and J-2. Dr R G Deshpande of BARC has been most cooperative in providing us timely bombardments in the reactors at BARC.

References

- Becker D A and La Fleur P D 1974 Characterization of a nuclear reactor for neutron activation analysis; *J. Radioanal. Chem.* **19** 149–157
- Becker R H and Pepin R O 1984 Solar composition noble gases in the Washington County iron meteorite; *Earth Planet. Sci. Lett.* **70** 1–10
- Goel P S and Murty S V S 1983 Presolar grains in microinclusions of iron meteorites; *Adv. Space Res.* **2** 13–18
- Goel P S and Thakur A N 1987 Isotopically anomalous Hg in meteorites; Presented at the 50th Annual Meeting of the Meteoritical Society at Newcastle Upon Tyne
- Murty S V S, Shukla P N and Goel P S 1982 Non-cosmogenic lithium-6 in iron meteorites; *Earth Planet. Sci. Lett.* **60** 1–7
- Murty S V S, Goel P S, Minh D Vu and Shukolyukov Yu A 1983 Nitrogen and xenon in acid residues of iron meteorites; *Geochim. Cosmochim. Acta* **47** 1061–1068
- Oliver L L, Ballad R V, Richardson J F and Manuel O K 1981 Isotopically anomalous tellurium in Allende: another relic of local element synthesis; *J. Inorg. Nucl. Chem.* **43** 2207–2216

- Prombo C A and Clayton R N 1985 A striking nitrogen isotope anomaly in the Bencubbin and Weatherford Meteorites; *Science* **230** 935–937
- Reed G W and Jovanovic S 1969 ^{196}Hg and ^{202}Hg isotopic ratios in chondrites; *J. Inorg. Nucl. Chem.* **31** 3783–3788
- Takahashi H, Higuchi H, Gros J, Morgan J W and Anders E 1976 Allende meteorite: Isotopically anomalous xenon is accompanied by normal osmium; *Proc. Natl. Acad. Sci. USA* **73** 4253–4256
- Thakur A N and Goel P S 1985 $^{203}\text{Hg}/^{197}\text{Hg}$ ratio measurement in meteorites by neutron activation analysis; *Proc. Radiochem. Radiation Chem. Symposium*, Dept. of Atomic Energy, IIT, Kanpur, pp 542–554

Gold-bearing rocks of Mangalur greenstone belt, Gulbarga District, Karnataka

S G TENGINKAI and A G UGARKAR

Department of Studies in Geology, Karnatak University, Dharwad 580 003, India

MS received 12 December 1985; revised 20 August 1986

Abstract. The Mangalur greenstone belt of Dharwar Craton, South India, is an Archaean schist belt dominated by metavolcanic rocks. The gold mineralization occurs within the metavolcanics and the fabric, mineralogy and geochemistry of these host rocks indicate that they were tholeiitic basalts regionally metamorphosed under medium to low-grade greenschist facies. The basic metavolcanic rocks occur as tholeiitic metabasalts and amphibolites. The rocks have undergone some fractionation and appear to be derived from melts generated by 10 to 25% melting of the mantle at depths 30 to 35 km around temperature 1200°C and pressure 12 kb. The source of gold is mainly in the basalts and not in the surrounding granites.

Keywords. Gold-quartz veins; metavolcanic rocks; tholeiites; geochemistry; petrogenesis; Mangalur greenstone belt.

1. Introduction

Gold mineralization of gold-quartz vein type in India is essentially confined to the eastern gold field province of the Dharwar Craton. This province includes the region lying to the east of the N-S trending band of younger granites. A feature common to all greenstone belts falling within this province is the gold mineralization associated with the metavolcanics. Since these belts are largely made up of steeply inclined mafic volcanic rocks, they have been compared with the classical greenstone belts of South Africa, Canada and Western Australia (Radhakrishna 1983). There are four gold-bearing Archaean greenstone belts in this province namely, Kolar, Ramagiri, Hutti and Mangalur, the last one of which constitutes the subject of this paper (figure 1).

The Mangalur greenstone belt (lat. 16°30' and 16°44' and long. 76°32'30" and 76°40') has geological characteristics akin to the above gold deposits. The difference, however, lies in the size of the belt and in the mineralization characteristics. Bruce Foote (1875) first reported the occurrence of hornblende and micaceous schists of this belt as forming the northern continuation of Hutti-Maski belt in the hills of NW of Shorapur. Mahadevan and Krishnamurthy (1945) reported Löllingite in the pegmatite vein exposed near Mavinmatti. Mahadevan (1945) described ripple marks in certain rocks of Mangalur belt and arrived at the conclusion that the Dharwars were originally sedimentary.

The Mangalur gold mine is located at Mukangavi village. Exploration by the Geological Survey of India and development of the mines by Hutti Gold Mines during recent years have resulted in establishing a sizable gold ore reserve of 70,000 metric tonnes of an average grade of 3 g/ton, and a strong plea was made by the

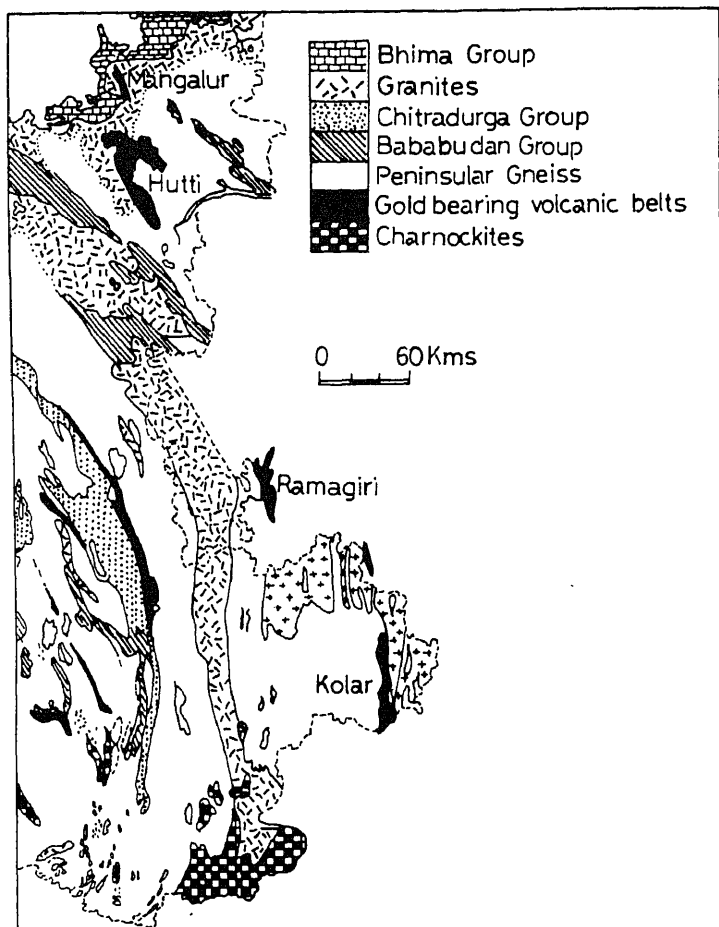


Figure 1. Geological map of Eastern Gold Fields Province of the Dharwar Craton (after Ananta Iyer and Vasudev 1979).

Geological Survey of India for reopening the Mangalur Gold Mine (Ramachandra Rao 1980). The mine was reopened in 1981 and developed by the Hutti Gold Mines Co Ltd. Apart from this, there exists no literature on the detailed geological setting of the deposit, mineralogy, geochemistry, controls of mineralization and genetic aspects of Mangalur greenstone belt. Ugarkar (1986) opined that there exists a geochemical similarity of the Archaean gold-bearing metabasic volcanic rocks of Mangalur with the oceanic tholeiites generated at marginal basin tectonic environment. The present paper describes preliminary geology and geochemistry of the gold-bearing host rocks of this belt.

2. Geology of the Mangalur greenstone belt

nantly represented by metabasalts and amphibolites. These rocks are exposed in the western part of the belt. Terrigenous metasedimentaries are exposed in the eastern part of the belt. The general strike of the formations varies from N-S to N 20°W with a westerly dip of 65 to 75°. The rock formations are tightly folded into isoclinal folds with axial planes dipping west. In addition, shear zones parallel to the strike of foliation are observed near Mukangavi and Mangalur villages, and in the Temple hill Δ 449.

Migmatites are the oldest lithounits of the area. Although there are no direct field evidences to infer the migmatites to form the basement, the presence of a conglomerate horizon within the belt, with well-rounded pebbles of light-coloured quartzite that succeeds them, suggests a pre-existing sialic crust. The schistose rocks of Mangalur belt are intruded by granites, pegmatites, quartz veins and lastly by dolerite dykes (figure 2). The gold-quartz veins and lenses occur within the

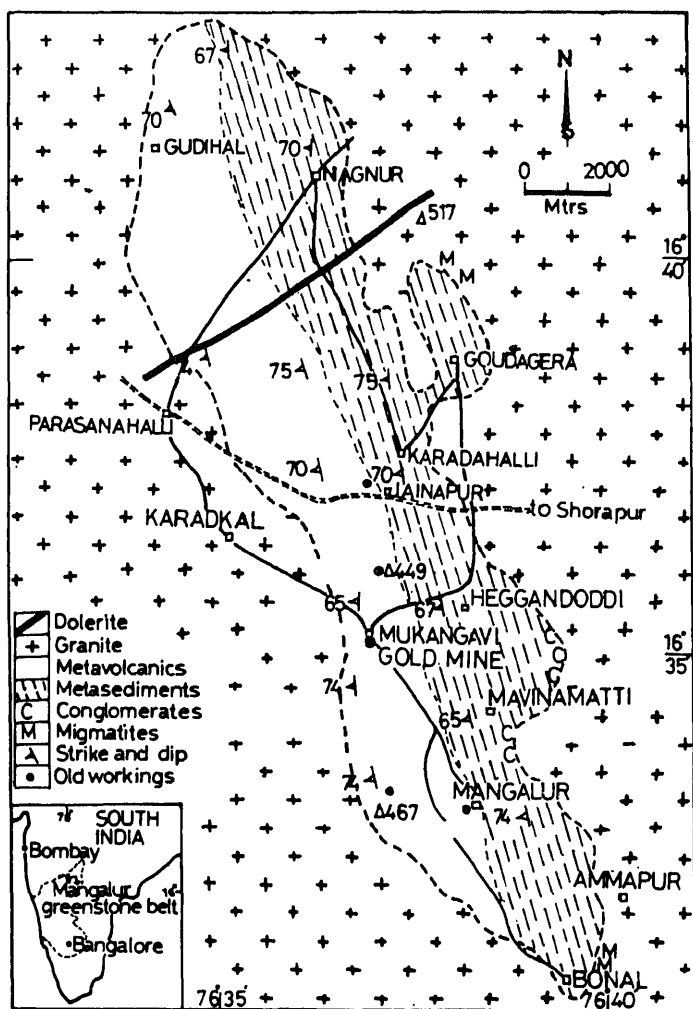


Figure 2. Regional geological map of the Mangalur greenstone belt.

narrow shear zones in the metamorphosed basic volcanic rocks. The volcanic suite shows well-developed pillow structures in the central and southern portions of the belt (figure 3).

3. Petrography and mineralization

Mangalur gold-bearing rocks exhibit variation in grain size from medium to fine. The thin section studies reveal that the massive rocks exhibit slender porphyroblasts of actinolite/tremolite without any apparent alignment whereas in schistose variety, they show parallel alignment exhibiting segregation banding. Plagioclase occurs as slender, tabular crystals exhibiting polysynthetic twinning and saussurization. Actinolite/tremolite are set in a ground mass of chlorite. Epidote and zoisite are the alteration products of earlier pyroxenes. Relic euhedral pyroxenes are seen occasionally. Hornblende grains sometimes exhibit preferred orientation in coarse-grained amphibolites.

The host metabasic volcanic rocks in the shear zones are chloritized, biotitized and carbonitized and can be called chlorite-biotite schists and biotite-chlorite schists. In Mangalur deposit, gold occurs only in native state. Gold mineralization is represented by the presence of disseminated streaks and grains of sulphides in the schistose amphibolites associated with thin quartz veins parallel to the schistosity and the abundant occurrence of biotite, chlorite and influx of carbonates (ankerite + calcite) indicating wall-rock alterations suggests the broad mechanism underlying gold mineralization in the area. The dominated sulphide phase is pyrrhotite-pyrite assemblage with little amount of arsenopyrite, chalcopyrite and sphalerite.

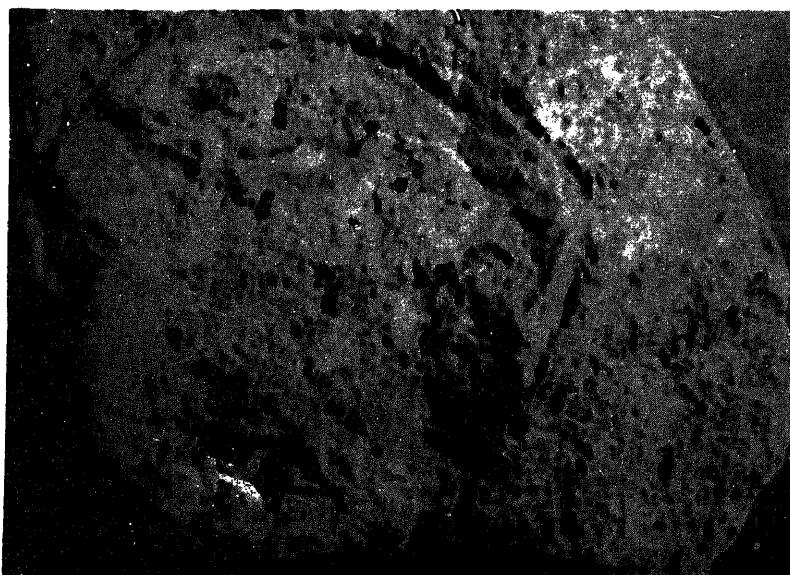


Figure 3. Pillow structure in Mangalur metavolcanic suite.

4. Sampling and analytical techniques

For our present study, samples have been collected from the ore-zones as well as least altered zones. Twentyfour least altered metavolcanic rocks have been analysed chemically (table 1). While collecting these samples, care was taken to sample rocks that are free from quartz, calcite and epidote veins, and intense chloritization and biotitization. These samples were collected from the surface outcrops and drilled cores. For petrogenetic consideration, the analyses of only these 24 samples are plotted on carefully chosen discriminant diagrams (figures 4 to 8). Five samples collected across the shear zone representing rich-ore to non-ore bodies in a cross-cut at 370' level have been analysed chemically (table 2).

Pulverized (–300 mesh) and homogenized samples were analysed for major and trace elements by using an atomic absorption spectrophotometer (Schimadzu, AA-10, Japan). Standardization was based on USGS natural rock standards, W-1, DR-N, AGV-1, PCC-1 and BCR-1 (Flanagan 1973). Gold contents were determined by fire assay techniques of Schuler (1971).

5. Geochemistry of metavolcanic rocks

Analyses of Mangalur metavolcanic rocks (table 1) exhibit variations of SiO_2 (47.83–53.93%) and K_2O (0.18–0.44%), probably due to the alteration of these rocks. These rocks have high FeO (av. 12.52%), low TiO_2 (av. 0.95%), Al_2O_3 (av. 13.74%) contents and low M ($\text{Mg}/\text{Mg} + \text{Fe}$) values (av. 0.30) when compared to MORB ($\text{FeO} = 10.00\%$, $\text{TiO}_2 = 1.50\%$, $\text{Al}_2\text{O}_3 = 6.00\%$ and $M = 0.44$) quoted by Condie (1976). FeO/MgO ratios of Mangalur metavolcanic rocks (av. 2.12) are higher than MORB (1.33) reflecting their iron-rich chemistry.

Cr content (av. 189 ppm) is comparable and Ni content (av. 163 ppm) is slightly higher than MORB (Cr = 300 ppm and Ni = 100 ppm). Rb content (av. 4.5 ppm) is slightly less whereas Sr content (av. 127 ppm) is comparable to MORB (Rb = 10 ppm and Sr = 135 ppm). The K/Rb ratio (308) is less and Rb/Sr ratio (0.046) is more than MORB (K/Rb = 1160 and Rb/Sr = 0.007).

6. Petrogenetic discussion

Mafic and ultramafic extrusive rocks of Archaean greenstone belts are generally tholeiitic and komatiitic (Rajamani *et al* 1985). From the geochemical criteria available for discriminating tholeiitic and komatiitic rocks, the gold-bearing metavolcanic rocks (least altered) of the Mangalur greenstone belt would be considered as tholeiite.

Mangalur metavolcanic rocks are characterized by typical quartz/or hypersthene-normative mineralogy and total absence of normative olivine (Ugarkar 1986). The MgO content of metavolcanic rocks varies from 4.42 to 7.46% and $\text{CaO}/\text{Al}_2\text{O}_3$ ratios < 0.9 , which would suggest a tholeiitic affinity. Similar opinions were expressed by Glikson (1983) for the Archaean tholeiites. On $\text{CaO}-\text{Al}_2\text{O}_3$ -MgO ternary diagram (figure 4) of Viljoen and Viljoen (1969) and Condie (1981), all the metavolcanic rocks plot in the tholeiitic field.

Table 1. Major and trace element data for Mangalur metavolcanic rocks.

	1	2	3	4	5	6	7	8	9	10	11	12
SiO ₂	50.21	52.39	51.30	50.30	49.56	50.38	51.43	47.83	49.89	52.26	48.78	50.98
Al ₂ O ₃	13.15	13.08	14.19	14.23	14.44	10.03	13.93	12.39	11.96	13.39	11.32	14.40
TiO ₂	0.81	0.79	0.94	0.93	0.99	0.86	0.92	1.13	1.23	0.81	1.13	0.98
FeO(t)	14.88	12.10	12.67	12.85	12.98	14.57	12.74	12.90	12.07	12.47	14.01	11.90
MgO	4.93	5.81	5.68	5.76	5.69	5.31	5.58	7.46	6.90	5.38	6.37	6.90
CaO	11.38	11.46	9.31	10.02	10.27	11.41	9.46	10.20	11.03	11.51	11.83	10.00
Na ₂ O	2.23	2.30	2.25	2.28	2.48	2.27	2.43	2.38	2.61	2.29	2.39	2.69
K ₂ O	0.17	0.33	0.40	0.34	0.42	0.19	0.43	0.43	0.39	0.36	0.44	0.28
MnO	0.14	0.16	0.26	0.25	0.26	0.16	0.21	0.24	0.27	0.32	0.28	0.29
LOI	2.29	1.65	2.97	2.99	2.95	2.01	2.85	5.09	3.74	1.17	3.30	1.27
Total	100.19	100.05	99.97	100.00	100.00	100.02	99.98	99.06	100.09	99.96	98.88	99.69
Ni	231	203	112	109	208	228	110	177	165	123	121	175
Cr	136	120	170	159	118	140	161	210	153	189	189	313
Zr	50	66	60	44	67	53	61	68	51	52	52	58
Sr	142	104	115	119	113	139	118	149	158	133	130	99
Rb	2.3	5.1	4.8	4.9	5.2	2.5	4.9	5.1	6.1	5.2	5.8	3.6
K/Rb	302	269	346	288	311	313	364	350	265	287	318	321
Rb/Sr	0.017	0.049	0.042	0.041	0.046	0.018	0.042	0.034	0.039	0.039	0.045	0.036
CaO/Al ₂ O ₃	0.87	0.87	0.66	0.70	0.70	1.14	0.68	0.84	0.92	0.86	1.05	0.69
FeO/MgO	2.02	2.08	2.23	2.23	2.28	2.74	2.22	1.87	1.75	2.32	2.20	1.72
M	0.22	0.28	0.31	0.30	0.30	0.24	0.30	0.37	0.36	0.27	0.30	0.34
θ	36	37	38	37	35	32	36	31	38	30	36	35
Mole% FeO	11.41	9.28	9.67	9.85	9.95	11.17	9.76	9.89	9.25	9.56	10.74	9.12
Mole% MgO	7.02	8.28	8.09	8.21	8.11	7.57	7.95	10.63	9.83	7.67	9.08	9.83
(Fe) %	16.93	13.76	14.41	14.62	14.76	16.57	14.49	14.67	13.73	14.18	15.94	13.54
(Mg) %	10.92	12.86	12.58	12.75	12.60	11.76	12.36	16.52	15.28	11.91	14.10	15.28

Table 1. (Contd.)

	13	14	15	16	17	18	19	20	21	22	23	24
SiO ₂	51.42	50.28	51.59	52.86	52.61	52.14	53.93	52.69	50.59	49.10	50.43	52.33
Al ₂ O ₃	14.03	13.96	14.77	13.81	13.89	14.52	12.46	11.74	12.70	12.36	13.15	13.14
TiO ₂	0.86	0.91	0.96	0.96	0.99	0.80	0.98	0.96	0.96	1.31	0.93	0.78
FeO(t)	12.44	12.33	11.00	12.95	10.50	10.07	12.81	12.58	11.06	11.60	12.85	12.28
MgO	5.42	6.10	6.50	4.42	6.20	5.60	5.23	5.60	6.50	7.10	6.31	5.92
CaO	10.01	11.50	10.68	9.61	10.60	10.38	9.86	10.81	10.68	10.98	10.04	11.41
Na ₂ O	2.74	2.80	2.81	2.81	2.60	3.51	2.41	2.72	2.81	2.57	2.34	2.33
K ₂ O	0.26	0.43	0.19	0.32	0.31	0.43	0.41	0.31	0.19	0.26	0.34	0.32
MnO	0.27	0.19	0.24	0.23	0.17	0.28	0.18	0.18	0.24	0.20	0.24	0.18
LOI	2.32	1.30	1.24	1.57	1.82	1.02	0.81	1.69	4.21	4.34	3.35	1.36
Total	99.77	99.80	99.81	99.54	99.19	100.70	100.01	99.18	100.48	99.82	100.02	100.05
Ni	116	141	208	156	168	151	186	131	208	169	111	204
Cr	168	149	361	138	139	160	211	248	361	141	157	130
Zr	57	57	64	61	58	66	65	64	66	68	45	61
Sr	128	102	109	160	123	166	124	132	109	163	117	100
Rb	3.5	4.7	2.7	4.9	4.2	6.3	5.6	4.1	5.3	3.6	4.6	4.4
K/Rb	310	380	297	271	308	283	304	315	295	302	310	299
Rb/Sr	0.030	0.046	0.024	0.031	0.034	0.040	0.045	0.031	0.049	0.022	0.039	0.044
CaO/Al ₂ O ₃	0.71	0.82	0.72	0.70	0.76	0.71	0.79	0.92	0.84	0.89	0.76	0.85
FeO/MgO	2.39	2.02	1.69	2.92	1.62	1.80	2.45	2.24	1.70	1.63	2.04	2.07
M	0.30	0.31	0.34	0.25	0.34	0.30	0.29	0.30	0.35	0.37	0.32	0.29
θ	35	33	36	36	37	32	37	34	33	32	35	37
Mole% FeO	9.54	9.45	8.43	9.93	8.05	7.72	9.82	9.60	8.48	8.90	9.85	9.41
Mole% MgO	7.72	8.69	9.26	6.30	8.83	9.98	7.45	7.98	9.26	10.12	8.99	8.44
(Fe) %	14.15	14.01	12.51	14.73	11.94	11.45	14.57	14.24	12.48	13.20	14.62	13.97
(Mg) %	12.00	13.51	14.39	9.79	13.73	12.40	11.58	12.40	14.39	15.72	13.97	13.11

Table 2. Major and trace element data for rich-ore to non-ore bodies across shear zone.

	1	2	3	4	5
SiO ₂	40.82	43.68	45.82	49.36	50.98
Al ₂ O ₃	11.80	12.02	12.42	12.98	13.33
TiO ₂	0.97	0.78	1.13	0.79	0.86
FeO(t)	14.46	12.91	12.99	12.84	12.68
MgO	6.53	6.70	7.49	6.18	6.33
CaO	12.38	11.28	11.08	10.98	10.88
Na ₂ O	0.98	1.21	2.21	2.18	2.82
K ₂ O	2.46	2.22	0.96	0.65	0.39
MnO	0.20	0.23	0.16	0.18	0.27
LOI	9.83	8.82	5.32	2.90	1.27
Total	100.43	99.85	99.58	99.02	99.81
Au	10.35	3.80	3.24	0.72	Tr
Ni	150	198	142	182	146
Co	78	58	73	58	57
Cu	192	136	184	129	150
Cr	190	265	228	142	264
Zr	75	63	72	49	54
Sr	98	140	93	148	104
Rb	8	7	7	6	6

Samples 1 to 5 were collected from the rich-ore to non-ore bodies.

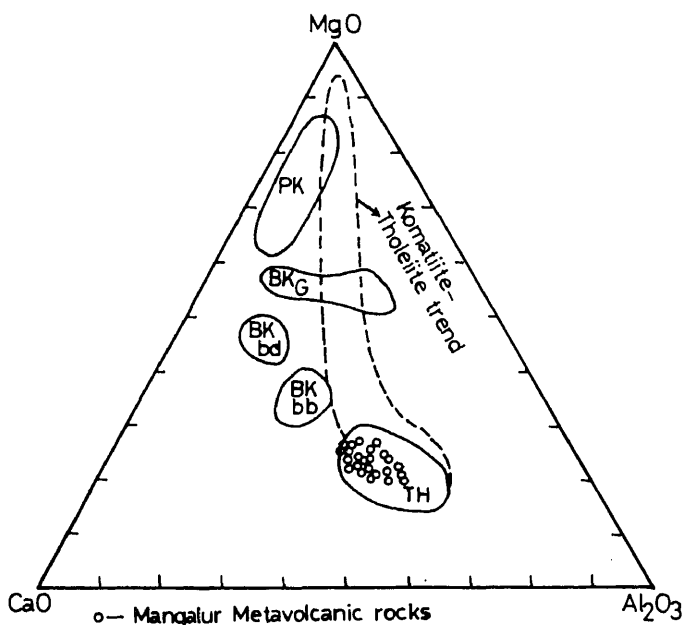


Figure 4. CaO-MgO-Al₂O₃ ternary diagram (after Viljoen and Viljoen 1969 and Condie 1981). PK refers to Barberton peridotitic komatiites; BK to basaltic komatiites, G to Geluk type, bd to Badglass type and bb to Barberton type; and TH refers to tholeiites. Komatiite-tholeiite trend is defined by ultramafic and mafic rocks of Archaean greenstone belts. Note the Mangalur metavolcanic rocks showing tholeiitic affinity.

Ringwood (1975) has shown that quartz or olivine tholeiites are generated from the basaltic magma formed by a high degree of partial melting of the mantle under low pressure at shallow depths. The quartz-normative nature of the metavolcanic rocks of the area might indicate their formation around temperature 1200°C and pressure 12 kb, as suggested by Ewart (1981) for similar rocks of Central Queensland, Australia. Several workers have utilized the theta (θ) index of Sugimura (1968) to estimate the depth of magma genesis (Please refer Naqvi *et al* 1974). The θ values of the Mangalur metavolcanic rocks range from 30 to 35 with an average of 34, and suggest that the depth of magma generation was about 30 to 35 km. The quartz tholeiitic nature of the Mangalur metavolcanic rocks and their geochemistry would suggest their derivation from a magma generated under the above conditions. The low M values (av. 0.30) could have been generated through the fractional crystallization of Mg-rich phases. Wilkinson (1981) suggested that basaltic melts with low M values relate to the degree of partial melting and to mantle heterogeneity.

Hanson and Langmuir (1978) developed a model based on major elements, particularly MgO and FeO (figure 5), to obtain such quantitative petrogenetic information for mafic and ultramafic rocks. All the samples of Mangalur metavolcanic rocks plot well below the melt fields (0% melting line) in the figure at temperatures < 1300°C suggesting that they do not represent primary melts from a pyrolite mantle. From the plot it is clear that these rocks have been derived by 10–25% melting of the mantle. These conclusions are substantiated for the Mangalur metavolcanic rocks on the MgO-Ni diagram (figure 6) of Hanson and Langmuir (1978), as they plot near the field of primary melts, and on the (Mg) % vs (Fe) % diagram (figure 7) of Ford *et al* (1983) wherein they fall well below the field of melt.

The total range in (Fe) % of Mangalur metavolcanic rocks is more than 4%. If the mantle sources were homogeneous, the large range in (Fe) may be due to ranges in the extent of melting and depths of melting as suggested by Rajamani *et al* (1985) for Kolar tholeiites. Samples with the highest incompatible element abundances (Zr = 68 ppm), i.e. those formed at lowest extents of melting, have both higher and lower (Fe) contents. This could result in a homogeneous source only as a result of higher and lower melting pressures respectively. For example, if the parent magmas of samples 8 and 18 were generated at similar depths and temperatures and had similar differentiation histories, then sample 8 with 14.67 cation % (Fe) would represent a magma generated by a lower extent of melting than would sample 18 with 11.45% (Fe). If the mantle source had been heterogeneous, some variation in the FeO abundances of the rocks of Mangalur could be attributed to variations in the FeO/MgO ratios of their source region. Due to the apparent large extent of fractionation involving olivine, pyroxene and plagioclase, it may be difficult to evaluate the relative importance of extents of melting, temperatures of melting and FeO/MgO ratios of the source regions in causing observed spread in the FeO contents of these rocks.

Zr and Ni abundances are plotted in the Zr vs Ni diagram (figure 8). Using the criteria suggested by Rajamani *et al* (1985) to evaluate the melting, the plots of Mangalur metavolcanic rocks in the diagram indicate that these rocks could be derived by 10 to 30% melting of a mantle with 7.8 ppm Zr and 2000 ppm Ni.

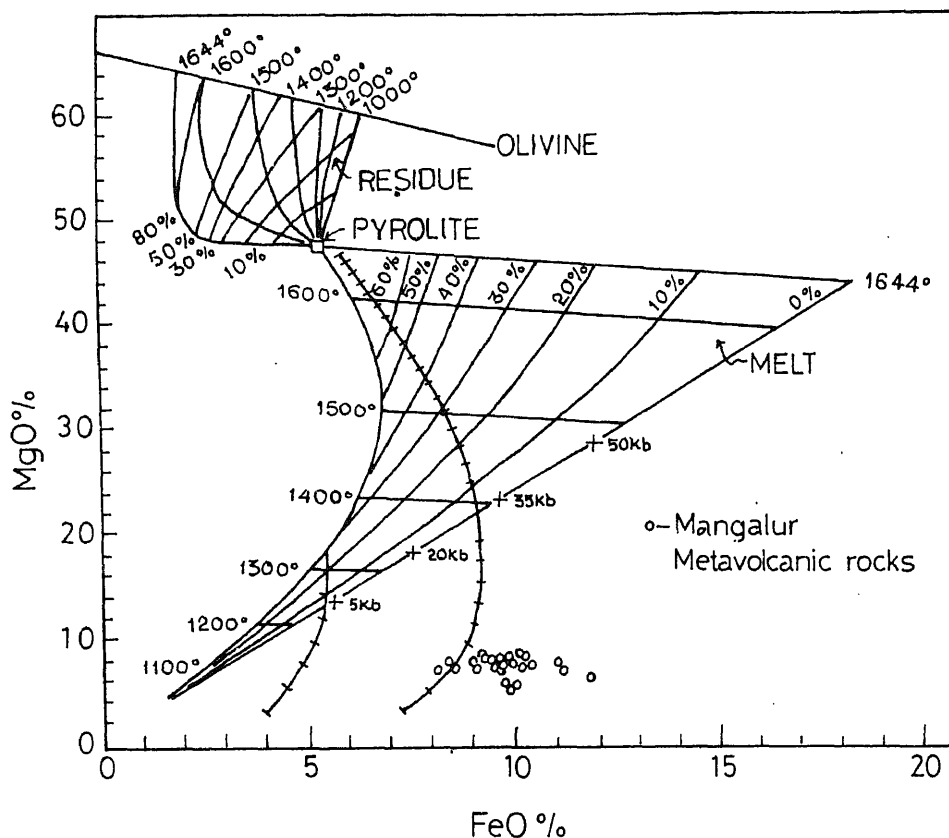


Figure 5. Plot of MgO against FeO (cation mole%) abundances in Mangalur metavolcanic rocks. Melt and residue fields are contoured for temperature and extents of melting of pyrolite (38.9 wt% MgO and 7.6 wt% FeO) at 1 atm. (Hanson and Langmuir 1978). The two curves with ticks indicate the liquid line of descent for fractional crystallization of olivine. Each tic represents 5% fractionation from the previous tic. Mantle solid at 5, 20, 35 and 50 kb are those given by Langmuir and Hanson (1980). The plots of Mangalur metavolcanic rocks indicate that these rocks have been derived by 10–25% melting of the mantle at about 10 kb.

7. Metamorphism

Actinolite/tremolite, epidote, plagioclase, chlorite, biotites, sericite, quartz and carbonate are the typical minerals found in the basic igneous rocks which have been metamorphosed under greenschist facies of regional metamorphism (Deer *et al* 1962). Typically, the gold-bearing rocks of Mangalur are devoid of either the traces of olivine or its alteration products and hence they can be very well compared with the Karroo lavas which are known to be olivine free. The authors feel that the pyroxenes and plagioclases of the volcanic rock of basaltic character have been broken down to yield actinolite/tremolite, chlorite, biotite and epidote under

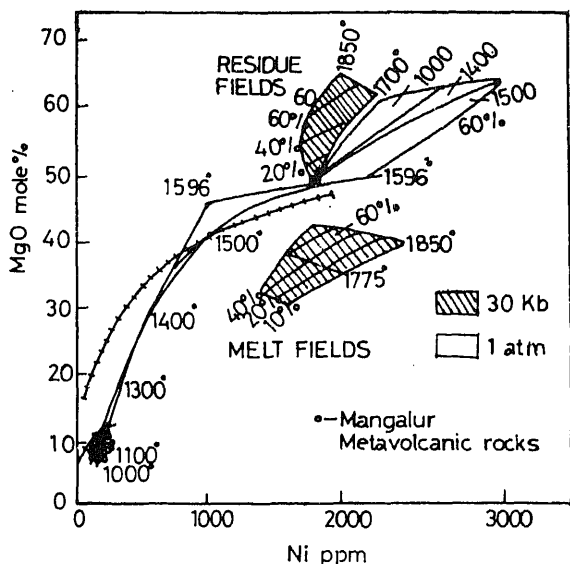


Figure 6. Ni-MgO diagram for batch melting of a pyrolite mantle with 1800 ppm Ni (after Hanson and Langmuir 1978). Fields for melting at 1 atm. and 30 kb are shown. Curves for fractional crystallization of olivine at 1 atm. are shown with marks at intervals of 5% fractional crystallization of olivine. The residue and melt fields are contoured for temperature and fractions of batch melting. The plots of Mangalur metavolcanic rocks do not represent primary melts from a pyrolite mantle.

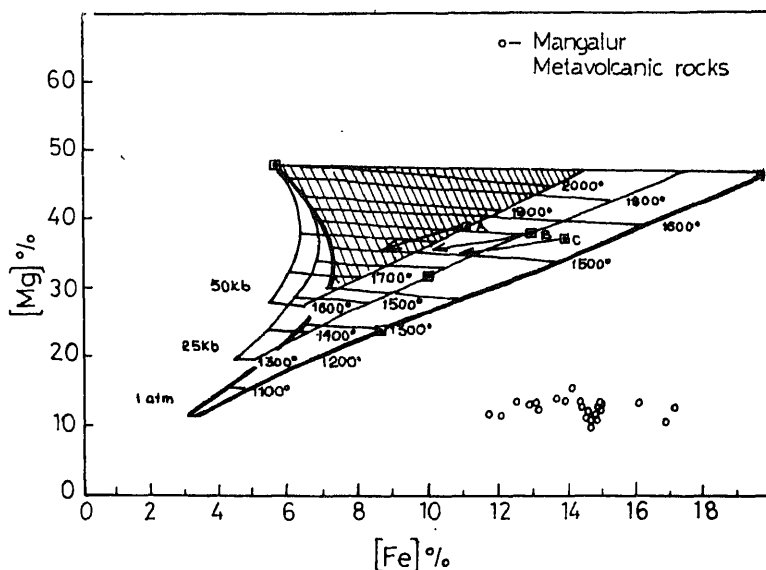


Figure 7. Plot of (Mg) % against (Fe) % (cation mole %) for the Mangalur metavolcanic rocks after Ford *et al* (1983). Three melt fields are shown for melting of pyrolite (38.9 wt MgO and 7.6 wt % FeO) with isotherms at different pressures. On the 0% melt line for each melt field the square symbol is the estimated location of the solidus for melting of an hydrous mantle (Langmuir and Honson 1980). The arrows from the square symbols labelled A, B and C are adiabatic paths of melting starting at 50 kb, for mantles with 38.9 wt.% MgO and 7.6, 9.0 and 10.2 wt.% FeO respectively.

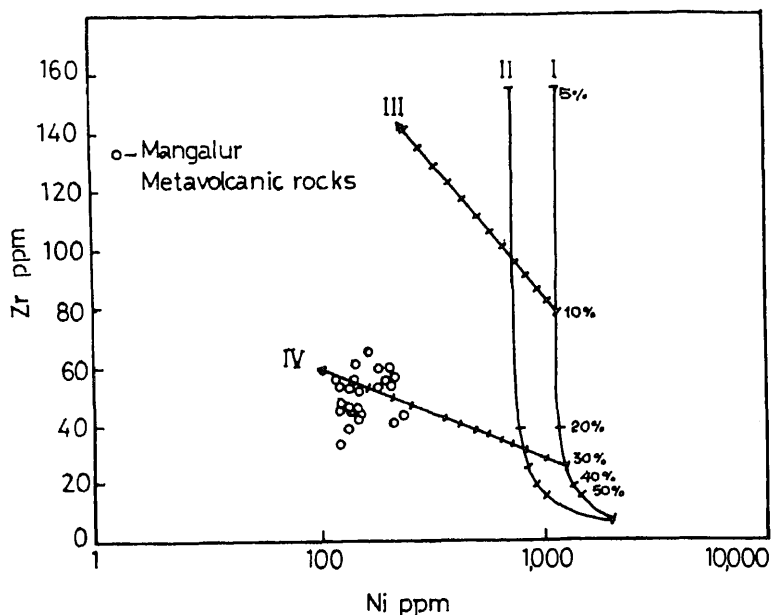


Figure 8. Plot of Zr against Ni abundances in Mangalur metavolcanic rocks. Curves I and II are calculated batch melting curves at 1850°C, 50 kb and 1575°C, 2 kb respectively, and are marked with percentages of melting. Curves III and IV represent olivine fractionation trends at 1 atm. with ticks marking increments of 5% olivine fractionation from the previous tick (Rajamani *et al* 1985). Mantle source is assumed to have 7.8 ppm Zr and 2000 ppm Ni (Taylor and McLennan 1981). Zr is assumed to be incompatible during melting.

the formation of quartz veins from the silica released during the breakdown of pre-existing minerals. Since quartz veins are found occupying the fractures and schistosity planes, it is suggested that the silica released during metamorphism moved towards low pressure sites and formed veins and lenses.

8. Origin and enrichment of gold

The origin of gold in gold-quartz vein type deposits has been a long-standing question. The Mangalur deposit occurs in the schist belt, which is surrounded by granites. This setting would suggest that the gold deposit is of hydrothermal origin and that the solutions had their source in the granite intrusions. Geological relationships between the metavolcanic rocks and granites indicate that the granites have invaded. It seems possible, therefore, that the intrusion of granite plutons has indirectly played an important role in the concentration of gold.

The gold content of a number of various rock types originating from the granite-greenstone terranes of the Kaapvaal and the Rhodesian Cratons quoted by Meyer and Saager (1985), indicate that volcanic rocks (Komatiitic and tholeiitic) contain gold ranging from 0.1 to 372 ppb and granitic rocks of the basement contain 0.3 to 7.8 ppb. Gold contents of least altered basic metavolcanic rocks of the neoproterozoic

old contents (in ppb) of the least altered metavolcanic rocks of Mangalur. However, the gold contents of Hutti metabasic volcanic rocks mentioned above are considered for the least altered metavolcanic rocks of Mangalur as background values for the present purpose, keeping in view the similarities in these two belts (Ugarkar 1986).

Chemical changes of major elements are characterized by an appreciable gain of K_2O and volatile contents (S + LOI) and loss of Na_2O and SiO_2 towards the gold-quartz veins i.e. from non-ore to rich-ore bodies (table 2). Many of the elements like Au, Cu, Zr, Co and Ni show gradual enrichment towards the gold-quartz veins in the shear zones.

Mineralogical and geochemical studies of wall-rock alterations of Mangalur have shown that the gold and other gangue elements, initially present in the basic country rocks, were mobilized by metamorphically derived hydrothermal solutions and concentrated in a suitable tectonic structures and chemical traps during metamorphic overprinting. Similar opinions were expressed earlier for the gold-quartz type deposits elsewhere in the world (Wanless *et al* 1960, Boyle 1961, 1979; Kerrich and Fyfe 1981; Saager *et al* 1982; Fyfe and Kerrich 1984; Bernasconi 1985; Phillips 1986; Meyer and Saager 1985). A number of papers followed dealing with the relation between gold mineralization and volcanic rocks; many authors concede that the volcanic rocks are the sources of gold in the greenstone belts and that the intrusive granites did play an important role in producing the heat energy requirement and structural environments necessary for the migration and concentration of gold to form the gold-quartz vein deposits (Anhaeuser *et al* 1975; Hutchinson 1976; Keays and Scott 1976; Kwong and Crocket 1978; Fryer *et al* 1979; Boyle 1979; Kerrich and Fryer 1981; Fyfe and Kerrich 1984; Saager and Meyer 1984; Phillips 1986; Meyer and Saager 1985).

The chemical and mineralogical rearrangement associated with gold-quartz mineralization in the Mangalur belt has resulted in end products that are apparently similar to the products of magmatic hydrothermal activities, and the features like geological setting, shear zones and wall-rock alterations viz chloritization and biotitization are suggestive of hydrothermal deposits and a thousand fold concentration (in ppm) in the shear zones compared to the background values in the metavolcanic rocks (in ppb) compel the authors to doubt whether the hydrothermal solutions of magmatic origin also, though not mainly atleast partially, have taken part in contributing the gold concentrations in the Mangalur greenstone belt.

9. Conclusion

Gold mineralization in the Mangalur greenstone belt occurs within the metavolcanic rocks which were tholeiitic basalts regionally metamorphosed under medium to low-grade greenschist facies. These rocks are characterized by the presence of pillow structures and relic pyroxenes indicating their earlier basaltic nature.

From the petrogenetic discussion, it seems that the metavolcanic rocks of

basic volcanic rocks, structural deformation might have led to the development of shear zones which acted as links for gold and other elements transported by migrating metamorphically secreted hydrothermal solutions.

It is reasonable to assume that the magmatic hydrothermal solutions might have also taken part, atleast partially, in contributing the gold concentrations in the Mangalur greenstone belt, in addition to the major basaltic source.

Acknowledgements

The authors express their sincere thanks to the authorities of Hutti Gold Mines Co. Ltd., for all the facilities and help extended by providing the gold-bearing ore specimens for study. The authors are specially thankful to Dr V N Vasudevan (Mines and Geology Department, Bangalore) and C Chakrabarthi (Geological Survey of India, Bangalore) for useful discussion and suggestions. One of the authors (AGU) thanks the Karnatak University authorities for financial assistance towards his Ph.D. programme.

References

- Ananta Iyer G V and Vasudev V N 1979 Geochemistry of the Archaean metavolcanics of Kolar, Hutti Gold Fields, Karnataka, India; *J. Geol. Soc. India* **20** 419–432
- Anhaeusser C R, Fritz K, Fyfe W S and Gill R C O 1975 Gold in primitive Archaean volcanics; *Contrib. Mineral. Geol.* **16** 129–135
- Bernasconi A 1985 Archaean gold mineralization in Central Eastern Brazil: a review; *Miner. Depos.* **20** 277–283
- Boyle R W 1961 The geology, geochemistry and origin of the gold deposits of the Yellowknife district; *Geol. Surv. Can. Mem.* **310** 1–193
- Boyle R W 1979 The geochemistry of gold and its deposits; *Geol. Surv. Can. Bull.* **280** 58
- Bruce Foote R 1875 Geology of Southern Maharatta country; *Geol. Soc. India Mem.* **XII** 1
- Condie K C 1976 *Plate tectonics and crustal evolution*; (New York: Pergamon Press) 145–160
- Condie K C 1981 Archaean greenstone belts; *Developments in Precambrian geology* (Amsterdam: Elsevier) vol. 3, pp. 1–434
- Deer W A, Howie R A and Zussman J 1962 *Rock-forming minerals* (London: Longman) vol. 1, pp. 1–371
- Ewart A 1981 Petrochemical aspects of the tertiary anorogenic volcanism of Southern and Central Queensland, Australia. In: *Deccan volcanism and related basalt provinces in other parts of the world* (eds) K V Subba Rao and R N Sukheswala *Geol. Soc. India Mem.* **3** 377–393
- Flanagan F J 1973 Values for international geochemical reference samples; *Geochim. Cosmochim. Acta* **37** 1189–1200
- Ford C E, Russel D G, Craven J A and Fisk M R 1983 Olivine-liquid equilibria: temperature, pressure and composition dependence of the crystal/liquid partition coefficients for Mg, Fe^{2+} , Ca and Mn; *J. Petrol.* **24** 256–265
- Fryer B J, Kerrich R, Hutchinson R W, Peirce M G and Rogers D S 1979 Archaean precious-metal-bearing hydrothermal system, Dome Mine, Abitibi Greenstone Belt. I. Patterns of alteration and mineral distribution; *Can. J. Earth Sci.* **16** 421–439
- Fyfe W S and Kerrich R 1984 Gold: Natural concentration processes. In *Gold 82; The geochemistry and genesis of gold deposits* (ed) R P Forster *Geol. Soc. Zimbabwe Sp. Publ.* **1** (Rotterdam: Balkema) 99–127
- Glikson A Y 1983 Geochemistry of Archaean tholeiitic basalt and High-Mg to peridotite komatiites, with petrogenetic implications in *Precambrians of South India* (eds) S M Naqvi and J Rogers; *Geol. Soc. India Mem.* **4** 183–219

- Hanson G N and Langmuir C H 1978 Modelling of major elements in mantle-melt systems using trace element approaches; *Geochim. Cosmochim. Acta.* **42** 725–741
- Hutchinson R W 1976 Lode gold deposits: the case for volcanogenic derivation; *Proc. Pacific Northwest Mining and Metals Conference, Portland, Oregon* (Oregon Dept. of Geology and Mineral Industries) pp. 64–105
- Keays R R and Scott R B 1976 Precious metals in ocean-ridge basalts: implications for basalts as source rocks for gold mineralization; *Econ. Geol.* **71** 705–720
- Kerrick R and Fryer B J 1981 The separation of rare elements from abundant base metals in Archaean lode gold deposits: implications of low water/rock source regions; *Econ. Geol.* **76** 160–166
- Kerrick R and Fyfe W S 1981 The gold-carbonate association: source of CO₂ and CO₂-fixation reactions in Archaean lode deposits; *Chem. Geol.* **33** 265–294
- Kwong Y T G and Crocket J H 1978 Background and anomalous gold in rocks of an Archaean greenstone assemblage, Kakagi Lake area, Northwestern Ontario; *Econ. Geol.* **73** 50–63
- Langmuir C H and Hanson G N 1980 An evaluation of major element heterogeneity in the mantle sources of basalts; *Philos. Trans. R. Soc. London* **A297** 383–407
- Mahadevan C 1945 Sedimentary structures in Mangalur band of Dharwar; *J. Hyderabad Geol. Surv.* **4** 31–36
- Mahadevan C and Krishnamurthy L S 1945 Löllingite in pegmatite in the Mangalur band of Dharwar; *J. Hyderabad Geol. Surv.* **4** 18–21
- Meyer M and Saager R 1985 The gold content of some Archaean rocks and their possible relationship to epigenetic gold-quartz vein deposits; *Miner. Deposita* **20** 284–289
- Naqvi S M, Divakara Rao V, Satyanarayana K and Hussain S M 1974 Geochemistry of post-Dharwar basic dykes and the Precambrian crustal evolution of Peninsular India; *Geol. Mag.* **11** 229–236
- Phillips N G 1986 Geology and alteration in the Golden Mile, Kalgoorlie; *Econ. Geol.* **81** 779–808
- Radhakrishna B P 1983 Archaean granite-greenstone terrain of the South Indian Shield in *Precambrians of South India* (eds) S M Naqvi and J J W Rogers *Geol. Soc. India Mem.* **4** 1–46
- Rajamani V, Shivakumar K, Hanson G N and Shirey S B 1985 Geochemistry and petrogenesis of amphibolites, Kolar schist belt, South India: evidence for komatiitic magma derived by low percentages of melting of the mantle; *J. Petrol.* **26** 92–123
- Ramachandra Rao M N 1980 Mangalur Gold Prospect — A case study review; *Proc. Seminar on recent trends in gold mining practice, India* pp. 1–6
- Ringwood A E 1975 *Composition and petrology of the earth's mantle* (New York: McGraw-Hill) p. 618
- Saager R and Meyer M 1984 Gold distribution in Archaean granitoids and supracrustal rocks from Southern Africa: a comparison in *Gold 82; The geology, geochemistry and genesis of gold deposits* (ed) R P Forster *Geol. Soc. Zimbabwe Sp. Pub.* **1** (Rotterdam: Balkema) pp. 53–70
- Saager R, Meyer M and Muff R 1982 Gold distribution in supracrustal rocks from Archaean greenstone belts of South Africa and from palaeozoic ultramafic complexes of the European Alps: metallogenic and geochemical implications; *Econ. Geol.* **77** 1–24
- Schuler V C O 1971 Chemical analysis and sample preparation; In *modern methods of geochemical analysis* (eds) R E Wairnerdi and E A Uken (New York: Plenum Press) p. 66
- Sugimura A 1968 Spatial relations of basaltic magmas in island arcs; *Basalts-Poldervaart treatise on rocks of basaltic composition* (New York: Interscience) pp. 537–572
- Taylor S R and Mc Lennan S M 1981 The composition and evolution of the continental crust: rare earth element evidence from sedimentary rocks; *Philos. Trans. R. Soc. London* **A301** 381–399
- Ugarkar A G 1986 Mineralogy and geochemistry of sulphide-gold-quartz veins and gold bearing metavolcanics of Mangalur greenstone belt, Gulbarga district, Karnataka; *Ph.D. Thesis, Karnatak University, Dharwad*
- Vasudev V N 1980 Geology and geochemistry and mineralization in the greenstone belts of Hutti and Chitradurga, Karnataka; *Indian Natl. Sci. Acad. Lectures* pp. 28–36
- Viljoen M J and Viljoen R P 1969 Geology and geochemistry of the lower ultramafic unit of the Onverwacht group and a proposed new class of igneous rocks; *Spec. Pub. Geol. Soc. S. Africa* **2** 55–86
- Wanless R K, Boyle R W and Lowden J A 1960 Sulfur isotope investigation of the gold-quartz deposits of the Yellowknife district; *Econ. Geol.* **55** 1591–1621
- Wilkinson J F G 1981 Continental and mid-ocean ridge tholeiites: some similarities and contrasts in *Deccan volcanism and related basalt provinces in other parts of the world*; (eds) K V Subba Rao and R N Sukheswala *Geol. Soc. India Mem.* **3** 340–361

146-day signal in the geomagnetic field—a probable association with the periodicity of the solar flare index

D R K RAO and B D KADAM

Indian Institute of Geomagnetism, Bombay 400 005, India

MS received 7 February 1986; revised 18 May 1987

Abstract. Results on the spectral analysis using geomagnetic field at three low latitude stations and the planetary magnetic activity index have shown peaks in the power densities in a broad band centred around 146-day period. This periodic behaviour appears to be close to that shown by the solar flare activity index for the same interval. It is suggested that the geoeffectiveness of the flare activity signal in different phases of the solar cycle can be better worked out using long series of ground-based geomagnetic data.

Keywords. Flare index; 146-day period; geomagnetic planetary index; geomagnetic field.

1. Introduction

Recently, Rieger *et al* (1984) have shown clear evidence of regularity (≈ 154 day period) in the occurrence of energetic solar flares. This effect was recognized and worked out for flares giving emissions of > 300 keV which produce soft X-rays. They attributed the origin of these periodic solar flares in the deeper layers on the sun, possibly at the sub-photospheric layers. Ichimoto *et al* (1985) have examined the periodic nature of solar activity using the parameters like sunspot number, calcium plage areas and flare indices. According to them, the temporal variation of the flare activity on the sun based on H_α data during the years 1965 to 1984, has shown evidence for 155-day and also 17-month periodicity of the activity. Also, they have taken into account the location of the flares on the sun to further confirm the reality of the derived periodicities.

If there exists the periodic behaviour in the sporadic nature of certain flare activity on the sun, its effect can be discernible in the processes involving the geoeffectiveness of the flare activity. One such process is the temporal variations of the geomagnetic field. With this objective, this paper reports our search to detect the signal corresponding to the cyclic variation of the flare activity using the data on planetary index of geomagnetic activity and the geomagnetic field at three low-latitude stations in the Indian region.

2. Data and analysis

Daily mean values of the horizontal component of the earth's magnetic field (H) at Hyderabad (dip $\approx 20^\circ\text{N}$), Alibag (dip $\approx 25^\circ\text{N}$), Sabhawala (dip $\approx 44^\circ\text{N}$), the three low-latitude stations in the Indian region far from the influence of the equatorial electrojet, for the interval starting from 1 January 1979 to 31 December 1983 are taken for the analysis. This interval is nearly the same as the duration of the special

experiment conducted by Rieger *et al* (1984) which was from February 1980 to September 1983. For the same interval of H data, daily planetary index of geomagnetic activity, A_p , derived internationally, was also considered for analysis.

As both the H field and A_p series are known to have significant contributions from the annual and semi-annual variations and considering the fact that the wavelength at 180-day corresponding to the semi-annual variation is closer to the suspected signal of flare activity at 154-day, it is essential to filter the data to eliminate the annual cycles. The annual and semi-annual components (amplitudes and phases) are estimated for each of the calendar years separately via Fourier analysis and the synthesized values from the analysis are uniformly subtracted from the daily values. These residual daily series of H and A_p , which are free from annual and semi-annual components, form the basic data set for further analysis. Using the time series of 1826 filtered daily values over five years duration, spectral estimates via fast fourier transform (FFT) are obtained on each of the H and A_p series separately using Cooley and Tukey (1965) algorithm. Prior to the spectral analysis, the length of the time series is extended upto 4096 data points by appending zeros at the end of the zero mean based time series for increasing the resolution. The amplitude spectra of H at Alibag and A_p against the harmonic number for the first 35 estimates are shown in figure 1. Similar results in respect of Hyderabad and Sabhawala are shown in figure 2.

3. Results and discussion

The results in figures 1 and 2 show that there is an increase in the amplitudes of H in a band of frequencies, spanning from 164 to 132 day peaking at 146 day, at all the three low-latitude stations as well as in the spectra of A_p series. Apart from the peak at 146 day, all the spectra have shown two more peaks at 241- and 683-day periods. However, the amplitude of the peak at the estimate corresponding to 146

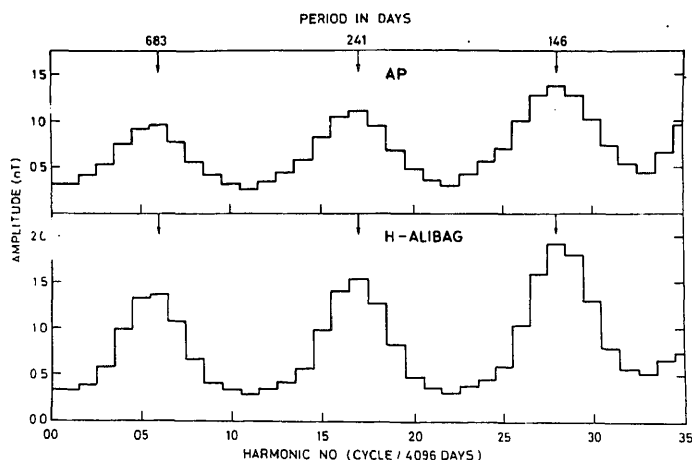


Figure 1. Plot of the amplitude spectra of the daily mean horizontal component of H at Alibag and the daily planetary index of magnetic activity, A_p in units of nT against the first

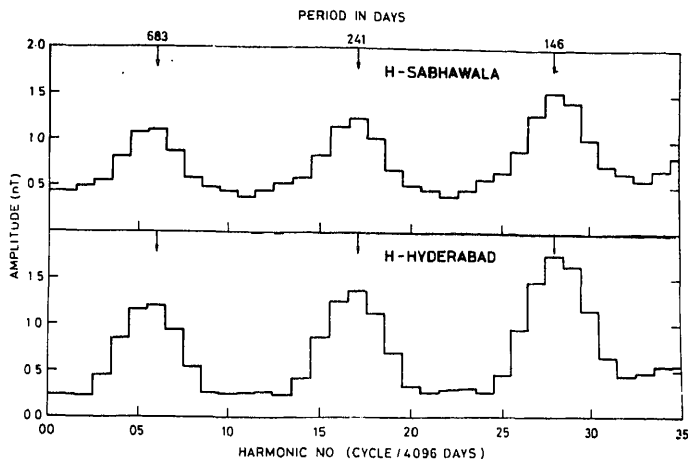


Figure 2. Plot of the amplitude spectra of the daily mean horizontal components of H at Hyderabad and Sabhawala against the first 35 harmonic numbers (units of cycles/4096 days).

Table 1. Spectral results (146-day period).

Parameter	Amplitude (nT)	Phase angle (degrees)
H -Hyderabad	1.7	275
H -Alibag	1.9	280
H -Sabhawala	1.5	284
A_p	1.4	106

day period is the highest in the field and A_p results. The amplitudes and phases of the spectra corresponding to peak are given in table 1.

The number of degrees of freedom (ν) of the spectra computed via FFT is approximately $2N/m$ where N is the total number of data points and m the maximum 'lag'. As the spectra are computed in FFT to half that of N , $m = N/2$. Thus ν works out to be 4. Assuming χ^2 distribution, the confidence limits of power spectra are 3.6 and 83.0 at 95% confidence level (Munk *et al* 1959). The continuum level under the 146-day signal in both the field and A_p spectra in figures 1 and 2 exceeds 100% and hence are considered to be statistically significant at 95% or beyond the confidence limits. Moreover, more reliable and purely empirical tests of significance, free from any assumptions, would be to produce spectra for several different samples and then compare spectra. Such methods are substantiated by Tukey (1961) who states that there is no substitute for some sort of repetition as a basis for assessing stability of estimates and establishing confidence limits. A simple and useful 'rule of thumb' is expressed by Stuart *et al* (1971) by which criterion a spectral line is considered to be significant if it contains at least three computed points which deviate from the noise and has a maximum twice greater than the surrounding noise level. It is also stressed by them that independent tests, by repeating the computation with different parameters or digitized data, are the only accurate method of eliminating doubts. Thus, the fact that the spectra computed

with data of three different stations and also the global index, whose results are given in table 1, will pass through tests of significance and stand out as the significant peak at 146-day period.

To further substantiate the reality of the observed signal, cross-spectral analysis, via FFT, has been performed between A_p and the H -field values at Alibag. The same filtered values, as were derived for auto-spectrum analysis earlier, are used. From the results of cross-spectrum analysis, it is found that the phase lead of H at Alibag over A_p is 175.4° and the magnitude of coherence is 0.99 at 146-day period. This high coherency and the near antiphase relationship observed support the contention of the origin of the same periodicity in both the series of A_p and the field.

The fact that statistically significant peaks are observed in the H field at three low-latitude stations and also in the globally derived parameter A_p , in the vicinity of 154-day period, suggests that these may be associated with the periodic nature of the high energy flares during the interval.

Ichimoto *et al* (1985) have done extensive analysis on flare activity using H_α flare data of importance 1, 2 and 3 during the solar cycles 20 and 21. The periodicity of the flare activity was examined by them subjecting the weighted flare numbers for cycles 20 (1965–1975) and 21 (1976–1984) to the maximum entropy power spectral analysis. A distinct peak in the spectrum at the period near 155 day is observed by them in both the solar cycles suggesting that the flare activity shows an inherent characteristic of periodic activity. The time longitude distribution of flares which can be compared with that of magnetic fields on the solar surface between 5°N and 15°N heliographic latitudinal zones for the interval January 1976 to February 1984, has shown two regular strips of long-lasting magnetic features. The power spectra of the daily number of flares that occurred in these two strips separately peaked between 150 and 160 days thereby suggesting that each stream has a tendency to produce many flares separately with a period of ≈ 155 days. According to them, the probable origin of this periodicity is the temporal variations in the strongly magnetized regions which lasts for a long time and drift in longitudes due to the differential rotations.

In conclusion, it is shown that the geoeffective parameters of the flare indices viz the ground geomagnetic field at low latitudes respond to the periodic behaviour of the flare regularity. The long term associations are being worked out in different phases of the solar activity and the same will be published elsewhere.

References

- Cooley J W and Tukey J W 1965 *Math. Compt.* **19** 297
 Ichimoto K, Kubota J, Suzuki M, Tohmura I and Munokawa H 1985 Periodic behaviour of solar flare activity; *Nature (London)* **316** 422–424
 Munk W H, Snodgrass F F and Tacker M J 1959 Spectra of low frequency ocean waves; *Bull. Scripps Inst. Oceanogr. Univ. Calif.* **7** 283–362
 Rieger E, Share G H, Forrest D J, Kanbach G, Reppin C and Chupp E L 1984 A 154-day periodicity in the occurrence of hard solar flares; *Nature (London)* **312** 623–625
 Stuart W F, Sherwood V and Macintosh S M 1971 The power spectral density technique applied to micropulsation analysis; *Pure Appl. Geophys.* **92** 150–154
 Tukey J W 1961 Discussion emphasizing the connection between analysis of variance and spectrum

Turbulent fluxes over east-central Arabian sea during MONEX

K K VARMA and N N RAMAN

College of Fisheries, Panangad, Cochin 682 506, India

MS received 2 June 1986; revised 18 April 1987

Abstract. Fluxes of momentum, latent heat and sensible heat at fixed stations in the east-central Arabian sea during MONEX were studied. Observations at the same locations at different periods as well as simultaneous observation at different locations were compared. During the advance of monsoon, momentum flux showed remarkable increase. Latent heat loss from sea also increased while sensible heat flux, in general, changed direction to become a gain by the sea. SST decreased by about 1.5°C and air temperature decreased by about 1°C during the advance phase. A north-south difference in SST in the study region seemed to be favourable for the genesis of onset vortex of monsoon. The possible differential effect of this storm at two different locations, depending upon the SST before the storm, is also discussed.

Keywords. MONEX; turbulent fluxes; onset vortex.

1. Introduction

Air-sea interaction is one of the factors that influence monsoons. Different aspects of air-sea interaction over Indian Ocean in general and the monsoon regions in particular have earlier been studied (Colon 1964; Pisharoty 1965; Hastenrath and Lamb 1979; Reddy *et al* 1984a; Rao 1984). In the present investigation, based on MONEX data, turbulent air-sea fluxes across sea surface at fixed locations in east-central Arabian sea in pre-onset and advance phases of monsoon have been examined. The possible differential effect of onset vortex at different locations has been discussed.

2. Data and methods

The locations and periods of observation and reference numbers used for each set of observation are given in table 1 (see figure 1). Surface meteorological data collected during MONEX from these locations were utilized for computing fluxes of momentum (τ), sensible heat (Q_s) and latent heat (Q_e) using bulk aerodynamic formulae

$$\tau = \rho C_D U^2, \quad (1)$$

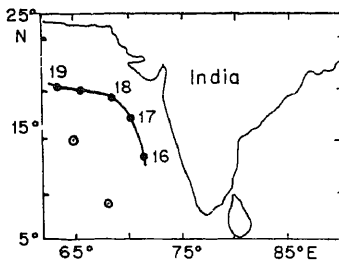
$$Q_s = \rho C_H C_P (T_s - T_a) U, \quad (2)$$

$$Q_e = \rho C_E L (q_s - q_a) U. \quad (3)$$

Here ρ is the density of air, C_p the specific heat at constant pressure, L the latent heat of evaporation, T_s the SST, T_a the air temperature at deck level and q_s and q_a

Table 1. Locations and periods of observations.

Name of ship	Number	Location	Period of observation	Phase of monsoon
Darshak	I	9°N 68°E	2.5.79 to 12.5.79	Pre-onset
Darshak	II	8.9°N 68°E	26.5.79 to 3.6.79	Pre-onset
Darshak	II-A	12°N 68°E	4.6.79 to 5.6.79	Pre-onset
Darshak	III	9°N 68°E	21.6.79 to 23.6.79	Advance
Deepak	IV	15°N 65°E	17.5.79 to 8.6.79	Pre-onset
Deepak	V	15°N 65°E	19.6.79 to 25.6.79	Advance

**Figure 1.** Station location and track of the storm showing the dates.

the specific humidities at these levels. U is the wind speed at deck level, C_D the drag coefficient and C_H and C_E the exchange coefficients for sensible heat and water vapour respectively. Fluxes computed at 6 hr intervals were used to obtain average daily fluxes.

2.1 Exchange coefficients

Although early studies assumed a single and constant value for C_D , C_H and C_E , subsequent investigations revealed that a single value is not adequate for computing different fluxes. Several investigators earlier indicated that C_D was not constant but increased with wind speed (Smith and Banke 1975; Garratt 1977; Smith 1980; Wu 1980; Large and Pond 1981) which agreed with the suggestion by Charnook (1955) based on theoretical considerations. C_D obtained by Smith (1980) was $(0.61 + 0.063 U) \times 10^{-3}$. Somewhat similar relationships were seen by Smith and Banke (1975) and Garratt (1977). Smith (1980) indicated that drag coefficient appeared to be nearly constant for winds below 10 m sec^{-1} but increased rapidly at higher wind speeds. Stability of the atmosphere also influences the air-sea flux and hence exchange coefficients. Stable stratification inhibits turbulence and decreases the flux. Under unstable conditions turbulent exchange is enhanced by buoyancy. Stability is mainly caused by vertical temperature gradient. The effect of moisture on stability is significant only in near neutral conditions of atmosphere (Launiainen 1979). Smith (1980) found a dependence of C_D on stability but a quantitative functional relationship was not obtained. Kondo (1975) plotted the exchange coefficients as a function of wind speed and air-sea temperature difference.

Various workers had suggested that $C_H = C_E$. According to most experiments this is still valid (Launiainen 1979). Pond *et al* (1974) obtained $C_H = C_E = 1.5 \times 10^{-3}$ for normal temperature conditions and Smith (1974) got 1.2×10^{-3} for C_H and C_E . Hicks (1972) found both coefficients to be 1.4×10^{-3} . C_H does not depend strongly on wind speed but depends on stability (Smith 1980). Friehe and Schmitt (1976) found that $C_E > C_H$. Exchange coefficients were reviewed by Garratt (1977), Bunker (1976), Smith (1980) and Friehe and Schmitt (1976). Extensive micrometeorological observations made using an automatic sea mast in the Gulf of Finland and various theoretical aspects of air-sea turbulent fluxes were discussed by Launiainen (1979).

Bunker (1976) presented C_D and C_E in the form of tables for different wind speeds and air-sea temperature differences and suggested that values of C_E could also be used for computation of Q_s . For studying wind stress over world oceans, Hellerman and Rosenstein (1983) developed a polynomial for C_D using the values of Bunker (1976). C_E presented by Bunker (1976) was used for latent and sensible heat computations by Rao *et al* (1978), Weare (1983) and Reddy *et al* (1984 a) using climatological data, and by Reddy *et al* (1984 b) and Anto *et al* (1982) using MONEX data. For the present study also, C_D and C_E , which varied with wind speed and air-sea temperature difference, were extracted from the tables given by Bunker (1976).

3. Results

3.1. Observations at same locations

3.1a *Observations at 9°N 68°E*: Observations from this location were taken on periods I, II and III. Observations made (at 12°N 68°E) between these observations are indicated as IIA (table 1).

I 2.5.1979 to 12.5.1979: During this period (figure 2) wind stress was generally low ($< 0.90 \text{ dy. cm}^{-2}$) excepting on the last two days when it increased to about 1.5 dy. cm^{-2} . Latent heat of evaporation mostly followed the trend of τ and varied between 130 and $570 \text{ cal. cm}^{-2} \text{ day}^{-1}$. Heat loss by sensible heat ranged between 5 and $45 \text{ cal. cm}^{-2} \text{ day}^{-1}$. The increasing trend of fluxes was due to increase in wind speed associated with a cyclone in Bay of Bengal. SST varied between 29.8°C and 31.0°C and air temperature was always less than SST by about 1°C .

II 26.5.1979 to 3.6.1979: Calm weather prevailed during this period. Stress was about 0.60 dy. cm^{-2} on 26th May and decreased considerably on subsequent days. Latent heat was generally about $200 \text{ cal. cm}^{-2} \text{ day}^{-1}$ except on 26th when Q_e was $400 \text{ cal. cm}^{-2} \text{ day}^{-1}$. Sensible heat loss of about $30 \text{ cal. cm}^{-2} \text{ day}^{-1}$ observed on 26th decreased on the following days. Both followed the pattern of momentum variation. SST varied between 30°C and 31°C . Air temperature was in general less than SST.

Observations for the next two days (IIA-table 1) at $12^\circ\text{N } 68^\circ\text{E}$ also showed low values of τ , Q_e and Q_s . SST was about 30.5°C and air temperature also had similar values.

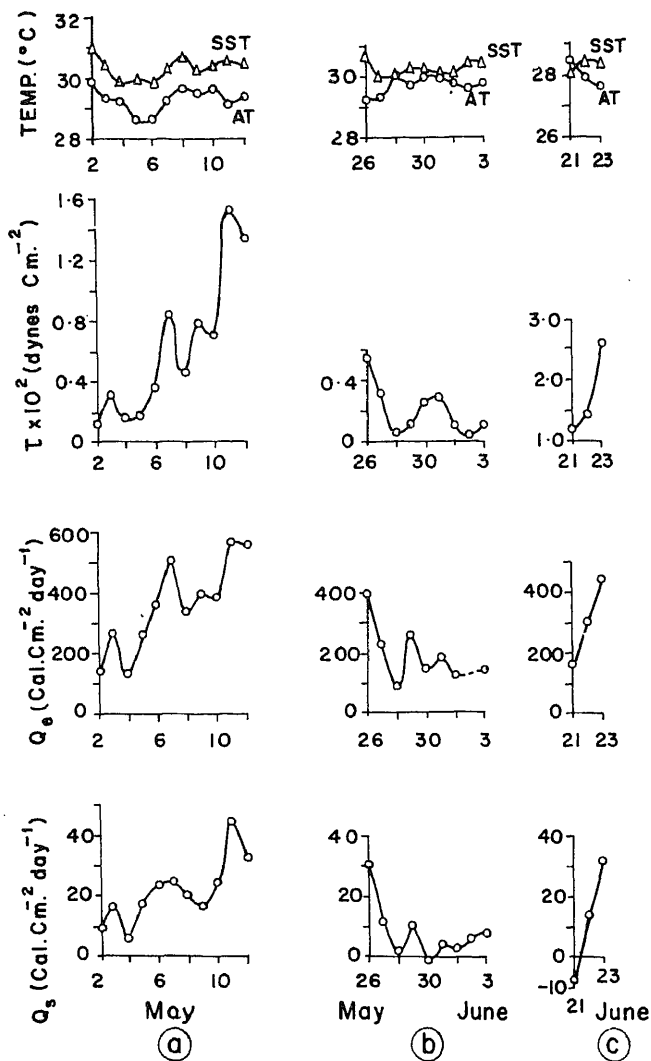


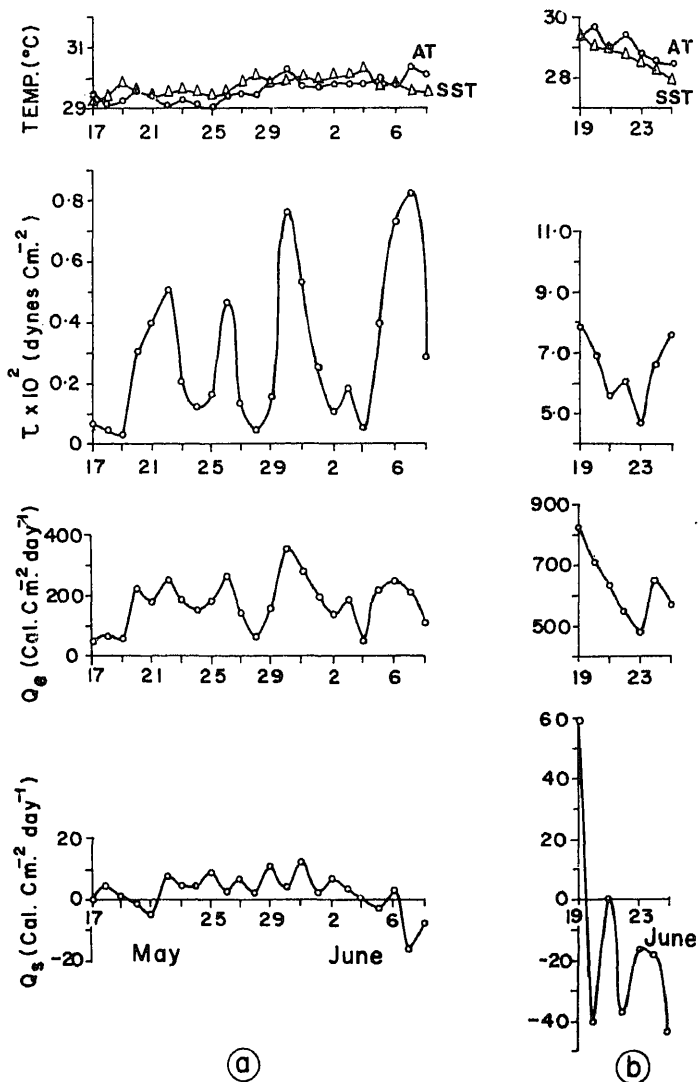
Figure 2. Variation of fluxes and temperature at southern station.

III 21.6.1979 to 23.6.1979: These observations were made after the monsoon set in, in the wake of an onset vortex which formed east of the station and moved away, intensifying into a storm. As compared to the earlier occasions, wind speed was higher (1.1 to 2.5 dy. cm^{-2}). The Russian ships which had formed a polygon south of this station also experienced an increase in wind speed associated with the storm (Shajahan 1980). Latent heat on the first day ($\sim 150 \text{ cal. cm}^{-2} \text{ day}^{-1}$) was similar to those during the earlier undisturbed weather conditions. Low evaporation, despite higher wind speed, was due to the presence of moist air as deduced from wetbulb depression. While wetbulb depression was about 3.8°C during the undisturbed situation, it decreased to about 1.3°C on 21st June. However, on the following days wetbulb depression increased to about 2.7°C and this, together with the increasing wind speed, resulted in increase of Q_e . On the first day of observa-

light gain of sensible heat by the sea was noticed and on the next two days the sensible heat loss steadily increased to about $30 \text{ cal. cm}^{-2} \text{ day}^{-1}$. SST had recorded a fall from the values of the previous set of observations and was about 28.5°C . Air temperature was slightly greater than SST on the first day and decreased to values less than SST on the next two days.

1b *Observations at $15^\circ\text{N } 65^\circ\text{E}$:* Two sets of observations (designated IV and V) were made from this station (table 1). As this station was nearer to the track of the onset vortex, these two observations will show situations before and after the storm.

V 17.5.1979 to 8.6.1979: During this period (figure 3), wind speed was low with the stress varying between 0.02 and 0.8 dy. cm^{-2} . Latent heat, in general, followed



the pattern of variation of stress and ranged between 40 and 350 cal. cm⁻² day⁻¹. Sensible heat exchange was also low and varied between -17 and 13 cal. cm⁻² day⁻¹. From 25th May onwards SST showed a slight increase of about 0.5°C and decreased from 4th June onwards. Air temperature was, in general, less than SST by about 0.5°C. From 25th May onwards air temperature increased suddenly by about 1.3°C upto 30th. From 6th to 8th June, the air temperature was greater than SST by about 0.8°C. This is because of a fall in SST as well as an increase in air temperature noticed on these days.

V 19.6.1979 to 25.6.1979: The onset vortex mentioned earlier had passed near the station two days before this set of observations commenced. Convective weather was present and the monsoon had set in. Wind stress was high and varied between 4.5 and 8.0 dy. cm⁻², with the minimum value on 23rd June. Nyenzi (1980) while studying zonal time sections of wind along 65°E during MONEX (the present longitude) had observed high westerly wind from 14th June to the end of the month with a break on 24th June at 850 mb surface. Latent heat was high and varied between 480 and 820 cal. cm⁻² day⁻¹. Minimum evaporation was observed when the wind speed was minimum. During this period, the air at this location was generally less moist (wetbulb depression of about 3°C) compared to southerly station. This, along with very high wind speed caused high evaporation. Sensible heat varied between -45 and 55 cal. cm⁻² day⁻¹. SST was 29.3°C on the first day of observation and progressively decreased by about 1.5°C on the subsequent days. Air temperature was, in general, greater than SST and showed a progressive decrease.

3.2 Simultaneous observations

As seen earlier, there are occasions when observations were made simultaneously at two locations. To make comparisons easier relevant parts are again presented in figure 4.

3.2a Observations at 9°N 68°E and 15°N 65°E from 26.5.1979 to 3.6.1979: The pattern of stress variations was similar at both the locations although slightly higher values were encountered at the northern location. In general, the variation of latent and sensible heats at both stations was comparable. SST was greater by about 1°C at the southern location on 26th and was more or less equal at both locations on the following days. The same data at the southern location (Shajahan 1980) also showed a decrease in SST after 26th. Although the present observations at the southern station was completed on 3rd June, the observation by Russian ship *Volna* at a closeby station (9.2°N 66.7°E) presented by Shajahan (1980) indicated equally high SST. However, the northern location (see § 3.1b) showed a decrease in SST from 4th June, thus exhibiting a north-south gradient in SST. Air temperature was in general comparable at both the stations.

3.2b Observations at the above locations from 21.6.1979 to 23.6.1979: As compared to the previous occasion, stress was greater at both locations. However, of the two stations, wind energy was considerably higher at the northern station. During this period of observation, wind stress decreased at the northern station while it showed a slight increase at the southern location. The decrease at the northern station is

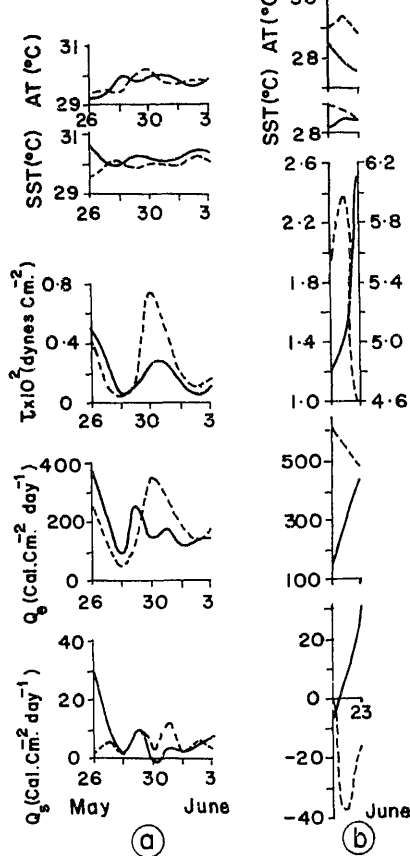


Figure 4. Variation of fluxes and temperature during simultaneous observations. (— southern station and ---- northern station)

associated with the fall in wind speed along 65°E (Nyenzi 1980). The meridional sections of wind further east, presented by Nyenzi (1980) do not exhibit this fall in wind speed. The southerly station which was located at 68°E, thus did not show the decrease in wind speed. Evaporation was greater at the northern station and at both the stations, in general, latent heat followed the pattern of wind stress. While there was a heat gain due to sensible heat at the northerly station on 22nd and 23rd, there was a heat loss at the southern location. Both SST and air temperature were higher at northern station.

4. Discussion

According to the terminology used during MONEX (FGGE 1981) the present observations can be classified as those during 'pre-onset' and the beginning of 'advance' phases of monsoon. Average fluxes for the two phases are presented in table 2. Average wind stress increased remarkably during the advance phase to

Table 2. Average fluxes during pre-onset and advance phases of monsoon.

	Pre-onset phase	Advance phase
No. of observations	185	38
Air temperature (°C)	29.6	28.7
SST (°C)	30.0	28.6
τ (dy.cm ⁻²)	0.4	5.3
Q_e (cal. cm ⁻² day ⁻¹)	219.0	546.0
Q_s (cal. cm ⁻² day ⁻¹)	8.0	-8.0

about 5.3 dy. cm⁻². Similar values associated with increase in monsoon activity were observed in the Arabian sea by Pant (1977). Average fluxes of latent heat and sensible heat during pre-onset phase were about 220 and 10 cal. cm⁻² day⁻¹ respectively. These values, in general, agreed with those by Hastenrath and Lamb (1979) for May. During advance phase, average fluxes were about 550 cal. cm⁻² day⁻¹ and -10 cal. cm⁻² day⁻¹ for latent and sensible heats respectively. Daily average fluxes of similar magnitude were reported from this area by Pant (1977) during ISMEX. Present fluxes were larger than the climatological average for June presented by Hastenrath and Lamb (1979) and the average for monsoon months of certain years by Saha (1970) and Saha and Suryanarayana (1972). This is because the present observations were made soon after the passage of a storm. Studying GATE data Senguin and Kidwell (1980) found that synoptic scale fields contained large fluxes. With the onset of monsoon, SST decreased by about 1.5°C. Using climatological data Rao *et al* (1976) had noticed a fall in SST of about 1.0°C in east-central Arabian sea from May to June. Air temperature also decreased after the onset of monsoon.

During this year, monsoon had set in under the influence of onset vortex which first appeared as a trough over Lakshadweep on 7th June. After becoming well marked, it persisted there till 13th June, then intensified into a depression over east-central Arabian sea by 16th June and later into a cyclone (Mukherjee and Paul 1980). During this period SST distribution in this area also underwent changes. At northern station from 4th June till the end of observations (8th June) SST decreased to about 29.2°C and became less than air temperature. SST at Russian polygon presented by Shajahan (1980) showed higher values (> 30°C) at 9.2°N 66.7°E and 7°N 66.7°E till 12th June and a decrease at a station further south (4°N 66.7°E) during this period. The situation in east-central Arabian sea was thus conducive for higher air-sea exchange at 7°N and 9°N with reduction towards north and south. This might have been one of the factors that contributed to the intensification of onset vortex. Mandal *et al* (1984) had shown that high SST which can result in large evaporation was one of the favourable conditions for observed intensification of a cyclone in Bay of Bengal. The genesis region of this vortex coincided with the area where SST exceeded 31°C (Ramesh Babu and Sastry 1984).

Another interesting observation is the slightly higher SST at the northern station during the first few days (21st and 22nd June) after the storm, explained in 3.2b. Although northerly station was nearer to the track of the storm (figure 1), both

tations were under the influence of the storm. Jet-like speeds existed during the storm over extensive areas (FGGE 1981). Hence a plausible explanation for the slightly higher SST at the northern station could be the differential impact of the storm on the locations depending on the thermal structure obtained before the storm. Elsberry and Raney (1978) had shown that cooling due to storm would be greater when the mixed layer is shallow and would be less when the mixed layer is deep. SST in the present study and those recorded by Russian polygon (Shajahan 1980) indicates variation in thermal structure. Observations II at 9°N 58°E recorded higher SST upto 3rd June. A nearby station occupied by Russian ship *Volna* (9.2°N 56.8°E) continued to record high temperature upto 12th June. Present observations II at 15°N 65°E indicated a fall in SST from 4th June onwards. Before storm, the higher surface temperature at the southerly station would have inhibited the formation of deep mixed layer while the decreasing SST at the northern station could have induced convection and deeper mixed layer. Ramesh Babu and Sastry (1984) had shown deeper mixed layer exceeding 40 m at stations close to the present northerly station (15°N 65°E) just before the vortex crossed the area. Such variations in mixed layer depth might have caused a differential effect of the storm and resulted in increased cooling and lower SST at the southerly station soon after the passage of the storm.

Conclusions

Wind stress and evaporation increased during advance phase of monsoon. Sensible heat was less than latent heat by an order of magnitude. While sensible heat was lost from sea during pre-onset it was gained by sea during advance phase. North-south SST gradient in early June might have contributed to the formation of onset vortex. Southerly station, where SST was greater before the vortex, had registered greater surface cooling as a result of this storm.

Acknowledgements

The authors thank Dr M J Sebastian for his keen interest and Dr P G Kurup, Head of the Oceanography and Meteorology Division, University of Cochin for a critical reading of the manuscript. Thanks are also due to the India Meteorological Department for the supply of data. Authors are thankful to the referees for valuable comments for improving the paper.

References

- Anto A F, Rao L V G and Somayajulu Y K 1982 Surface layer conditions of the atmosphere over western Bay of Bengal during MONEX; *Indian J. Mar. Sci.* **11** 15-20
- Unkrer A F 1976 Computations of surface energy flux and annual air-sea interaction cycles of north Atlantic oceans; *Mon. Weather Rev.* **104** 1122-1140
- Charnook H 1955 Wind stress on water surface; *Q. J. R. Meteorol. Soc.* **81** 639-640
- Polon J A 1964 On interactions between the southwest monsoon current and the sea surface over the Arabian sea; *Indian J. Meteorol. Geophys.* **15** 183-200

- Elsberry R L and Raney S D 1978 Sea surface temperature response to variations in atmospheric forcing; *J. Phys. Oceanogr.* **8** 881-887
- FGGE 1981 Summer MONEX field phase report; *FGGE Operations Report* **8** Section 2 WMO
- Friehe R L and Schmitt 1976 Parametrization of air-sea interface fluxes of sensible heat and momentum; bulk aerodynamic formulae; *J. Phys. Oceanogr.* **6** 801-809
- Garratt J R 1977 Review of drag coefficients over oceans and continents; *Mon. Weather Rev.* **105** 915-929
- Hastenrath S and Lamb P J 1979 *Climatic atlas of Indian Ocean Part II: The oceanic heat fluxes* (Madison; University of Wisconsin Press)
- Hellerman S and Rosenstein M 1983 Normal monthly wind stress over the world ocean with new estimates; *J. Phys. Oceanogr.* **13** 1093-1104
- Hicks B B 1972 Some evaluation of drag and bulk transfer coefficients over water bodies of various sizes; *Boundary-Layer Meteorol.* **3** 201-213
- Kondo J 1975 Air-sea bulk transfer coefficients in diabatic conditions; *Boundary - Layer Meteorol.* **9** 111-112
- Large W F and Pond S 1981 Open ocean measurements of flux in moderate to strong winds; *J. Phys. Oceanogr.* **11** 324-336
- Launiainen J 1979 Studies of energy exchange between the air and sea surface on the coastal waters of the gulf of Finland; *Finn. Mar. Res.* **246** 3-110
- Mandal G S, Gupta G R and Mookerjee N 1984 Orissa cyclone 1-4 June 1982; *Vayumandana*
- Mukherjee A K and Paul D K 1980 Influence of Arabian sea cyclonic systems on the onset of the southwest monsoon; *Results of summer MONEX field phase research part A; FGGE Operations Report* **9** WMO, Geneva 62-67
- Nyenzi B S 1980 Influence of low tropospheric flow on the onset of summer monsoon flow over the Indian subcontinent; *Results of summer MONEX field phase research part A; FGGE Operations Report* **9** WMO, Geneva 68-80
- Pant M C 1977 Wind stress and fluxes of sensible and latent heat over the Arabian sea during the summer monsoon; *Indian J. Meteorol. Hydrol. Geophys.* **28** 189-196
- Pisharoty P R (ed) 1965 Evaporation from Arabian sea and the Indian southwest monsoon; *Proceedings of the symposium on the Indian Ocean expedition of meteorological results*; Meteorological Department, Bombay (India Meteorological Dept.) 43-54
- Pond S, Fissel D B and Paulson C A 1974 A note on bulk aerodynamic fluxes for sensible heat and moisture fluxes; *Boundary - Layer Meteorol.* **6** 333-339
- Ramesh Babu V and Sastry J S 1984 Summer cooling in the east-central Arabian sea - A preliminary study of the dynamic response to the southwest monsoon; *Mausam* **35** 17-26
- Rao D P, Sarma R V N, Sastry J S and Premchand K 1976 On the lowering of surface temperature over the Arabian sea with the advance of southwest monsoon; *Proceedings of the symposium on the Indian Ocean expedition of meteorological results*; (Pune: Indian Institute of Tropical Meteorology) 106-115
- Rao R R 1984 A case study on the influence of summer monsoon vortex on the thermal structure of the upper central Arabian sea during onset phase of MONEX-79; *Deep Sea Res.* **31** 151-164
- Rao R R, Somanadhan S V S and Nizamuddin S 1978 Study of the influence of surface energy fluxes on the north Indian ocean on the behaviour of Indian summer monsoon; *Indian J. Meteorol. Geophys.* **29** 253-258
- Reddy K G, Rao M V, Prasad P H and Rao G R L 1984a Net energy exchange at the surface of the Arabian sea during the summer monsoon; *Mausam* **35** 499-502
- Reddy K G, Rao M V, Prasad P H and Rao G R L 1984b Fluxes of sensible and latent heat over the Arabian sea during MONEX-79; *Indian J. Mar. Sci.* **13** 134-135
- Saha K R 1970 Zonal anomaly of sea surface temperature in equatorial Indian ocean and its effect on monsoon; *Tellus* **22** 403-409
- Saha K R and Suryanarayana R 1972 Mean monthly fluxes of sensible heat and latent heat from the Indian ocean; *J. Mar. Biol. Assoc. India* **14** 663-670
- Senguin W R and Kidwell K B 1980 Influence of synoptic scale disturbances on surface fluxes of momentum and sensible heat; *Supplement I to Deep Sea Res. Part A* **26** 51-64
- Shajahan Shah Md 1980 An evaluation of near surface fluxes of momentum, sensible and latent heat over the Arabian sea during the onset phase of monsoon; *Results of MONEX field phase research part A; FGGE Operations Report* **9** WMO, Geneva 187-206
- Smith S D 1974 Eddy flux measurements over lake Ontario; *Boundary - Layer Meteorol.* **8** 1-12

- Smith S D and Banke E K 1975 Variation of sea surface drag coefficient with wind speed; *Q. J. R. Meteorol. Soc.* **101** 665–673
- Weare B C 1983 Interannual variation in net heating at the surface of the tropical Pacific ocean; *J. Phys. Oceanogr.* **13** 873–885
- Wu J 1980 Wind stress coefficients over sea surface near neutral conditions – A revisit; *J. Phys. Oceanogr.* **10** 727–740

Geochemical studies on Kashmir loess profiles

G S LODHA, K J S SAWHNEY, H RAZDAN, D P AGRAWAL*
and N JUYAL*

Nuclear Research Laboratory, Bhabha Atomic Research Centre, Srinagar 190 006, India

*Physical Research Laboratory, Ahmedabad 380 009, India

MS received 3 July 1986; revised 21 May 1987

Abstract. Major and trace element concentrations of a few representative loess profiles in Kashmir valley are studied using EDXRF spectroscopy. Principal component analysis for pattern recognition has been employed to study association between elemental concentration variations in various horizons. The present study reveals that elements related to clay illuviation (K, Rb, Fe, Ti, Mn) and plant activity (Cu, Zn) are generally higher in B horizon of the palaeosols whereas Ca and Sr have a high concentration in the loess layers. Such an elemental concentration variation provides us with an objective index for identification and confirmation of palaeosols. There is further a close association in the movement of (i) K, Rb, (ii) Fe, Ti, Mn, (iii) Cu, Zn and (iv) Ca, Sr. These clusters of elements are also present in modern soils, suggesting that the soil characteristics in palaeosols have been preserved. Concentration of iron and titanium is also observed to be higher in loess profiles on Pir Panjal mountain flank which is dominated by basic rocks, compared to profiles on Himalayan flank, suggesting that the loess in Kashmir might have been derived from the nearby rocks in a localized way.

Keywords. Loess; palaeosol; energy dispersive X-ray fluorescence; principal component analysis.

1. Introduction

The late cenozoic Karewa deposits in Kashmir are the products of glacio-fluvio-lacustrine conditions and are capped by a mantle of aeolian loess deposits (Pant *et al* 1978; Agrawal *et al* 1979). The average thickness of loess deposits is ~ 25 m. A variety of techniques have been used to date these loess deposits. The loess deposits in the valley are possibly younger than 200 KYrs and lie in the upper part of Brunhes normal chron. Main loess palaeosol sequences have been dated using ^{14}C (Kusumgar *et al* 1980). The topmost palaeosol at Burazhom is dated at 18 KYr BP and the top soil at Khanchikhol I at 6 KYr BP. The ^{14}C dates lie in five main date clusters (table 1) (Kusumgar *et al* 1986).

We have used the energy dispersive X-ray fluorescence (EDXRF) technique to determine the concentration of major and trace elements in the loess palaeosol sequences of Kashmir valley. The technique has an advantage of multielement analysis of major and trace elements in a single run without any chemical treatment to the sample. We present the elemental data on loess profiles exposed at Burazhom, Wagahoma and Khanchikhol. The present study was undertaken with the following aims:

(i) To generate geochemical data which will aid in the investigation of the source of loess deposits in the Kashmir valley (Taylor *et al* 1983).

Table 1. Five main date clusters of ^{14}C dates of the Kashmir palaeosols.

C	$5,000 \pm 1000$ yrs.B.P.
C	$13,500 \pm 1500$ yrs.B.P.
C	$18,000 \pm 1500$ yrs.B.P.
C	$25,000 \pm 2000$ yrs.B.P.
C	$>31,000$ yrs.B.P.

(ii) Once the sediments are deposited they are subjected to local weather conditions. The weathering conditions depend to a great extent on the prevail climate. Major and trace elements in the loess palaeosol sequence would provide a measure of the weathering intensity which in turn can be used to obtain some information on the past climate of the region (Retallack *et al* 1984).

(iii) Traditionally, a vertical repetition of morphological features such as color, structure and compaction has been used to identify palaeosols buried in loess. We have instead attempted to use the major and trace elemental variation in a profile to distinguish various horizons. The elemental data approach for recognition of loess palaeosol horizons has earlier been used for loess in New Zealand (Childs and Searle 1975) and China (Qi-Zhong *et al* 1982).

(iv) Power spectrum analysis of geochemical data for loess has been carried out on Chinese loess (Qi-zhong *et al* 1984). We have used the principal component analysis (PCA) technique for statistical analysis of the multielement data. PCA is a good technique to describe the multidimensional data. The technique has helped us in identifying elements with similar collective behaviour and the identification of loess palaeosol horizons on the basis of collective behaviour has become more reliable compared to interpretation obtained on the basis of elemental concentrations seen in isolation.

2. Experimental technique

2.1 Sample preparation

The samples are dried in a hot air oven at $\sim 150^\circ\text{C}$. The dried samples are ground in an agate mortar and pestle. The sample is pelletized into a 30 mm dia. pellet at 3.9 ton per square cm pressure using a hydraulic press. The weight of the pellets is kept around 20 to 30 mg/cm^2 . As the samples contain large quantities of fine sand and clay, the pellets can be made without adding any binder. Standards for EDXRF analysis were synthesized by mixing pure element compounds in silicon dioxide matrix.

2.2 EDXRF spectrometer

The multielement analysis has been carried out on an EDXRF spectrometer (Bertin 1975) comprising a Si(Li) detector of resolution 155 eV at 5.9 keV. The excitation source used is a laboratory built transmission anode molybdenum X-ray

tube. The tube gives photon flux of MoK lines with very little continuum bremsstrahlung background. The multielement data are acquired on a pulse height analyzer (ECIL 4K). The data are analysed on the on-line data processing system consisting of a micro-computer (HCL MICRO-2200) with a floppy disk attachment.

2.3 Quantitative estimation method

We have used the Compton-scattered radiation standardization for quantitative estimation of analytes in the sample (Nielson 1979). The experimental Compton peak normalized excitation efficiencies were obtained using synthetic standards prepared in silicon dioxide matrix. For matrix absorption correction we have used the effective mass absorption cross-section (μ_{eff}) of the sample (Van Dyck and Van Grieken 1980). The (μ_{eff}) at various energies was obtained in an iterative loop using the tabulated mass absorption cross-sections (McMaster *et al* 1969). The initial estimate of (μ_{eff}) was obtained assuming the sediment matrix to be composed of SiO_2 and Al_2O_3 in the ratio of 80:20. Once the estimates of the major elements present in the sample are obtained the new (μ_{eff}) is computed. This procedure is repeated till a converging (μ_{eff}) is obtained. The final (μ_{eff}) is used to compute the absorption correction term for each analyte in the sample. This quantitative estimation procedure was tested for a large number of synthetic standards and accuracies better than 10% were obtained.

For the interpretation of multielement data at various sections, principal component analysis technique (Llinas and Ruiz 1986) was adopted. The reliability of the technique is apparent from its capability to characterize loess palaeosol sequences from the multielement data despite the fact that the sections have undergone post-depositional changes. The technique involves reduction of the elemental data set with a large number of variables (which are often correlated and sometimes redundant) to smaller number of independent variables. Furthermore, the analysis provides a graphical representation of objects and variables in a vector subspace with reduced number of dimensions. In our analysis we have used concentration values of K, Ca, Ti, Mn, Fe, Cu, Zn, Rb and Sr obtained from EDXRF analysis. The concentration of Ni and Br has not been included in the analysis due to high estimated errors in their concentration. The two major principal components account for 75% to 80% of the features in all the sections which is adequate for the interpretation of geochemical data on loess palaeosols.

3. Observations

We have studied the geochemical profiles of seven loess sections in Kashmir valley (figure 1 and table 2). However, here we present three representative loess sections namely, Burazhom, Wagahoma and Khanchikhol II. Burazhom and Wagahoma are plateau loess profiles on the Himalayan flank. The thickness of loess profiles on this flank varies from 6–20 m and they rest on upper Karewa laminated silt members. Khanchikhol II is a plateau loess section on the Pir Panjal mountain flank exposed by streams of recent origin (Khol is a Kashmiri term for stream). The loess sections on this flank are generally 20–25 m thick and rest on lower Karewa gravel

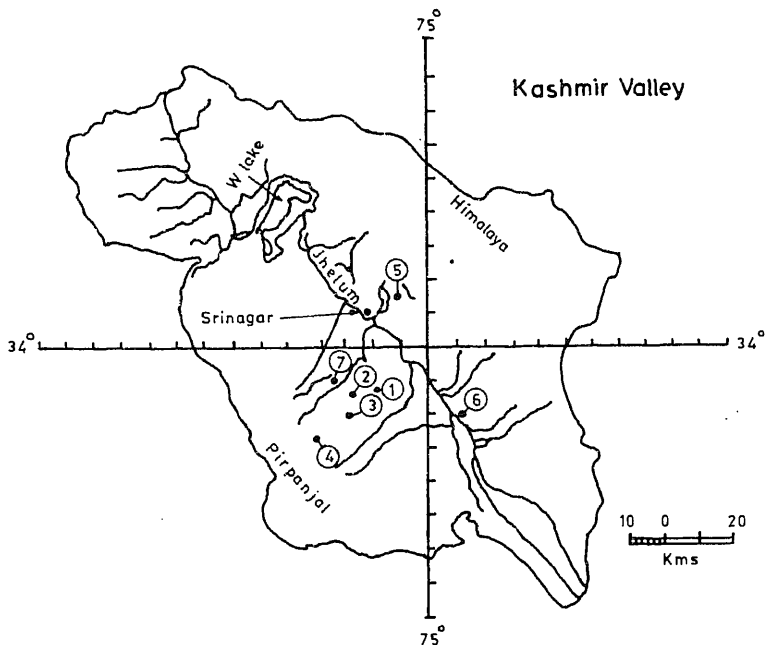


Figure 1. Map of Kashmir valley showing loess sections undertaken for geochemical studies using EDXRF spectrometer.

Table 2. Loess sections undertaken for geochemical studies.

Section	Location	Altitude (metres)	Thickness (metres)
Burzahom	E 74°53' N 34°30'	1620	6
Wagahoma	E 74°0'99'' N 33°46'	1700	21
Khanchikhol I (Karpura)	E 33°50' N 74°47'	2000	23
Khanchikhol II (Malpura)	E 33°54' N 74°49'	1740	22
Romu	E 33°53' N 74°50'	1850	22
Kanier	E 74°30'65'' N 33°45'94''	1800	20
Dilpur	E 74°57' N 34°30'	1800	19

beds. The stratigraphy of the main sections studied has been drawn according to our field observation. The various horizons have been marked on the basis of colour, structure, compaction and morphological features.

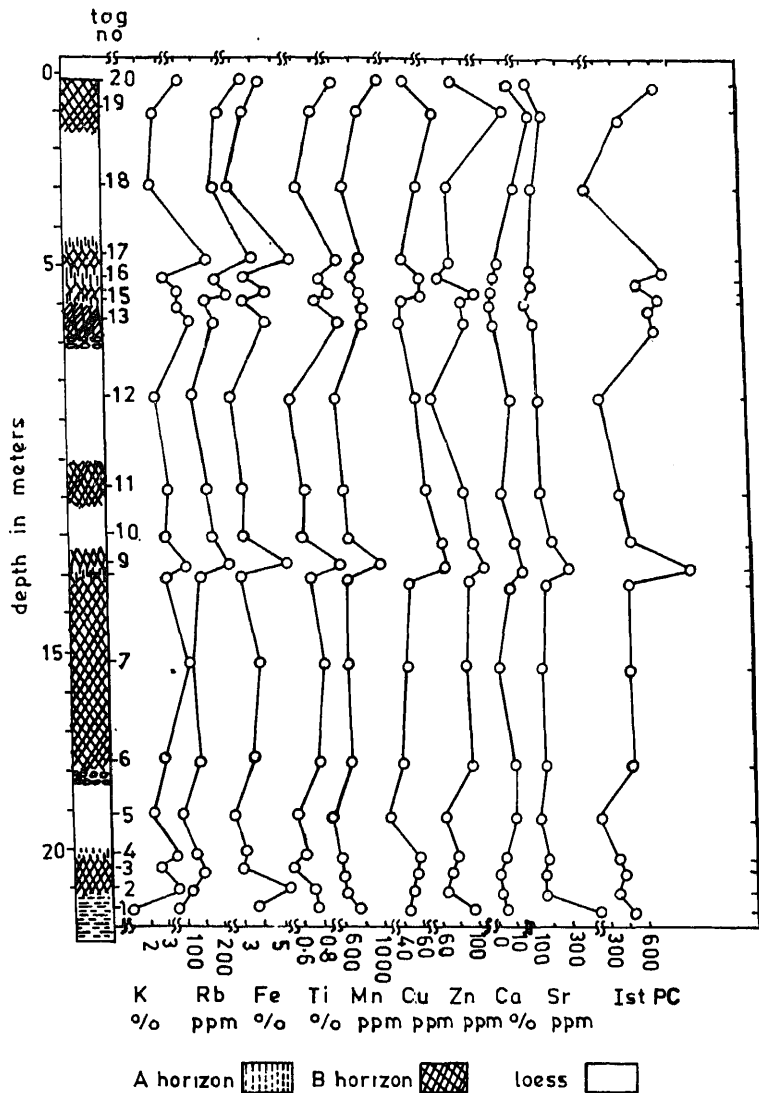


Figure 2. Wagahoma loess field stratigraphy, variation of various elemental concentrations and the first principal component.

3.1 Wagahoma loess profile

Wagahoma loess section near Brijbihara on Jammu Srinagar highway, is 21 m thick and located on the Himalayan mountain flank. Figure 2 shows the field stratigraphy, the variation of various elemental concentrations and the variation of the first principal component in the various horizons. The main results are summarized below:

- (i) The concentrations of K, Rb, Fe, Ti and Mn are generally higher in B horizons of the palaeosols compared to the A horizon and the loess.

(iii) The loess layer between 10 and 11.25 m was marked as doubtful B horizon during our field observation as it appeared slightly darker in colour with low secondary calcium carbonate. However, the elemental concentration values as also the values of first principal component for this horizon are similar to the loess horizon above and below it. Thus elemental data help in identifying it correctly as part of the loess.

(iv) The average value of Fe is $\sim 3.8\%$ and Ti is $\sim 0.8\%$.

(v) For this section the first principal component is high for B horizons of the palaeosol and low for the loess. The first and the second principal components account for 46% and 28% of the total variance respectively. The variation of concentration of K, Rb, Fe, Ti and Mn dominates in the first principal component while Ca and Sr variation dominates in the second principal component. Thus instead of seeing the variation of all the individual elemental concentrations in the horizons, the variation of the first and the second principal component with horizon gives their diagnostic characteristics.

(vi) The results for the association in movement among the elements in various horizons are shown in figure 3 by the variation in latent vector 1 (LV1) vs latent vector 2 (LV2). The clusters of elements with similar variability in concentration are (i) K, Rb, (ii) Fe, Ti, Mn, (iii) Cu, Zn and (iv) Ca, Sr.

(vii) These clusters show that the movement of elements within these groups follows a similar chemistry. The associated movement of the elements mentioned in the above groups occurs in the modern soils because of similar chemical changes they undergo under various stages of weathering. The principal component analysis brings out the above association for loess palaeosol sequences suggesting that the section has probably not undergone considerable post-depositional reworking.

3.2 Burazhom loess profile

This section is ~ 20 km northeast of Srinagar on the Himalayan flank. The section has already been studied for stable isotope ratios of carbon to study the pleistocene climatic changes (Krishnamurthy *et al* 1982). The palaeosols at 3.5 m and 4.5 m

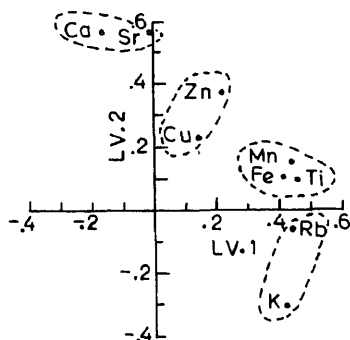


Figure 3. Two major latent vector plots for Wagahoma loess section.

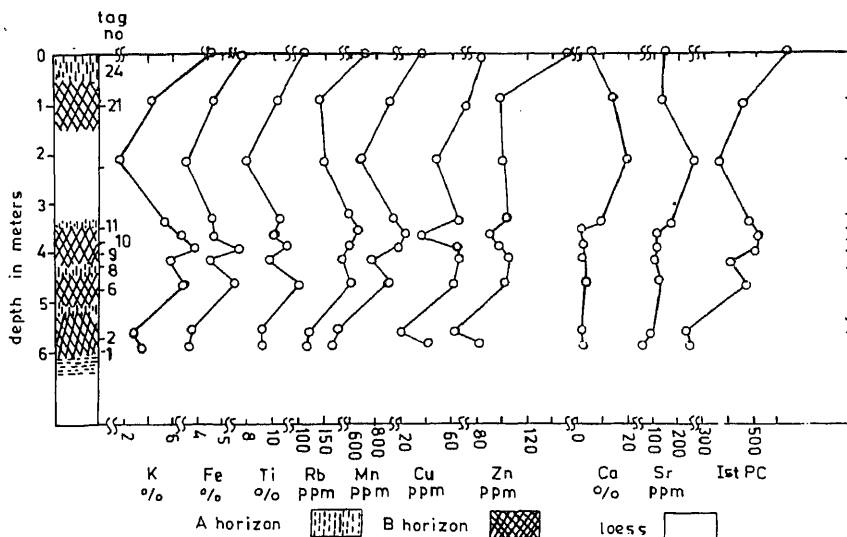


Figure 4. Burazhom loess field stratigraphy, variation of various elemental concentrations and the first principal component.

have been dated at 18 KYr BP and 31 KYr BP respectively using ^{14}C technique. The field stratigraphy, the concentration profiles of various elements and the variation of first principal component are shown in figure 4. The main results are summarized below:

- (i) The B horizons of the palaeosols are marked by generally high concentration of K, Rb, Fe and Ti compared to A horizons and the loess. The low concentration values of K, Rb, Fe and Ti in the bottom-most B horizon (tag no. 2) are probably due to the fact that this B horizon got mixed with laminated silt members, and some of these elements got removed in lacustrine environment.
- (ii) Calcium is high in loess layers and low in palaeosols.
- (iii) The average Fe concentration is $\sim 4.5\%$ and the average Ti concentration is $\sim 0.9\%$.
- (iv) The first principal component accounts for 60% of the total variability in concentration of the elemental data set. It is high for palaeosols and low for loess. The maximum contribution in the variation of the first principal component for this section comes from the variation in concentration of K, Rb, Fe and Ti. Ca and Sr variations are dominated in the principal component 2.
- (v) The clusters of elements with similar variability in concentration are (figure 5) (i) K, Rb, Fe, Ti, (ii) Mn, Cu, Zn and (iii) Ca, Sr.
- (vi) The clustering of various elements is not so well as in the Wagahoma section because the number of variables is equal to the number of samples while for optimum class separation the number of samples should be much larger than the number of variables. This is probably the reason why Mn does not fall in the Fe, Ti cluster as seen for all other sections.

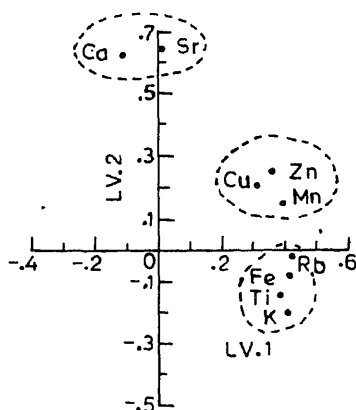


Figure 5. Two major latent vector plots for Burazhom loess section.

3.3 Khanchikhol II loess profile

This plateau loess section is ~ 22 m thick and is located on the Pir Panjal mountain flank. The section is situated at Malpura which is ~ 3 km north of Pakharpura and ~ 4 km southwest of Pulwama. The field stratigraphy, concentration profile of various elements and the variation of first principal component are shown in figure 6. The main results are summarized below:

(i) The B horizons between 0.75 and 2.5 m, 6.25 and 6.75 m and 15.5 and 19.0 m are accumulation horizons for K, Rb, Fe, Ti and Mn. The horizon marked B at 13–14 m does not however act as the accumulation zone for these elements. Rather the accumulation takes place in the horizon marked loess at 14–15 m on the basis of field observation. It appears that the field stratigraphy for this horizon has to be modified with A horizon extending down to 14 m and the horizon between 14 and 15 m should be marked as B rather than a loess horizon. This inference drawn from the elemental data is further supported by mineral magnetic analysis (Agrawal *et al* 1986).

(ii) The horizon marked loess was observed in the field to be highly weathered. For this horizon, Ca, Sr, Fe, Ti and Mn are observed to be high. High Ca and Sr are due to a thick carbonate nodular horizon above this horizon but the high concentration of Fe, Ti and Mn suggests accumulation of the elements during secondary weathering process.

(iii) The average concentration of Fe is ~ 5.5% and that of Ti is ~ 1.2%.

(iv) The first and the second principal component account for 56% and 25% of the variance respectively.

(v) The principal component analysis for associations among elements show the following groupings (figure 7): (i) K, Rb, (ii) Fe, Ti, Mn, (iii) Cu, Zn and (iv) Ca, Sr.

4. Conclusions

The main conclusions drawn from the present study are:

(i) The elemental analysis of loess palaeosols reveals that elements related to clay

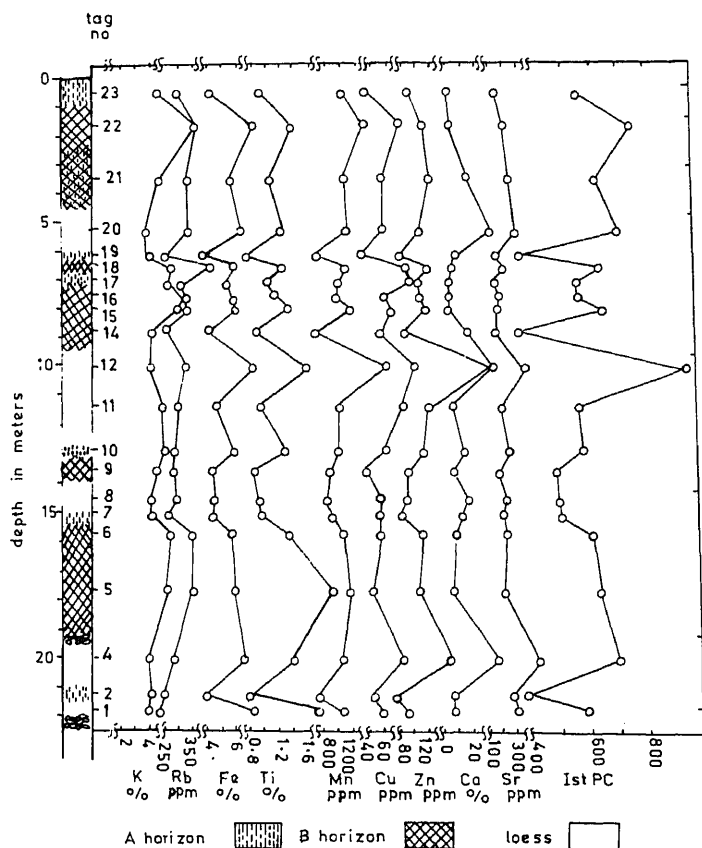
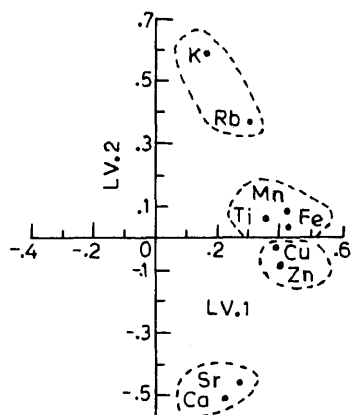


Figure 6. Khanchikhol II loess field stratigraphy, variation of various elemental concentrations and the first principal component.



illuviation (K, Rb, Fe, Ti and Mn) are generally higher in B horizons of palaeosols whereas Ca and Sr are low in palaeosols compared to the loess layers. The concentration of these elements in palaeosols is closely related to the process of soil formation.

(ii) Palaeosol horizons which are rich in clay fraction (B horizons) are generally high in K concentration. This is due to the fact that K gets fixed in the inter-layer spaces of the clay minerals. Likewise the behaviour of Rb in the soil-forming process is controlled to a large extent by its absorption in clay minerals. Illites and montmorillonites are common clay minerals that absorb K and Rb which explain the high concentration of K and Rb in B horizons of the palaeosols. The concentration of Fe, Ti, Mn and Cu, Zn in palaeosols is controlled by clay minerals and organic activity of plants. The mechanisms include surface adsorption and penetration to the interior of the crystals. Ca and Sr have a high leaching rate and get deposited below the B horizon of the palaeosol in the loess layers.

(iii) The principal component analysis for the associations among elements reveals that despite some post-depositional perturbations there is a close association in the movement of the elements such as (i) K, Rb, (ii) Fe, Ti, Mn, (iii) Cu, Zn, (iv) Ca, Sr. These associations are not obvious from the individual elemental concentration data seen in isolation. As these associations are also observed in modern soils due to their similar chemistry during various stages of weathering, the results suggest that the palaeosols have preserved the soil characteristics to a large extent.

(iv) The concentration of Fe and Ti is high in loess profiles on the Pir Panjal mountain flank compared to the Himalayan flank. The average Ti value for the Khanchikhol II loess section is ~ 1.2% which is higher than that for the Wagah and Burzahom loess section on the Himalayan flank (Ti ~ 0.8%). Likewise the average Fe value for loess profiles on the Pir Panjal flank (Fe ~ 5.5%) is higher than the value for the Himalayan flank (Fe ~ 4.5%). Further the movement of Fe and Ti is closely correlated in our data, suggesting the presence of ilmenite (FeTiO_3). The Pir Panjals are dominated by basic igneous rocks which usually have a relatively high concentration of ilmenite. The Himalayan flank is made up of limestone which generally has lower concentration of Ti. Thus it appears that the source material for the loess deposits at various sections was derived from the nearby rocks.

Acknowledgements

We thank C K Bhat and S S Choudhary for their help in the analysis of samples. Thanks are due to Drs B S Kotlia, R Dodia and P Sharma for help rendered in sample collection and for discussions. We thank Shri J Arunachalam and Gangadharan for providing software for principal component analysis.

References

- Agrawal D P, Krishnamurthy R V, Kusumgar S, Nautiyal V, Athavale R N and Radhakrishnamurthy V (1979) Chronostratigraphy of loess and lacustrine sediments in the Kashmir valley; *Acta Geol. Sci. Hungary Thmus* 22 185-196

- Agrawal D P, Juyal N, Kusumgar S and Sharma P 1986 A mineral magnetic study to characterise loess palaeosol sequences in Kashmir, *Proc. of National Workshop on EDXRF/PIXE Techniques and their Applications*, Srinagar (in press)
- Bertin E P 1975 Pulse height selection; energy dispersive analysis; non-dispersive analysis in *Principles and practice of X-ray spectrometric analysis* (New York: Plenum Press) 2nd ed. Ch 8
- Childs C W and Searle P L 1975 Elemental distribution in loess columns at Claremont table flat and Stewarts Clain, New Zealand: *N.Z. Soil Bureau Sci. Rep.* **20** 1-59
- Krishnamurthy R V, DeNiro M J and Pant R K 1982 Isotopic evidence for paleistocene climatic changes in Kashmir, India: *Nature (London)* **298** 640-641
- Kusumgar S, Agrawal D P and Krishnamurthy R V 1980 Studies on the loess deposits of the Kashmir valley and ^{14}C dating; *Radiocarbon* **22** 757-762
- Kusumgar S, Agrawal D P, Juyal N and Sharma P 1986 Palaeosols within loess: dating palaeoclimatic events in Kashmir; *Radiocarbon* **28** 561-565
- Linias J R and Ruiz J M 1986 Multivariate analysis of chemical data sets with factor methods, in *Computer aids to chemistry* (eds) G Vernin and M Chanon (Chichester: Ellis Horwood Limited) ch 5
- McMaster W H, Del Grande N K, Mallett J H and Hubbell J H 1969 Compilation of X-ray cross sections Sec 2, Rev 1, Univ. of California, Livermore, U.S. At. Energy Comm. Rep. UCRL-50174
- Nielson K K 1979 Progress in X-ray fluorescence correction method using scattered radiation; *Adv. X-ray Anal.* **22** 303-315
- Pant R K, Agrawal D P and Krishnamurthy R V 1978 Scanning electron microscopy and other studies on the Karewa beds of Kashmir, India; in *Scanning electron microscopy in the study of sediments* (ed) W B Whalley (Norwich: Geol Proc) p 275-282
- Qi-zhong W, Gui-yi D, Su-hua Y, Fu-ying S, Xiong-fee G, Qing-mu C and Yu-lan L 1982 Some problems of loess geochemistry in China; in *Quaternary dust mantles of China, New Zealand and Australia*, (ed.) R J Wasson (Canberra: Australian National University) p. 69-83
- Qi-zhong W, Wei-hua Y, Gui-yi D, Fu-qing S, Su-hua Y and You-mei L 1984 The evolution of chemical elements in loess of China and palaeoclimatic conditions during loess deposition; in *Lithology and stratigraphy of loess and palaeosols* (ed.) M Pecs (Budapest: Geographical Research Institute) p. 161-169
- Retallack G, Grandstaff D and Kimberley M 1984 The promise and problems of precambrian palaeosols; *Episodes* **7** 8-12
- Taylor S R, McLennan S M and McCulloch M T 1983 Geochemistry of loess, continental crustal composition and crustal model ages; *Geochem. Cosmochem. Acta* **47** 1897-1905
- Van Dyck P M and Grieken R E V 1980 Absorption correction via scattered radiation in EDXRF analysis for samples of variable composition and thickness; *Anal. Chem.* **52** 1859-1864

On global summer monsoonal drought mechanics

M SANKAR-RAO and S V SACHIDANANDA

Department of Aerospace Engineering and Centre for Atmospheric Sciences, Indian Institute of Science, Bangalore 560 012, India

MS received 8 August 1986; revised 14 April 1987

Abstract. It is shown that within the framework of a linear five-level quasi-geostrophic steady state global model the middle latitude systems can always have significant influence on the Asian summer monsoonal system through the lower tropospheric monsoonal westerly window region around 80°E . It is hypothesized that quasistationarity of the middle latitude longwave systems results in stronger teleconnections through this window and the consequent monsoon breaks when the phase is right.

Keywords. Monsoon; break; Rossby waves; middle latitudes; teleconnections.

1. Introduction

It is well known that the Asian summer monsoon, which is an important feature of global climate during June to September exhibits interesting interannual variations. The rainfall for some years is well distributed spacially and is normal or above normal while for some years it is below normal and spacially distributed differently from the normal years. Such years with below-normal rainfall are termed by Asian meteorologists as 'drought years' or 'bad monsoon' years. The anomalies for drought situation over Indian region were studied extensively by a number of workers (Ramamurty 1969; Joseph 1978; Alexander *et al* 1978). The main observations for drought situation are that (i) the rainfall is well below normal or completely absent over north Indian plains region, (ii) the surface pressure shows a positive anomaly of about 2 mb over this region, (iii) the westerlies replace the easterlies in the lower troposphere over this north Indian region, (iv) the temperature shows a negative anomaly of about 1°C over the north-west Indian region, (v) this 'drought' situation or 'break monsoon' situation is a temporal phenomenon, the break lasting from a period of about a week to about three weeks after which the monsoon may revive again and (vi) the wave numbers of the intruding midlatitude Rossby waves, when such intrusion occurs during the break, are about 5 to 10 around the globe.

Any dynamic theory must be able to explain eventually all the above general quantitative findings. The mechanics of such an abnormal monsoon is not yet known. A perusal of the linear and nonlinear general theory of monsoon tells us that the abnormalities in the monsoons can be due to abnormalities either in the zonal global general circulation, diabatic heating pattern or in transient effects. Almost all the hypotheses advanced till now for monsoon drought mechanics are based on the fundamentals of the above said general theory of monsoons. There are at present three different lines of thought, all still in a speculative stage. They

can be categorized as the SST-based Walker teleconnection hypothesis (SSTWTC), tropical internally forced or free oscillation hypothesis (TIFFO) and latitudinal teleconnection hypothesis (LTC).

We shall briefly describe the idea of each hypothesis and the work done in that regard.

2. Hypotheses

2.1 SSTWTC hypothesis

The idea behind this hypothesis is based on the classical work of Bjerknes (1969) who found that the thermal equator is characterized by longitudinal Walker cells with rising limbs over the warm waters of the western Pacific and the corresponding sinking limbs over cooler oceanic waters about 50° to the east and to the west. For any reason, if the warm centre shifts towards the east by about 10 to 15° , the Indian subcontinent comes under the sinking limb and there can be a widespread drought. Kanamitsu and Krishnamurti (1978) working with the best available data showed such an eastward shift of the Tibetan anticyclone. They even suggested a chain mechanism (warmer waters over west equatorial pacific, more typhoons, more upper level divergence and hence such an eastward shift of Tibetan anticyclone) for such a shift.

Another important observation in this regard is that the El Niño years are correlated with drought years. The ENSO was observed to show a positive correlation with the monsoon drought (Angell 1981; Rasmusson and Carpenter 1982; Shukla and Paolino 1983). Whether such a connection is a direct longitudinal Walker connection or a more complicated connection via the general circulation (see Wallace and Gutzler 1981; Simmons 1982) is not yet known.

The implication of the above hypothesis is that the SST controls the monsoon variability and hence the forced monsoon predictability is much longer than the dynamic predictability limit.

2.2 TIFFO hypothesis

According to this, the monsoon is modulated by tropical modes such as 30–50 day mode or 10–20 day mode. The 30–50 day mode was observationally documented. (cf. Madden and Julien 1971; Sikka and Gadgil 1980; Krishnamurti *et al* 1984; Murakami and Nakazawa 1984). Krishnamurti and Subrahmanyam (1982) showed that the trough and ridge lines of 30–50 day mode coincide with the active and break monsoon conditions. This mode was observed to be of a global scale with a zonal wave number one, a wind amplitude of 3 to 6 m sec^{-1} .

Webster and Chow (1980) and Goswami and Shukla (1984) simulated the 30–50 day mode as a result of forcing feedback mechanism such as cloud radiation feedback and hydrology, and radiation dynamics feedback.

The implication of such an internal oscillation and modulation hypothesis is that the monsoon every year is expected to have active and break spells at quasi-periodic intervals. The active and break spells are but natural quasi-cyclic phenomena and so are predictable, hopefully, in a quasi-periodic sense at least.

2.3 LTC hypothesis

The main idea behind this hypothesis is that the monsoon breaks are due to direct interaction of midlatitude circulation with the monsoon circulation. Ramaswamy and co-worker first observed (Ramaswamy 1962; Ramaswamy and Pareek 1978) that during a monsoon break the midlatitudes enter a strong low index regime and the Rossby waves propagate into the monsoon region, dramatically modifying the rainfall pattern. If a trough intrudes into the Indian region, major parts of the central and western India fall under the rear part of the trough where air descends and hence a dry spell starts. To the east of the trough where air ascends, rainfall will be good. Due to the cold air advection from the north, the temperatures are below normal over North India during such spells. Normalcy returns after the passage of such a trough. As an example, we give in figure 1, the 500 mb map for a severe drought day of 1979 for which year the drought period was from 15th to 31st August. One can easily see the intrusion of these waves and the strong interaction with the monsoon circulation. We notice a huge ridge situated over Scandinavia and the corresponding trough over Asia and the resulting strong interaction between middle latitudes and the Asian monsoon system. Another possibility suggested by Pant (1983) was that these waves drive a mean meridional circulation by their transient forcings at the northern boundary of the monsoon system, and this mean meridional circulation is opposite to that of normal monsoon. However the computed vertical velocities due to transient forcing given by Pant are too weak to make any difference when compared with the normal ones.

The implication of the Rossby wave interaction hypothesis discussed above is that the monsoon prediction is closely linked to the general circulation prediction and hence the predictability of the monsoon is only as good as that for middle latitude phenomena.



Figure 1. 500 mb contours for the intense drought day 20th August 1979 (Synoptic Bulletin, USSR)

The theoretical works of Charney and Drazin (1961), Booker and Bretherton (1967), Lindzen and Holton (1968), Charney (1969), Mak (1969), Bennet and Young (1971), Opsteegh and van Den Dool (1980), Branstator (1983) and Nigam and Held (1983) suggest that the Rossby wave energy cannot cross the zero wind line and hence the tropics are insulated from extratropics in the wave number domain. Webster and Chow (1980) showed that waves of the right wavelength can pass through window regions. Gille (1968) also expected the same much earlier basing on physical results of optics and quantum mechanics. Thus the overall theoretical results show that the Rossby waves can interact with tropics under special conditions.

The Asian monsoon system is characterized by westerly winds in the lower troposphere over large parts of tropical Asia around 80°E. Besides, the important heat sources of the monsoon system such as the Saharan heat source, Arabian heat source and the Thar heat source are all located at the boundary between global westerlies and easterlies. These two special characteristics of the Asian monsoonal system can give rise to sensitive interactions between the monsoon system and the midlatitude systems through the window region around 80°E (see figures 4a and 4b).

This study is aimed at probing such a possibility in realistic situations. The method adopted is very simple. A five-level global spherical quasi-geostrophic linear model is adopted. Northern middle latitudes were perturbed by the lower boundary mountain forcing at one latitude. The effect of such a perturbation, especially over tropics, was computed. Sensitivity experiments were performed. Finally it was shown that during the monsoon season, the interaction between middle latitudes and the monsoon system is always possible in the wave number domain.

3. The model equations and solutions

The master potential vorticity equation for this linear quasi-geostrophic model is the one given by Saltzman (1965, 1968) It can be written as

$$\nabla^2 v_* + S_1 \frac{\partial^2 v_*}{\partial \xi^2} + S_2 \frac{\partial v_*}{\partial \xi} + S_3 v_* = \frac{CFR}{m U_0} + a \cos \phi \nabla^2 v_* + G_*,$$

where any axially asymmetric perturbation-dependent variable D_* is expanded as

$$D_* = \tilde{D} \exp (i m \lambda).$$

The corresponding top and bottom boundary conditions can be written as

$$(\partial v_* / \partial \xi) + b v_* = d H_{*T} \text{ at } \xi = \xi_T, \quad (1a)$$

$$\begin{aligned} & \frac{\partial v_*}{\partial \xi} + B v_* + \frac{\nu}{a \cos \phi} \left[\frac{\partial v_*}{\partial \lambda} + \frac{\partial}{\partial \phi} \cos \phi \frac{\partial}{\partial \phi} \int v_* \cos \phi d \lambda \right] \\ & = - \frac{M}{a \cos \phi} \frac{\partial h_*}{\partial \lambda} + N H_* \text{ at } \xi = \xi_\delta. \end{aligned} \quad (1b)$$

The symbols are described in Appendix 1. At the north and south poles the boundary conditions are

in the above system for the boundary conditions (1a) and (1b), the equator is a singular point. Hence at the equator the corresponding boundary conditions at ξ_T and ξ_δ are taken as

$$v_* = 0 \text{ at the equator at } \xi = \xi_T \text{ and } \xi_\delta \quad (1d)$$

Note that (1d) is used only at the lower and upper boundaries at the equatorial grid point. The first term on the right side of (1) represents Rayleigh friction with the coefficient of friction CFR . G_* represents all other forcings due to orography, diabatic heating and transient eddy effects described in detail by Saltzman. The third term on the left side of (1b) represents Ekman frictional effect while the first term on the right side of (1b) represents mountain effect in a simplified form.

The zonal mean state parameters U_0 and T_0 and the forcings are the inputs for (1). The master equation (1) is not separable and has a singular point at $U_0 = 0$ for inviscid case. In numerical finite difference models it is implicitly assumed that the solution is continuous across such singular zones which are made to lie between grid points only. This is a drawback of discrete grid models like the one adopted here for inviscid cases. Because (1) is quasi-geostrophic, it cannot be a good approximation very near the equator. However, beyond $\pm 5^\circ$ from the equator it can be expected to be accurate enough for Rossby wave description e.g. Matsuno (1966). The homogenous part of (1) possesses eigenmodes and hence for forcing corresponding to these eigenmodes there can be resonance. However one cannot be certain without actual computation whether or for what location or distribution of forcing such resonance occurs when one considers realistically observed zonal mean states. The response and resonance point depend critically on the upper boundary condition (see Smith 1979).

To study such questions, utilizing (1) we have adopted finite difference techniques. Two different techniques, one being a direct method given by Richtmyer and Morton (1967) and the other being an iterative conjugate gradient method for sparse matrices given by Jacobs (1981) were tried. The iterative method did not converge for some wave numbers for reasons not yet understood, while the direct method gave solution for all waves comparatively very fast. However for those waves for which the iterative method converged, the two methods gave almost identical solutions. In all the experiments to be described here, the direct method was adopted due to its greater efficiency as stated above.

Regarding the grid, we conducted a few sensitivity experiments with 10° , 5° and 2.5° horizontal (North-South) resolution. In all other experiments we used only the 2.5° grid. In the vertical, we considered only five levels (900, 700, 500, 300, 100 mb). Centred finite differences internally and one-sided differences at the top and bottom boundaries were utilised. In all the experiments reported here, we took $f = 10^{-4} \text{ sec}^{-1}$ and $-10^{-4} \text{ sec}^{-1}$ in the northern and southern hemispheres respectively. At the equator $f = 0$. β was taken as constant equal to $1.7 \times 10^{-11} \text{ m}^{-1} \text{ sec}^{-1}$. The Ekman frictional parameter $\nu = 0$ in all the experiments. The effects of changing these parameters more realistically will be studied later. For the Rayleigh friction parameter CFR , we took a constant value of 10^{-6} sec^{-1} which corresponds to a time constant of about 10 days. For all waves the amplitude of the topography is taken as a constant (200 meters) to have a comparison with the earlier results of Saltzman. The form of the orography is taken as $A \cos m\lambda$ where A is

4. Some test experiments and results

Experiment 1. The input zonal mean state for this experiment is taken from the data given by Oort (1983) at every 5° for winter season. The resolution of the grid is 10° in the north-south. The mountain is placed at 45°N and the friction is suppressed. The results of this experiment will only be mentioned without showing any figures. We noticed from the results that the phases, the general magnitudes and the nodal lines in the vertical are all in general agreement with the earlier results of Saltzman. As we progress from wave number 1 to wave number 5, a vertical node descends and disappears at wave number 5. For higher wave numbers the response is damped in the vertical. However, even for wave number 10, this damping is not really very high for winter season. The geopotential amplitude sections show that only the sub-critical ultralong waves establish global teleconnections whereas supercritical long waves have local effects only. The wave numbers 4 and 5 appear to be quasi-resonant with maximum v_* response of 1 m sec^{-1} and 2 m sec^{-1} respectively. The results of this experiment show that the numerical results obtained here are in line with the earlier detailed results of Saltzman for a model for which the zonal mean state was only a function of p but not a function of ϕ .

Experiment 2. For this experiment we included the Rayleigh friction ($CFR = 10^{-6} \text{ sec}^{-1}$) keeping everything else the same as in experiment 1. For this experiment also, the results will only be mentioned without showing any figures. The results show in general, slightly reduced amplitudes. However in the cases of $m = 2$ and 3, significant amplitude amplification as compared to experiment 1 can be noticed, mainly because of a kind of quasi-resonance at about 15°N . Rayleigh friction, thus in this case, amplifies the response in some places. Such a thing can happen due to slight shifts introduced in the eigenvalues by the Rayleigh friction. This result indicates that the resonant mode need not be determined by the structure at the forcing latitude but may be determined by the structure at a latitude which is closest to resonance. However this point has to be further looked into.

Experiment 3. For this experiment, we changed the grid resolution to 5° interval and used $CFR = 0$. Everything else is kept the same as in experiment 1. The geopotential amplitude response for this experiment will be described now without showing any figures. The response for wave number 2 is different compared to that of experiment 1. For $m = 4$ and 5, again the solution shows a sort of quasi-resonance as in experiment 1. These results indicate that for at least some wave numbers the results are grid sensitive.

Experiment 4. For this experiment everything is kept the same as in experiment 3 except that $CFR = 10^{-6} \text{ sec}^{-1}$. The results will only be mentioned briefly. The response for $m = 2$ is very much diminished compared to experiment 3. Again the wave numbers 4 and 5 show a quasi-resonant character as in the earlier experiments.

Experiment 5. In this experiment, we used 2.5° grid with $CFR = 0$. The results will only be described here briefly. Again for $m = 4$ and 5 there appears to be a sort of

quasi-resonance. But for all other wave numbers, including $m = 2$, the response is weaker compared to 5° grid experiment 3.

Experiment 6. In this experiment everything is kept the same as in experiment 5 except that $CFR = 10^{-6} \text{ sec}^{-1}$. We only describe the results here. For all wave numbers the response is weaker compared to experiment 5. There are no dramatic differences between experiments 5 and 6. Hence the results of 2.5° grid seem to be less sensitive to frictional effects compared to 10° and 5° grid results. For this reason for all the experiments hereafter, only 2.5° grid was used.

Experiment 7. To see how different the response can be for an individual month in a season compared to that of the season, we performed this experiment. In this the monthly mean state is that of January and $CFR = 0.0$. The results are given in figure 2. The results are qualitatively similar to those of the season, but in January the response is stronger, especially for the resonant wave number 4.

Experiment 8. This experiment is for July mean state for 2.5° grid, with $CFR = 0$. The results are given in figure 3. The most interesting aspect about this figure is that all ultra long waves seem to be equally important. The response is weaker than for winter. For $m = 2$ and 4 the response near 25°N is comparable to that of middle latitude response.

Experiments for contrasting drought and good monsoon months

In the following experiments, we took August 1965 as the representative drought month (break from 4th to 15th August). We considered August 1963 as a good monsoon month because the rainfall records show that the precipitation distribution was normal in August 1963. We have also taken from published data records the monthly mean upper air station data around 80°E longitude as representative of the monthly mean state over Asia. The mean structure for August 1965 and 1963 is given in figure 4. Note that over $25-32.5^\circ\text{N}$ in August 1965, the westerlies prevail in the lower troposphere. In 1963 August there are easterlies right up to the ground level about $25-32.5^\circ\text{N}$. The westerlies to the south are stronger for 1963 than for 1965 indicating a stronger monsoon current. We conducted the following experiments.

Experiment 9. This is for August 1965 with 2.5° grid and $CFR = 0$. The results are given in figure 5. One can see that $m = 7$ is a resonant mode. In general, the perturbation amplitude at about 20°N is about 20% of that at 45°N for many waves. Higher wave numbers such as $m = 9$ and 10 show no influence at 20°N .

Experiment 10. To see what happens if we shift the forcing to 30°N , we conducted this experiment. The mountain of the same amplitude of 200 m is placed at 30°N which is the general latitudinal location of the Himalayas. Everything else is kept the same as in experiment 9. The results are given in figure 6. Not only do we find dramatic differences for many waves but we get a catastrophic resonance for $m = 7$ which was also resonant in the earlier experiment in which the forcing was at 45°N . The influence on the tropics is much more enhanced in this experiment in general.

Experiment 11. This experiment is conducted with 1963 August mean data. The results are given in figure 7. Due to the stronger westerlies to the south of 25°N indicating strong monsoon current, the perturbations are stronger compared to

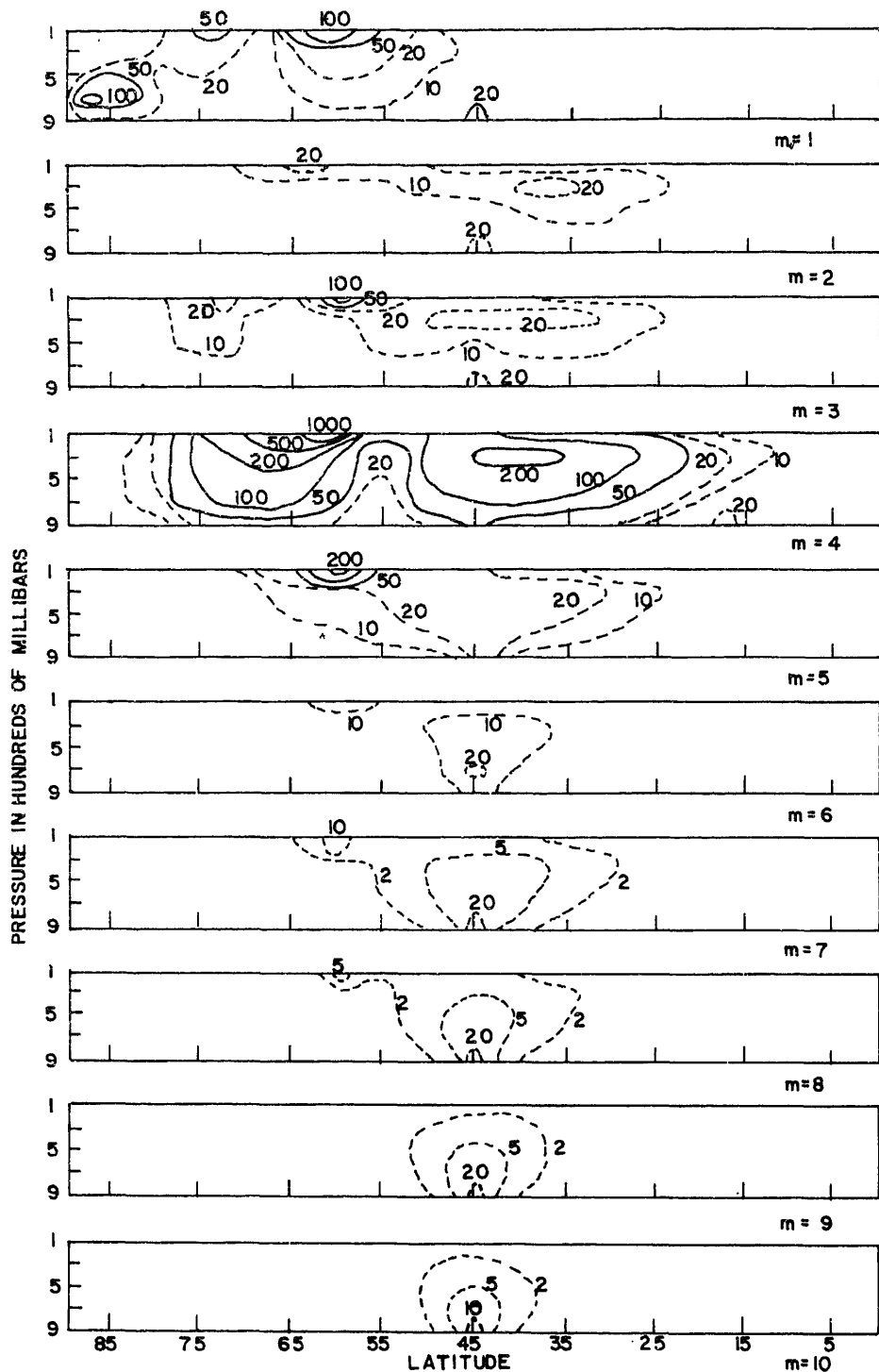


Figure 2. Geopotential amplitude response for different wave numbers (m) for 2.5° grid, in $\text{m}^2 \text{sec}^{-2}$ for January for $\text{CFR} = 0.0 \text{ sec}^{-1}$ with forcing at 45°N .

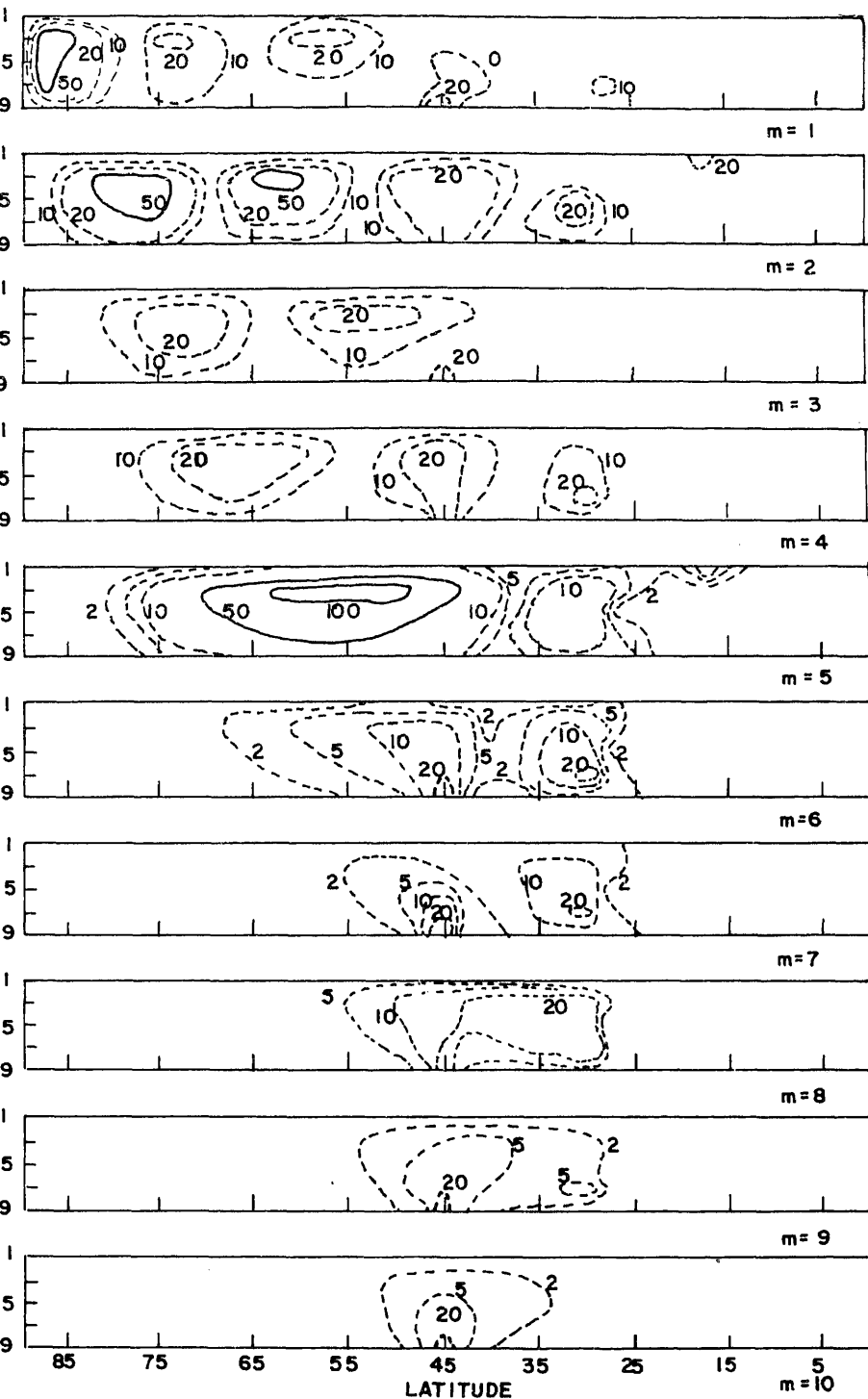


Figure 3. Geopotential amplitude response for different wave numbers (m) for 2.5° grid, in $m^2 \text{ s}^{-2}$ for 1 hPa of GPP.

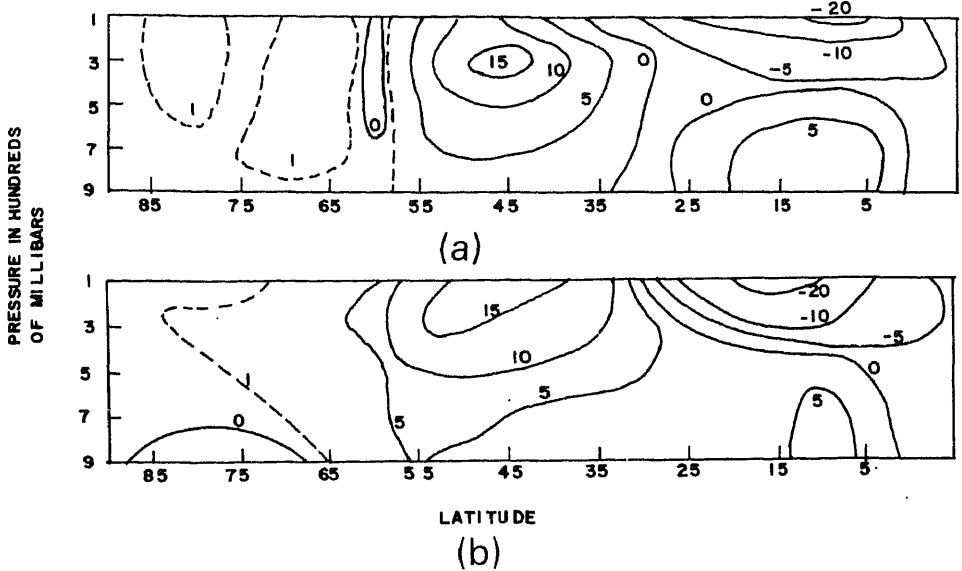


Figure 4. Zonal mean U_0 (m sec^{-1}) a. August 1963 2.5° grid. b. August 1965 2.5° grid.

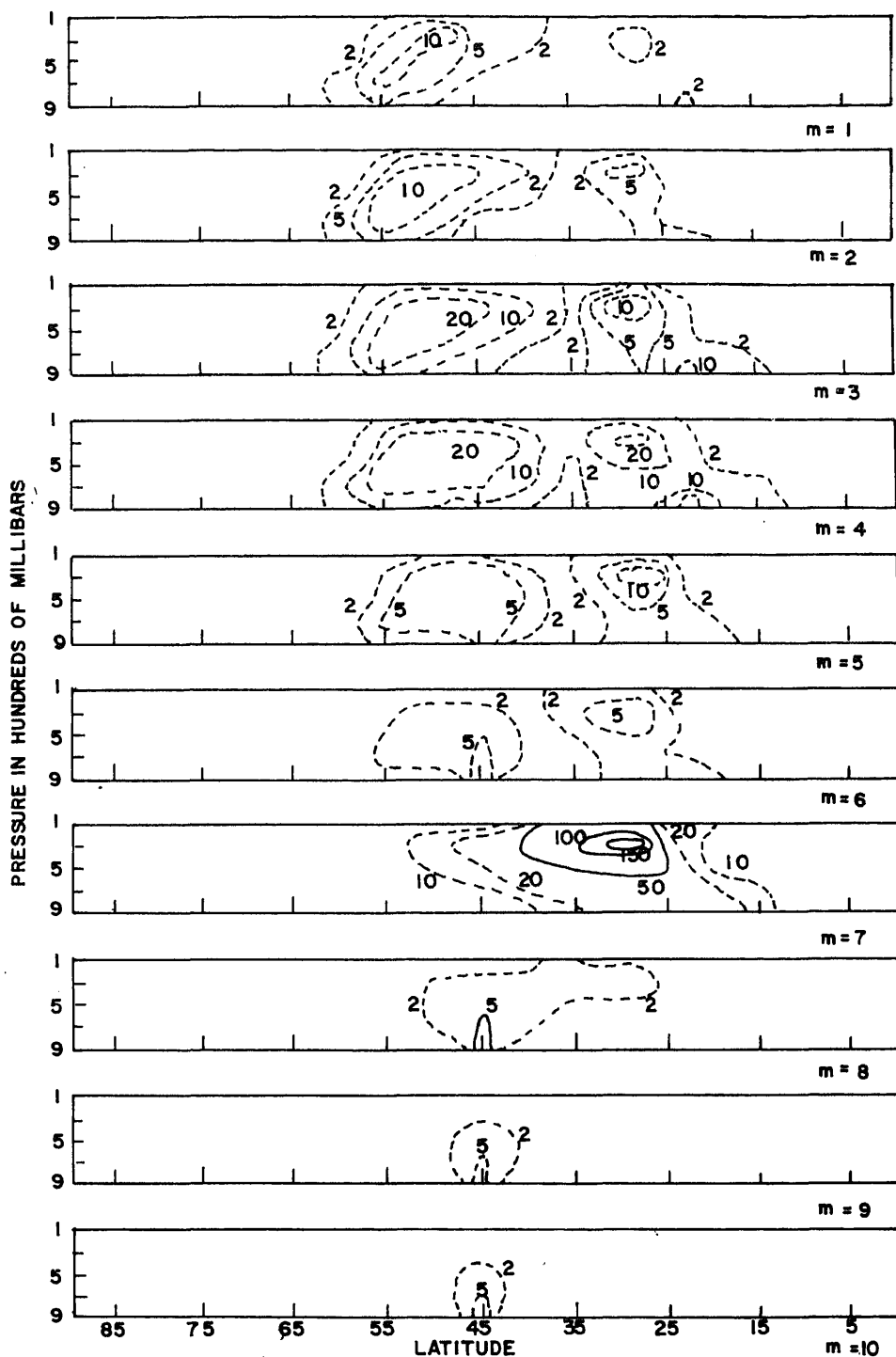
1965 in the monsoon region. This means that the strong monsoon must attract more midlatitude interaction. We notice that for $m = 10$, there is a strong resonance for this August. Note that the low level easterly barrier at $25-32.5^\circ\text{N}$ is no barrier at all.

Experiment 12. In this experiment we placed the forcing at 30°N using the 1963 August mean data as in experiment 11. The results are given in figure 8. Because there are zonal easterlies at 30°N , the response is very weak for all wave numbers as can be expected.

Finally we show in table 1 the response amplitude at 15°N normalized with that at the latitude for forcing for experiments 9 to 12. One can see from the table that there can be 20% influence at some levels at 15°N , both for good and bad monsoon seasons. If 10 mb is the pressure perturbation at 45°N due to transient disturbances, then the influence at 15°N can easily be about 2 mb perturbation which is of the right order.

6. A hypothesis, a test and some conclusions

We have shown that the monsoon, good or bad, can always interact with middle latitudes in the wave number domain. Then the question arises as to why should such an interaction be seen in the synoptic maps and the zonal mean winds so clearly, mainly during bad break monsoon periods. We venture the following tentative explanation, leaving the task of finding the true answer for future work. All experiments described herein are for the steady state. In reality the situation is dynamic. These waves might be moving in which case we will have $(U_0 - C_R)$ instead of U_0 as the denominator in S_3 term which is dominant in (1). The pattern of the refractive index in tropics and middle latitudes generally is to some extent similar to



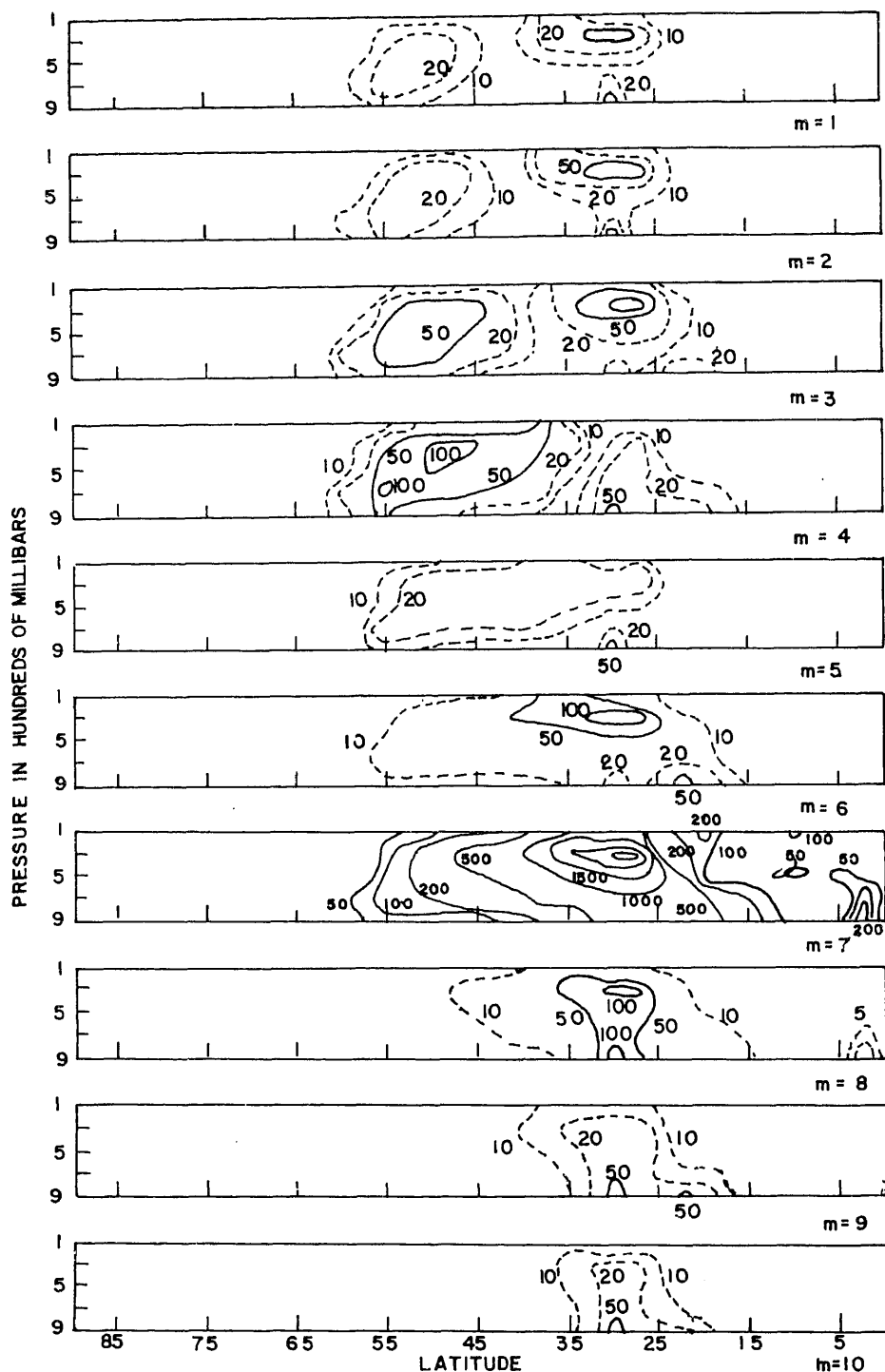


Figure 6. Geopotential amplitude response for different wave numbers (m) for 2.5° grid

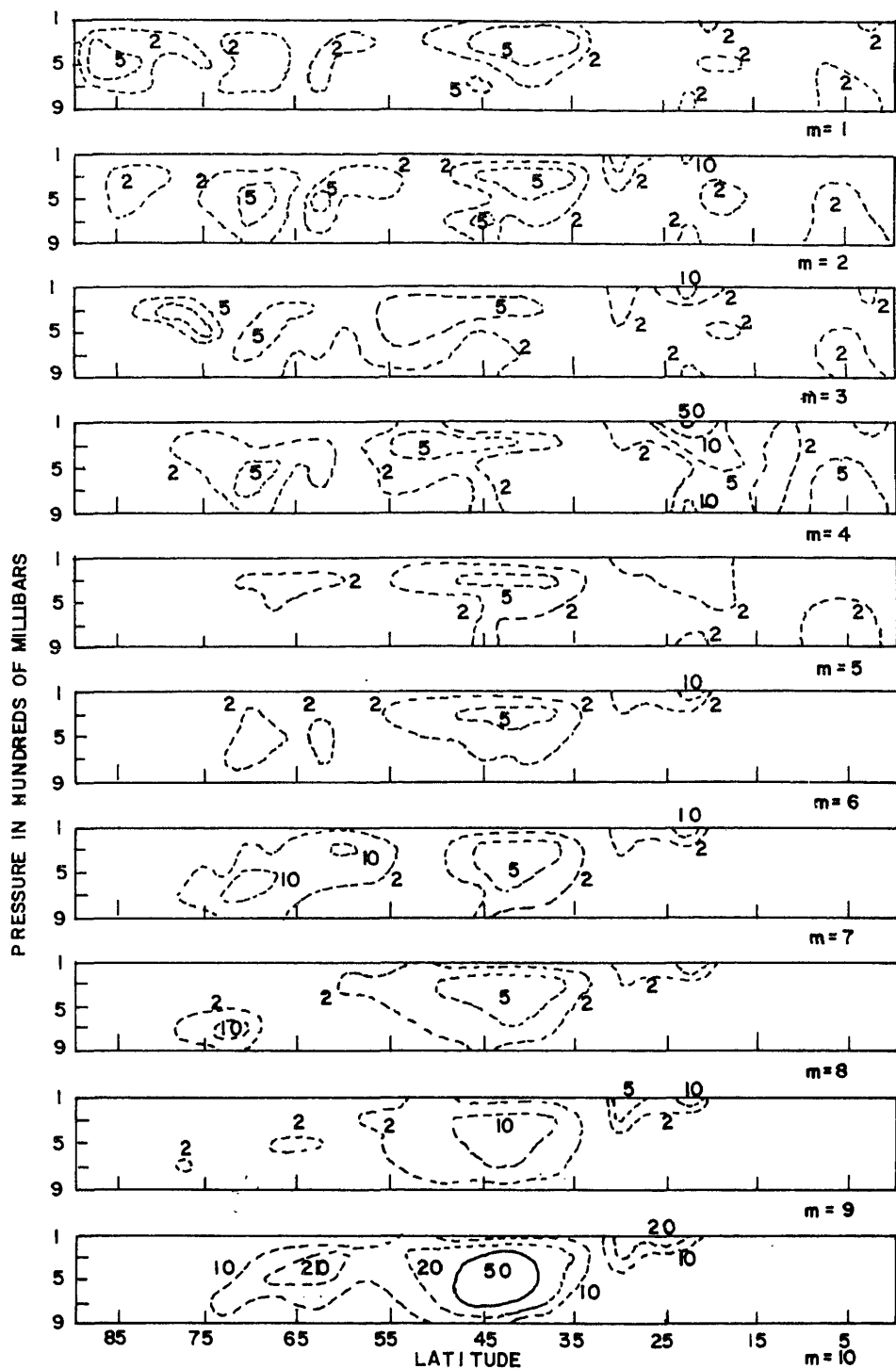


Figure 7. Geopotential amplitude response for different wave numbers (m) for 2.5° grid,

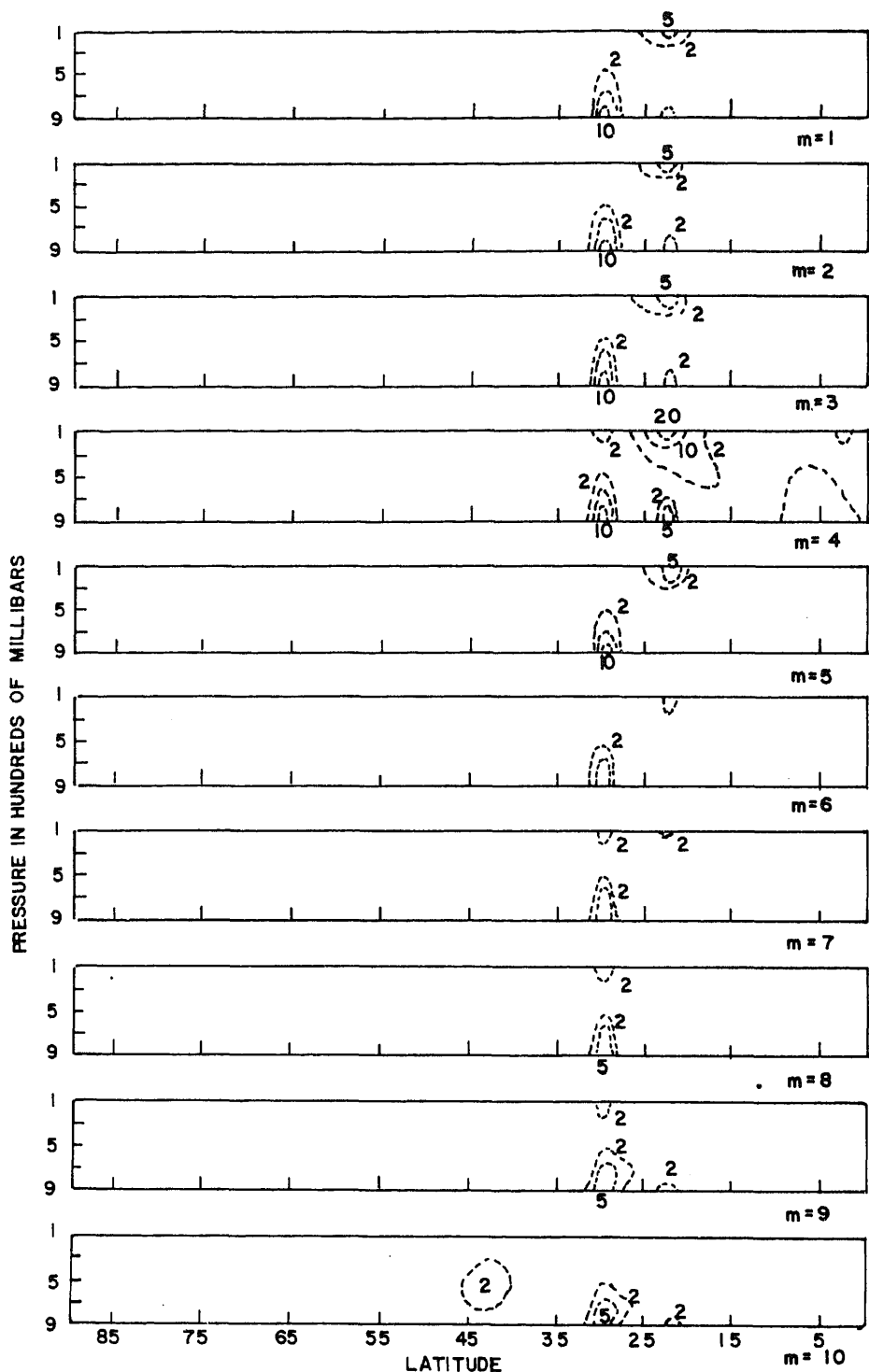


Figure 8. Geopotential amplitude response for different wave numbers (m) for 2.5° grid, in $\text{m}^2 \text{sec}^{-2}$ for August 1963 for $\text{CFR} = 0.0 \text{ sec}^{-1}$ with forcing at 30°N .

Table 1. Geopotential amplitude ratios at 15°N normalised with respect to the corresponding amplitudes at the forcing latitude.

Wave No.	Pressure (mb)	August 1965 Forcing at		January Forcing at 45°	July Forcing at 45°	August 1963 Forcing at	
		45°	30°			45°	30°
m = 1	100	0.03	* 0.1	0.004	*1.0	* 2.0	*0.2
	300	0.009	0.01	0.008	0.06	* 0.1	*0.2
	500	0.007	0.0006	0.01	0.01	* 2.0	0.06
	700	*0.3	0.04	0.0005	0.005	* 0.2	0.002
	900	*0.1	0.02	0.0003	0.002	* 0.3	0.002
m = 2	100	0.04	* 0.1	0.06	*0.7	* 2.0	*0.2
	300	0.01	0.01	*0.2	0.03	* 0.2	*0.2
	500	0.006	0.003	*0.4	0.02	*20.0	0.08
	700	*7.0	* 0.1	0.04	0.009	* 0.2	0.008
	900	*0.2	0.05	0.02	0.006	* 0.3	0.006
m = 3	100	0.05	* 0.1	0.05	*0.3	* 1.0	*0.2
	300	0.01	0.02	*0.1	0.01	* 0.1	*0.3
	500	0.005	0.008	*0.2	0.02	* 1.0	*0.1
	700	*0.2	* 0.7	0.05	0.006	* 0.1	0.01
	900	*0.6	* 0.2	0.02	0.001	* 0.2	0.009
m = 4	100	0.06	* 0.4	0.04	*0.6	* 4.0	*0.6
	300	0.02	0.05	0.07	0.03	* 0.3	*0.7
	500	0.005	0.01	0.06	0.01	* 5.0	*0.5
	700	*0.1	* 0.2	0.02	0.007	* 0.3	0.07
	900	*0.4	* 0.1	0.04	0.003	* 0.4	0.05
m = 5	100	0.08	0.09	0.02	*0.4	* 2.0	*0.2
	300	0.02	0.01	0.04	0.02	* 0.1	*0.3
	500	0.005	0.0003	0.03	0.01	* 0.7	*0.1
	700	*0.1	0.05	0.006	0.02	0.06	0.03
	900	*0.2	0.02	0.007	0.01	0.007	0.02
m = 6	100	*0.2	* 0.1	0.02	*0.6	* 0.5	0.02
	300	0.04	0.01	0.03	0.03	0.04	0.03
	500	0.007	0.005	0.02	0.009	0.04	0.02
	700	*0.1	*10.0	0.001	0.004	0.03	0.003
	900	*0.2	* 0.2	0.001	0.002	0.02	0.002
m = 7	100	*0.2	*0.1	0.01	*4.0	* 0.3	0.01
	300	0.07	0.01	0.02	*0.2	0.02	0.01
	500	0.02	0.006	0.008	0.03	0.004	0.01
	700	*1.0	*0.2	0.004	0.007	* 0.2	0.004
	900	*4.0	*0.3	0.0004	0.002	0.05	0.003
m = 8	100	0.05	*0.1	0.006	*0.7	0.03	0.05
	300	0.01	0.01	0.01	0.03	0.02	0.05
	500	0.002	0.005	0.004	0.01	0.02	0.06
	700	0.03	*0.1	0.0001	0.007	* 0.1	0.01
	900	0.04	*0.1	0.00009	0.003	0.07	0.01

Table 1. *Contd.*

Wave No.	Pressure (mb)	August 1965 Forcing at		January Forcing at 45°	July Forcing at 45°	August 1963 Forcing at	
		45°	30°			45°	30°
$m = 9$	100	0.002	*0.1	0.04	*0.2	0.07	0.07
	300	0.006	0.01	0.007	0.01	0.006	0.08
	500	0.0006	0.004	0.002	0.003	0.02	*0.1
	700	0.01	0.09	0.00002	0.001	0.04	0.03
	900	0.01	0.07	0.00001	0.0004	* 0.3	0.02
$m = 10$	100	0.01	*0.1	0.003	*0.1	* 0.2	*0.2
	300	0.003	0.01	0.005	0.005	0.01	*0.2
	500	0.0002	0.003	0.001	0.001	0.02	*0.2
	700	0.004	0.07	0.00001	0.0004	0.03	0.04
	900	0.004	0.05	0.000008	0.0001	* 0.2	0.03

* denotes the amplitude ratio values ≥ 0.1

that of the pattern of S_3 . If $C_R > U_0$ atleast in the lower tropospheric regions, $(U_0 - C_R)$ will be negative in the lower levels and the waves get trapped and are evanescent. A moving supercritical long wave ($m = 5$ to 10) therefore is more evanescent while it is eastward moving than when it is stationary or retrogressive. If these waves are more evanescent while eastward moving, it seems plausible to think that these waves become quasi-stationary with the correct phase during bad monsoon spells and one of them can even resonate and propagate into the tropical monsoon regions and cause the break spell. In other words lower tropospheric blocking in middle latitudes can usher in the monsoon break. Such quasi-stationarity of midlatitude systems was already noticed (e.g. Ramaswamy 1962; Bedi *et al* 1981; Raman and Rao 1981). During good monsoon years, such blocks do not occur. However, note that such blocks with a different phase can result in abnormally good monsoon season. For a quick look type check for the above blocking effect hypothesis, we conducted a spectral analysis of 500 mb geopotential 5° grid data for July 1972 for which month there was a severe break from 17th to 31st. The results for 40°N are given in Hovmoller type table 2 with wave form taken as $A \cos(m\lambda - \epsilon)$ where A is an amplitude and ϵ is the phase. Here the grid resolution is about 0.1 radians. We focus on the following most important aspects of this table.

- (i) Wave number $m = 1$ shows the highest amplitude uniformly almost throughout the month of July 1972. Its average amplitude is about 50 m.
- (ii) From 14th to 25th, $m = 1$ is almost stationary or retrogressive.
- (iii) During the first half of the month, wave numbers 3 and 4 show amplitudes of about 40 m (comparable to those of $m = 1$) only for four days.
- (iv) On the other hand $m = 4$ begins to grow from 14th and maintains an amplitude of 30 m or more till 22nd. $m = 5$ takes over from $m = 4$ from 18th and continues to grow almost to the end of the month with an average amplitude of about 45 m. Thus $m = 4$ and 5 together attain highest amplitudes from 15th to 31st.
- (v) $m = 5$ retrogresses during this time from 15th to almost the end of the month.
- (vi) $m = 7$ attains stationarity from 13th to 16th, 17th to 20th and 22nd to 26th.
- (vii) $m = 8$ is stationary from 22nd to 28th.
- (viii) Thus $m = 7$ or 8 together show almost stationarity from 13th to 28th.

Table 2. Amplitude of contour height (metres) and phases (radians) of different wave numbers (m) at 40°N for July 1972 at 500 mb.

	Amplitude										Phase									
	1	2	3	4	5	6	7	8	9	10	1	2	3	4	5	6	7	8	9	10
1	31.7	11.5	49.4	47.6	26.7	7.2	20.6	2.7	9.5	14.7	1.4	-0.4	-0.7	-1.5	-0.3	0.3	-1.3	1.4	-0.4	-0.2
2	46.2	11.3	42.7	26.4	21.7	18.8	16.1	9.6	3.3	7.0	-1.0	-1.0	-0.8	1.2	0.8	-0.3	-0.2	0.9	-0.7	1.5
3	60.8	10.7	39.3	20.0	16.8	29.1	16.1	12.6	3.1	6.9	-1.1	0.3	-1.4	1.0	1.5	0.3	1.1	0.2	-1.6	0.5
4	68.9	8.8	25.8	23.3	7.7	29.7	27.5	28.6	9.3	10.7	-1.5	0.3	-1.4	0.4	-0.7	0.9	-0.7	1.0	-0.9	0.9
5	64.7	18.2	25.4	43.1	11.2	28.8	28.0	33.3	11.6	20.3	1.4	-1.5	-1.5	0.3	0.1	1.3	-0.4	-1.3	1.3	1.5
6	42.6	30.3	20.4	43.8	23.0	36.6	21.1	26.8	16.7	19.1	1.0	-1.4	-1.5	0.7	0.3	1.5	0.1	-0.9	-1.5	-1.0
7	35.5	47.3	16.6	39.0	22.7	33.8	25.8	22.5	13.3	16.0	-1.3	-1.3	-1.2	0.7	-0.1	-1.5	0.2	-0.7	-1.1	-0.7
8	42.6	34.5	17.7	25.9	13.0	26.8	32.3	7.8	15.3	3.9	-0.7	-1.5	-0.8	-1.5	-0.4	1.2	0.4	-0.1	-1.5	0.2
9	71.7	8.8	36.9	19.4	9.9	21.0	40.3	4.6	17.4	7.2	-0.6	0.1	-1.3	-1.1	-0.3	1.3	0.9	-0.9	-1.2	-0.9
10	85.1	11.2	28.9	24.2	9.0	13.0	30.9	9.6	19.7	8.4	-0.8	1.4	-1.5	-1.9	0.5	-0.3	1.2	0.6	-1.1	-0.3
11	93.5	10.9	30.1	13.7	25.8	25.7	11.8	12.9	10.6	5.7	-1.1	-1.0	1.1	1.4	0.8	-0.9	0.1	0.2	-0.3	-0.9
12	83.7	28.6	13.8	32.3	26.7	23.5	10.9	5.4	10.4	6.3	-1.3	0.2	1.0	0.6	0.9	-1.3	-0.4	-1.2	-0.7	0.2
13	74.1	21.4	5.4	34.8	19.2	25.0	23.0	14.4	11.6	6.9	-1.5	-0.2	-0.4	0.5	0.5	-1.1	-1.0	1.4	-0.6	0.1
14	52.5	13.3	20.8	27.1	28.3	15.6	17.6	21.1	24.3	3.0	1.4	0.4	0.6	0.6	-0.5	-0.8	-0.9	-1.0	-0.6	1.4
15	49.6	33.9	19.6	41.3	10.3	9.1	26.8	14.9	22.9	10.7	1.3	0.2	-0.4	0.2	1.6	0.6	-1.0	0.6	-0.2	-0.4
16	56.4	35.0	26.0	46.0	19.0	5.2	31.2	12.5	20.7	10.7	1.4	0.1	-0.9	0.1	1.3	0.1	-0.9	-1.5	-0.3	1.3
17	58.7	48.9	17.2	40.8	20.3	6.6	32.3	6.9	28.5	9.2	1.4	-0.2	-0.6	-0.3	0.5	1.6	-0.6	-0.1	-0.3	-0.7
18	67.7	40.0	12.5	38.5	34.7	19.6	26.7	4.7	20.2	17.5	1.1	0.0	-0.4	-0.4	0.5	-1.5	-0.5	-1.5	0.3	-0.1
19	62.6	31.4	22.4	36.1	41.3	20.5	16.4	15.5	15.5	10.7	1.0	-0.1	-0.3	-0.8	0.2	-0.2	0.4	-0.9	-0.4	0.2
20	57.4	22.7	32.2	33.6	47.9	21.3	6.1	26.2	10.7	3.9	0.8	-0.3	-1.0	-1.1	0.0	1.2	-0.3	-0.3	-1.1	0.4
21	49.7	13.8	36.2	47.2	54.7	22.5	6.7	28.0	9.0	18.7	0.5	-1.1	-0.8	1.3	-0.6	0.8	1.1	0.4	0.3	0.7
22	47.7	26.5	18.3	42.8	58.1	16.1	13.6	21.5	3.6	10.3	0.7	-1.2	-1.2	1.2	-0.7	0.3	-1.2	0.6	-0.7	0.8
23	50.9	17.3	7.5	27.1	43.4	20.7	26.8	22.3	6.1	18.6	1.1	-1.5	-0.9	0.7	-0.7	-0.2	-1.2	0.7	1.4	0.3
24	31.7	31.1	6.8	18.3	40.0	23.8	24.3	17.8	12.3	23.7	1.3	1.5	1.4	0.1	-1.0	-0.1	-0.9	0.7	-7.0	0.4
25	22.1	32.2	4.7	7.1	42.5	30.1	30.5	19.8	8.9	21.9	1.4	1.4	-1.5	1.4	-1.5	-0.5	-1.0	0.7	1.0	0.1
26	33.1	3.0	15.4	8.3	52.1	36.8	21.7	19.9	11.8	19.7	-1.4	0.7	-0.7	1.5	1.3	-0.8	-1.3	0.6	0.3	-0.3
27	55.6	20.0	7.4	5.0	51.7	30.9	24.2	38.0	18.8	32.0	-1.4	0.1	-0.9	-1.1	1.1	-1.0	0.8	0.5	-0.9	-0.3
28	59.3	13.3	35.5	11.8	47.7	16.9	25.9	22.0	24.4	5.6	1.3	-0.7	-0.7	-1.3	0.7	-1.5	0.1	0.3	1.5	-1.5
29	51.7	18.3	38.7	20.4	54.3	14.4	28.0	13.7	35.7	5.7	1.2	0.0	-0.7	-1.3	0.4	0.7	0.0	-0.1	-1.5	-1.0
30	40.9	26.2	34.5	24.9	51.2	14.1	22.6	8.0	23.4	8.5	1.1	-0.2	-0.8	-1.0	0.5	0.9	0.2	-0.7	-0.9	0.0
31	31.1	23.7	28.0	37.4	44.9	7.6	28.2	8.5	20.5	8.3	1.4	-1.4	-0.4	-0.7	0.3	-0.3	0.5	-1.2	-0.7	-0.4

amplitudes in the earlier half of the month.

The above results suggest in general that $m = 1$, (4, 5) and (7, 8) are almost stationary or retrogressive from 13th to 31st. $m = (4, 5)$ attains large amplitudes if some instability mechanism such as the baroclinic instability is operating during this period. Under these conditions, according to our above stated hypothesis, $m = 4, 5, 7$ and 8 can propagate to the southern latitudes and if the phases are correct a severe monsoon break can result.

7. Some questions and the future

The following questions arise:

- (a) Are there always such interactions for all the severe drought monsoon situations with breaks of duration of about a week or more than a week?
- (b) Are there such interactions during abnormally good monsoon situations with durations of about a week or more than a week?
- (c) How do these waves effect the heat sources of the global monsoon?
- (d) What is the precise role of Himalayas? Do they accentuate the interaction or do they act always as either reflecting or diffracting barriers for some long waves?
- (e) Are there preferred locations for Asian blocks? If so, what are the factors responsible for such a geographical preference?
- (f) What triggers such a severe low index regime in the general circulation? Is it instability, vacillation or blocking mechanism?
- (g) Can such sudden changes in global regime be predicted with the existing models with sufficient lead and accuracy?
- (h) What are the energetics in the wave number domain during such situations?
- (i) What did the existing models predict for such situations in the past? How do the model diagnostics compare with the observational diagnostics?

A large amount of observational data have to be studied in the near future to check the above said blocking hypothesis more thoroughly. Similar experiments reported here can be repeated with better models (P.E. models) with better vertical resolution on the global monsoonal system. For the present, despite a large volume of work done, monsoon drought mechanics still remains an understood and unsolved problem in global meteorology.

Acknowledgements

One of the authors (MSR) is indebted to the Department of Science and Technology for granting a project on this problem. He is also thankful to the Indo-US collaboration (DST-NSF) committee on monsoon research for enabling him to visit the University of Maryland where he had the benefit of useful discussions with US colleagues. The authors thank Kusuma G. Rao for the zonal wind data for 1963 and 1965 from her thesis. The authors thank R. Ravindrakumar and A V Kirankumar for their help.

we give below only the most important parameters.

$B =$	$-(RP_s/U_{0\delta} f P_\delta) (1/a) (\partial T_{0\delta}/\partial \varphi)$
$b =$	$-(RP_s/U_{0\delta} d2T f P_T) (1/a) (\partial T_{0\delta}/\partial \phi)$
D	any dependent variable
\bar{D}	time mean of $D = D_0 + D_*$
D_0	zonal mean of \bar{D}
D_*	Axially asymmetric perturbation part = $\hat{D} \exp(im\lambda)$
\hat{D}	amplitude of D_*
$\bar{d} =$	$-(RP_s/U_{0T} f P_T)$
$f =$	$2 \Omega \sin \phi$
$K_0 =$	$[(\partial T_0/\partial P) - (RT_0/PC_p)]^{-1}$
l	Ekman friction constant
$M =$	$-(RP_s/U_{0\delta} f P_\delta) U_{0\delta} g \rho_\delta / K_{0\delta} a$
m	longitudinal wave number
$N =$	$-RP_s/U_{0\delta} f P_\delta$
P	pressure
P_s	surface standard pressure
$S_1 =$	$-f^2 PK_0/RP_s^2$
$S_2 =$	$[-f^2(\partial/\partial P)(PK_0)]/RP_s$
$S_3 =$	$(1/U_0) [(1/a) (\partial \eta_0/\partial \phi) + (f\partial/\partial P)(K_0/a) (\partial T_0/\partial \phi)]$
T	temperature
u	eastward velocity
v	northward velocity
ζ	relative vorticity
$\eta =$	$f + \zeta$, the absolute vorticity
λ	longitude
$\nu =$	$-(RP_s/U_{0\delta} f P_\delta) (gP_\delta l / K_{0\delta} a)$
ξ	P/P_s , the usual coordinate in many GCMs.
ρ	density
ϕ	latitude
Ω	angular velocity of the earth
$\omega =$	dp/dt
∇^2	horizontal spherical Laplacian

Suffixes T and δ denote top and bottom of the atmosphere considered.

References

- Alexander G, Keshavamurthy R N, De U S, Chellappa R, Das S K and Pillai P V 1978 Fluctuations of monsoon activity; *Indian J. Meteorol. Hydrol. Geophys.* **29** 76-87
- Angell J K 1981 Comparison of variations in atmospheric quantities with sea surface temperature variations in the equatorial eastern pacific; *Mon. Weather Rev.* **109** 230-243
- Bedi H S, Billa H S and Mookerjee N 1981 Interaction between northern middle latitudes and summer monsoon circulation. International Conf. on early results of FGEE and large scale aspects of its monsoon experiments. GARP, Tallahassee, Florida 12-17 Jan. 81, pp 5-25 to 5-29

- Bennet J R and Young J A 1971 The influence of latitudinal wind shear upon large scale wave propagation into the tropics; *Mon. Weather Rev.* **99** 202–214
- Bjerknes J 1969 Atmospheric teleconnections from the equatorial Pacific; *Mon. Weather Rev.* **97** 163–172
- Booker J R and Bretherton F P 1967 The critical layer for internal gravity waves in a shear flow; *J. Fluid Mech.* **27** 513–519
- Branstator G 1983 Horizontal energy propagation in a barotropic atmosphere with meridional and zonal structure; *J. Atmos. Sci.* **40** 1689–1708
- Charney J G 1969 A further note on large-scale motions in the tropics; *J. Atmos. Sci.* **20** 607–609
- Charney J G and Drazin P G 1961 Propagation of planetary scale disturbances from the lower to the upper atmosphere; *J. Geophys. Res.* **66** 83–109
- Gille J C 1968 The general nature of acoustic gravity waves, in *Winds and turbulence in stratosphere, mesosphere and ionosphere* (ed.) A Rawer (Amsterdam: North-Holland) p. 299
- Goswami B N and Shukla J 1984 Quasi-periodic oscillations in a symmetric general circulation model; *J. Atmos. Sci.* **41** 20–37
- Jacobs D A H 1981 The exploitation of sparsity by iterative methods in *Sparse matrices and their uses* (ed.) I S Duff (New York: Academic Press) p. 191
- Joseph P V 1978 Subtropical westerlies in relation to large scale failure of Indian monsoon; *Indian J. Meteorol. Hydrol. Geophys.* **29** 412–418
- Kanamitsu M and Krishnamurti T N 1978 Northern summer tropical circulations during drought and normal rainfall months; *Mon. Weather Rev.* **106** 331–347
- Krishnamurti T N, Jayakumar P K, Sheng J, Surgi N and Kumar A 1984 Divergent circulation on the 30–50 day time scale, F S U Report No. 84 2
- Krishnamurti T N and Subrahmanyam D 1982 The 30–50 day mode at 850 mb during MONEX; *J. Atmos. Sci.* **39** 2088–2095
- Lindzen R S and Holton J R 1968 A theory of quasi-biennial oscillations; *J. Atmos. Sci.* **25** 1095–1107
- Madden R A and Julien P R 1971 Detection of a 40–50 day oscillation in the zonal wind in the tropical Pacific *J. Atmos. Sci.* **28** 702–708
- Mak Man Kin 1969 Laterally driven stochastic motions in the tropics; *J. Atmos. Sci.* **26** 41–64
- Matsuno T 1966 Quasi-geostrophic motion in the equatorial area; *J. Meteorol. Soc. (Jpn)* **44** 25–42
- Murakami T and Nakazawa T 1984 On the 40–50 day oscillations during the 1979 northern hemisphere summer Part I: phase propagation; *J. Meteorol. Soc. (Jpn)* **63** 250–271
- Nigam S and Held I M 1983 The influence of critical latitude on topographically forced stationary waves in a barotropic model; *J. Atmos. Sci.* **40** 2610–2622
- Oort A H 1983 Global atmospheric circulation statistics 1958–1973 NOAA Professional paper 14 pp. 180
- Opsteegh J D and van Den Dool H M 1980 Seasonal differences in the stationary response of a linearized primitive equation model, prospects for long range forecasting; *J. Atmos. Sci.* **37** 2169–2185
- Pant P S 1983 A physical basis for changes in the phases of the summer monsoon over India; *Mon. Weather Rev.* **111** 487–495
- Ramamurty K 1969 Monsoons of India: Some aspects of the “break” in the Indian southwest monsoon during July and August. Indian Meteorological Department Forecasting Manual Part IV, No. N–18, 3
- Raman C R V and Rao Y P 1981 Interaction of waves in middle latitude westerlies over Asia with the southwest monsoon over India. International conference on early results FGGE and large scale aspects of its monsoon experiments, GARP, Tallahassee, Florida, 12–17 Jan. 1981, p. 5–30 and 5–37
- Ramaswamy C 1962 Breaks in the Indian summer monsoon as a phenomenon of interaction between the easterly and the subtropical westerly jet streams; *Tellus* **14** 337–349
- Ramaswamy C and Pareek R S 1978 The southwest monsoon over India and its teleconnections with the middle and upper tropospheric flow patterns over the southern hemisphere; *Tellus* **30** 126–135
- Rasmusson E and Carpenter T 1982 Variations in tropical sea-surface temperature and surface wind fields associated with the southern oscillation/El Nino; *Mon. Weather Rev.* **110** 354–384
- Richtmyer R D and Morton K W 1967 Difference methods for initial value problems (New York: Interscience publishers) p. 405
- Saltzman B 1965 On the theory of the winter average perturbation in the troposphere and stratosphere; *Mon. Weather Rev.* **93** 195–211

- Saltzman B 1968 Surface effects on the general circulation and macro-climate: A review of the theory of the quasi-stationary perturbations in the atmosphere; *Meteorol. Monogr.* **30** 4–19
- Shukla J and Paulino D A 1983 The southern oscillation and long range forecasting of the summer monsoon rainfall over India; *Mon. Weather Rev.* **111** 1830–1837
- Sikka D R and Gadgil S 1980 On the maximum cloud zone and the ITCZ over Indian longitudes during the southwest monsoon; *Mon. Weather Rev.* **108** 1840–1853
- Simmons A J 1982 The forcing of stationary wave motion by tropical diabatic heating; *Q. J. Meteorol. Soc.* **108** 504–534
- Smith R B 1979 The influence of mountains on the atmosphere; *Adv. Geophys.* **21** 87–230
- Wallace J M and Gutzler D S 1981 Teleconnections in the geopotential height field during the northern hemispheric winter; *Mon. Weather Rev.* **109** 784–812
- Webster P J and Chow I C 1980 Low frequency transition of a simple monsoon system; *J. Atmos. Sci.* **37** 368–382

Characteristics of air flow over Andaman Islands including precipitation

SARAT C KAR and N RAMANATHAN

Centre for Atmospheric Sciences, Indian Institute of Technology, New Delhi 110 016, India

MS received 9 October 1986; revised 1 July 1987.

Abstract. The characteristics of simulated air flow over Andaman Islands are studied with a two-dimensional version of the University of Virginia meso scale model (UVM). Using the observed synoptic data as initial conditions, 24 hr simulations are obtained for a day each in April and November. These days are chosen to study the variations in the simulated flow pattern under different synoptic conditions including precipitation effects. A large scale condensation scheme is employed to consider the effect of latent heat release on the perturbations. The results show that the latent heat released by condensation strengthens the intensity of perturbations and the topography accelerates the arrival of sea breeze by about an hour. The model-simulated results, given in graphical form, are discussed and compared with available observations.

Keywords. Meso scale island circulations; sea/land breeze studies; numerical simulation; weather forecast.

1. Introduction

Meso scale atmospheric circulations, such as land/sea breeze and formation of cloud streets are caused by differential heating and cooling of islands and coastal land masses. Studies with linear approximations to the governing equations or including the nonlinear effects on the formation of perturbations induced by heated islands are reported by Delage and Taylor (1970), Mahrer and Pielke (1976) and Bhumralkar (1973) to mention a few. Mahrer and Pielke (1978) have shown the importance of including topography in meso scale circulations. However, the above studies refer to Atlantic or Pacific islands. No detailed meso scale numerical study has so far been undertaken for an island in the Indian ocean. As a pilot study, the Andaman Islands (10–14°N; 92–94°E) with an average width of 25 km was chosen for the following reasons: (i) suitability for two-dimensional numerical simulations as the length-to-width ratio is of the order of 10, (ii) simple topographical features and (iii) proximity to cyclogenetic area. The last aspect is important for identifying energy transport from local to large scale circulation by the presence of an island.

The best known model which has topography, temporal variation of the PBL as a response to surface heating/cooling and elaborate boundary layer parametrization has been developed by Mahrer and Pielke (1977) (UVM). The two-dimensional version of this model was adopted for our study with modifications. These modifications are (i) an observed synoptic flow for initialization above PBL instead of constant unidirectional flow, (ii) precipitation scheme to consider the condensation effects on perturbations, (iii) inclusion of terrain data and (iv) PBL depth variations in stable stratification calculated with the formulation given by Smeda (1979).

The present investigation attempts to evaluate the importance of the island for modifying ambient air flow including precipitation effects and to evaluate the accuracy of the model in obtaining local forecasts.

The governing equations and the description of the model are given in § 2. In § 3 the initial and boundary conditions and the condensation schemes are described. The model simulated results are discussed in § 4 and finally our conclusions.

2. Model equations

The governing equations of the model are written with the following vertical coordinates

$$Z^* = \bar{S} \frac{Z - Z_G}{S - Z_G},$$

$$\begin{aligned} \frac{du}{dt} = & f v - f V_g - \theta \frac{\partial \pi}{\partial x} + g \frac{(Z^* - \bar{S})}{\bar{S}} \frac{\partial Z_G}{\partial x} - g \frac{Z^*}{\bar{S}} \frac{\partial S}{\partial x} \\ & + \left(\frac{\bar{S}}{S - Z_G} \right)^2 \frac{\partial}{\partial Z^*} \left(K_Z^m \frac{\partial u}{\partial Z^*} \right) + \frac{\partial}{\partial x} \left(K_H \frac{\partial u}{\partial x} \right), \end{aligned} \quad (1)$$

$$\frac{dv}{dt} = -fu + fU_g + \left(\frac{\bar{S}}{S - Z_G} \right)^2 \frac{\partial}{\partial Z^*} \left(K_Z^m \frac{\partial v}{\partial Z^*} \right) + \frac{\partial}{\partial x} \left(K_H \frac{\partial v}{\partial x} \right), \quad (2)$$

$$\frac{d\theta}{dt} = \left(\frac{\bar{S}}{S - Z_G} \right)^2 \frac{\partial}{\partial Z^*} \left(K_Z \frac{\partial \theta}{\partial Z^*} \right) + \frac{\partial}{\partial x} \left(K_H \frac{\partial \theta}{\partial x} \right) + F_\theta, \quad (3)$$

$$\frac{dq}{dt} = \left(\frac{\bar{S}}{S - Z_G} \right)^2 \frac{\partial}{\partial Z^*} \left(K_Z^q \frac{\partial q}{\partial Z^*} \right) + \frac{\partial}{\partial x} \left(K_H \frac{\partial q}{\partial x} \right) + F_q, \quad (4)$$

$$\frac{\partial u}{\partial x} + \frac{\partial w^*}{\partial Z^*} = \frac{1}{(S - Z_G)} \left(u \frac{\partial Z_G}{\partial x} \right) - \frac{1}{(S - Z_G)} \left(\frac{\partial S}{\partial t} + u \frac{\partial S}{\partial x} \right), \quad (5)$$

$$\frac{\partial \pi}{\partial Z^*} = - \left(\frac{S - Z_G}{\bar{S}} \right) \frac{g}{\theta}, \quad (6)$$

where

$$\pi = C_p (P/P_0)^{R/C_p},$$

$$\frac{d}{dt} = \frac{\partial}{\partial t} + u \frac{\partial}{\partial x} + w^* \frac{\partial}{\partial Z^*},$$

$$w^* = \frac{\bar{S}}{S - Z_G} w - \frac{Z^*}{S - Z_G} \left(\frac{\partial S}{\partial t} + u \frac{\partial S}{\partial x} \right) + \frac{Z^* - \bar{S}}{S - Z_G} \left(u \frac{\partial Z_G}{\partial x} \right),$$

$$\frac{\partial T_s}{\partial t} = \frac{\partial}{\partial Z} \left(K_s \frac{\partial T_s}{\partial Z} \right), \quad -D \leq Z \leq 0, \quad (7)$$

$$\frac{\partial S}{\partial t} = -\frac{1}{\bar{S}} \int_0^{\bar{S}} \frac{\partial}{\partial X} \{ u(S - Z_G) \} dZ^*, \quad (8)$$

where \bar{S} and S are the initial and instantaneous heights of the material surface, Z_G the ground elevation above sea level, U_g and V_g the geostrophic components of wind, K_Z and K_H the vertical and horizontal exchange coefficients while the superscripts denote the corresponding variables, T_s and K_s the soil temperature and soil diffusion coefficients respectively.

Equations (1) and (2) are the equations of motion. Equations (3) through (6) are the energy, moisture, continuity and hydrostatic equations respectively. F_θ and F_q in (3) and (4) are the diabatic source or sink terms of heat and moisture respectively. The heat conduction in the soil is described by (7). The above set of seven equations forms a complete set in seven unknowns (u , v , θ , q , w , π and T_s).

The growth of the PBL(H) during clear days are given by

$$\frac{\partial H}{\partial t} + u \frac{\partial H}{\partial x} = \bar{w} + \frac{1.8 w_*^3 + 1.1 u_*^3 - 3.3 u_*^2 f \cdot H}{g \frac{H^2}{\theta} \frac{\partial \theta^+}{\partial Z^*} + 9 w_*^2 + 7.2 u_*^2}, \quad (9)$$

or,

$$\frac{\partial H}{\partial t} + u \frac{\partial H}{\partial x} = \frac{C_1 u_*^2}{Hf} \left[1 - \left(\frac{C_2 H f}{u_*} \right)^\alpha \right], \quad (10)$$

where

$$w_* = \left(-\frac{g}{\theta} u_* \theta_* H \right)^{1/3},$$

$$C_1 = 0.06, \quad C_2 = 3.3 \text{ and } \alpha = 3.0,$$

u_* and θ_* are the surface layer friction parameters. Other terms have their usual meanings.

2.1 Description of the model

The basic equations of the model, (1) to (7) are for hydrostatic incompressible flow with transformation to the terrain following coordinate (Z^*). The sub-grid scale parametrization, given below, along with radiation formulations is given in detail in Mahrer and Pielke (1977). Numerical and computational aspects are discussed in Mahrer and Pielke (1978). In this model, three layers above the ground and a soil layer below the earth surface are used; a surface layer with height h , a planetary boundary layer (PBL) with height H and a layer in the free atmosphere extending to the upper troposphere. The soil layer extends below the ground to a depth D . To account for vertical spreading of mass due to hydrostatic adjustment this model

are given by (9) and (10). Equation (8) is used to calculate S at every time step. We now briefly mention the remaining features of this model.

(i) *Boundary layer.* Calculation of the surface fluxes of momentum, heat and moisture is based on the work of Businger *et al* (1971). These are based on similarity theory. The exchange coefficients in PBL in an unstable convective boundary layer utilizes O'Brien's (1970) formulation as below.

$$\begin{aligned}
 K_Z(Z^*) &= K(H) = 1 \text{ cm}^2/\text{sec} \quad (Z^* \geq H) \\
 &= K_Z(H) + \frac{(H-Z^*)^2}{(H-h)^2} [K_Z(h) - K_Z(H) + \left\{ \frac{\partial}{\partial Z^*} K_Z(h) + 2 \left(\frac{K_Z(h) - K_Z(H)}{(H-h)} \right) \right\} (Z^* - h)] \quad h \leq Z^* \leq H \\
 &= \frac{Z^*}{h} K_Z(h) \quad 0 \leq Z^* \leq h.
 \end{aligned} \tag{11}$$

The exchange coefficient for the stable boundary layer when the surface heat flux is positive is given by (Blackadar 1979)

$$K_m = K_\theta = \begin{cases} 1.1 \left(\frac{R_{ic} - R_i}{R_{ic}} \right) l^2 s & R_i < R_{ic}, \\ 1.0 & R_i > R_{ic} \end{cases} \tag{12}$$

where R_{ic} is the critical Richardson number, l the mixing length and S the local wind shear. The mixing length l is taken as a linear function of Z^* near the surface and constant of 70 m elsewhere i.e.

$$\begin{aligned}
 l &= 0.35 Z^* & Z^* \leq 200 \text{ m}, \\
 l &= 70 \text{ m} & Z^* > 200 \text{ m}.
 \end{aligned} \tag{13}$$

The remaining parameters are given by

$$\begin{aligned}
 R_i &= \frac{g}{\theta} \frac{1}{s^2} \frac{\partial \theta}{\partial Z^*} \\
 s &= \left[\left(\frac{\partial u}{\partial Z^*} \right)^2 + \left(\frac{\partial v}{\partial Z^*} \right)^2 \right]^{1/2}
 \end{aligned} \tag{14}$$

and $R_{ic} = (\Delta Z^*)^{0.175} \times 0.115$; ΔZ^* is the grid interval. An alternate formulation given by Blackadar (1979) for K_Z is used when the super-adiabatic layer remains aloft over a stably stratified layer with a positive surface heat flux. It is given by the relation

$$K_m = K_\theta = (1 - 18 R_i)^{1/2} l^2 s. \quad (15)$$

The above relations for K_Z were used to simulate full diurnal cycle of boundary layer behaviour (McNider and Pielke 1981). Instead of using a functional relationship for horizontal exchange coefficient (K_H), a low pass filter which removes $2\Delta x$ waves completely is used in this study.

ii) *Evaluation of surface temperature.* In this model, the land surface temperature is computed using a heat balance equation which includes solar radiation, incoming longwave radiation, latent, sensible and soil heat fluxes and outgoing long wave radiation from the surface. The initial soil temperature profile (T_s) in the soil layer $-D \leq Z \leq 0$, is specified at the beginning of the simulations. The temporal variations of T_s are obtained by (7) above. The relevant formulations for radiation terms and calculation of atmospheric heating rate etc are given elsewhere.

3. Initial and boundary conditions

The initial distribution of soil temperature (T_s), air temperature θ , wind field V and specific humidity q over the entire domain are obtained from the observed data (table 1 and figure 1). The initial wind profile within PBL is obtained by integrating steady state Ekman equation, assuming that u and v components of velocity are functions of height only. The large scale surface pressure P and air temperature are taken as 1013 mb and 300°A respectively. Above PBL, the observed data are used to initialize the u and v fields.

(i) Boundary conditions at $Z^* = 0$ (lower boundary)

$$u = v = w^* = 0,$$

$$q_G = F_W q_{G\text{Sat}} + (1 - F_W) q(1),$$

Table 1. Initial conditions for start of model simulation (wind speed and direction).

Z(m)	1st April 1969		13th November 1968	
	V(m/sec)	Direction from north (degree)	V(m/sec)	Direction from north (degree)
2	0	0	0	0
500	1	60	3	120
1000	1.5	75	5	120
1500	2	90	7	120
2000	6	100	7	110
2500	6	110	7	90
3100	6	120	7	80
3700	4	105	7	90
4400	4	100	7	90
5000	7	50	8	55
6600	8	70	3	20
7500	9	80	4	125

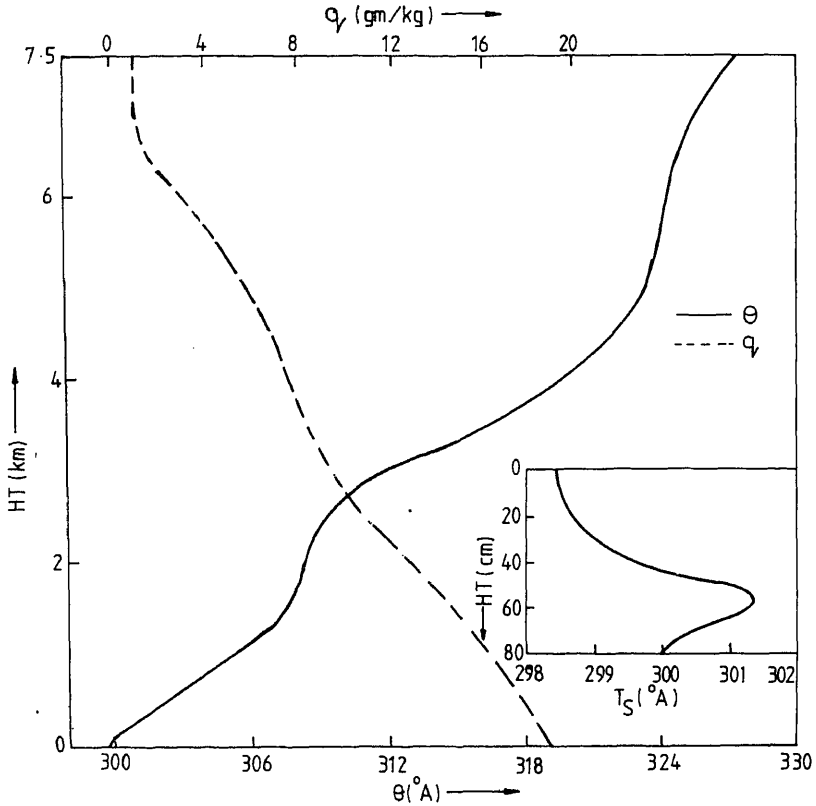


Figure 1. Profiles of potential temperature θ , specific humidity q and soil temperature T_s (inset diagram) — (initial data 1st April 1969).

where F_w is the soil wetness expressed as fraction and $q(1)$ is the specific humidity at the first grid level above the surface.

(ii) At the top of the model $Z^* = \bar{S} = 7.5$ km

$$u = U_g, \quad v = V_g, \quad w^* = 0; \quad \theta(\bar{S}) = \text{constant}, \quad q(\bar{S}) = \text{constant}$$

$$\pi = \pi(\bar{S}) - g(S - \bar{S}) / [\bar{\theta}(\bar{S}) + \frac{1}{2} \gamma_{\text{top}} (S - \bar{S})],$$

where γ_{top} is the potential temperature lapse rate at the top of the model.

(iii) At lateral boundaries, zero gradient boundary conditions are used.

$$w^* = \frac{\partial S}{\partial x} = \frac{\partial}{\partial x} (\theta, q, \pi, Z_G) = 0.$$

To ensure smooth variation, the terrain data obtained from topographical map are smoothed using a 3-point smoother

The soil wetness (F_w), conductivity (K_s), specific heat (C_s) and density (ρ_s) are taken to be 0.05, 0.003 cm²/sec, 0.31 cal g⁻¹ K⁻¹ and 1.5 g/cm³ respectively. The albedo and the roughness length for land are specified to be 0.2 and 4 cm respectively. The roughness length over water is defined as

$$Z_0 = 0.032 u_*^2/g$$

with the condition that $Z_0 > 0.0015$ cm.

(iv) Precipitation scheme

In the present study, a large scale precipitation scheme by Manabe *et al* (1965) is employed in which the temperature and moisture fields are adjusted for the latent heat release and condensation so as not to permit supersaturation at any grid point. It is assumed that the condensate falls to the ground instantaneously. To prevent large temperature gradients that may arise due to inadequate dispersions, the θ field is smoothed with 3-point smoother at regular intervals.

4. Results and discussion

On the chosen day for simulation, 1st April 1969, no large scale disturbance such as the movement of low pressure systems into the integrated domain, was evident. The weather was clear with no ground precipitation. Thus, the developed perturbations are entirely governed by the island features. With the synoptic observations listed in table 1 and the evaluated terrain height as initial data, two-dimensional simulations were performed on a 21 × 11 or 21 × 16 grid. The model grid lattice was stretched, in the X direction, near the boundaries as far as possible from the region of interest. This eliminated the lateral boundary effects into the integrated domain. In the vertical also, a variable distance grid was utilized to obtain a better resolution near the ground and a coarse resolution near the top of the model. The simulations were started at sunrise.

The principal factors that govern the intensity and horizontal extent of perturbations are (i) the island's topography, (ii) the diurnal variation of temperature, (iii) the direction and magnitude of synoptic flow and (iv) the addition of latent heat release by condensation. To understand the individual influence of these factors, it is necessary to have several runs with alteration of a single parameter at a time. The following cases are considered.

Case 1. Flat island with no condensation.

Case 2. Flat island with condensation.

Case 3. Island with topography and condensation.

Model-simulated results in graphical form are given at the end.

4.1 Horizontal velocities

The horizontal wind speed predicted by the model at 20 m height, on the extreme ends of the island, is shown in figure 2 for case 1. Similar results were also obtained in other cases (not shown here). At the eastern or windward edge of the island, from late evening hours (2200 LST) till sunrise, wind speeds developed are usually

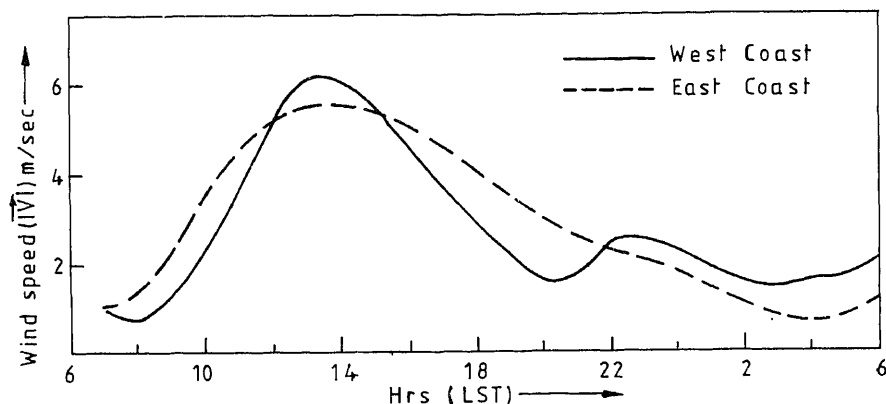


Figure 2. Simulated horizontal wind speed ($|\vec{V}|$) in m/sec at 20 m height over the western (lee) and eastern (windward) edges of the island.

lower than those found at the western or lee edge. Maximum wind speeds of the order of 6.2 m/sec and 5.7 m/sec were noticed in the afternoon hours at the west and east ends of the island respectively. The higher wind speeds at the western end in the early afternoon hours are due to the higher surface temperature and enhanced turbulence. With topography, wind speeds at western end are of higher magnitude and persist for a longer time till 2000 LST when compared with a flat terrain (not shown here). The difference in wind speed and time lag is due to difference in heating and cooling rates of the sloping surfaces.

The diurnal variation of horizontal wind speed ($u^2 + v^2$)^{1/2} over Port Blair is shown in figure 3 (case 2) and figure 4 (case 3). These patterns show that winds with higher speed occur in the PBL during daytime due to enhanced turbulence. Above 5 km the wind speeds remain unaffected by the heating or cooling of the land surface. The maximum amplitude of the diurnal oscillations occurs within lower 2 km over Port Blair around local noon, which is the time of the maximum surface heating. At higher levels (4 km height) a time lag of 2 hr at which the maximum occurs, is noticed. With condensation and topography effects, the wind speeds during daytime at all levels are generally higher than those obtained with flat island case.

4.2 Development/decay of sea breeze

The onset of sea breeze is accompanied by an increase in wind speed, a change in wind direction, a fall in temperature and a rise in humidity. In this simulation, the sea breeze is decided by the change in the direction of east-west component u and the normal component of wind to the coastline. The vector wind variations of the wind at the west edge of the island on selected hours at 20 m height are shown in figure 5. A similar pattern obtained including topography is shown in figure 6. From these figures, it is clear that due to the arrival of sea breeze at 0900 LST (figure 5) and 0800 LST (figure 6) the wind direction at the west coast remains steady from west to west-north-west till its retreat from the island. On the other hand, from daylight hours till midnight, northeast to east-north-east winds occur at the eastern end (windward end) of the island (not shown here).

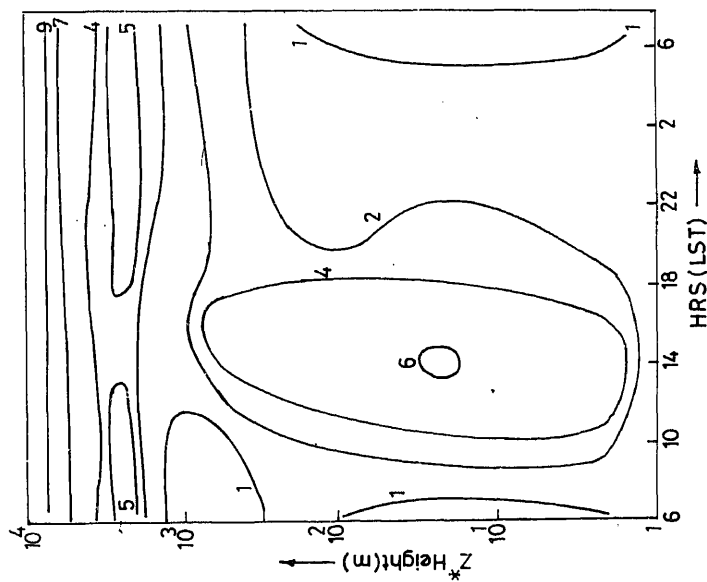


Figure 3. Diurnal variation of $(|\vec{V}|)$ at Port Blair for flat island with condensation. Magnitudes of velocities are marked in near isolines.

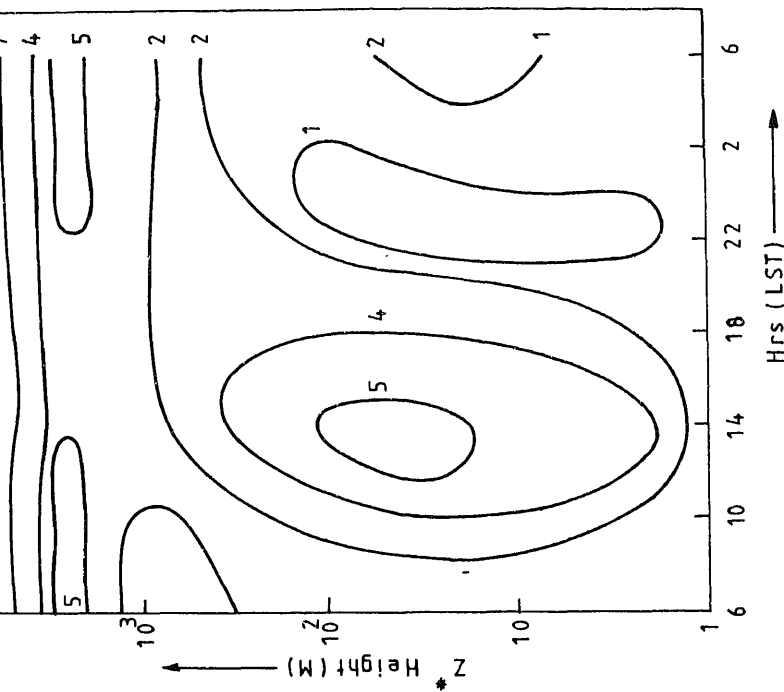
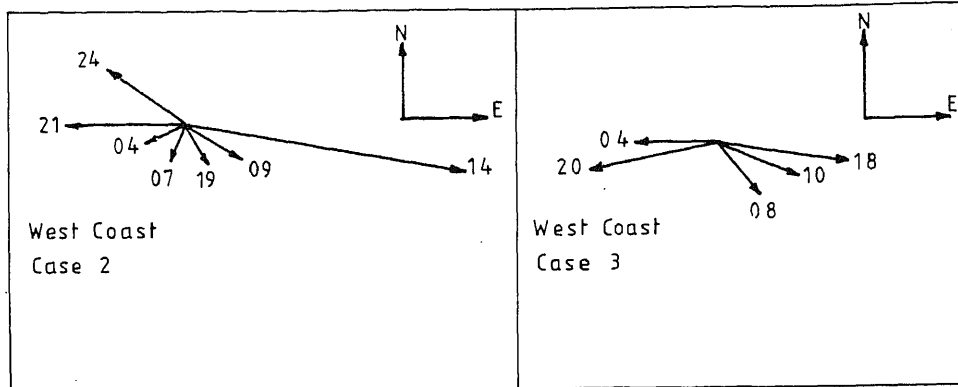


Figure 4. Same as figure 3 for island with topography and condensation.



Figures 5 and 6. Wind direction variations in the lee edge of the island for island with condensation and island with topography and condensation respectively. (The local times are marked at the end of arrows).

The temporal variations of u at the west end at selected hours are shown in figure 7 for case 3. The depth of sea breeze can be deduced from the above figure by the change in wind direction. The maximum intensity occurs around 1400 LST at a height of 20 m with the depths of about 600 m. A comparison with case 2 results shows that the elevated terrain strengthens the intensity of sea breeze. For example, at 20 m and 100 m height, the wind speeds at 1200 LST are 6.2 m/sec and 5.3 m/sec, while in case 2, the values are 5.4 m/sec and 4.6 m/sec respectively at the same time.

An analysis of horizontal penetration distance of the sea breeze at different hours has shown that the on-shore flow from the east and west meet at a distance of 8 km from the west coast at their peak intensities. This distance remains the same in all cases. The spatial intensity variations reveal an increase from the time of arrival to 1400 LST and decreases after 1400 LST. The convergence zone created at 8 km is the most likely region of formation of clouds and precipitation. A comparison of cases 1 and 2, shown in figure 8, reveals an increase in intensity but with the same horizontal extent of penetration, when the latent heat released by condensation is added.

4.3 Land breeze

The land breeze was inferred by the directional changes of the wind at the edges of the island. These changes are marked in figures 5 and 6. From early hours in the morning (0200 LST) till sunrise, the wind direction at both ends of the island occurs with a phase difference exceeding 90° . Clearly due to the island, a land breeze develops over it. At 0400 LST, the wind direction on either side of the island is 180° out of phase. At a height of 20 m, at the west and east ends of the island, wind speeds of magnitude 1.5 m/sec and 0.6 m/sec are observed respectively over a flat terrain (case 2). With topography (case 3) wind speeds of 2.5 m/sec and 2.1 m/sec develop at the above locations. The increase in wind speed is caused by down slope winds due to surface cooling, in addition to an offshore pressure gradient created by the differential cooling between land and water.

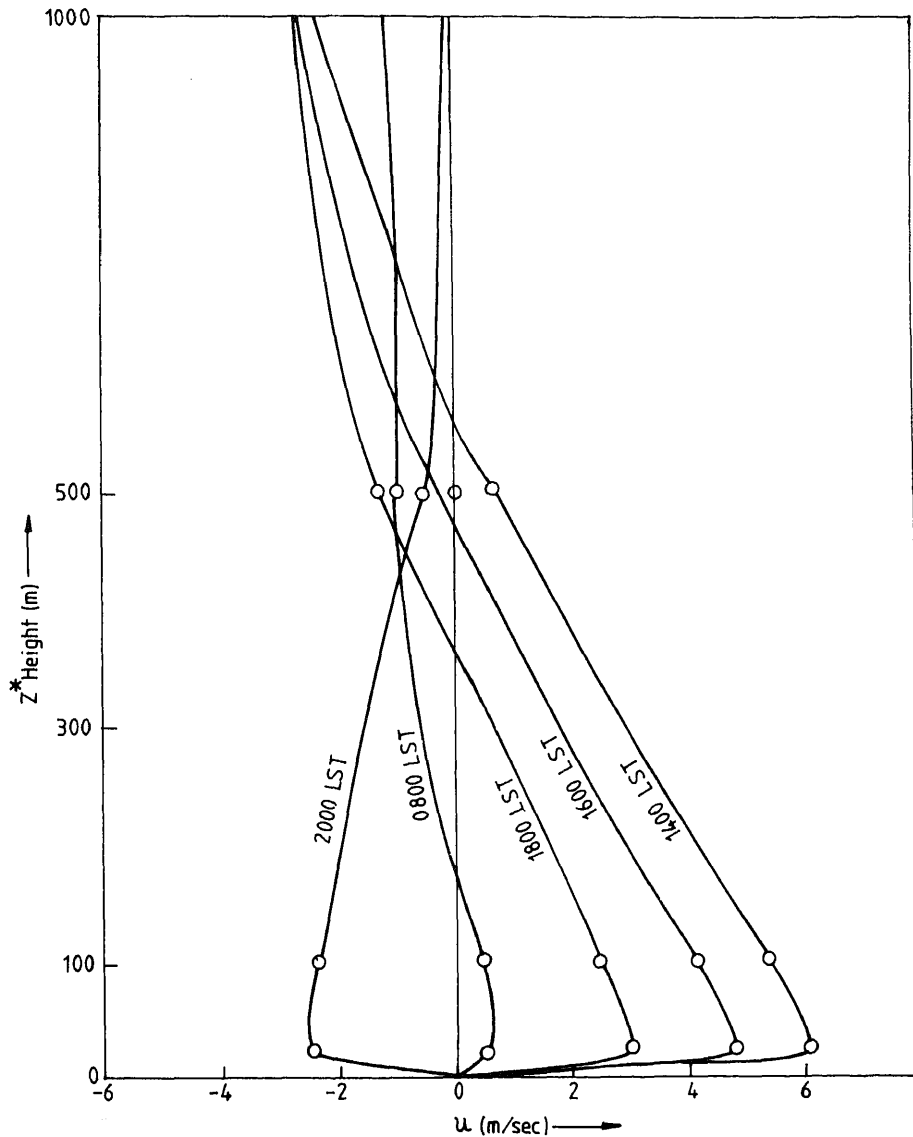


Figure 7. u velocity vertical profile at selected hours — for island with topography and condensation.

The vertical velocity pattern also shows a subsidence over the entire island. The hourly relative humidity changes at a screen height (2 m) indicate that the east end has uniform high relative humidity over a full diurnal cycle than the rest of the two locations. The effect of sea breeze on the west end is marked by higher relative humidity than the centre of the island. A comparison of relative humidity with and without topography, shown in figure 9, reveals that during night-time air over sloping terrain is drier than that over flat island.

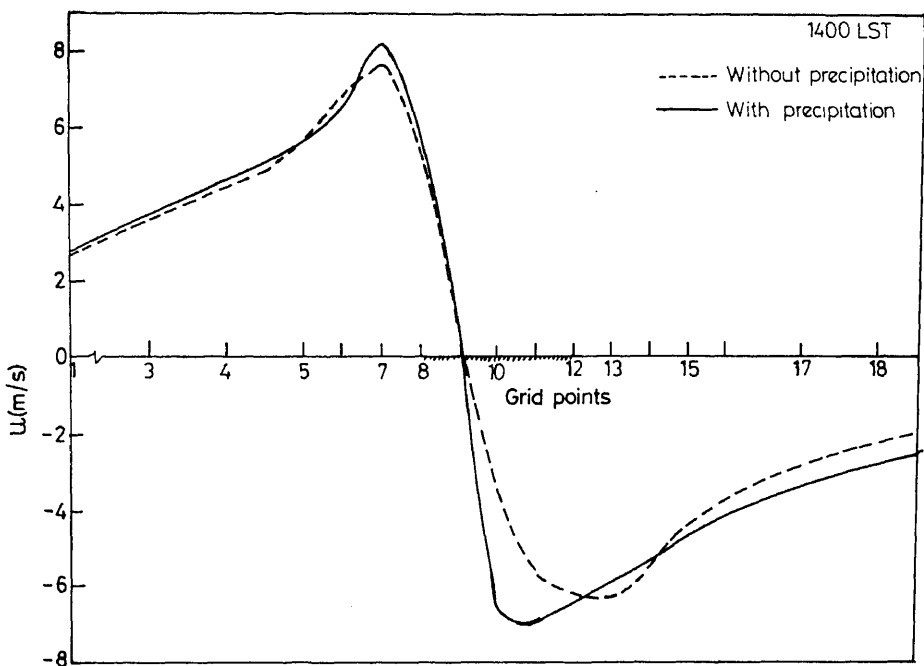


Figure 8. Spatial variation of u at 10 m height — cases 1 and 2 (1200 LST). Island is located between 8 to 12th grid point on x-axis.

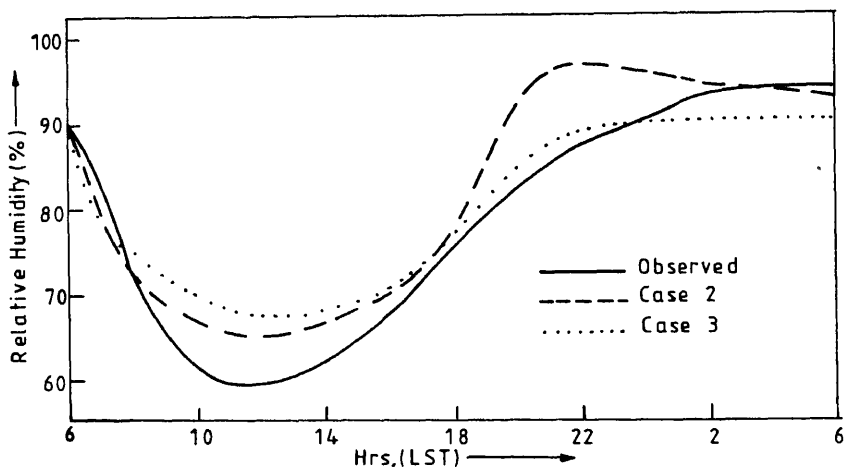


Figure 9. Hourly relative humidity changes with and without topography over Port Blair at 2 m height. The recorded values are shown as (O).

Thus a comparison of the results reveals that the intensities of sea and land breezes are increased by the presence of topography. However the horizontal extent of penetration of the sea breeze during daytime remains the same in both cases. The maximum speed (6 m/sec) occurs at an altitude of 20 m. This low value may be attributed to the development of a stable layer at low levels (500 m). The

addition of latent heat by condensation and the presence of topography increase the wind speed to higher levels during daytime as shown in figure 4.

4.4 Vertical velocity (w)

The time sequence of vertical velocity (w) patterns are shown in figures 10, 11 and 12 for cases 2 and 3. During maximum development, 1400 LST (figures 10 and 11), the following features are observed. The primary upward motion cell with velocities 60 cm/sec is over the west end of the island at an elevation of 1 km above the surface in both the cases. Such a large velocity near the convergence zone is not uncommon (Findlater 1964). The downward motion of cells appears with a magnitude of -20 cm/sec and -10 cm/sec at an elevation of 1.5 km and 3.7 km. The cell with higher magnitude appears at a distance of 6 km from the east end while the weaker cell occurs at a distance of 10 km away from the west end to the lee of the island. At levels below 500 m, the windward slope, upward motion with subsidence to the lee appears. They have magnitudes of 15 cm/sec and -5 cm/sec. The rising motion and sinking cell developed in the lower layer is due to the ascent of air over the slope and descent downwards. Over-flat terrain (figure 10) and uniform rising motion is noticed upto 100 m. A comparison of the results at sunset (not shown here) almost close to the time of sea breeze withdrawal from the west end, exhibits similar features but with reduced magnitudes.

At 0400 LST, weak subsidence is noticed over the entire island. With topography (figure 13) two identifiable subsidizing cells with equal magnitudes -3 cm/sec are noticed at the eastern and western slopes. The drainage flow over the eastern and western slopes occurs within 100 m. This could be due to higher rate of cooling at

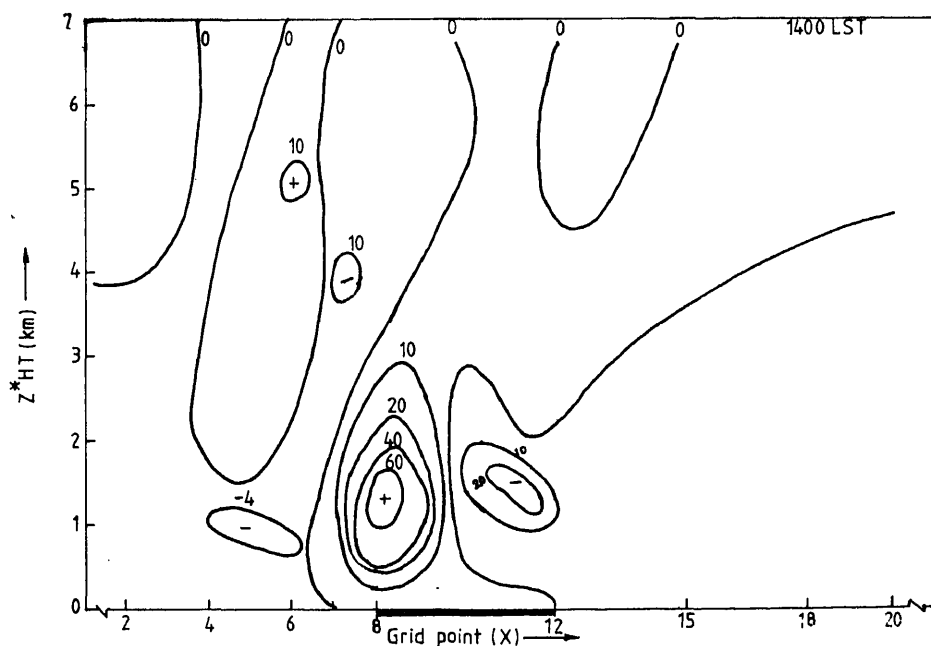


Figure 10. Vertical velocity w pattern in cm/sec at 1400 LST for island with condensation.

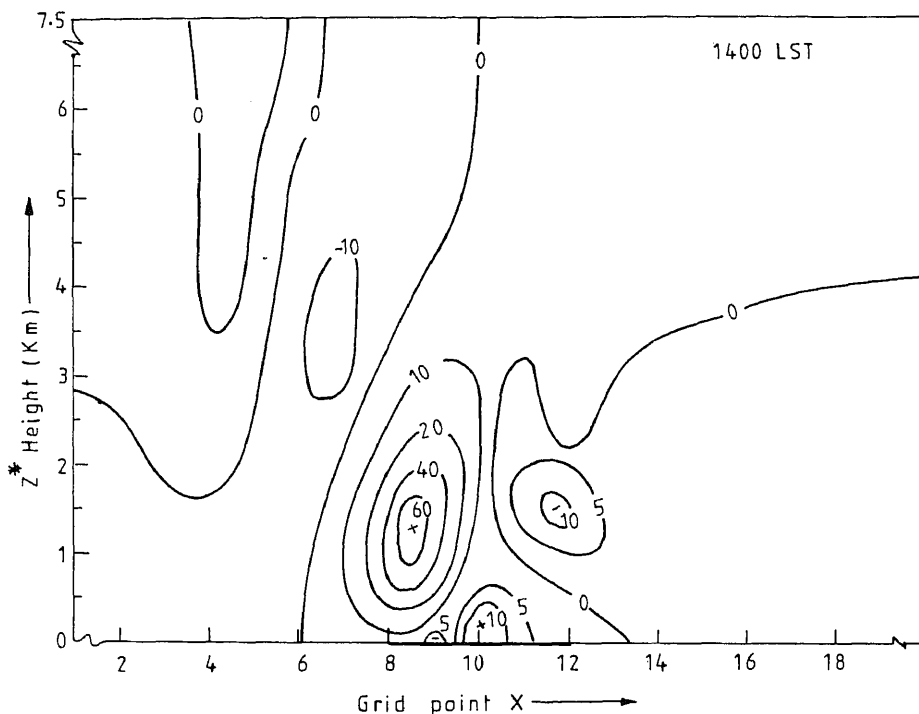


Figure 11. Same as figure 10 for island with topography and condensation.

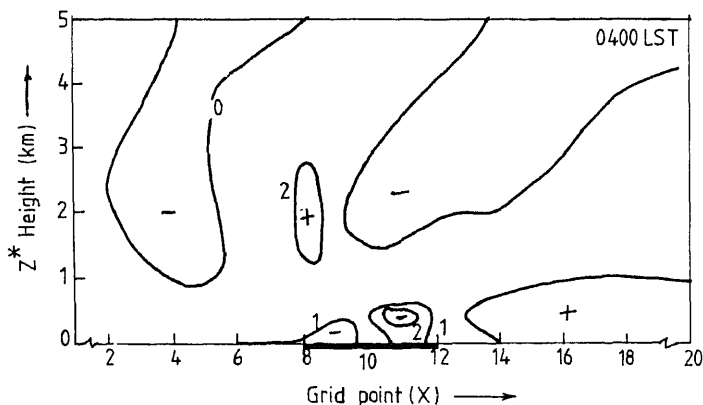


Figure 12. Same as figure 10 at 0400 LST for island with topography and condensation.

eastern slopes. The surface temperatures developed reveal that the east coast has a lower temperature than the west coast after sunset.

The effect of latent heat released by condensation can be obtained by comparing case 2 results with case 1 results for a flat terrain. A comparison of vertical velocity patterns obtained with and without condensation shows that the addition of latent heat release by condensation intensifies the rising motion over lee of the island and windward side sinking motion considerably. The leeside sinking motion is eliminated (-5 cm/sec). Similar results (not shown here) are also obtained by

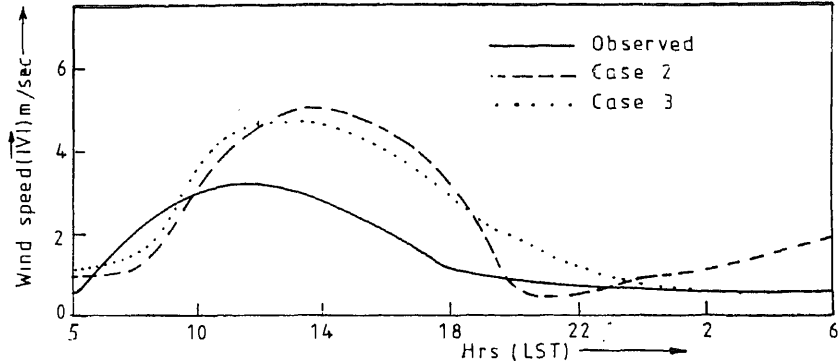


Figure 13. Comparison of predicted V values at 10 m height with observed data.

Comparing cases 2 and 3. Thus, irrespective of terrain features, the addition of latent heat increases the intensity of perturbations. A similar conclusion is obtained by Hjelmfelt and Brahm (1983).

5 Surface temperature

Similar to Barbados results obtained by Mahrer and Pielke (1976), despite a small width (25 km) the island surface does not uniformly get heated during daytime. The leeward edge develops a higher temperature than windward edge. A temperature difference of 2°C is developed between these ends at local noon. The cooling at these ends is also not uniform. A rapid cooling is noticed at the eastern end beginning from early afternoon hours. This is due to the advance of cooler marine air into the island by weakening of sea breeze and reduction of insolation at the eastern end.

6 Comparison of results with observations

In figures 13 and 14, the model-predicted horizontal wind speed at anemometer height (10 m) and air temperature at 2 m height are compared with observations at Port Blair. The simulated values are in good agreement for relative humidity (figure 9) and temperature during most of the daytime. However, considerable deviations are noticed at night starting from 2200 LST. Similarly the model overestimates the wind speeds, especially in daylight hours. These deviations may be due to the inadequate representation of physical effects such as forest coverage, albedo and soil wetness changes that are not considered here.

The 12 hr simulated vertical profile of wind speed shown in figure 15 is slightly different from that of the observed profile, as expected, since the actual atmospheric system will, in general, be non-realistic without inclusion of third spatial dimension. With the condensation scheme, a precipitation of 0.14 mm at Port Blair and 0.8 mm at the west end is obtained at the end of 24 hr simulation.

7 PBL height

The spatial and temporal variations at selected hours are illustrated in figure 16. At 200 LST results of cases 2 and 3 are compared; the depth variations by topography

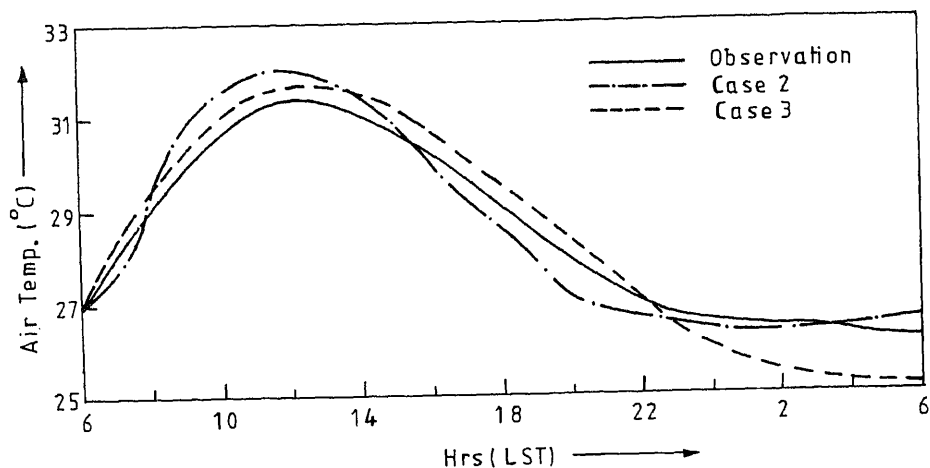
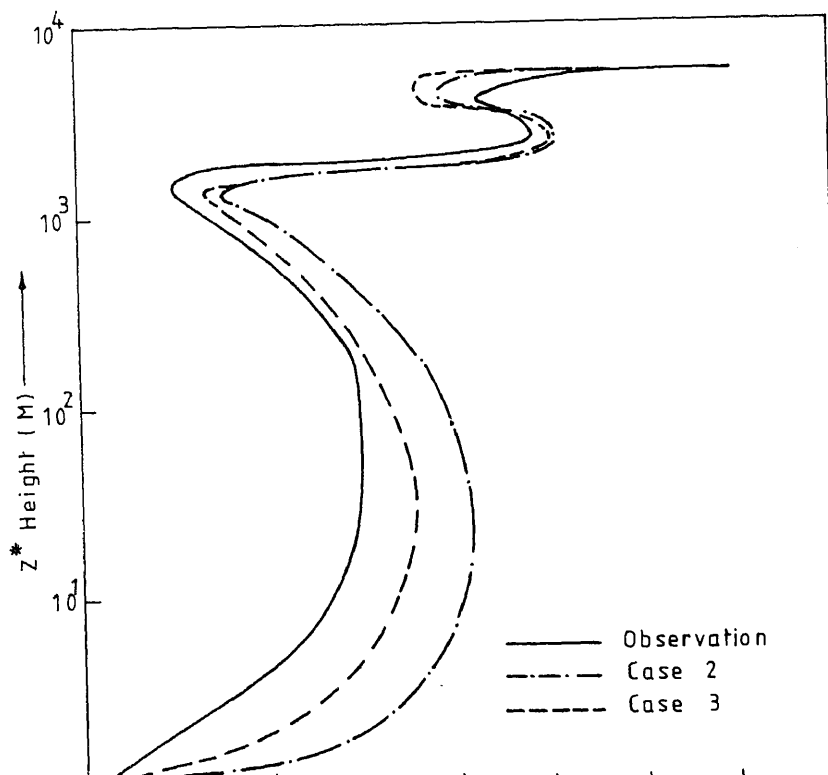


Figure 14. Same as figure 13 for temperature at 2 m height.



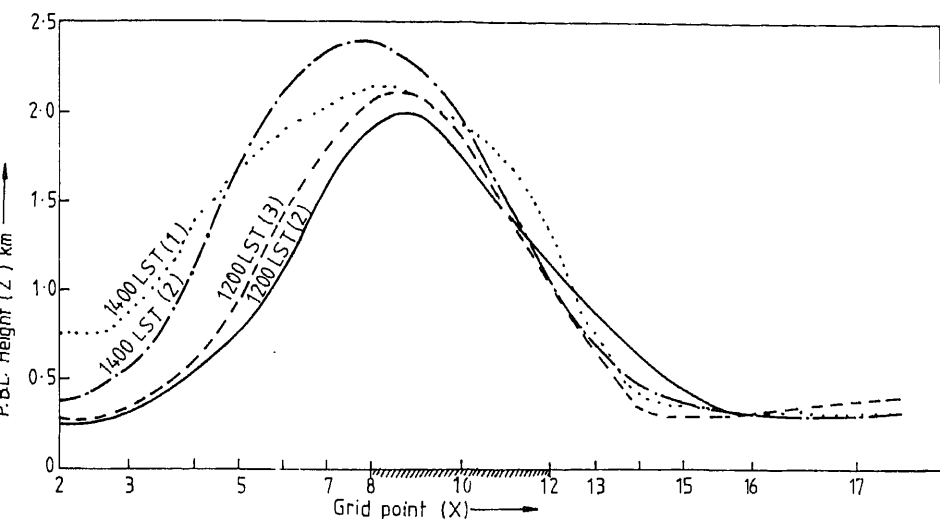


Figure 16. Spatial and temporal PBL depth variations at selected hours for island with condensation and island with topography and condensation.

alone can be obtained from this. At Port Blair, the inflow (east) end of the island, the depth is about 1 km for both the cases. In the downward direction, a maximum depth difference of about 100 m, about half the height of topography, is noticed. The hourly variations at the ends of the island (not given here) show that the west end developed a higher depth by a steep rise beginning from 1000 LST and a slower rate of fall in the afternoon hours than the east end. The temperature contrast, the reduction of insolation at the east end in the afternoon hours and different cooling rates are the reasons for the steep rise and subsequent slow changes at the west end. The addition of heat by condensation increases the PBL depth by around 300 m, considerably more than that of topography as shown by 1400 LST results (cases 1 and 2). We can conclude from this that the thermal effects are far more important than topography in the development of deeper PBL. This may be due to the low elevation and gentle slope of the topography considered in this study. The above results, so far not obtained for this area, may have a practical application in the location of industrial effluent chimneys for efficient pollutant dispersal with minimum hazard.

4.8 Simulated results with November data

On this day, stratus clouds covering 3/10th of the sky were noticed at sunrise. There was no development or approach of large scale pressure systems in the vicinity of the island. At the start of simulations, general wind direction was from NE and wind speeds at low levels were higher than that observed in April. An increase in cloudiness during daytime and 7 mm rainfall was reported in synoptic observations at the end of 24 hr. The synoptic observations are given in table 1 and figure 17 (θ and q profiles). The relevant soil temperature profile was used.

The simulated flow features (u , w components) with condensation are shown in figure 18. For clarity, only the positive vertical velocity area and pattern below

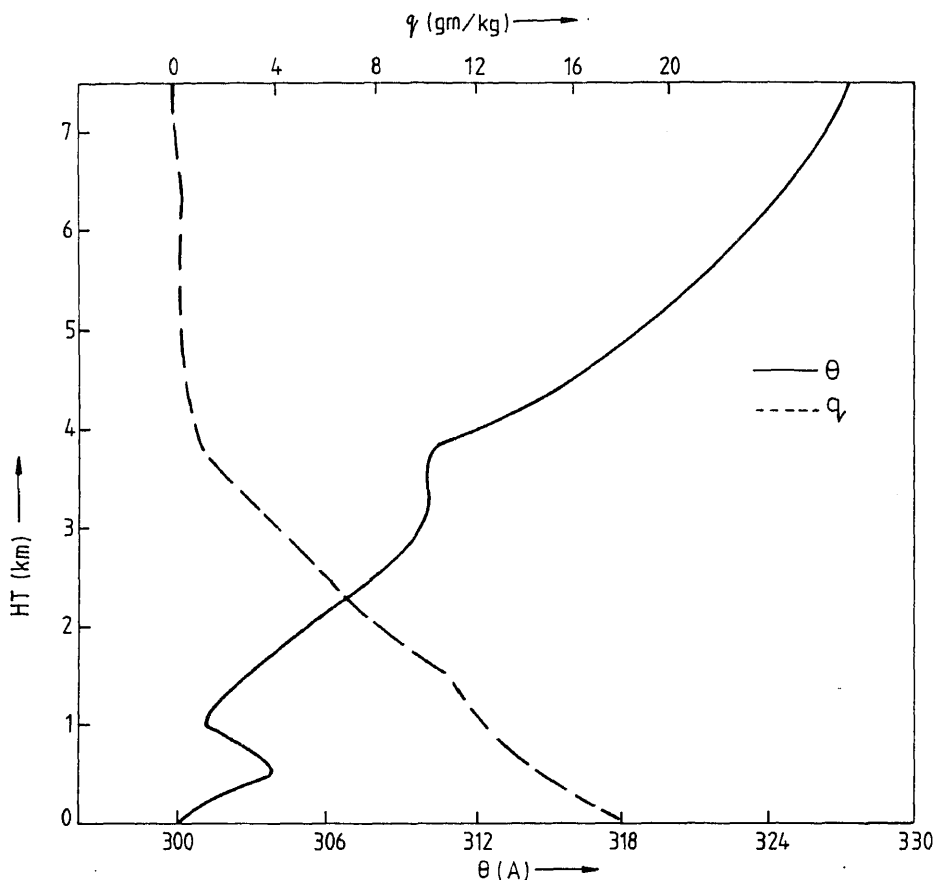


Figure 17. θ and q profiles — 0600 LST — 13th November 1968.

2.5 km are shown in above figure. During maximum surface heating (1200 LST), the following features are observed.

Within 1 km height strong winds of magnitude 5–6 m/sec develop over the island. Over the sea, comparatively weak winds with magnitude 2–3 m/sec occur at the same levels. At heights 1.5 km and above the situation is reversed, viz wind speeds with higher magnitude develop over the sea than over the island itself at the same heights. Counter gradient westerly winds in response to differential pressure gradient are seen at a distance of 20–25 km in leeward side of the island. The developed westerly flow is shallow (20 m) with no condensation (not shown here) and with condensation it reaches to a height of 100 m. There is no inland sea breeze penetration during the entire day. During maximum development the westerly flow is at a distance of 20 km from the west end of the island. The region of maximum vertical velocity development, shown in figure 18 by stapled lines, is located above the wind shift line at a distance of 20 km. Without condensation, velocity of 15 cm/sec (not shown here) and with condensation 25 cm/sec are developed at 1 km height. Over the island itself subsidence with velocity 2–3 cm/sec is noticed. The appearance of upward motion cell away from the island is due to strong

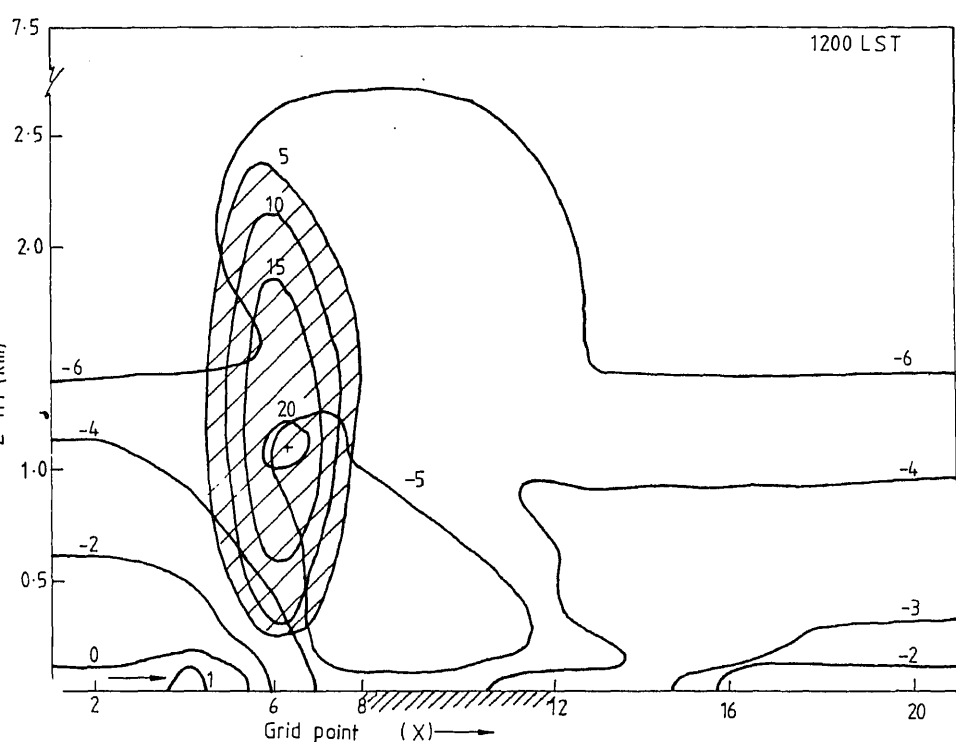


Figure 18. u and w patterns at 1200 LST for 13th November 1968 for island with condensation.

advection by the winds that develop over the island. The reduced intensity and the shallow vertical development of sea breeze are also due to the strong winds. Thus, the intensity of prevailing flow remains a crucial factor in the development of sea breeze and location of upward velocity cell over heated surface. In general, as noted before, the effect of latent heat release by condensation strengthens the intensities of the perturbations with no major change in the location of flow features. Close to the region of convergence a precipitation of about 2.4 mm in 24 hr was simulated. On the island itself negligible precipitation was obtained. The simulated horizontal wind and precipitation pattern or the quantum of rainfall do not agree with the observations. The discrepancy may be due to the neglect of cloud cover in radiation calculations or the neglect of horizontal convergence of water vapour at low levels which increases the amount of cloudiness during the day and application of stable large scale condensation scheme in place of more sophisticated schemes.

5. Conclusions

The adopted model-simulated results are in reasonable agreement with the observations for a clear day. Realistic sea and land breeze characteristics are obtained with topography. Further refinements such as inclusion of cloud cover

changes, vegetation coverage and a better condensation scheme are necessary for a more realistic simulation for days with precipitation.

Acknowledgement

We gratefully acknowledge Prof. R A Pielke for providing us a listing of his model. We also thank the referee for his suggestions in improvement of the paper. We appreciate the technical assistance of Shri P Gulati.

References

- Bhumralkar C M 1973 An observational and theoretical study of atmospheric flow over a heated island. Parts I and II; *Mon. Weather Rev.* **101** 719–745
- Blackadar A K 1979 High resolution models for the planetary boundary layer; *Adv. Environ. Sci. Eng.* **1** 50–85
- Businger J A, Wyngaard J C, Izumi Y and Bradley E F 1971 Flux profile relationships in the atmospheric surface layer; *J. Atmos. Sci.* **28** 181–189
- Deardorff J W 1974 Three-dimensional numerical study of the height and mean structure of a heated planetary boundary layer; *Boundary-Layer Meteorol.* **7** 81–106
- Delage Y and Taylor P A 1970 A numerical study of heat island circulations; *Boundary-Layer Meteorol.* **1** 201–226
- Findlater J 1964 The sea breeze and inland convection — an example of their interrelation; *Meteorol. Mag.* **93** 82–89
- Hjelmfelt M R and Brahm R R 1983 Numerical simulation of the airflow over lake Michigan for a major lake effect snow event; *Mon. Weather Rev.* **111** 205–219
- Mahrer Y and Pielke R A 1976 Numerical simulation of the airflow over Barbados; *Mon. Weather Rev.* **104** 1392–1402
- Mahrer Y and Pielke R A 1977 A numerical study of the airflow over irregular terrain; *Contrib. Atmos. Phys.* **50** 98–113
- Mahrer Y and Pielke R A 1978 A test of an upstream spline interpolation technique for the advective terms in a numerical mesoscale model; *Mon. Weather Rev.* **106** 818–830
- Manabe S, Smagorinsky J and Strickler R F 1965 Simulated climatology of a general circulation model with a hydrological cycle; *Mon. Weather Rev.* **93** 769–798
- McNider R T and Pielke R A 1981 Diurnal boundary layer development over sloping terrain; *J. Atmos. Sci.* **38** 2198–2212
- O'Brien J J 1970 A note on the vertical structure of the eddy exchange coefficient in the planetary boundary layer; *J. Atmos. Sci.* **27** 1213–1215
- Smeda M 1979 Incorporation of planetary boundary layer processes into numerical forecasting model; *Boundary-Layer Meteorol.* **16** 115–129

Distribution of particulate organic carbon in the central Bay of Bengal

K NANDAKUMAR, K VENKAT and N B BHOSLE

National Institute of Oceanography, Dona Paula 403 004, India

MS received 10 November 1986; revised 25 May 1987

Abstract. Particulate organic carbon (POC) was measured for 77 water samples collected over a 3000 m water column along 88° E in the central Bay of Bengal. The POC values varied from 80 to 895 μg per litre at the surface and 171 to 261 μg per litre at 2000 m. The POC decreased with increasing water depth at all the stations. Deep water concentrations of POC were higher than those reported from other oceanic waters. Distribution of POC was not influenced by water masses. The POC was not significantly correlated with chlorophyll *a*.

Keywords. Particulate organic carbon; Bay of Bengal; chlorophyll *a*.

1. Introduction

Earlier studies on particulate organic matter (POM) of small particles ($< 50 \mu\text{m}$) collected by conventional sampling bottles produced contradictory results. In his review, Riley (1970) argued that POM is biodegradable and varied spatially and temporally. Subsequently, Menzel (1974) opined that POM is refractory and homogeneous below a depth of 300 m water column. However, studies using $\delta^{13}\text{C}$ data indicate that the former is the case (Eadie and Jeffrey 1973; Eadie *et al* 1978). Recent studies based on a large number of samples and covering wider geographic areas demonstrate that particulate organic carbon (POC) generally decrease with water depth (Gordon and Cranford 1985; Wangersky 1976; Copin-Montegut and Copin Montegut 1983), show a small scale variability (Wangersky 1974; Gordon *et al* 1979) and are correlated with surface primary productivity (Wangersky 1976; Gordon 1977).

As compared with the large POC data collected over the years from different oceanic regions, very little information is available on the POC distribution in the oceanic waters of the Bay of Bengal. Few studies carried out earlier are restricted to the euphotic zone (Radhakrishna 1978; Radhakrishna *et al* 1978; Bhattachiri *et al* 1980).

This paper presents the data on the distribution of POC in the oceanic waters (0 to 3000 m) of the Bay of Bengal. The general feature emerging from the results are compared and discussed with the data collected from other oceanic regions.

2. Materials and methods

Seawater samples were collected using Niskin water samplers (5–10 l) from surface to 3000 m depth at nine stations during 19th cruise of ORV SAGAR KANYA in the central Bay of Bengal from 10 October to 15 November 1985 (figure 1). For POC analysis, duplicate aliquots of 1 to 1.5 l were filtered through precombusted (450°C,

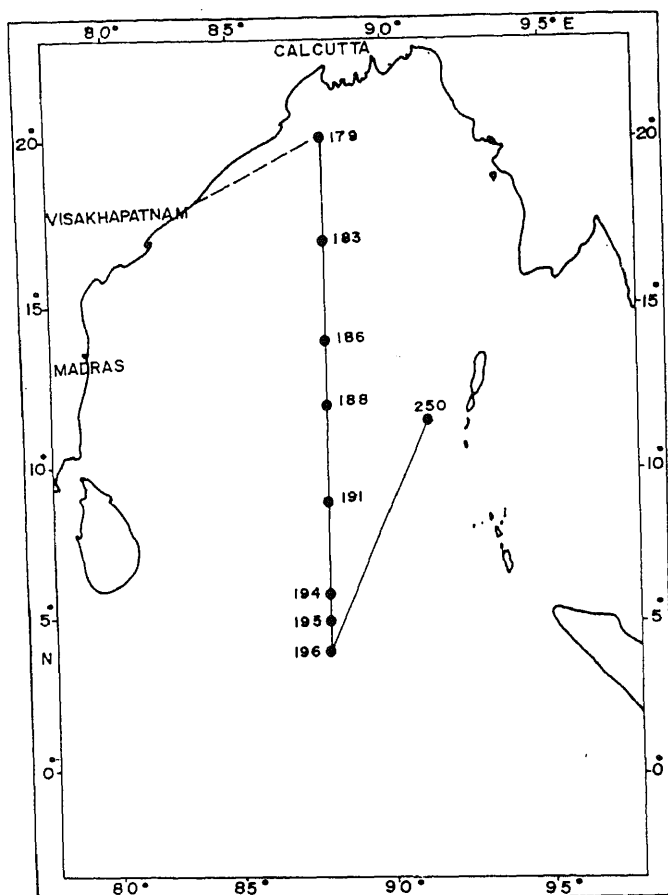


Figure 1. Location of sampling sites.

3 hr) 47 mm GF/C ($1.0 \mu\text{m}$ pore size) glass fibre filters. The suspended matter left on the filters was analyzed for POC and Chl *a*.

The POC was analyzed spectrophotometrically after wet oxidation of carbon by acid dichromate (Parsons *et al* 1984). The precision of the method at $50 \mu\text{g C}$ was ± 1.2 ($n = 6$). The Chl *a* concentration was also measured spectrophotometrically after extracting with 90% acetone (Parsons *et al* 1984). The precision of the analysis at $5 \mu\text{g l}^{-1}$ was ± 0.2 ($n = 5$). The Chl *a* values were not corrected for pheopigment. Temperature and salinity data were collected using ME-Multisonde CTD profiling system installed on board. The accuracy of the measurement of the system was temperature ± 0.02 and salinity $\pm 0.01^\circ$.

3. Results and discussion

Particulate matter collected from the central Bay of Bengal was analyzed for POC and Chl *a*. In the upper 100 m water column, POC concentrations ranged from 80

those reported earlier (Radhakrishna 1978; Radhakrishna *et al* 1978; Bhattathiri *et al* 1980). The mean surface concentration of POC decreased regularly with increasing depth upto 2000 m (figure 2). At 2000 m these values varied from 171 to 51 $\mu\text{g l}^{-1}$ ($\bar{x} = 205 \pm 37 \mu\text{g l}^{-1}$; $n = 4$). A single observation at 3000 m showed a small increase in POC concentration (figure 2).

Throughout the water column, POC concentrations showed large variations at all the stations and were similar to those reported for other oceanic regions (Gordon *et al* 1979). Such spatial differences could be either due to variations in the surface primary production or allochthonous organic matter inputs at these stations. Despite these large variations, POC concentration decreased with increasing depth at all the stations (figure 2). This gradual decrease with depth indicates biological utilization as particulate matter settles to the sea floor (Gordon and Cranford 1985).

A considerable differences of opinion has arisen regarding the distribution of POC in the deep waters. Menzel (1974) concluded that the distribution of POC in deep waters is homogeneous in depth, time and space, while others have reported regional and vertical variabilities of POC (Riley 1970; Wangersky 1976; Gordon 1977; Copin-Montegut and Copin-Montegut 1983; Gordon and Cranford 1985). Vertical distribution of POC in the Bay of Bengal suggests that the latter is the case.

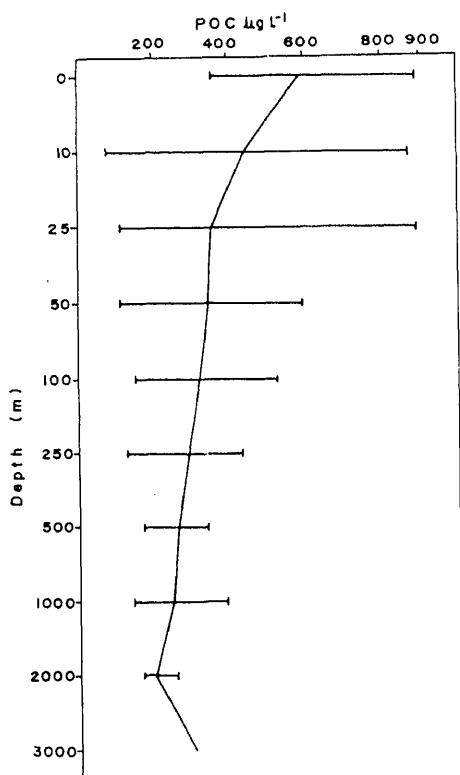


Figure 2. POC concentration vs depth profiles from the oceanic waters of the Bay of Bengal. Bar value indicates the range variations, the central value being the mean.

Table 1. Watermasses and POC in the Bay of Bengal.

Watermass	Depth (m)	Salinity (‰)	Temperature (°C)	n*	Mean POC $\mu\text{g l}^{-1}$ (Range)
Bay of Bengal subtropical water	0–100	31.22–35.04	20.50–29.16	45	443.57 \pm 160 (80.1– 895.85)
A mixture of Persian Gulf and Red Sea water	250–1000	34.98–35.09	6.48–13.24	18	270.68 \pm 89 (131.8– 436.5)
Indian Ocean deep and bottom water	> 1000	34.74–34.8	1.61–2.87	5	262.83 \pm 55 (171.4– 361.7)

*Number of samples

The POC values of the Bay of Bengal are comparatively higher than those reported from other seas and oceans (Menzel 1974; Wangersky 1976; Gordon 1977; Gordon and Cranford 1985). Higher values were in fact expected because surface primary production is high in the Bay of Bengal (Qasim 1977). Moreover large amount of suspended matter containing high organic matter is introduced into the Bay by six major rivers flowing through the various geological formations of Indian subcontinent (Rao 1985). Probably this high amount of organic matter and primary production are responsible for the higher values of POC observed here.

In order to assess the influence of hydrographical features on the distribution of POC, temperature and salinity data were collected. These values were used to characterize the water masses (Mamayev 1975). Three well-defined water masses were identified (table 1). Based on this, water column was divided into surface (< 100 m), intermediate (250 to 1000 m) and deep waters (> 1000 m). Irrespective of water mass, the mean and range of POC decreased in these depth groups (table 1). This strongly suggests active transport of POC from surface to deep water rather than advection of water masses containing higher and lower levels of POC.

Phytoplankton biomass (as Chl *a*) is generally the main source of POC in the marine environment. A simple regression analysis between Chl *a* and POC was used to find out the contribution of Chl *a* carbon to POC. A non-significant relationship ($r = 0.20$; $n = 45$; $Y = 428.80 + 45.10 X$) between these two parameters suggests that not much of Chl *a* carbon was associated with POC. On the other hand, this indicates that POC is detrital in nature.

Acknowledgements

The authors thank the late Dr H N Siddiquie for constant encouragement. We also thank the referees for suggesting improvements in the manuscript.

References

- Bhattathiri P M A, Devassy V P and Radhakrishna K 1980 Primary production in the Bay of Bengal during southwest monsoon of 1978; *Mahasagar-Bull. Natl. Inst. Oceanogr.* **13** 315–323

- Copin-Montegut C and Copin-Montegut G 1983 Stoichiometry of carbon, nitrogen and phosphorus in marine particulate matter; *Deep Sea Res.* **30** 31–46
- Eadie B J and Jeffrey L M 1973 $\delta^{13}\text{C}$ analyses of oceanic particulate matter; *Mar. Chem.* **1** 199–209
- Eadie B J, Jeffrey L M and Sackett W M 1978 Some observations on the stable carbon isotope composition of dissolved and particulate organic carbon in the marine environment; *Geochim. Cosmochim. Acta* **42** 1265–1269
- Gordon D C 1977 Variability of particulate organic carbon and nitrogen along the Halifax–Bermuda section; *Deep Sea Res.* **24** 257–270
- Gordon D C and Cranford P J 1985 Detailed distribution of dissolved and particulate organic matter in the Arctic Ocean and comparison with other oceanic regions; *Deep Sea Res.* **32** 1221–1232
- Gordon D C, Wangersky P J and Sheldon R W 1979 Detailed observations on the distribution and composition of particulate organic material at two stations in the Sargasso Sea; *Deep Sea Res.* **26** 1083–1092
- Mamayev O I 1975 *Temperature salinity analysis of world ocean waters* (Amsterdam: Elsevier) pp. 369
- Menzel D W 1974 in *The sea* (ed.) E D Goldberg (New York: Interscience) pp. 659
- Parsons T R, Matai Y and Lalli C M 1984 *A manual of chemical and biological methods of seawater analysis* (Oxford: Pergamon) pp. 63–104
- Qasim S Z 1977 Biological productivity of the Indian Ocean; *Indian J. Mar. Sci.* **6** 122–137
- Radhakrishna K 1978 Primary productivity of the Bay of Bengal during March–April 1975; *Indian J. Mar. Sci.* **7** 58–60
- Radhakrishna K, Bhattathiri P M A and Devassy V P 1978 Primary productivity of the Bay of Bengal during August–September 1976; *Indian J. Mar. Sci.* **7** 94–98
- Rao C H M 1985 Distribution of suspended particulate matter in the waters of eastern continental margin of India; *Indian J. Mar. Sci.* **14** 15–19
- Riley G A 1970 Particulate organic matter in seawater; *Adv. Mar. Biol.* **8** 1–118
- Wangersky P J 1974 Particulate organic carbon: Sampling variability; *Limnol. Oceanogr.* **19** 980–984
- Wangersky P J 1976 Particulate organic carbon in the Atlantic and Pacific oceans; *Deep Sea Res.* **23** 457–465

North-south asymmetry in response of geomagnetic activity to different solar events*

G K RANGARAJAN

Indian Institute of Geomagnetism, Colaba, Bombay 400 005, India

MS received 13 February 1987; revised 8 June 1987

Abstract. Study of the response of geomagnetic activity to five different kinds of solar events reveals that an average north-south asymmetry of about 15% exists which diminishes with enhanced geomagnetic activity. The response of the geomagnetic field is quite significant only when high speed solar wind stream in association with sector boundary of interplanetary magnetic field (IMF) or solar proton streams near sector boundary sweeps past the earth. When the frequency of occurrence of indices of geomagnetic activity is considered, the index zero shows a marked difference in its response characteristics for the southern hemisphere. This appears to be a real feature and not attributable to any artefact of the index or its derivation.

Keywords. Asymmetry; geomagnetic activity; solar wind streams; solar proton events; sector boundary.

1. Introduction

It is well known that geomagnetic activity is substantially enhanced following solar particle events, passage of high speed solar wind streams and sector boundaries of interplanetary sector structure past the earth (Svalgaard 1978; Rangarajan 1980, 1981). Mayaud (1968) derived geomagnetic activity indices K_n and K_s separately for the northern and southern hemisphere in an effort to improve the existing K_p indices. In his analysis of 9 years of these indices, Mayaud (1970) found a real asymmetry of about 5–7% between the northern and southern hemisphere even after allowing for improper scaling, contamination by regular daily variation, (S_R) and ground induced effects. Siebert (1968) showed that the magnetic activity in the northern (southern) hemisphere was higher for the IMF directed away from (toward) the sun. These results were confirmed using longer series of a_n and a_s indices by Berthelier and Guerin (1973). Berthelier (1979) (quoted by Mayaud 1980) gave a quantitative estimation of 5.4% for the asymmetry during 1964–69. The intensity of the asymmetry was shown to depend on the direction and magnitude of the N–S component of IMF. Using frequencies of occurrence as well as the magnitude as the crucial parameters, Rangarajan (1979, 1980) brought out the nature of the N/S asymmetry related to IMF sector structure and pointed out that the occurrence of very quiet intervals ($K_s = 0$) prior to the passage of a $+/-$ sector boundary passage was far in excess of the corresponding $K_n = 0$ and that the distinction vanished for higher values of the index.

Response of geomagnetic activity to passage of IMF sector boundary has been shown to be more enhanced when the boundaries are associated with solar protons with energies in the range of few MeV (Wilcox 1979) and with high speed solar

wind streams (Rangarajan 1983). Yoshizawa (1984) recently demonstrated that (i) the effect of sector polarity of IMF on the N/S asymmetry is due to the B_y and not the B_x component and (ii) the asymmetry appears only when IMF is directed southward, increasing with enhanced magnitude of the southward component.

In this paper we derive the response of the geomagnetic activity in the N and S hemispheres separately following well-defined solar events to bring out the nature of the asymmetry. We also confirm the peculiar occurrence characteristics of the southern hemisphere index $K_s = 0$, found earlier in association with polarity of IMF.

2. Data and analysis

Three hourly indices K_n , K_s and their equivalent amplitudes a_n and a_s introduced by Mayaud (1968) form the basic data set. The 3-hourly data were analysed according to their magnitudes 0, 1, 2, 3 and 4. As the occurrence frequencies of indices with magnitude greater than 4 were small, all were consolidated as group 5. Five different choices of solar events have been made as detailed below. References in brackets give the source of the choice of key days. (i) Onset of low energy solar proton event during 1959–1969 coincident with transit of well-defined sector boundaries (Svestka *et al* 1976). (ii) Transit of well-defined sector boundaries without associated solar proton events during 1959–69 (from Svalgaard 1975). (iii) Onset of low energy solar proton events without associated sector boundary passage during 1959–69 (from Svestka and Simon 1975). (iv) Solar flares which are sources of particle events during 1959–69 (from Svestka and Simon 1975). (v) High speed solar wind streams associated with solar proton events (from Lindbladt and Lundstedt 1981).

In a recent study, Shah *et al* (1984) showed that geomagnetic field is more prone to disturbances around June solstice than December solstice leading to a significant solstitial asymmetry. In order to avoid contamination of the magnitude of the N/S asymmetry by this factor we have chosen the dates of onset of the 5 categories listed above to be as near to each other as possible. Basing our list of proton events (with 43 key dates) as the guideline, the other lists were reduced to closely match the key day list for the first category. As the dates covered all the months of the year, the solstitial asymmetry is expected to average out. Any residual effect would be comparable by the choice of key days. Adopting a procedure of superposed epoch analysis similar to that explained by Rangarajan (1979, 1980) the response of the daily index A_n and A_s of geomagnetic activity as well as the occurrence frequency of different magnitudes of the indices 0, 1, 2, 3, 4, 5 are computed. The percentage asymmetry given by $2 [(A_n - A_s)/(A_n + A_s)] \times 100$ for the responses in five categories are derived and discussed.

3. Results and discussion

3.1 Response characteristics in magnitude of geomagnetic activity

The change of magnitude of A_n and A_s (daily equivalent amplitude for the northern and southern hemispheres respectively) is shown in figure 1 for the five classes of

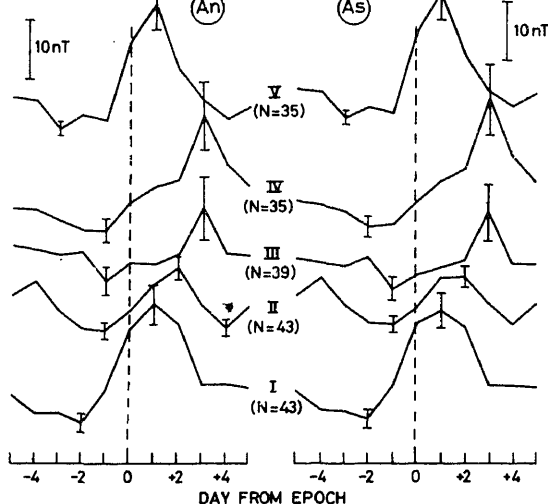


Figure 1. Changes in the magnitude of the northern (A_n) and southern hemisphere (A_s) activity indices associated with the passage of five categories of solar events (please see text for description). Vertical bars on the curves are standard error of the mean value. The number in parentheses gives the number of key days used in the analysis.

solar events. It is readily apparent that solar proton events (SPE) associated with sector boundaries (cat. i) and high speed solar wind streams associated with SPI (cat. v) are most geoeffective compared to the other three categories. These results are consistent with the finding of Wilcox (1979) that geomagnetic activity showed a large increase following proton boundary transit and no significant change following other boundary transits. Rangarajan (1981) had earlier analysed the response of low latitude geomagnetic field to the passage of high speed solar wind streams with or without associated sector boundary of IMF. He found that the enhanced solar wind stream affected the low latitude geomagnetic field through the symmetric ring current intensification but when the streams are associated with sector boundary, the field depression was more significant as also the asymmetric component of the low latitude field. Rangarajan (1983) also showed that when the duration of the high speed stream was shorter, the geoeffectiveness was larger. Here it is found again that high speed solar wind stream has the largest associated response for both A_n and A_s . Enhanced geomagnetic activity is also found to be significant following solar flares identified as responsible for particle events and the peak activity occurs 3 days after the flare, equivalent to transit time of solar wind velocity of about 550–600 km/sec corresponding to fast stream velocities. From the insignificant response for categories (ii) and (iii) it appears that IMF polarity change not accompanied by enhanced low energy proton flow or vice versa and are not geoeffective.

As the magnitudes of the response of the hemisphere indices are different for the various epochs considered, we can check the strength of the N/S asymmetry associated with these solar events. The asymmetry (percentage) computed as $[(A_n - A_s)/(A_n + A_s)] \times 100$ (Svalgaard 1978; Shah *et al* 1984) for 5 days on either side of the key days is shown in figure 2. Two points are worthy of note; (i) there exists an average asymmetry of about 15% for all categories which is independent

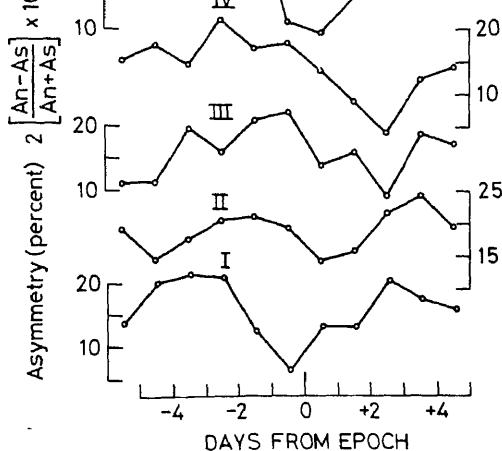


Figure 2. Percentage asymmetry in the response of geomagnetic activity derived from A_n and A_s for five classes of solar events.

of the choice of key days. This is a little higher than the figures of 10% given by Mayaud (1970) (and that shown by Yoshizawa 1984). On the other hand it is well below the asymmetry of about 60% in June solstice and about -5% in December solstice leading to an average above 30% shown by Shah *et al* (1984). It seems difficult to envisage any physical mechanism that can explain the magnitude of nearly 60% for the asymmetry derived by Shah *et al* (1984). However, if one computes the asymmetry from the response of A_n and A_s to solar flares during summer solstice given by them (their figure 5), the percentage of asymmetry shown in their figure 6 appears to be erroneous. Again in contrast to their results that the hemispheric asymmetry in geomagnetic activity is independent of the chosen solar event (flares or Forbush decrease) we find that when the activity responds, the percentage asymmetry varies inversely with the strength of activity (i.e. when geomagnetic activity is enhanced the asymmetry decreases). Mayaud (1980) had earlier demonstrated that the ratio A_n/A_s decreases with enhanced activity almost becoming unity for higher activity. For categories (i) and (v) we find that the percentage sharply drops by about 15% before rising up again in the post-passage period. Yoshizawa (1984) found that the asymmetry appears only when IMF is directed southward and is augmented by the solar wind velocity. Here we find that when high speed solar wind sweeps past the earth the asymmetry shows a significant reduction. In other words, enhanced solar wind velocity when most geoeffective, diminishes the asymmetry. Similar reduction in the strength of the asymmetry associated with passage of solar proton events suggests that, perhaps in both categories (i) and (v) the asymmetry is brought about by parameters other than solar wind velocity. It should also be borne in mind that Yoshizawa's results are for B_y dependent N/S asymmetry as a function of the magnitude of southward IMF whereas in our analysis magnitudes of B_z will be averaged out. Our results are also in conformity with Mayaud's (1970) finding that the ratios A_n/A_m and A_s/A_m tend to unity leading to diminished asymmetry as geomagnetic activity increases.

2.2 Response characteristics in frequency of occurrence of K_n and K_s

The frequency of occurrence of the K index as a parameter provides meaningful and additional information on the nature of geomagnetic activity associated with solar events. It also enables distinguishing between quiet and disturbed intervals and the threshold separating them. We had earlier shown (Rangarajan 1979, 1980) that when the index has magnitude 0, the occurrence frequency in K_s is significantly larger compared to K_n and that the response in frequency of occurrence for the IMF polarity change \pm is significantly different for $K_s = 0$. To test the reality of these findings and to assess the nature of the response for the five different solar events, we computed the frequency of occurrence prior to and following the key days for different magnitudes of the indices K_n and K_s .

In figure 3 is shown the change in occurrence frequency of index 0. For all categories, $K_s = 0$ occurs about two to three times as often as $K_n = 0$. Superposed on this average difference, there exists a clear signature of the passage of high speed solar wind streams and solar proton events associated with sector boundaries for $K_s = 0$. Interestingly, in contrast to the result of the previous section, even for category (ii), $K_s = 0$ responds significantly. For all cases occurrence of $K_n = 0$ shows similar dependence on the key day, but with reduced magnitudes.

Occurrence of other magnitudes of the indices K_n and K_s for the 5 classes of solar events is shown in figure 4. The striking dissimilarity between K_n and K_s occurrence frequency observed in figure 3 is conspicuously absent. Even for the next higher magnitude ($K = 1$) there is no apparent N/S asymmetry and both indices respond similarly to the passage of the solar events. As would be expected the responses for $K = 1$ and $K = 4$ are reversed indicative of quiet and disturbed features.

Mikerina and Ivanov (1974) showed that when K_p index has magnitude < 1.33 , IMF could be inferred to have a northward component ($B_z > 0$) and when K_p is ≥ 3 , B_z would be directed southwards. The interval 1.5 to 3.0 of K_p coincided with

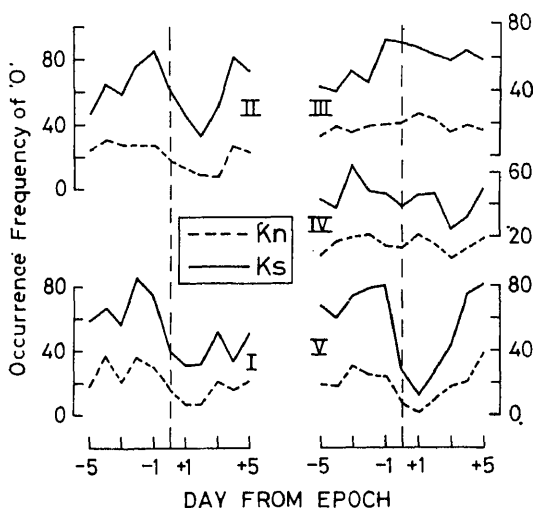


Figure 3. Change in occurrence frequency of the index 0 in northern (K_n) and southern (K_s) hemisphere associated with the passage of solar events. Note the consistently higher frequency for K_s .

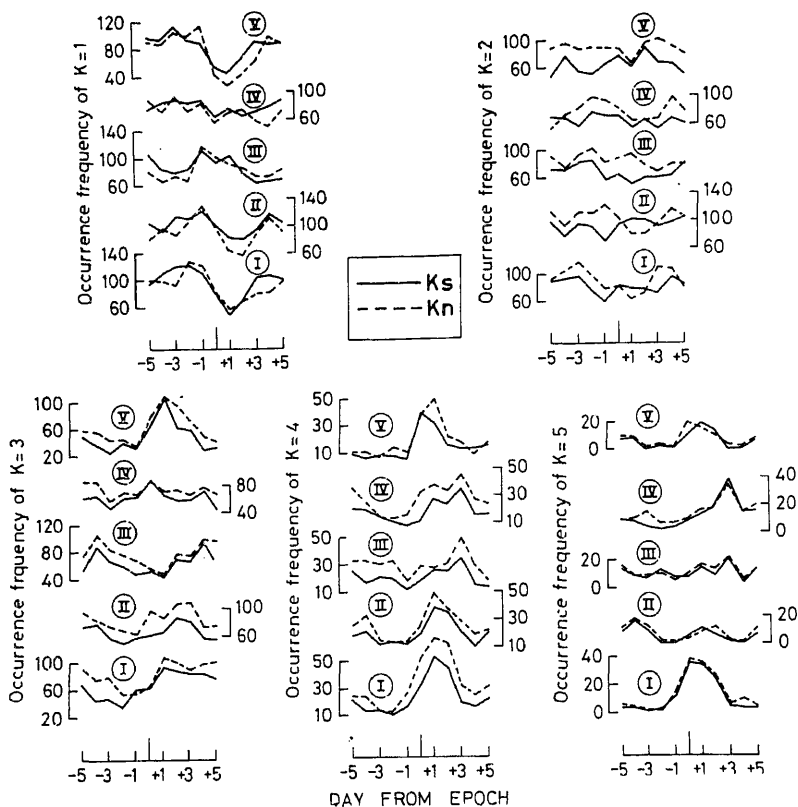


Figure 4. Change in occurrence frequency of different magnitudes of K_n and K_s index (1, 2, 3, 4 and 5) associated with the passage of five classes of solar events.

equal probability of occurrence of $B_z > 0$ and $B_z < 0$. In their study of the occurrence of quiet and disturbed intervals in association with sector polarity of IMF, Bhargava and Rangarajan (1971) could narrow down the interval of uncertainty for sign of B_z between 1.5 and 2.5. Mayaud (1980) had shown that the asymmetry in N and S hemispheric activity was larger when the indices had magnitude ≥ 1.5 . These results clearly indicate that $K = 0$ and 1 should be definitely indicative of $B_z > 0$ and $K \geq 3$ that of $B_z < 0$. If the responses shown in figures 3 and 4 are real effects during quiet conditions of magnetosphere then one should expect similarity of the behaviour of $K = 0$ and 1. The striking dissimilarity for the index 0 between K_n and K_s of figure 3 not seen for $K = 1$ could perhaps be attributed to residual effects of improper elimination of regular daily variation in one hemisphere vis-a-vis the other. However, Mayaud (1980) from his personal experience of scaling K -indices at the Km observatories concluded that this contamination is larger at the northern stations, implying that K_s data could be more reliable for lower values. The larger occurrence of $K_s = 0$ in comparison with $K_n = 0$ is consistent with the real feature of $A_n > A_s$ during quiet periods, mentioned earlier. It is tempting to ascribe the difference to the eccentricity of the earth's dipole and consequent asymmetry in the geometry of the magnetosphere during very quiescent condition. However, the conspicuous absence of the

difference between K_s and K_n for magnitude 1 (still considered to be representative of quiet magnetosphere) precludes this possibility. An aspect lending credence to the reality of the difference is the significant decrease in occurrence of $K_s = 0$ following high speed solar wind streams, solar proton events and solar sector boundary passage which would have been absent if it were only an artefact of improper scaling or elimination of S_R . The fact that $K_s = 0$ occurs more frequently irrespective of the choice of solar events suggests that the degree of magnetic disturbance in southern hemisphere is significantly less than in the northern hemisphere. If this feature were related to the direction of IMF being parallel or anti-parallel to the geomagnetic field direction in the tail, then the response of K_n or K_s with sector boundary passage should show dissimilarity. This dissimilarity should vanish when averaged over both types of sector boundaries — positive to negative and negative to positive polarity change. Figure 3 clearly shows that this is not true. A contributing factor could be the anomalous-induced magnetic field in southern hemisphere due to the presence of oceans. Some of the stations contributing to K_s index are islands. Support for this conjecture comes from the analysis of Rangarajan and Bhattacharyya (1983) who found anomalous behaviour for the strength of recurrent magnetic activity at Kerguelen islands (one of the K_s stations) when compared to its northern conjugate station Nurmijarvi. If the disturbance field magnitude is inhibited by induction effects, then the tendency to scale 0 more after in southern hemisphere can be explained. Alternatively we may have to infer a hitherto unknown difference between solar wind-magnetosphere interaction during very quiescent conditions of geomagnetic activity which would introduce a striking asymmetry. This could not be attributed to the solsticial asymmetry brought out by the geometry of the sun-earth configuration as the choice of data rules out this eventuality.

Figure 4 also reveals that $K = 2$ is again the transitory stage between quiet and disturbed intervals with differences in occurrence of K_n and K_s unrelated to the epochs under consideration. When $K \geq 5$ the asymmetry practically vanishes. Similar feature was reported earlier by Rangarajan (1980) for indices of magnitude ≥ 5 in association with IMF polarity change.

4. Conclusion

In conclusion it is suggested that there exists a real difference between the northern and southern hemisphere geomagnetic activity under very calm conditions of the magnetosphere. Conjugacy studies at suitable pairs of stations can throw some light on the precise nature of the difference. Global geomagnetic activity is significantly enhanced when the earth is immersed in a high speed solar wind stream associated with a proton boundary. During the enhanced activity periods the north-south asymmetry reduces or even vanishes.

Acknowledgement

This paper is based on the poster presentation at the National Space Science Symposium, Guwahati, February, 1986. The author is grateful to his colleague Dr

References

- Berthelier A and Guerin C 1973 Influence of the polarity of the interplanetary magnetic field on magnetic activity at high latitudes; *Space Res.* **13** 661–665
- Bhargava B N and Rangarajan G K 1977 Sector polarity of IMF and annual variation in occurrence of quiet and disturbed intervals; *J. Geomag. Geoelec.* **29** 1–7
- Lindbladt B A and Lundstedt H 1981 A catalogue of high-speed plasma streams in the solar wind; *Sol. Phys.* **74** 197–206
- Mayaud P N 1968 Indices K_n , K_s , K_m 1964–1967, CNRS 156 pp. Centre National de la Recherche Scientifique, Paris
- Mayaud P N 1970 Sur quelques proprietes de l'activite magnetique deduites de l'analyse d'une serie de neuf annees des indices K_n , K_s et K_m 1 Comparaison des niveaux d'activite dans chaque hemisphere; *Ann. Geophys.* **26** 109–131
- Mayaud P N 1980 *Derivation-meaning and uses of geomagnetic indices* Washington D C: American Geophysical Union pp. 154
- Mikerina N U and Ivanov K G 1974 Probability of identifying normal interplanetary magnetic field component from the planetary K_p index; *Geomag. Aeron.* **14** 123–124
- Rangarajan G K 1979 Irregular geomagnetic activity in the northern and southern hemispheres and sector boundary passage; *Proc. Int. Workshop on selected topics of magnetospheric physics, Tokyo* (ed) T Obayashi, Japanese IMS Committee 150–160
- Rangarajan G K 1980 Global geomagnetic activity and IMF sector boundary passage; *Indian J. Radio Space Phys.* **9** 73–76
- Rangarajan G K 1981 Solar wind streams sector boundary passage and low latitude geomagnetic field; *Indian J. Radio Space Phys.* **10** 54–57
- Rangarajan G K 1983 Solar wind stream characteristics and low latitude geomagnetic field changes; *Indian J. Radio Space Phys.* **12** 65–67
- Rangarajan G K and Bhattacharyya A 1983 Worldwide features of the strength of recurrent geomagnetic activity; *Proc. Indian Acad. Sci. (Earth Planet. Sci.)* **92** 5–13
- Shah G N, Kaul R K, Kaul C L, Razdon H, Merryfield W J and Wilcox J M 1984 Solsticial and hemispherical asymmetry in the response of geomagnetic field; *J. Geophys. Res.* **89** 295–300
- Siebert M 1968 Magnetic activity difference between the two hemispheres following the sector structure of the interplanetary magnetic field; *J. Geophys. Res.* **73** 3049–3053
- Svalgaard L 1975 An atlas of interplanetary sector structure 1957–1974; Rep. 629, Inst. for Plasma Res., Stanford University, California
- Svalgaard L 1978 Geomagnetic activity: Dependence on solar wind parameters; in *Coronal holes and high speed wind streams* (ed.) J B Zirker (Boulder: Colorado Asso. Univ. Press) 371–441
- Svestka Z and Simon P 1975 Catalog of solar particle events 1955–1969 (Dordrecht: D. Reidel) pp. 428
- Svestka Z, Fritzova, Svestkova L, Nolte J T, Dodson-Prince H W and Hedeman E R 1976 Low energy particle events associated with sector boundaries; *Sol. Phys.* **50** 491–500
- Wilcox J M 1979 Tropospheric circulation and interplanetary magnetic sector boundaries followed by MeV proton streams; *Nature (London)* **278** 840–841
- Yoshizawa K 1984 Influence of IMF sector polarity on the north-south asymmetry of geomagnetic activity and its relationship with solar wind parameters; *Planet. Space Sci.* **32** 605–610

Relationship between pedogenetic manifestations in some arid soil and age of the landforms

J S CHOUDHARI

Central Arid Zone Research Institute, Jodhpur 342 003, India

MS received 27 May 1986; revised 1 January 1987

Abstract. Arid soils with slight variations in parent material, vegetation and climate were studied for their morphological, chemical and mineralogical characteristics. Results show that the soils are at different stages of profile development. Varying degrees of pedogenic features have been tied up with data on palaeoenvironment to develop a relationship between the soil and age of the landform. Studies reveal that Dune and Shergarh sandy soils with least degree of manifestation belong to early Holocene to latest Pleistocene, whereas Chirai sandy soil with weakly developed B horizon belongs to the upper Holocene. Soils (Khajwana and Gajsinghpura) with well-developed B horizon and a calcic layer with lime segregations belong to mid-Pleistocene whereas Pali and Pipar soils with illuvial clay in B horizon belong to early Pleistocene.

Keywords. Arid soils; pedogenetic manifestations; landforms.

1. Introduction

While preparing the inventory of natural resources of some arid regions, it was observed that despite slight variations in the parent material, vegetation and climate, the soils showed striking variation in morphological expression (CAZRI 1978). Some soils are devoid of pedogenic features, some show cambic horizon and others show a moderately-developed argillic and strongly-developed calcic horizons. The age of landform evolution of arid Rajasthan has been dated earlier (Singh 1971; Allchin *et al* 1972, 1978; Goudie *et al* 1973; Ghose *et al* 1977). The pedogenic features or pedogenetic manifestations which result from mineral weathering, accumulation of weathering products, lime redistribution and translocation of mineral and organic matter are considered to be time-dependent and their expression increases with time (Ruhe 1956; Arkley 1963; Birkeland 1969). There is therefore a need to study the relationship between the pedogenetic manifestation and the age of landform evolution in the arid region of Rajasthan and the present study is an attempt in this direction.

2. Study area

The study area, a Pleistocene alluvial plain, is located in the central part of western Rajasthan, covering parts of Jodhpur, Nagaur and Pali districts (figure 1) and lying between 27°N and 25°45'N latitude and 72°E and 73°55'E longitude.

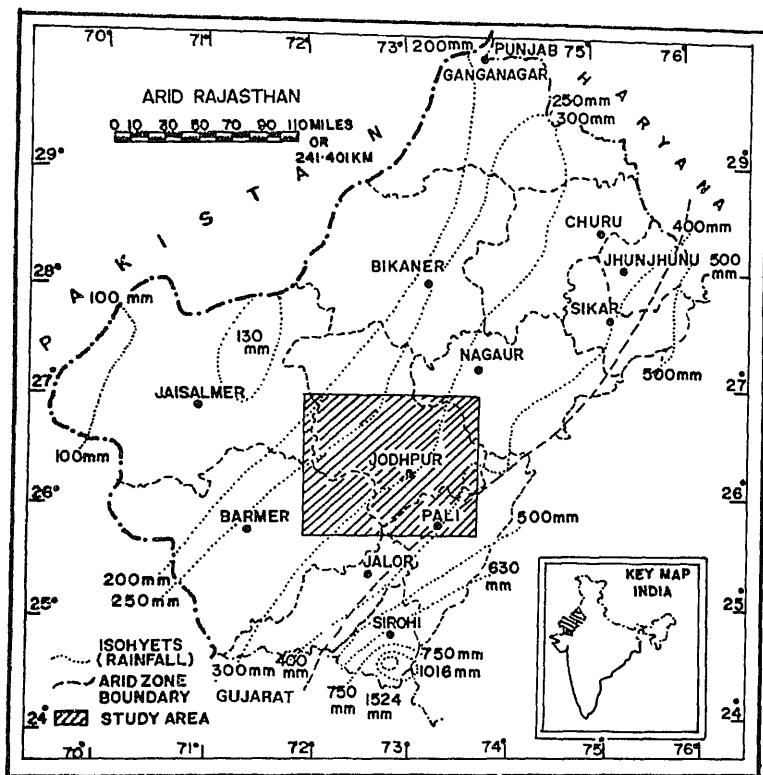


Figure 1. Location of study area.

The major part of the area is further transformed by the wind action of the late quaternary to dune field comprising high dunes and flat interdunal plains. Although hummocky coarse-textured alluvial plains are the dominant landforms, medium-to-fine textured flat-aggraded alluvial plains also occupy a sizeable part of the area. At many places rock outcrops and hills of Aravallis and buried pediments break the continuity of these plains.

The soils in these landforms have considerable heterogeneity. The western part representing the dune field are covered by Dune and Shergarh soils. The centrally located coarse-textured plains with Chirai and Kolu and the eastern flat plains are covered by moderately fine-textured strongly calcareous soils (Khajwana, Gajsinghpura, Pipar and Pali).

3. Methodology

To bring out the pedological essence of the soils, profiles on each of the dominant landforms were opened up to 1.5–2 m depth and studied for their morphological features. Site characteristics are briefly described in table 1. Soil samples from each horizon were collected and analysed for physical, physico-chemical and mineralogical characteristics using standard procedures (Piper 1947; Jackson 1979).

Table 1. Site characteristics.

Major landform	Landform unit	Soil	Elevation (m)
Dune field	(A) Coalesced parabolic dune	Dune	273
	(B) Interdune	Shergarh	221
Coarse-textured old aggraded alluvial plain	(A) Flat plain	Chirai	293
	(B) Flat plain with hardpan	Kolu	273
Fine textured old aggraded alluvial plain	(I) Vindhyan sandstone limestone region		
	(A) Flat plain	Khajwan	327
	(B) Accumulative upland	Gajsinghpura	324
	(II) Granite and phyllite region		
	(A) Flat plain	Pipar	257
	(B) Flat plain	Pali	247

4. Results and discussion

4.1 Characteristics of soils

Soils of the study area vary in their morphology and characteristics as evident by the morphological and analytical data (tables 2 and 3). The Dune and Shergarh soils are light brown, sandy (90–95% fine sand) and slightly calcareous whereas the Chirai soil which is also sandy has a higher proportion of silt and clay (table 3). Besides, these also have secondary lime in the form of concretions in substratum (table 2). Medium and fine-textured soils are still darker in colour (dark brown) and have higher proportions of clay and segregated lime.

4.2 Pedogenetic manifestations

Striking features of the pedogenesis in these soils are reflected by darker B horizon with stronger structure and higher silt and clay content. Also, there is an accumulation of secondary lime in the C horizon of these soils. These features, which result from the leaching of lime, development of chroma, weathering of minerals and illuviation processes on the parent material of these soils after their deposition, are far from uniform (table 4). The ratio of quartz and feldspar, used to evaluate soil weathering, varied from 1.0 to 2.14. Further, this ratio plotted horizon-wise (figure 2) shows that the surface horizons are strongly weathered, the weathering extending to the C horizon of Chirai and Pipar soils. Relatively higher ratio of Pali and Pipar soils (figure 2) reveals that these soils are formed over longer periods of time compared to Dune and Chirai soils.

The data (tables 2 and 3) show a textural difference between the surface and subsoils. A plot of clay content against depth (figure 3) shows a significant increase in the amount of clay in the B horizon of soils. The increase is significant in Gajsinghpura and Pali (C and D on figure 3) soils. The difference in A and B horizons could be due to *in situ* formation and/or due to illuviation (Ritche *et al*

Table 2. Morphology of the important pedogenic horizons.

Soil	Horizon	Colour [†]	Texture ^{**}	Structure ^{***}	Reaction	Segregation
Dunc	Ap	10YR6/3(PB)	FS	Sg	Nil	Nil
	C	10YR6/4(LYB)	FS	Sg	Slight	Nil
Shergarh	Ap	10YR6/4(LYB)	FS	Sg	Nil	Nil
	C1	10YR6/3(YB)	FS	Sg	Slight	Few
	C2	10YR6/3(YB)	FS	Sg	Slight	Common
Chirai	Ap	10YR5/3(B)	FLS	Sg	Nil	Nil
	B	10YR6/3(PB)	FSL	M1 Sbk	Strong	Few fine
	C1Ca	10YR6/3(PB)	FSL	M1 Sbk	Violent	Common
Kolu	Ap	10YR6/4(DYB)	FS	F1 Sbk	Strong	Few
	C1Ca	10YR6/3(PB)	FSL	M1 Sbk	Violent	Common
	IIC2Ca	10YR6/3(PB)	FSL	Massive	Violent	Abundant
Khajwan	Ap	7.5YR5/4(B)	FSL	F1 Sbk	Slight	Nil
	B21	7.5YR4/4(DRB)	FSL	M2 Sbk	Strong	Nil
	C1Ca	7.5YR6/4(RB)	FSL	M1 Sbk	Violent	Many
Gajsinghpura	Ap	10YR4/4(DYB)	L	M2 Sbk	Slight	Nil
	B22	7.5YR4/4(B)	Cl	C2 Sbk	Strong	Few
	C1Ca	5YR5/6(YR)	Cl	Massive	Violent	Many
Pipar	Ap	10YR4/4(DB)	L	M1 Sbk	Nil	Nil
	B22	10YR3/3(DB)	Cl	M3 Sbk	Slight	Few
	C1Ca	10YR5/3(B)	Cl	Massive	Strong	Common
Pali	Ap	10YR5/3(B)	SiCl	M2 Sbk	Slight	Nil
	B22	10YR3/3(DB)	SiCl	M2 Abk	Strong	Nil
	C1Ca	10YR4/4(PB)	SiCl	Massive	Violent	Common

* PB, pale brown; LYB, light yellowish brown; B, brown, DRB, dark reddish brown.

** FS, fine sand; FLS, fine loamy sand; FSL, fine sandy loam; L, Loam; Cl, clay loam; Sil, Silt loam; SiCl, silty clay loam.

*** Sg, single grain; M1, medium weak; M2, medium moderate; M3, medium strong; Sbk, subangular blocky; Abk, angular blocky.

the parent material (Olson 1958). Through radio carbon dating, Gile *et al* (1966) showed that the lime-plugged horizon had an average age of 18000 years as against the indurated horizon of 14000 years. The segregations (concretions and nodules) seem to be a better indicator of age. Agrawal *et al* (1980) reported the age of lime concretions of coarse-textured plain of study area between 22900 and 17270 years.

4.3 Pedogenetic manifestations and age of the landforms

The dunes, the soils of which have been studied, are of coalesced parabolic type. These are large dune bodies belonging to an old cycle of aeolian activity (Ghose *et al* 1979) as compared to barchan and shrub coppice type, which are of new cycle and attributable to excessive biotic interference of the recent period. Allchin *et al* (1972, 1978) and Goudie *et al* (1973) suggest major dry phases during pre-Middle stone age and then again during upper Palaeolithic age (25000 to 10000 years BP). According to Singh (1971) the period from 10000 to 4000 years BP was moist after which another dry phase sets again. Now the dune soils show an extremely weak pedogenetic manifestation (table 4) and in no case the soil formation appears to be

Table 3. Characteristics of a few important horizons of soils.

Soil	Depth (cm)	Horizon	pH	O.M. (%)	Silt (%)	Clay (%)	CaCO ₃ (%)	Frec Fe (%)	FLM *
Dune	0-50	C1	8.4	0.138	1.0	2.0	0.0	0.33	5.0
	50-100	C2	8.4	0.138	1.2	2.0	0.4	0.35	4.2
	150-200	C4	8.4	0.138	2.0	2.2	3.3	0.30	4.6
Chergarh	0-30	Ap	8.3	0.121	5.3	3.7	0.0	0.32	3.9
	30-66	C1	8.2	0.121	5.4	3.7	0.0	0.34	3.6
	66-120	C2	8.4	0.138	5.9	4.4	2.0	0.42	3.8
Chirai	0-10	Ap	8.4	0.104	5.4	3.6	0.0	0.24	5.5
	35-68	B21	8.3	0.174	10.7	8.8	0.9	0.32	5.1
	95-135	C1Ca	8.3	0.061	7.8	9.7	7.7	0.28	7.8
Golou	0-15	Ap	8.5	0.244	9.1	9.0	1.8	0.29	5.2
	15-45	B	8.4	0.244	9.0	10.8	3.9	0.18	5.2
	63-90	C1Ca	8.4	0.241	9.5	10.5	12.6	0.20	6.9
Chajwan	0-10	Ap	8.1	0.487	16.6	14.3	0.4	0.54	4.1
	28-44	B22	8.1	0.365	16.7	22.2	5.4	0.73	3.9
	54-66	C1Ca	8.2	0.522	16.2	22.2	12.8	0.63	4.5
Gajsinghpura	0-20	Ap	8.2	0.626	20.3	17.6	6.7	5.7	2.7
	30-46	B21	8.3	0.696	16.4	33.0	16.1	0.74	1.0
	78-110	C1Ca	8.2	0.556	20.8	30.0	42.2	0.57	2.6
Tipar	0-12	Ap	8.0	0.505	18.2	17.5	1.3	0.57	2.7
	28-48	B22	7.9	0.560	18.7	27.0	1.6	0.74	4.9
	65-105	C1Ca	8.0	0.287	16.8	19.1	16.2	0.50	6.2
Ali	0-10	Ap	8.0	0.644	38.6	28.9	2.0	0.78	5.1
	10-35	B22	8.0	0.554	37.2	43.1	7.3	1.04	4.0
	35-50	B23	8.0	0.447	39.9	32.6	8.8	0.94	3.3

FLM, fraction light minerals (Plagioclase)

Table 4. Degree of manifestations of various pedogenic processes in the studied soils.

Soil	Segregation of carbonated and formation of concretions and nodules	Pedality and structure development	Chroma development	<i>In situ</i> weathering and formation of clay	Alluviation of clay
Dune	N	N	Ng	N	A
Chirai	M	W	W	VW	A
Chajwan	M	M	M	W	A
Gajsinghpura	S	M	S	M	SI
Tipar	S	S	S	D	M
Ali	S	S	S	D	M

The leaching of carbonates was well marked in all the cases.

A, absent; D, distinct; M, moderate; N, none; Ng, negligible; SI, slight; S, strong; VW, very weak; W, weak.

as old as the pre-Middle stone age. At the same time the dunes are not of the recent cycle as well. Therefore, pedological evidences suggest that the dunes studied are of the latest upper Pleistocene to sub-recent period.

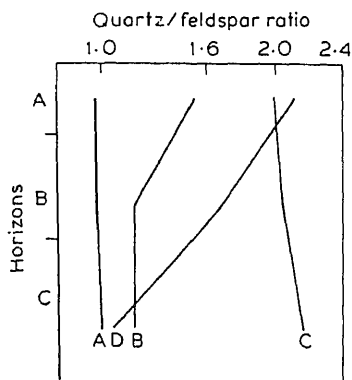


Figure 2. Average ratios of resistant to non-resistant minerals. A. Dune field. B. Chirai. C. Gajsinghpura. D. Pipar soils.

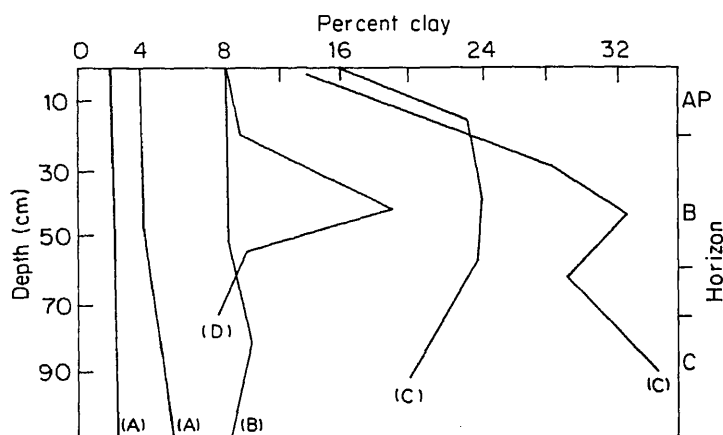


Figure 3. Clay size particle variation with depth for soils. A. Dune. B. Chirai. C. Gajsinghpura and Khajwana. D. Pali.

On the other hand, the Chirai soils on coarse-textured plain show development of calcic horizon with lime concretions, chroma and structure (table 4) though not as strong as those in the soils of medium and fine-textured plains. Theoretically there can be three possible reasons for this: (i) the extraordinary resistance of the parent material to weathering, (ii) the extremely arid conditions, and (iii) the relatively young age of the parent material. Of these, the first cause is ruled out since the parent material of Chirai soil has a somewhat high content of weatherable minerals (table 3). Harshness of the climate also cannot be a contributing factor since the geographic nearness of these coarse and fine-textured plains makes it impossible for such a large differential to exist in such a short distance. Therefore, the only factor seems to be the relatively younger age of the coarse-textured plain compared to medium and fine-textured plains. Allchin *et al* (1978) also indicated a major wet phase during 45000 to 25000 years BP. Since no wet phase of this magnitude is indicated during the succeeding period, coarse-textured alluvial plains seem to belong to upper pleistocene. Singh and Ghose (1977), on the basis of lime

concretion dating, estimated the sediments of this plain to be of 30000 to 28000 years BP.

Soils of medium to fine textured plains of Vindhyan sandstone and limestone region show significant evidences of *in situ* weathering despite the relatively resistant nature of the parent material. This is also evident from the average ratio of resistant to non-resistant minerals (figure 2). These soils also show a marked chroma and structure development in solum and a well-developed lime concretionary layer (table 2). The formation is therefore undoubtedly older than the above described coarse-textured plains which are of late pleistocene age. Therefore, the plain seems to belong to upper to mid-pleistocene.

The soils on the plains of granite and slate region not only show maximum profile differentiation (table 2) in the development of chroma, structure and formation of the concretionary strata (table 4), but also show some illuviation of clay (figure 3). The soils show a very high degree of maturity amongst the soils studied. Therefore, the formation seems to belong to middle to early pleistocene. This is also supported by the fact that the alluvium is on the weathering zone of granite and slate which are of lower Vindhyan or even older. Absence of lithification of weathering zone precludes the parent material from being as old as the pleistocene.

Acknowledgement

The author is grateful to Drs K A Shankarnarayan and R P Dhir for encouragement.

References

- Agarwal D P, Dhir R P, Krishnamurti R V, Misra V N, Nanda S C and Rajaguru S N 1980 Multiple evidence for climatic changes in Rajasthan. In *Arid zone research and development* (ed.) H S Mann (Jodhpur: Scientific Publisher) pp. 1-10
- Allchin B, Goudie A and Hegde K T M 1978 *The pre-history and palaeogeography of the great Indian Desert* (London : Academic Press) pp. 77-113
- Allchin B, Hegde K T M and Goudie A 1972 Pre-history and environmental changes in western India. A note on Budha Puskar Basin, Rajasthan; *Man* **74** 542-564
- Blackley R J 1963 Calculation of carbonate and water movement in soil from climatic data; *Soil Sci.* **96** 239-248
- Brinkeland P W 1969 Quarternary palaeoclimatic implications of soil clay mineral distribution in a Sierra Nevada Great Basin transect; *J. Geol.* **77** 239-302
- CAZRI 1978 Report on basic and human resources survey of Jodhpur district, Rajasthan (Jodhpur: Central Arid Zone Research Institute)
- Choudhury B, Singh S and Kar A 1977 Geomorphology of the Rajasthan desert. In: *Desertification and its control* (New Delhi: ICAR) pp. 69-76
- Conley L H, Peterson F F and Grossman R B 1966 Morphological and genetic sequences of carbonate accumulation in desert soils; *Soil Sci.* **101** 347-360
- Goudie A, Allchin B and Hegde K T M 1973 The former extension of the Great Indian Sand Desert; *Geog. J.* **139** 243-257
- Hickson M L 1979 *Soil chemical analysis: advance course* (Madison: University of Wisconsin)
- Hettler W D, Witty J E, Nelson R E and Hawley J W 1975 Genesis of argillic horizons in soils of desert areas of the southwestern United States; *Soil Sci. Soc. Am. Proc.* **39** 105-133
- Johnson J S 1958 Rates of succession and soil changes on southern Lake Michigan sand dunes; *Bot. Gaze.* **119** 125-170

- Piper C S 1947 *Soil and plant analysis* (Adelaide: University of Adelaide)
- Ritche A, Wilding L P, Hall G F and Stahnke C R 1974 Genetic implications of B horizons in aqualls of north-eastern Ohio; *Soil Sci. Soc. Am. Proc.* **38** 351–358
- Ruhe R V 1956 Geomorphic surfaces and the nature of soils; *Soil Sci.* **82** 441–450
- Singh G 1971 The Indus valley culture seen in the context of post-glacial climatic and ecological studies in the north west India; *Archaeol. Phys. Anthropol. Oceanic* **6** 177–189
- Singh S and Ghose B 1977 Geomorphology of the Luni Basin and its palaeoclimatic inferences; In *Ecology and archaeology of western India* (eds) D P Agrawal and B M Pande (New Delhi: Concept Publishing Co.) pp. 135–146

Auxiliary functions of the Hilbert transform in the study of gravity anomalies

G RAMADASS, I ARUNKUMAR, S M VARAPRASADA RAO,
N L MOHAN and N SUNDARARAJAN

Centre of Exploration Geophysics, Osmania University, Hyderabad 500 007, India

MS received 27 October 1986; revised 30 November 1987

Abstract. The auxiliary functions, namely amplitude, phase, envelope and instantaneous frequency of Hilbert transform over gravity anomalies of 2-D sphere, vertical fault block and horizontal circular cylinder are studied. The characteristics of these functions are established in locating and identifying the sources. The method is illustrated with a theoretical example in each case and supported by field data of gravity anomaly over Humble dome and spherical model of the Satak-Mansar area, Nagpur District, India.

Keywords. Auxiliary functions; Hilbert transform; instantaneous frequency; amplitude; phase and envelope.

1. Introduction

Hilbert transform is widely used in processing and interpretation of gravity and magnetic anomalies (Nabighian 1974, 1984; Stanley and Green 1976; Green and Stanley 1975; Rao and Ram Babu 1981; Mohan *et al* 1982; Sundararajan 1982; Sundararajan *et al* 1983). The characteristics of the amplitude of the analytic signal over magnetic bodies with polygonal cross-section were discussed by Nabighian (1972, 1974). Such studies are valid even in gravity anomalies in addition to spontaneous potential and induced polarization data. In general, the amplitude is useful not only in determining the location of structures and their dimensions etc. but also in the direct interpretation of geophysical data. The Hilbert transform with some auxiliary functions plays a significant role in the resolution of geophysical signals (Ramadass *et al* 1986).

We present here a simple note on the phase and envelope pertaining to some 2-D gravity anomalies namely, sphere, vertical fault block and horizontal circular cylinder.

If $g(x)$ is the vertical component of the gravity field which is measurable, its horizontal component $h(x)$ can be obtained by Hilbert transform. In other words, $g(x)$ and $h(x)$ form a Hilbert transform pair. That is,

$$g(x) \xleftrightarrow{H} h(x) \quad (1)$$

and

$$h(x) = \frac{1}{\pi x} * g(x), \quad (2)$$

where H is the Hilbert transform operator and the asterisk denotes convolution.

Now, the analytic signal which is a complex function can be defined as

$$f(x) = g(x) + ih(x). \quad (3)$$

It may be noted here that $g(x)$ can also be a horizontal derivative of any order, correspondingly $h(x)$ is the vertical derivative of the same order of $g(x)$.

The amplitude of the analytic signal is defined as

$$A(x) = [\{g(x)\}^2 + \{h(x)\}^2]^{1/2}. \quad (4)$$

According to Sundararajan (1982) this amplitude can be modified as

$$A(i\Delta x) = [\{g(i\Delta x)\}^2 + \{h(\overline{N-i} + i\Delta x)\}^2]^{1/2}, \quad (5)$$

where the magnitudes of the Hilbert transforms (4) and (5) remain the same with a phase difference of 180° . Equations (4) and (5) are identical.

The phase which is also useful in direct interpretation is defined as

$$PH(x) = \tan^{-1}[-h(x)/g(x)]. \quad (6)$$

Another auxiliary function which is of some use in delineating the structural characteristics is defined as

$$EN(x) = g(x)/\cos[PH(x)]. \quad (7)$$

The instantaneous frequency which is the space derivative of envelope function is expressed as

$$IF(x) = (d/dx)[PH(x)]. \quad (8)$$

In general, the instantaneous frequency is highly oscillating and hence is not included here, although the utility of this frequency function is the same as that of phase and envelope.

The following are the phase and envelope characteristics of the gravity anomalies over sphere and vertical fault block.

2. Theoretical models

2.1 Sphere

The first horizontal derivative of the gravity effect and the corresponding Hilbert transform (vertical derivative) due to a spherical structure (figure 1) are given as

$$g(x) = \frac{4}{3} \pi R^3 \sigma G [xz/(x^2 + z^2)^{5/2}] \quad (9)$$

and

$$h(x) = \frac{4}{3} \pi R^3 \sigma G [(x^2 - 2z^2)/(x^2 + z^2)^{5/2}], \quad (10)$$

where R is the radius of the sphere and Z the depth to the centre. The amplitude in this case is given as

$$A(x) = \frac{4}{3} \pi R^3 \sigma G [(x^4 + 4z^4 - 3x^2 z^2)^{1/2}/(x^2 + z^2)^{5/2}]. \quad (11)$$

At $x = 0$, $A(x)$ reduces to

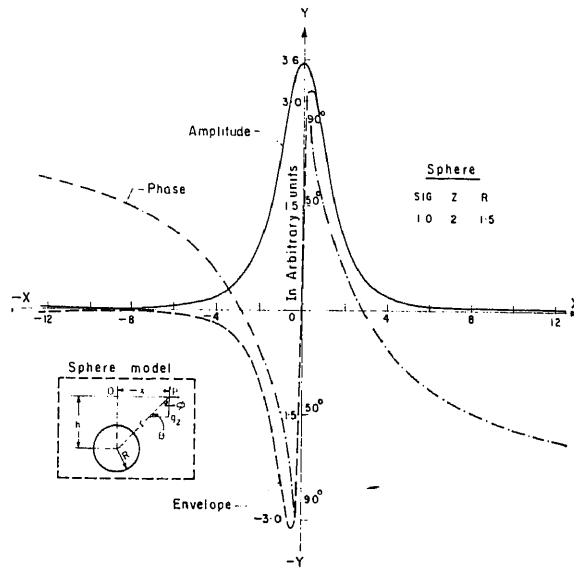


Figure 1. Amplitude, phase and envelope components simulated using gravity effect and its Hilbert transform over a spherical model.

$$A(x) \Big|_{x=0} = \frac{8}{3} \pi R^3 \sigma G \frac{1}{z^3} \quad (12)$$

and at $x = z$.

$$A(x) \Big|_{x=z} = \frac{1}{3} \pi R^3 \sigma G \cdot \frac{1}{z^3}.$$

The phase can be defined as

$$PH(x) = \tan^{-1} [(x^2 - 2z^2)/xz]. \quad (13)$$

At $x = 0$

$$PH(x) \Big|_{x=0} = \pi/2$$

and at $x = z$

$$PH(x) \Big|_{x=z} = \pm \pi/4$$

and at $x = 2z$

$$PH(x) \Big|_{x=2z} = 0$$

The envelope can be written as

$$EN(x) = \frac{[4\pi R^3 \sigma G xz / (x^2 + z^2)^{5/2}]}{\cos \{ \tan^{-1} [(x^2 - 2z^2)/xz] \}} \quad (14)$$

At $x = 0$, $EN(x)$ reduces to

$$EN(x) \Big|_{x=0} = 0$$

and at $x = z$

$$EN(x) \Big|_{x=z} = \pi R^3 \sigma G / 4(2)^{1/2} \cdot z^3. \quad (15)$$

2.2. A semi-infinite thin fault block

The first horizontal derivative of the gravity effect and its Hilbert transform due to semi-infinite thin fault block (figure 2) are expressed as (Sundararajan *et al* 1983)

$$g(x) = 2G\sigma t[z/(x^2 + z^2)] \quad (16)$$

and

$$h(x) = 2G\sigma t[x/(x^2 + z^2)], \quad (17)$$

where z and t are the depth to the centre and thickness of the thin fault block respectively.

The amplitude of the thin fault according to (9) is given as

$$A(x) = 2G\sigma t/(x^2 + z^2)^{1/2}. \quad (18)$$

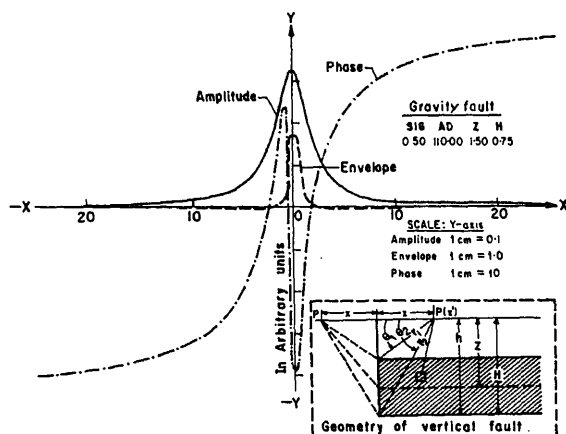


Figure 2. Amplitude, phase and envelope components simulated using the gravity effect and its Hilbert transform over a vertical fault block

$$A(x) \Big|_{x=z} = 2G\sigma t/z. \quad (17)$$

At $x = z$ (where the depth is equal to the abscissa of the point of intersection of $g(x)$ and $h(x)$, Sundararajan *et al* 1983)

$$A(x) = 2G\sigma t/z. \quad (20)$$

The phase function in this case is obtained as

$$PH(x) = \tan^{-1}(-x/z). \quad (21)$$

Again at $x = 0$

$$PH(x) \Big|_{x=0} = 0$$

and at $x = \pm z$

$$PH(x) \Big|_{x=z} = \pm \pi/4. \quad (22)$$

Now, the equation of envelope can easily be written as

$$EN(x) = \frac{2G\sigma tz/(x^2 + z^2)}{\cos[\tan^{-1}(x/z)]} \quad (23)$$

At $x = 0$, (23) reduces to

$$EN(x) \Big|_{x=0} = 2G\sigma t/z$$

and at $x = z$,

$$EN(x) \Big|_{x=z} = (2)^{1/2} G\sigma t/z.$$

2.3 Horizontal cylinder

The gravity effect and the corresponding Hilbert transform due to a horizontal circular cylinder are given as

$$g(x) = 2\pi R^2 G\sigma z/(x^2 + z^2) \quad (24)$$

and

$$h(x) = 2\pi R^2 \sigma G \cdot z/(x^2 + z^2), \quad (25)$$

where R and Z are the radius of the cylinder and the depth to the centre respectively. G and σ are the universal gravitational constant and the density contrast respectively.

Since the gravity effect of the cylinder is similar to the first horizontal derivative of the vertical fault block, the amplitude, phase and envelope are also similar to that for the fault block. However, the constant form is different which is not of much significance in the study of the auxiliary functions.

3. Theoretical examples

In the case of sphere and fault block, the amplitude, phase and envelope are computed using the respective equations (figures 1 and 2). The instantaneous frequency which is highly oscillating, however, is not shown in the figures. In both cases, the amplitude curve is a bell-shaped symmetric one which is useful in locating the origin as well as parametric interpretation (Nabighian 1972). For all the structures where the width is less than the depth of the burial, the amplitude is a symmetric function. The phase in the case of a sphere varies from $0-90^\circ$ as x varies from $x = 2z$ to $x = 0$. On the other hand, the phase in the case of a fault block varies from 0 to 45° as x varying from $x = z$. However, the phase attains a value of 90° when x approaches infinity. Finally, the envelope for the sphere is an asymmetric curve, characterizing a positive and a negative peak on either side of the origin whereas it is a symmetric curve as that of the amplitude.

The characteristics of the amplitude, phase and envelope due to a horizontal circular cylinder are similar to those of the fault block and hence they are not shown in figures.

4. Field examples

4.1 Humble dome gravity anomaly

A profile in a line AA' of the gravity map (figure 3) of the Humble dome near Houston (USA) is considered for the present analysis. The residual gravity anomaly is digitized at an appropriate interval. The first horizontal derivative and its Hilbert transform were computed, and using these two components the amplitude, phase and the envelope are shown in figures 4 and 5. In this case the

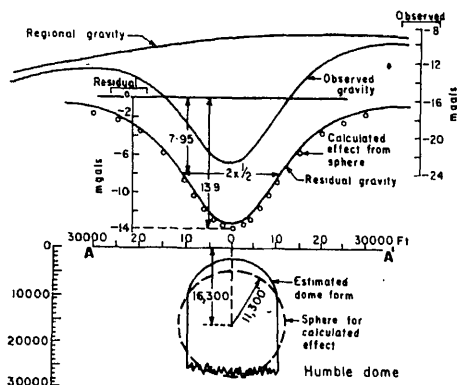


Figure 3. Gravity profile over Humble dome (Nettleton 1976).

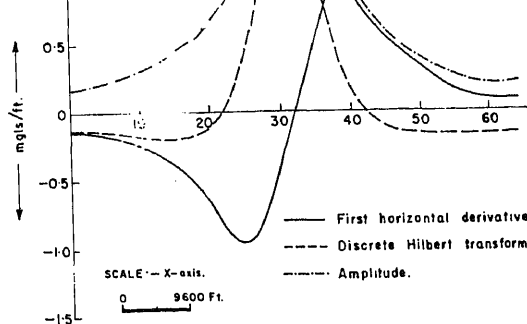


Figure 4. Computed first horizontal derivative of the gravity effect and its discrete Hilbert transform and the amplitude components over a line AA' (Humble dome).

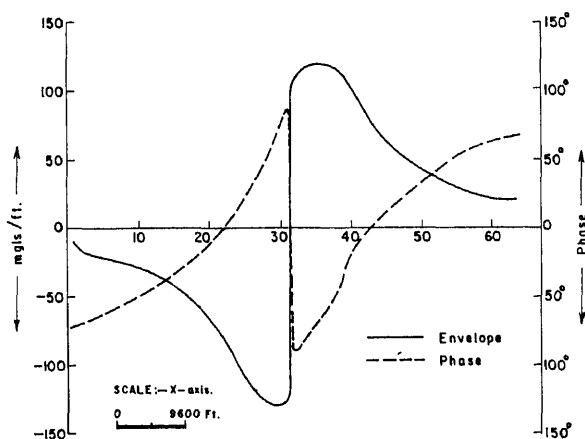


Figure 5. Phase and envelope components computed using the gravity effect and its Hilbert transform across the line AA' (Humble dome).

amplitude is not a symmetric bell-shaped one because the diameter of the sphere is greater than the depth to the centre of the sphere. Therefore the minimum found between the two maxima of the amplitude corresponds to the origin. This is also confirmed from the phase and envelope.

4.2 Indian field example

A gravity profile survey conducted at the Satak-Mansar area of Ramtek Tehsil, Nagpur District, Maharashtra, India (Dash *et al* 1979) was taken in order to demonstrate the technique. This area forms part of the well known Chindwara, Nagpur-Bhandara-Balaghat belt of Central India made up largely of the Sausar series of rocks which have been subjected to complicated folding, thrust faulting and shearing. They are made up of calc-granulites, marbles, garnetiferous-schists, manganese, silicates and metamorphosed manganiferous sediments called gon-

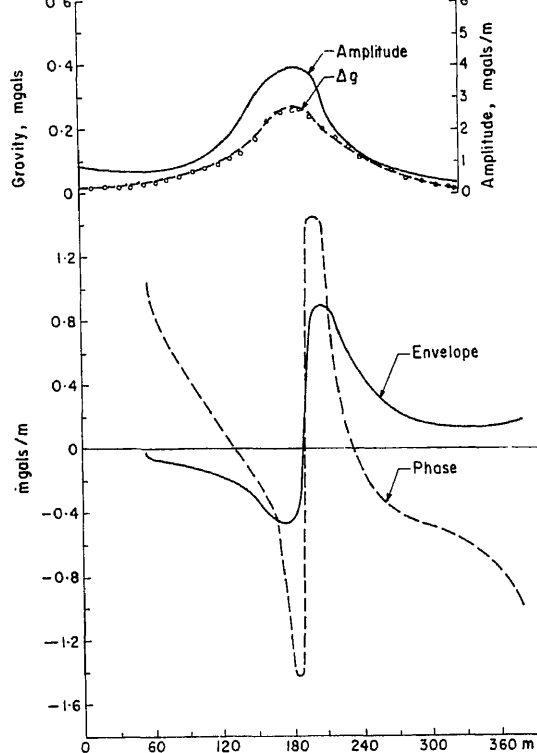


Figure 6. Gravity profile over a Satak-Mansar area. The amplitude, phase and the envelope components over a spherical body.

dites. The manganese ore body as revealed by drilling is in the form of a lensoid which in the present case is approximated as a spherical body. The first horizontal derivative and its Hilbert transform were computed and using these two components amplitude, phase and envelope were computed and shown in figure 6. These components clearly indicate that the anomaly is caused due to a spherical structure. Thus the validity of the method has been established.

5. Discussion

The auxiliary functions are of much significance in processing the geophysical data obtained particularly in a large scale regional survey in delineating the structural features as well as for the subsequent interpretation. Invariably, in all the cases the amplitude remains a bell-shaped symmetric curve which directly helps in the comprehension of the structural characteristics.

On the other hand, the phase in the case of spherical structures, crosses the horizontal axis exactly at a distance equal to the diameter of the sphere. Also, the envelope which is an asymmetric function gives rise to a positive and a negative peak through origin (figure 1).

For a fault block, the phase varies from 0 to 45° as x varies from $x = 0$ to z . The envelope is similar to the amplitude because its function is symmetric. The amplitude, phase and envelope for cylinder model are the same as those for the fault block. In such cases, it is possible to establish some empirical relation between the parameter and some characteristic points on these curves.

References

- Desh B R, Venkateshwarulu P O and Reddy A G B 1979 *Geophysical case histories of India*, AEG 131–137
- Green R and Stanley J M 1975 Applications of Hilbert transform to the interpretation of surface vehicle magnetic data; *Geophys. Prosp.* **23** 18–27
- Mohan N L, Sundararajan N and Seshagiri Rao S V 1982 Interpretation of some two-dimensional magnetic bodies using Hilbert transform; *Geophysics* **47** 376–387
- Nabighian M N 1972 The analytic signal of the two-dimensional magnetic bodies with polygonal cross-section, its properties and use for automated anomaly interpretation; *Geophysics* **37** 507–512
- Nabighian M N 1974 Additional comments on the analytic signal of two-dimensional magnetic bodies with polygonal cross-section; *Geophysics* **39** 85–92
- Nabighian M N 1984 Toward a three-dimensional automatic interpretation of potential field data via generalized Hilbert transforms: Fundamental relations; *Geophysics* **69** 780–786
- Nettleton L L 1976 *Gravity and magnetic in oil prospecting* (New York: McGraw Hill)
- Ramdas G, Varaprasada Rao S M and Mohan N L 1986 Resolution of magnetic anomalies by using Hilbert transforms: A new technique; *Aust. Soc. Expl. Geophys.* **17** 97–104
- Rao D A and Ram Babu H V 1981 Properties of the complex gradient of gravity anomalies due to spheres and cylinders; *Geoviews* **9** 41–50
- Shuey R T 1972 Application of Hilbert transforms to magnetic profiles; *Geophysics* **37** 1043–1045
- Stanley J M and Green R 1976 Gravity gradients and the interpretation of the truncated plate; *Geophysics* **41** 1370–1376
- Sundararajan N, Mohan N L and Seshagiri Rao S V 1983 Interpretation of gravity anomalies due to some two-dimensional structures — A Hilbert transform technique; *Proc. Indian Acad. Sci. (Earth Planet. Sci.)* **92** 179–188
- Sundararajan N 1982 *Interpretation techniques in geophysical exploration using Hilbert transforms* Ph.D. thesis, submitted to Osmania University, Hyderabad, India (unpublished)

Petrographic criteria for establishing the copper potential in granitoid plutons

M S NAIK and R K TRIVEDI

Department of Applied Geology, Indian School of Mines, Dhanbad 826 004, India

MS received 30 October 1986; revised 1 May 1987

Abstract. A petrographic investigation and its possible relevance in mineral exploration have been studied for a mineralized granitoid pluton in Malanjkhand. Using a matrix of mineralogical, textural and structural features, the types and intensities of mineralogical changes by post-magmatic metasomatic processes can be deduced from thin sections of the rocks. The resulting petrological score provides a measure of establishing the copper potential of a granitoid pluton.

Keywords. Granitoid pluton; petrographic features; petrological record; petrographic score.

1. Introduction

Based on a petrographic study of the Malanjkhand mineralized granitoid pluton an attempt has been made to identify the geologic environment favourable for copper metallization in felsic plutons. It is believed that a large number of copper deposits are genetically related to acid magmatism (Garrett 1973; Tauson and Kozlov 1973; Tauson 1974; Allen *et al* 1976; Ahmad 1977). Beus and Grigoryan (1977) and Govett (1983) suggested that the granitoid intrusions that have suffered post-magmatic hydrothermal or metasomatic alterations are potentially ore-bearing. Fischendorf (1973) proposed a close relationship between the geochemical and petrographic characteristics of silicic magmatic rocks associated with tin mineralization.

2. Geological setting

The granodiorite of the present investigation occurs as an irregular batholithic body covering about 130 km² area around Malanjkhand in Madhya Pradesh (figure 1). It is emplaced within the Chilpi Ghat formation. The country rocks consist of conglomerate, arkosic grit and phyllite. The granodiorite shows cross-cutting relationship with the country rocks. The contacts between them are sharp and at places thermal aureoles have been observed (Trivedi 1986).

Towards the southwestern part of the granodiorite pluton a well-defined metasomatised zone has been observed. The Cu mineralization is restricted to this zone (figure 2). The pluton shows different degrees of hydrothermal alteration and replacement. An intense potassic metasomatism is inferred from the abundant

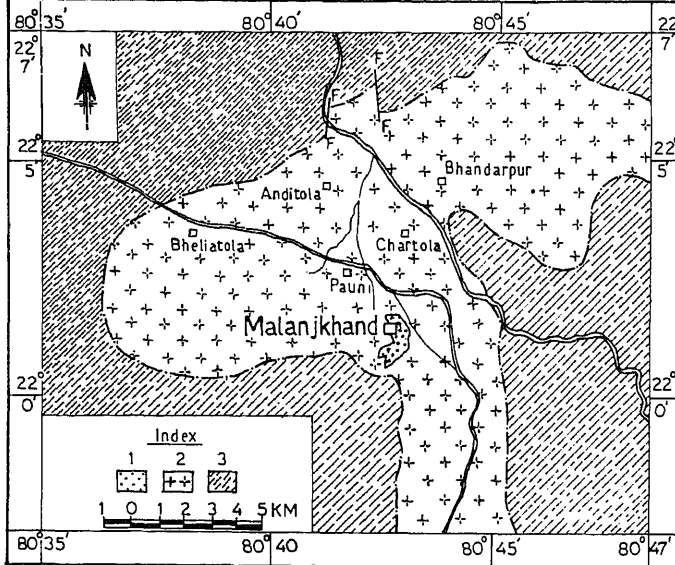


Figure 1. Geological map of the area around Malanjkhanda. 1. Metasomatised granodiorite. 2. Granodiorite. 3. Phyllite.

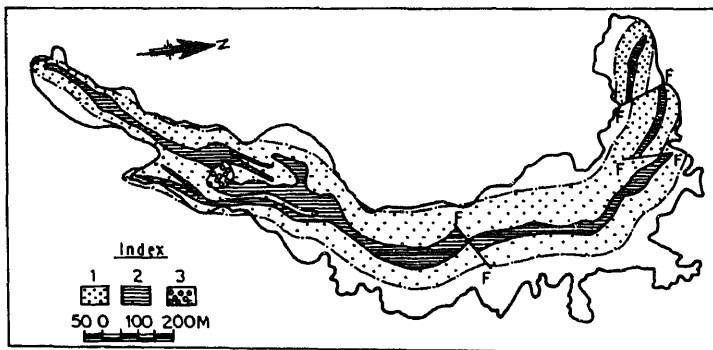


Figure 2. Geological map of the mineralized area. 1. Metasomatised granodiorite. 2. Mineralized quartz vein. 3. Conglomerate.

occurrence of pink potash feldspar which gives a distinct pink appearance to the rock. It forms an arcuate band which is about 2.5 km long and 200 m wide. In this band the interplay between the hydrothermal fluids and the granodiorite parent rock or rock fluid interactions are well preserved.

3. Petrographic features

Two textural variants have been observed within the pluton such as the granodiorite proper and the metasomatized granodiorite. The granodiorite is principally made up of plagioclase, quartz and potash feldspar. Subhedral grains of plagioclase range in composition from $Ab_{90}An_{10}$ to $Ab_{75}An_{25}$. It is partly

saussuritized. Quartz occurs as subhedral to anhedral independent grains. The potash feldspar is microcline which is occasionally perthitic. Brown biotite is the common mafic mineral. Sphene, magnetite and apatite are the common accessory minerals. The modal compositions are shown in table 1.

The metasomatized granodiorite is a coarser pinkish rock consisting of quartz, K-feldspar and plagioclase. Green biotite is the major mafic mineral. Sphene, magnetite, apatite and fluorite are the common accessory minerals. Occasionally pyrite and chalcopyrite are also noted. The potash feldspar is microcline which is generally perthitic and is found to replace plagioclase in different stages. It is fresh and exhibits cross-hatched twinning of different intensities. Occasionally kaolinization of potash feldspar has been observed. Plagioclase is highly saussuritized. Biotite is green in colour and partly altered. Invariably exsolved granules of sphene are found within biotite. The rock shows different degrees of diagenetic alteration and metasomatic change resulting in a moderate mineralogical and textural changes.

4. Geochemistry of the granodiorite

The mean chemical composition of each group of granodiorite and their standard deviations are given in table 1. The average chemical composition of group A rocks indicates its granodioritic nature. Na_2O exceeds K_2O which is characteristic of granodiorite. Based on K_2O vs Na_2O , Harpum (1963) chemically classified granitic rocks. When the Na_2O and K_2O contents of the granodiorite of Malanjkhanda are plotted (figure 3) the rocks are found to be granodiorite (Trivedi 1986).

From the chemical analyses of the metasomatized granodiorite (Group B, table 2) it can be seen that the metasomatism has brought about depletion of Al_2O_3 , Na_2O , MgO and CaO . In contrast, SiO_2 and K_2O contents increase with the degree of metasomatism (Trivedi 1986).

5. Petrological record

In order to know the progressive mineralogical and textural changes related to residual magmatic fluids and the parent rock or solid-fluid interactions between post-magmatic hydrothermal solution and the granodiorite parent, a detailed

Table 1. Modal compositions of Malanjkhanda granodiorite.

	RT-14	RT-22	RT-63	RT-104	RT-125	RT-136
Quartz	23	26	25	21	25	22
K-feldspar	22	16	24	10	15	20
Plagioclase	44	39	37	47	37	44
Biotite	8	14	10	15	18	10
Sphene, apatite and others	3	5	4	7	5	4

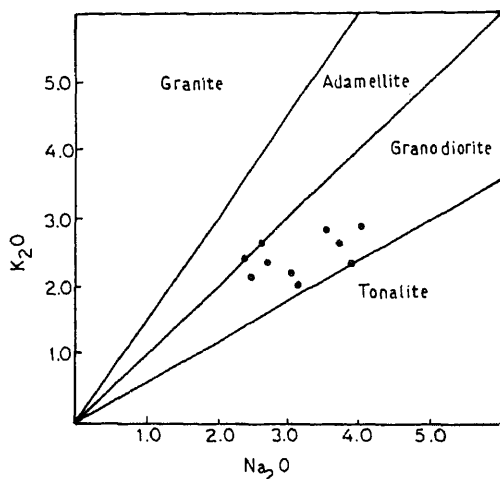


Figure 3. Na_2O vs K_2O plot of Malanjkhanda granodiorite rock classification (after Harpum 1963).

Table 2. Mean contents of major elements (in wt %) of the granodiorites from Malanjkhanda.

Element	Group A		Group B	
	Granodiorites \bar{x}	Mean of 60 S	Metasomatised \bar{x}	Group of 40 S
SiO_2	64.81	1.8	69.13	1.5
TiO_2	0.47	0.12	0.40	0.08
Al_2O_3	16.85	0.59	14.53	0.62
Fe_2O_3	2.34	0.61	2.04	0.55
FeO	3.46	0.42	1.83	0.38
MnO	0.04	0.01	0.05	0.01
MgO	1.57	0.35	0.91	0.22
CaO	3.68	0.53	2.42	0.41
Na_2O	3.50	0.38	2.51	0.26
K_2O	1.81	0.35	4.14	0.31
P_2O_5	0.16	0.02	0.23	0.03

\bar{x} , arithmetic mean; S , standard deviation

statistical study of rock thin sections has been undertaken. A systematic petrological record has been prepared from the thin sections.

The minerals, their textures and the various replacement and alteration products, as observed in thin sections of the rocks reveal the history of subsolidus processes. 115 thin sections from the Malanjkhanda granodiorites were studied and the observations grouped into different petrographic features based on the degree of metasomatism and the degree of mineralogical and textural changes. On the basis of these petrographic observations (table 2) a composite sketch of textures observed in thin sections has been drawn (figure 4). It is a sketch of all the main types and intensities of textural and structural changes as well as replacement of

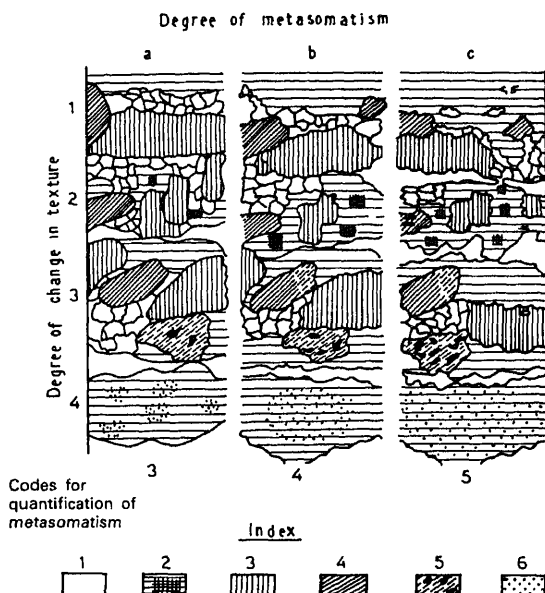


Figure 4. Composite sketch of textures observed in thin sections. 1. Quartz. 2. Microcline. 3. Plagioclase. 4. Biotite. 5. Altered biotite with exsolved phases. 6. Alteration products in feldspar (saussurite, sericite, kaolinite etc.).

Table 3. Quantification of alterations and metasomatism.

Degree of change	Change in Original mineral	
	Texture	Composition*
Low to moderate 3	Granular Subhedral Grain boundaries are slightly concave or convex	Sericite, saussurite < 1/3 Perthite < 1/6 Alteration of biotite < 1/4 Exsolution of sphene in biotite
Moderate to strong 4	Anhedral Grain boundaries are slightly amoeboid	Sericite, saussurite 1/3 to 2/3 Perthite of replacement type partly interlocked 1/4 to 1/2 Alteration of biotite 1/4 to 1/2 Exsolution of sphene in biotite
Very strong 5	Symplectic texture Perthitic intergrowths Grain boundaries amoeboid Pseudomorph	Sericite, saussurite > 2/3 Perthite of replacement type > 1/2 Patchy remnants of feldspar in high amount Alteration of biotite > 3/4 Exsolution of sphene in biotite

* Figures indicate the proportion of the area of the original mineral occupied by the new mineral.

minerals present are shown with increasing degree of crystalloblastesis from top (1) to bottom (4).

All the observations namely the textures, structures, minerals and newly-formed minerals can be assigned scores according to the codes along the abscissa (3, 4, 5). In addition, the proportion of the area of original minerals occupied by new minerals (alteration and replacement products) is indicated by a co-ordinate and transformed into a code. The coding used can be illustrated with the following examples:

Co-ordinate C/3 indicates an area of bleached biotite with considerable exsolution of opaque mineral. This observation is typical of the rock section as a whole and this feature has been given the code 5.

Co-ordinate C/1 indicates the high degree of microclinization or K-metasomatism and this feature results in code 5.

6. Petrographic score

Once all the data (numerical coding of mineral types, grain size, textures and field information) have been recorded the new characteristic called the petrographic score is arrived at (table 4). This is the sum of all the codes obtained from a thin section. The petrographic score was found to range from 27 to 96 for the rocks investigated. An increase in metasomatic alteration with all its resultant characteristics increases the petrographic score.

The frequency distribution of the score for all 115 samples studied is shown in figure 5a. Closer examination of field relationship between the rock samples and copper ore occurrences revealed a well-defined split into two statistical populations. The population of unmineralized part of granodiorite pluton was found to have a modal score of 45 while the modal score for mineralized part of granodiorite is 75 (figure 5b).

From these results it is clear that petrographic score can help to evaluate the copper potential of an acid pluton and is eminently suited for application as a tool for decision making in prospect acquisition within the known mineralized belt or to eliminate non-potential granitoid masses on a regional scale exploration.

Table 4. Statistical study of thin section.

Petrological score interval	Frequency of the total thin sections	Frequency of thin sections in granodiorite	Frequency of thin sections from metasomatized granodiorite
20-30	2	2	—
30-40	15	13	2
40-50	24	18	6
50-60	13	7	6
60-70	24	7	17
70-80	27	4	23
80-90	8	—	8
90-100	2	—	2

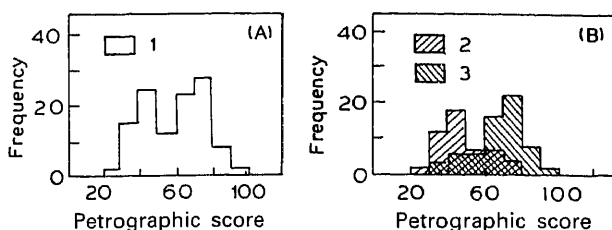


Figure 5. Frequency distribution of petrographic scores for all samples. 1. Total (115 samples). 2. Granodiorite (51 samples). 3. Mineralized granodiorite (64 samples).

References

- Ahmad S N 1977 The geochemical distribution and source of copper in the metalliferous mining region of South-west England; *Miner. Deposita* **12** 1-21
- Allen P M, Copper D C, Fuge R and Rea W J 1976 Geochemistry and relationships to mineralisation of some igneous rocks from the Harlech Dome Wales; *Inst. Min. Metall. Trans.* **B85** 100-108
- Beus A A and Grigoryan S V 1977 *Geochemical exploration methods for mineral deposits*. (Wilmette: Applied Publishing Company) Vol. 3, pp. 287-293
- Garrett R G 1973 Regional geochemical study of Cretaceous acidic rocks in the Northern Canadian Cordillera as a tool for broad mineral exploration. In: *Geochemical exploration* (ed.) M J Jones (London: Inst. Min. Metall.) Vol. 3, pp. 203-219
- Govett G J S 1983 *Rock geochemistry in mineral exploration*. (Amsterdam: Elsevier) pp. 62-78
- Harpum T R 1963 Rock classification; *Rec. Geol. Surv Tanganyika* **10** 80-86
- Tauson L V 1974 The geochemical types of granitoids and their potential ore capacity. In: *Metallization associated with acid magmatism* (ed.) M Stemprok (Prague: Geol. Surv.) Vol. 1, pp. 30-54
- Tauson L V and Kozlov V D 1973 Distribution function and ratios of trace element concentrations as estimator of the ore-bearing potential of granites. In: *Geochemical exploration* (ed.) M J Jones (London: Inst. Min. Metall.) pp. 37-44
- Tishendorf G 1973 The metallogenetic basis of tin exploration in Erzgebirge; *Inst. Min. Metall. Trans.* **B82** 9-24
- Trivedi R K 1986 *Acid magmatism and copper mineralization in Malanjkhand*. Ph.D. thesis, Indian School of Mines, Dhanbad (unpublished)

Estimation of hypocentral parameters of local earthquakes when crustal layers have constant P -velocities and dipping interfaces

IRENE SARKAR, R CHANDER, K N KHATTRI and V K GAUR*

Department of Earth Sciences, University of Roorkee, Roorkee 247 667, India

* National Geophysical Research Institute, Hyderabad 500 007, India

MS received 7 November 1986; revised 14 December 1987

Abstract. The paper describes an algorithm for estimating the hypocentral coordinates and origin time of local earthquakes when the wave speed model to be employed is a layered one with dipping interfaces. A constrained least-squared error problem has been solved using the penalty function approach, in conjunction with the sequential unconstrained optimization technique of Fiacco and McCormick. Joint confidence intervals for the computed parameters are estimated using the approach of Bard for nonlinear problems. These results show that when a hypocentre lies outside the array of recording stations and head waves from a dipping interface are involved, then its inclination must be taken into account for dip angles exceeding 5° .

Keywords. Hypocentral parameters; dipping interfaces; sequential unconstrained optimization; penalty function approach; earthquakes.

1. Introduction

Seismicity studies provide an illuminating perspective for seismic risk assessment in specific regions of interest. These studies, in turn, require accurate and systematic mapping of hypocentral parameters of local earthquakes in space and time. Determination of the four hypocentral parameters i.e. epicentral latitude and longitude, depth and time of occurrence are made from the arrival times of seismic P (and S) waves at a number of stations. Since arrival time observations may contain some errors, a minimum of 5 station data pertaining to each earthquake are required to obtain, in some prescribed sense, an optimized estimate of its hypocentral parameters, provided of course that the distribution of P -wave speeds in the region is known. When this latter information is not available, one proceeds by making some arbitrary assumptions. Alternatively, the P -wave distribution is considered as a set of unknowns to be determined along with the hypocentral parameters. But the number of station records required for this analysis has to be adequate enough to render the inverse problem an overdetermined one.

A number of algorithms have been developed for estimating hypocentral parameters, in a horizontally layered earth, from P -arrival times at 5 or more local stations i.e. for ray paths short enough to justify the neglect of the earth's curvature; (Flinn 1960; Norquidst 1962; Bolt 1960; Lee and Lahr 1975; Hermann 1979). These broadly fall into two groups depending upon whether the P -wave speed distribution is assumed or posed as unknowns to be determined by inverting P -arrival times at a larger number of recording stations.

boundaries dip variously in different regions. The algorithm is indeed quite versatile and capable of simulating a wide variety of P -wave speed distributions over small regions of the earth. It can easily deal with a horizontally layered earth simply by setting all dip angles to zero. It also allows one to seek solutions where the crustal structure is more representative of a framework of constant speed blocks, by simulating their vertical faces with an appropriately striking boundary that has a dip of 90° . The algorithm works very well for a small number of relatively larger blocks. However, it begins to pose some difficulties, largely of a book keeping nature, for a larger number of smaller blocks.

The motivation for developing this algorithm arose from an anticipated need of having to analyse P -wave arrival times recorded in the structurally complex region of Garhwal-Kumaon Himalaya (Gaur *et al* 1985), where an array of portable seismographs had been deployed to investigate the space-time regime of local earthquakes. It was of course realized at the time of initiating this exercise that the stage when P -wave speed distributions will be actually simulated for hypocentral locations, on the level of detail actually inferred from outcropping boundaries in the Himalaya, was still far off. However, it was felt that if crustal layers were indeed found to have appreciable inclination in the Himalayan region, then they would have to be modelled with care.

Estimation of hypocentral parameters from arrival times of seismic waves, constitutes a geophysical inverse problem which requires that the solution to the corresponding forward problem be already available. The direct problem here is to obtain a formalism whereby P -wave arrival times from a given hypocentre may be calculated at a given recording station, for a given P -wave speed distribution in the region. This, in turn, requires that the ray path between the known hypocentre and the recording stations should be traceable. The ray tracing problem has been discussed by Julian and Gubbins (1977), Pereyra *et al* (1980) and Chander (1977). Here we adopt Chander's ray tracing algorithm for our formalism. Recently, Kanasewich and Chen (1985) also assessed Chander's approach and adopted it for crustal investigations in parts of Canada.

2. The algorithm

Optimized estimates of hypocentral parameters are obtained using the least-squared error criterion. Let (X_H, Y_H, Z_H) be the three spatial coordinates of the hypocentre in a convenient local coordinate system and T_H the time of earthquake occurrence; then we optimize the function $E(X_H, Y_H, Z_H, T_H)$ with respect to its arguments.

$$E(X_H, Y_H, Z_H, T_H) = \sum_{i=1}^n [T_{i0} - T_{ic}(X_H, Y_H, Z_H, T_H)]^2. \quad (1)$$

Here T_{i0} is the observed arrival time at the i th station with known coordinates (X_i, Y_i, Z_i) and T_{ic} is the corresponding calculated time

$$T_{ic} = T_H + t_{ic}(X_H, Y_H, Z_H), \quad (2)$$

where t_{ic} is the P -travel time between the assumed hypocentre and the i th recording station. As indicated above, we assumed that the wave speed distribution between the hypocentre and all the stations can be simulated by constant wave speed layers with plane interfaces which may dip. The algorithm of Chander (1977) is used to trace rays between the hypocentres and the stations and thus to calculate t_{ic} 's and T_{ic} 's.

After Geiger (1912), the optimization of E in equation (1) has been traditionally conducted by first linearizing the t_{ic} 's (defined in (2)) with respect to X_H, Y_H, Z_H and estimating the hypocentral parameters iteratively (Flinn 1960; Bolt 1960; Norquidst 1962; Lee and Lahr 1975; Hermann 1979). If at each iteration the expected changes in hypocentral parameter estimates are represented by a column vector $\Delta\mathbf{X}$, then

$$\Delta\mathbf{X} = (A^T A)^{-1} A^T \mathbf{b}, \quad (3)$$

where the matrix A is composed of derivatives of T_{ic} 's with respect to hypocentral parameter estimates and \mathbf{b} is the column vector involving T_{i0} 's. Both matrix A and column vector \mathbf{b} are evaluated at current estimates of hypocentral parameters.

The common experience is that the matrix $A^T A$ is often near singular and the column vector $\Delta\mathbf{X}$, instead of tending to zero, grows without limit with each iteration. This arises from a number of situations notably (a) poor initial estimates of hypocentral parameters (b) majority of the recording stations being on one side of the hypocentre (c) excessive random errors in T_{i0} 's and (d) extremely unrealistic seismic P wave speed model. Thurber (1985) advocated retention of nonlinearity of t_{ic} 's and solution of conditional equations using Newton's method. Aki and Lee (1976; Hermann 1979; Hawley *et al* 1981; Koch 1985; Kanasewich and Chen 1985) followed the method of Levenberg (1944) and added a damping term λI to $A^T A$ to overcome this problem, λ being a constant and I the identity matrix. Here we adopt a constrained optimization procedure.

The search for optimized values of hypocentral parameters is constrained as follows

$$X_{H\min} < X_H < X_{H\max},$$

$$Y_{H\min} < Y_H < Y_{H\max},$$

$$Z_{H\min} < Z_H < Z_{H\max},$$

$$T_{H\min} < T_H < T_{H\max}.$$

The values of $X_{H\min}, X_{H\max}, Y_{H\min}, Y_{H\max}, Z_{H\min}, Z_{H\max}, T_{H\min}$ and $T_{H\max}$ are prescribed

$$E^*(X_H, Y_H, Z_H, T_H) = E(X_H, Y_H, Z_H, T_H) + \lambda \left[\frac{W_{X \max}}{X_{H \max} - X_H} + \frac{W_{X \min}}{X_H - X_{H \min}} + \frac{W_{Y \max}}{Y_{H \max} - Y_H} + \frac{W_{Y \min}}{Y_H - Y_{H \min}} + \frac{W_{Z \max}}{Z_{H \max} - Z_H} + \frac{W_{Z \min}}{Z_H - Z_{H \min}} + \frac{W_{T \max}}{T_{H \max} - T_H} + \frac{W_{T \min}}{T_H - T_{H \min}} \right],$$

where λ is a weight function and $W_{X \max}$, $W_{X \min}$, $W_{Y \max}$, $W_{Y \min}$, $W_{Z \max}$, $W_{Z \min}$, $W_{T \max}$ and $W_{T \min}$ are constants to describe the relative importance of the different constraints. These constants too are prescribed.

Using the SUMT (sequential unconstrained optimization technique) of Fiacco and McCormick (1968) we solve a sequence of problems in which E^* is optimized with respect to its arguments. Always a smaller value of λ is used. The values of hypocentral parameters obtained in the preceding iteration are used as the starting values in the new iteration. In the limit, as λ tends to zero, the values of the hypocentral parameters optimizing E^* also optimize E of (1).

During each iteration, the conditional equations

$$\partial E^*/\partial X_H = 0, \partial E^*/\partial Y_H = 0, \partial E^*/\partial Z_H = 0, \partial E^*/\partial T_H = 0 \quad (4)$$

are solved using the Newton-Raphson technique. Alternative procedures may be used for the purpose, e.g., the Powell's algorithm (Kanasewich and Chen 1985).

Following Flinn (1965) joint confidence intervals around the estimated hypocentral parameters are also estimated. However, while Flinn adopted Geiger's method of linerization, we follow Bard (1974) whose procedure permits retention of the nonlinearity.

3. Tests of the algorithm

The algorithm has been tested extensively by (i) using the synthetic data generated by us (table 1a and 1b); (ii) using our algorithm on the synthetic data set provided by Lee and Lahr (1975) in their manual on HYPO 71 and also by comparing the results of our algorithm and HYPO 71 for other synthetic data sets generated by us. The results of some of these tests are reported below.

(i) A plane with equation $-0.02X - 0.02Y + Z - 5.0 = 0$ separating a region of P -wave speed 3 km/sec which overlies a region of P -wave speed 5 km/sec is taken

Table 1a. Coordinates of recorder positions and corresponding P -wave arrival time data.

Recorder coordinates	Arrival time data
$S_1(3.404, 3.404, 0.0)$	$0^h 0^m 7^s.142 (P)$
$S_2(68.079, 2.861, -200.0)$	$0^h 0^m 77^s.108 (P)$
$S_3(-35.545, 55.969, -100)$	$0^h 0^m 46^s.446 (P)$
$S_4(1.066, 5.782, 0.0)$	$0^h 0^m 7^s.366 (P)$
$S_5(-4.473, 5.614, -5.0)$	$0^h 0^m 12^s.289 (S)$

the seismic velocity model. The hypocentre is assumed to be in the higher velocity region. Table 1a gives details of the five assumed recorder coordinates and the arrival time data at these recording stations. Table 1b gives the starting and final values of the hypocentral parameters of the program well as the (true) assumed hypocentral parameters.

The poor agreement in Z-coordinate is because all the stations are on one side of the hypocentre.

(i) Table 2 displays the results of our program and those of HYPO 71 using P-wave arrival time data and wave speed model provided by Lee and Lahr (1975).

On 28 December 1979 an earthquake occurred within the recording array operated by our group in the vicinity of the Main Central Thrust in the Garhwal Himalaya. Hypocentral parameters of this earthquake were also estimated by NOAA using regional permanent stations. Our results are compared with those of NOAA for this earthquake (table 3).

Table 1b. Starting, final and assumed value of hypocentral parameters.

Starting value of hypocentral parameters	Final value of hypocentral parameters	Assumed value of hypocentral parameters
$X = 0.5$	$X = 1.07$	$X = 1.00$
$Y = 0.5$	$Y = 0.99$	$Y = 1.00$
$Z = 4.0$	$Z = 3.92$	$Z = 6.00$
$t = 0^h 0^m 4^s.0$	$t = 0^h 0^m 4^s.97$	$t = 0^h 0^m 5^s.00$

Table 2. Comparison of hypocentral parameters estimated by HYPO 71 and our algorithm.

Hypocentral parameters	HYPO 71	Our algorithm
Latitude	$38^{\circ}29'.53N$	$38^{\circ}29'.05N$
Longitude	$122^{\circ}42'.08W$	$122^{\circ}41'.94W$
Depth	3.85 km	1.95 km
Origin Time	$12^h 6^m 44^s.56$	$12^h 6^m 44^s.23$

Table 3. Comparison of hypocentral parameters estimated by NOAA and our algorithm.

Hypocentral parameters	NOAA	Our algorithm
Latitude	$30^{\circ}.628N$	$30^{\circ}.822N$
Longitude	$78^{\circ}.445E$	$78^{\circ}.521E$
Depth	33 km	15.531 km
Origin Time	$1^h 59^m 18^s.8$ GMT	$1^h 59^m 18^s.406$ GMT

The epicentre is thus found to shift 15.9 km to the NE using local data. Also a definite estimate of the focal depth (15.531 km) has now been obtained using local network data in contrast to the routine value of 33 km as assigned by NOAA.

We are thus led to conclude that our algorithm and the computer program based on it are working satisfactorily.

4. Results

The algorithm has been used to analyse the actual data obtained in the Garhwal Kumaon Himalaya (Gaur *et al* 1985). It may be mentioned that for the vast majority of local earthquakes whose data were reported in that study, a uniform half-space wave speed model was adapted and the ray tracing facility of our algorithm was not needed. However, as estimates of focal depths for a number of earthquakes turned out to be in excess of 70 km, the data were reanalysed with a layered wave speed model and making use of the ray tracing facility of the algorithm. It has also been used to analyse synthetic data with a view to investigate several questions of theoretical nature pertaining to hypocentral parameter estimation. One of these questions is to decide the angle of interface dip at which it is desirable to abandon the use of flat-layered *P*-wave speed simulation of the earth and adopt a dipping interface simulation. In its simplest form the problem can be posed and examined using synthetic data for a one-layer over a half-space *P*-wave speed model in which the top surface of the layer is horizontal and the bottom interface dipping.

The stations (S_1, S_2, S_3, S_4, S_5) in figure 1 represent in a schematic fashion one of the arrays used by Gaur *et al* (1985) to record microearthquakes in the Garhwal Kumaon Himalaya. The dashed MSL surface implies that the stations are situated above it at varying heights up to 1.5 km. The maximum array dimension is 45 km. According to the geotectonic model of Seeber and Armbruster (1981) for this section of the Himalaya, a wedge of metasedimentary rocks is resting on Indian shield material. We assume that the contact between the two is planar and dips in the NE direction. The *P*-wave speed in the sedimentary wedge is 5.2 km/sec after Chander *et al* (1986) while that in shield material is taken to be 6.2 km/sec after Ni and Barazangi (1983). Using synthetic data, we estimate the order of error incurred in hypocentral location if the interface is assumed to be horizontal while it actually has dips of 5°, 10° and 15°.

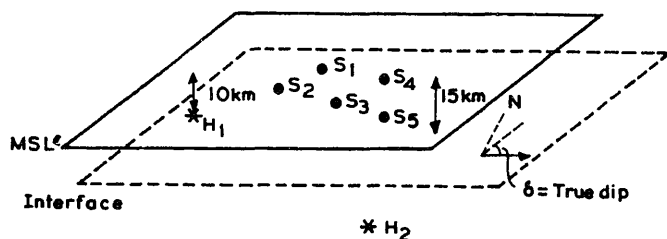


Figure 1. Schematic diagram showing recorder positions in the seismic array and the hypocentres H_1 and H_2 . MSL is mean sea level. Interface dips as shown by true dip vector.

The data displayed in tables 4 and 5 refer to two situations, one in which the epicentre is situated outside the array and the other in which it is inside the array. In this former case, H_1 (figure 1) is taken sufficiently far away so that the first arriving P waves at every station are head waves.

4. Discussion of results

We start by commenting on the errors in hypocentral parameter estimates when the correct dip model is used (see columns 2 in tables 4 and 5). They are ascribed firstly to round off errors in prescribing observed (actually synthetic in this hypothetical situation) arrival times. Secondly, although the rays leave the hypocentre in the same direction, downward in case of H_1 and upward in case of H_2 , the distance travelled along rays is much greater in the former case and so are the hypocentral shifts i.e. the respective distances between the estimated and known exact hypocentres.

In the no dip model calculations (see column 3 in tables 4 and 5) while both the above types of errors are present, the errors arising from the neglect of dip worsen with increase in dip of the interface in the actual model.

We conclude from this experiment that the effect of dip is much more pronounced when the epicentre is outside the array and head waves are involved. In this case, if the aim is to relate specific earthquakes to specific tectonic features

Table 4. Hypocentral parameter estimates when earthquake occurs outside the seismic array.

Earthquake occurs at H_1 in figure 1

Correct values $X_H = 200.0$ km, $Y_H = -130.0$ km,

$Z_H = 10$ km, $T_H = 0^h 0^m 0^s.0$

Apparent dip of interface	Parameter estimates		
	With correct dip model	With zero dip model	
15°	X_H	199.7	191.6
	Y_H	-128.6	-137.4
	Z_H	6.7	9.6
	T_H	0 ^h 0 ^m 0.4 ^s	0 ^h 0 ^m 0 ^s .1
	Hyp shift	3.6 km	11.2 km
10°	X_H	199.6	193.5
	Y_H	-128.7	-135.0
	Z_H	6.7	9.6
	T_H	0 ^h 0 ^m 0 ^s .4	0 ^h 0 ^m (-0 ^s .3)
	Hyp shift	3.4 km	8.2 km
5°	X_H	199.4	196.2
	Y_H	-128.8	-131.7
	Z_H	6.6	9.6
	T_H	0 ^h 0 ^m 0 ^s .4	0 ^h 0 ^m (-0 ^s .1)
	Hyp shift	3.6 km	4.2 km

Table 5. Hypocentral parameter estimates when earthquake occurs within the seismic array.

Earthquake occurs at H_2 in figure 1

Correct values $X_H = 120.0$, $Y_H = -60.0$,

$Z_H = 30.0$, $T_H = 0^h 0^m 0^s$

Apparent dip of interface	Parameter estimates	
	With correct dip model	With zero dip model
15°	X_H	120.0
	Y_H	-60.0
	Z_H	30.0
	T_H	$0^h 0^m 0^s$
	Hyp shift	0.0 km
10°	X_H	120.0
	Y_H	-60.0
	Z_H	30.0
	T_H	$0^h 0^m 0^s$
	Hyp shift	0.0 km
5°	X_H	120.0
	Y_H	-60.0
	Z_H	30.0
	T_H	$0^h 0^m 0^s$
	Hyp shift	0.0 km

(such as fault surfaces in 3D and fault traces in outcrops) then even 5° interface dip may be too significant to be ignored.

6. Discussion of the hypocentral parameters estimation algorithm

At this writing, hypocentral parameters of more than 500 earthquakes occurring in the Garhwal Kumaon Himalaya have been estimated using this algorithm. Between 150 and 200 synthetic data sets have been analyzed. We find that the constraints $Z_{H\min}$, $Z_{H\max}$ and $T_{H\max}$ are the most critical. A flag is put up during computations if a constraint is violated. The corresponding parameter is brought into the feasible region and the computations resume. But repeated violation of a constraint warn the operator that the prescription of that constraint needs scrutiny. When a converged constrained solution is obtained, a final run is carried out without any constraint ($\lambda = 0$ in equation (2)).

A somewhat unsatisfactory feature of the computer program as in current use is when for an assumed hypocentral location, a station is situated close to the crossover distance for direct and head waves. Then the ray path has to be changed from direct to critically refracted or vice versa and a fresh computation has to be started. But this is in no way an insurmountable programming problem. Otherwise we find that we have a well-tested and satisfactorily working algorithm and

7. Conclusion

A number of algorithms have been reported already in the literature for estimation of hypocentral parameters of local earthquakes using P -arrival time data. But in this domain a particular niche had remained vacant. It pertained to the need for an algorithm capable of handling of models with constant wave speed layers separated by dipping interfaces. That niche is now filled.

Within the overall framework of a least-squared error procedure whose tendency for instability is curbed through the use of constraints incorporated into the objective function via penalty functions, estimation of hypocentral parameters in quite general wave speed models is achieved using a variational ray tracing procedure. Joint confidence intervals around the estimated hypocentral parameters are also computed.

Use of such an algorithm is indicated when the interface dips exceed 5° .

References

- Aki K and Lee W H K 1976 Determination of three-dimensional velocity anomalies under a seismic array using first P arrival times from local earthquakes: Part I. A homogeneous initial model; *J. Geophys. Res.* **81** 4381–4399
- Bard Y 1974 *Nonlinear parameter estimation* (New York: Academic Press)
- Bolt B A 1960 The revision of earthquake epicentres, focal depths and origin times using a high-speed computer; *Geophys. J. R. Astron. Soc.* **3** 433–440
- Chander R 1977 On tracing seismic rays with specified end points in layers of constant velocity and plane interfaces; *Geophys. Prospect.* **35** 120–124
- Chander R, Sarkar I, Khattri K N and Gaur V K 1986 Upper crustal compressional wave velocity in the Garhwal Himalaya; *Tectonophysics* **124** 133–140
- Fiacco A V and McCormick G P 1968 *Nonlinear programming. Sequential unconstrained minimization technique* (London: John Wiley)
- Flinn E A 1960 Local earthquake location with an electronic computer; *Bull. Seismol. Soc. Am.* **50** 467–470
- Flinn E A 1965 Confidence regions and error determinations for seismic event location; *Rev. Geophys.* **3** 157–185
- Gaur V K, Chander R, Sarkar I, Khattri K N and Sinval H 1985 Seismicity and the state of stress from investigations of local earthquakes in the Kumaon Himalaya; *Tectonophysics* **118** 243–251
- Geiger L 1912 Probability method for the determination of earthquake epicentres from the arrival time only; *Bull. St. Louis Univ.* **8** 60–71
- Howley B W, Zandt G and Smith R B 1981 Simultaneous inversion for hypocentres and lateral velocity variations: An iterative solution with a layered model; *J. Geophys. Res.* **86** 7073–7086
- Hermann R B 1979 FASTHYPO—A hypocentre local program; *Earthquake Notes* **50** 25–37
- Julian B and Gubbins D 1977 Three-dimensional ray tracing; *J. Geophys. Res.* **43** 95–113
- Kanasewich E R and Chen W 1985 Least squares inversion of spatial seismic refraction data; *Bull. Seismol. Soc. Am.* **75** 865–875
- Koch M 1985 Nonlinear inversion of local seismic travel times for the simultaneous determination of the 3D-velocity structure and hypocentres-application to the Seismic Zone Vrancea; *J. Geophys.* **56** 160–173
- Lee W H K and Lahr J C 1975 HYPO 71 (Revised): A computer program for determining hypocentre, magnitude and first motion pattern of local earthquakes; U.S. Geological Survey Open-file Report 75–311
- Levenberg K 1944 A method for the solution of certain non-linear problems in least squares; *Maths.* **2** 164–168

- Ni J and Barazangi M 1983 High-frequency seismic wave propagation beneath the Indian Shield, Himalayan arc, Tibetan Plateau and surrounding regions: high uppermost mantle velocities and efficient Sn propagation beneath Tibet; *Geophys. J. R. Astron. Soc.* **72** 665–689
- Norquidst J M 1962 Computer program for earthquake location; *Bull. Seismol. Soc. Am.* **52** 431–437
- Pereyra V, Lee W H K and Keller H B 1980 Solving two-point seismic ray-tracing problems in a heterogeneous medium: Part 1. A general adaptive finite difference method; *Bull. Seismol. Soc. Am.* **70** 79–99
- Seeber L and Armbruster J G 1981 Great detachment earthquakes along the Himalayan arc and long-term forecasting in: *Earthquake prediction: An international review*, Maurice Ewing Ser, Vol. 4, (eds) D W Simpson and P G Richards (Washington: American Geophysical Union) 259–277
- Thurber C H 1985 Nonlinear earthquake location: Theory and examples; *Bull. Seismol. Soc. Am.* **75** 779–790

Weathering potential index for rocks based on density and porosity measurements

R PRATAP SINGH, VIJAY KUMAR UPADHYAY and
ASOK DAS

Bhagalpur College of Engineering, Bhagalpur 813 210, India

MS received 3 January 1987; revised 5 October 1987

Abstract. Rock samples belonging to ten lithological types under different stages of weathering, were collected from different stratigraphical horizons at Bhagalpur. Their densities and porosities were determined experimentally and the data obtained were fitted empirically in a linear equation for each lithological type. The slopes of the curves, which were negative in each case, showed that the increase in porosity for the same decrease in density were in the order, white sandstone > ferruginous sandstone > white claystone > porphyritic gneiss > quartzite > pegmatite > amphibolite = biotite gneiss > basalt = dolerite. A new weathering potential index based on the density-porosity data was proposed and the values for a specific stage of weathering for all the lithological types studied fall within the same range.

Keywords. Weathering classification; weathering potential index; rock density; rock porosity

1. Introduction

Several attempts have been made in the past to establish an index of weathering for the rocks. Reiche (1943) proposed a weathering potential index which can be computed either for a rock or for a mineral with the help of their usual chemical analysis. Fairbairn (1943) attempted to correlate the rate of alteration with packing index. Grant (1969) proposed an index of chemical weathering on the basis of abrasion pH. Branner (1937), Davis (1954), Daly *et al* (1966) and Ramana and Venkat Narayana (1971) studied various rock samples and found linear relationships between porosity and density. However, all these studies have not given due consideration to different weathering stages of the rock samples investigated. This paper presents densities and porosities of different lithological types under various stages of weathering in order to propose a weathering potential index based on the data collected.

2. Experimental

2.1 Materials

Based on standard classification (Geological Society of London 1970 and US Task Committee 1972) samples of six different weathering stages viz unweathered (UW), slightly weathered (SW), moderately weathered (MW), highly weathered

(HW), completely weathered (CW) and residual soil (RS), belonging to ten lithological types were selected from different stratigraphical horizons showing complete weathering profile located in Bhagalpur district (Bihar, India) and were collected from drill cores or freshly cut quarries. The residual soil samples were collected from 1B horizon (Patton and Deere 1970). Detailed specifications on the characteristics of the samples belonging to different weathering stages are given in table 1. Care was taken to ensure that the residual soil taken for investigation in each case was always a weathered product of once lithified sample (Legget and Karrow 1983) and not an unconsolidated sample of transported soil. The grain size of the representative residual soil samples was kept $< 250 \mu$ (passing BS sieve No 60).

2.2 Density determination

Each sample for density determination was first kept in an air oven at 110°C for 24 hr to remove any moisture present. Complete removal of moisture from the sample was ensured by weighing it to a constant weight. Its density was then determined at $30 \pm 1^{\circ}\text{C}$ by measuring its weight and corresponding volume. At first five such density determinations were carried out for each sample type and their average value was used for data analysis. The average experimental values of the densities so obtained are recorded in table 2.

2.3 Porosity determinations

The porosities of the rock samples collected were determined by using standard method available in published literature (ISI 1974) while the porosities of the

Table 1. Engineering classification of weathering*

Classification	Description of characteristics
Unweathered rock	No visible sign of weathering. Rock fresh, crystals bright. Few discontinuities may show staining.
Slightly weathered rock	Penetrative weathering developed on open discontinuity surfaces but only slight weathering of rock material. Discontinuities are discolored and discoloration can extend in to rock up to a few mm from discontinuity surface.
Moderately weathered rock	Slight discoloration extends through the greater part of the rock mass. The rock material is not friable (except in the case of poorly cemented sedimentary rocks). Discontinuities are stained and/or contain a filling comprising altered material.
Highly weathered rock	Weathering extends throughout the rock mass and the rock material is partly friable. Rock has no lustre. All material except quartz is discolored. Rock can be excavated with geologists' pick.
Completely weathered rock	Rock is totally discolored and decomposed and in a friable condition with only fragments of the rock texture and structure preserved. The external appearance is that of a soil.
Residual soil	Soil material with complete disintegration of texture and structure and mineralogy of the parent rock.

* after GSI (1970) and US Tech Committee (1973)

Table 2. Densities of various lithological types under different stages of weathering alongwith specific gravity of the residual soils.

Lithological types	Density d g/cc for rocks (UW to CW)					Residual soil (RS)	
	UW	SW	MW	HW	CW	Density γ_d^* g/cc	Sp. gr. G
Dolerite	3.012	2.940	2.741	2.520	2.222	1.321	2.773
Basalt	3.001	2.946	2.907	2.691	2.360	1.312	2.770
Biotite gneiss	2.636	2.610	2.590	2.483	2.234	1.271	2.660
Amphibolite	2.859	2.806	2.670	2.498	2.191	1.304	2.701
Pegmatite	2.701	2.668	2.660	2.570	2.340	1.260	2.661
Quartzite	2.617	2.592	2.582	2.486	2.442	1.282	2.660
Porphyritic gneiss	2.718	2.681	2.645	2.542	2.337	1.276	2.664
White claystone	2.091	2.034	1.962	1.897	1.812	1.223	2.661
Ferruginous sandstone	2.750	2.731	2.659	2.371	2.272	1.295	2.708
White sandstone	2.089	2.070	1.958	1.927	1.819	1.246	2.664

* minimum bulk density

corresponding residual soils were obtained by determining the dry bulk density and the specific gravity of their soil grains with the help of a pycnometer (ISI 1952) and using the following equation (Punmia 1977)

$$n = \rho / (\rho + 1), \quad (1)$$

where

$$\rho + 1 = G \gamma_w / \gamma_d, \quad (2)$$

where ρ is the void ratio, G the specific gravity of the grains of the residual soil and γ_d the dry bulk density for the same, whereas $\gamma_w = 1.01$ g/cc is the density of water sample used in the specific gravity determination. The values of γ_d and G , determined experimentally, are included in table 2. The average porosity value for each rock sample was obtained on the basis of at least five porosity determinations. The data so obtained are recorded in table 3.

3. Location and geology of the area

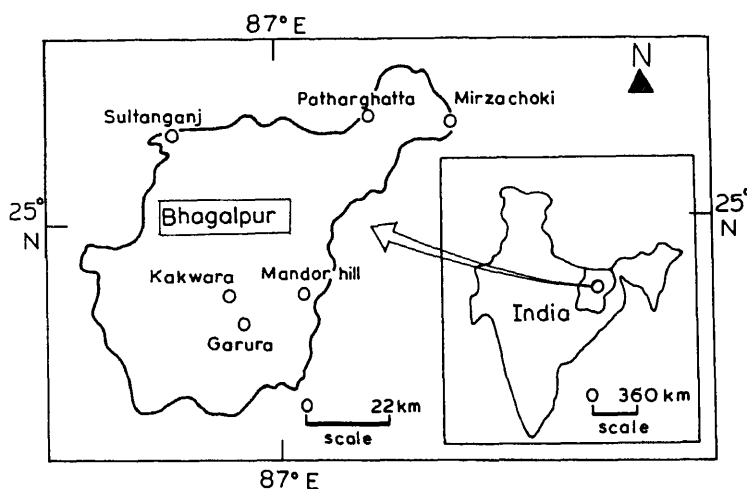
The area under study is located south of the river Ganges in Bhagalpur between $24^{\circ}29'$ and $25^{\circ}24'N$ lat, and between $86^{\circ}30'E$ and $87^{\circ}32'E$ long. The different places of sample collection are shown in figure 1 and table 4.

In this area the Precambrian rocks are distributed widely and are continuous with those forming the plateau of Chotanagpur. The available varieties of these include massive homogeneous granitoid and porphyritic gneiss showing extensive spheroidal weathering and also well-foliated gneiss, mica schists, amphibolites and quartzites. The Precambrian rocks have been traversed by a number of pegmatite veins as well as dolerite dykes and sills.

Table 3. Porosities of various lithological types under different stages of weathering.

Lithological types	Percent porosities % of samples under different stages of weathering					
	UW	SW	MW	HW	CW	RS
Dolerite	1.90	2.31	3.05	4.65	7.66	52.83
Basalt	1.35	1.69	2.06	3.50	6.31	53.10
Biotite gneiss	0.54	0.70	0.89	1.85	4.44	52.69
Amphibolite	2.19	2.46	3.96	5.06	8.64	52.20
Pegmatite	0.51	0.67	0.95	1.70	4.21	53.12
Quartzite	0.48	0.62	0.83	1.62	2.70	52.28
Porphyritic gneiss	1.28	1.65	2.36	3.76	6.31	52.58
White claystone	6.40	8.01	10.09			54.49
Ferruginous sandstone	3.56	4.41	6.47			52.65
White sandstone	10.09	11.68	15.78			53.69

* The sample disintegrates

**Figure 1.** Map of Bhagalpur district (area located south of the Ganges) showing places of sample collection along with a key map of India.

The rocks of the Damuda (Gondwana) are found at Patharghatta where nearly 50 m thick beds of white claystone, white sandstone and ferruginous sandstone rest unconformably over the Precambrian gneisses.

Dark black to greenish black basalts belonging to Rajmahal Traps overlie the Damuda sandstones on the eastern side of the Patharghatta hill. The same rocks are again found at Pirpainty and Mirzachoki. These are the outliers of the Rajmahal Traps.

The recent alluvium, varying in shades of gray, and known as Tal soils in this area, occupies a backwater belt of 8–10 km width along the south bank of the Ganges. The alluvial sediments underlying the recent alluvium and exposed in high grounds beyond the backwater belt where inundation does not reach now are

Table 4. Locations and stratigraphical horizons of different types of rocks studied

Lithological types	Locations			Stratigraphical horizons
	Place	Latitude	Longitude	
Dolerite	Garura	24°46'N	86°54'30"E	Precambrian
Basalt	Mirza Choki	25°15'N	87°32'E	Upper Jurassic (Rajmahal Traps)
Biotite gneiss	Sultanganj	25°15'N	86°45'E	Precambrian
Amphibolite	Kakwara	24°50'N	86°52'30"E	Precambrian
Pegmatite	Garura	24°46'N	86°54'30"E	Precambrian
Quartzite	Kakwarw	24°50'N	86°52'30"E	Precambrian
Porphyritic gneiss	Mandar hill	24°50'N	87°04'E	Precambrian
White claystone	Patharghatta	25°17'N	87°15'E	Permian (Damuda, Gondwana)
Ferruginous sandstone	Patharghatta	25°17'N	87°15'E	Permian (Damuda, Gondwana)
White sandstone	Patharghatta	25°17'N	87°15'E	Permian (Damuda, Gondwana)

Table 5. Stratigraphical succession in Bhagalpur district (Bihar)

Lithology	Stratigraphical horizons	Age
Alluvium	Recent Alluvium (Tal soils)	Recent
	Older Alluvium (Bhangar)	Pleistocene
Black and dark green basalts	Rajmahal Traps (Gondwana)	Upper Jurassic
White claystone, white sandstone and ferruginous sandstone	Damuda (Gondwana)	Permian
Gneisses, schists, quartzites, and amphibolites with veins of quartz and pegmatite, as well as dykes and sills of dolerites		Precambrian

istinguished as Older Alluvium (Roychoudhary 1962) with formation of kankar (ravertine) and at places ochre.

The geological cross-sections of the various places from which samples were collected are shown in figure 2. The stratigraphical succession in the area has been summarized (after Roychoudhary 1962; Krishnan 1968; Chatterjee and Sengupta 1980) in table 5.

Results and discussion

order to establish correlations between the densities and corresponding

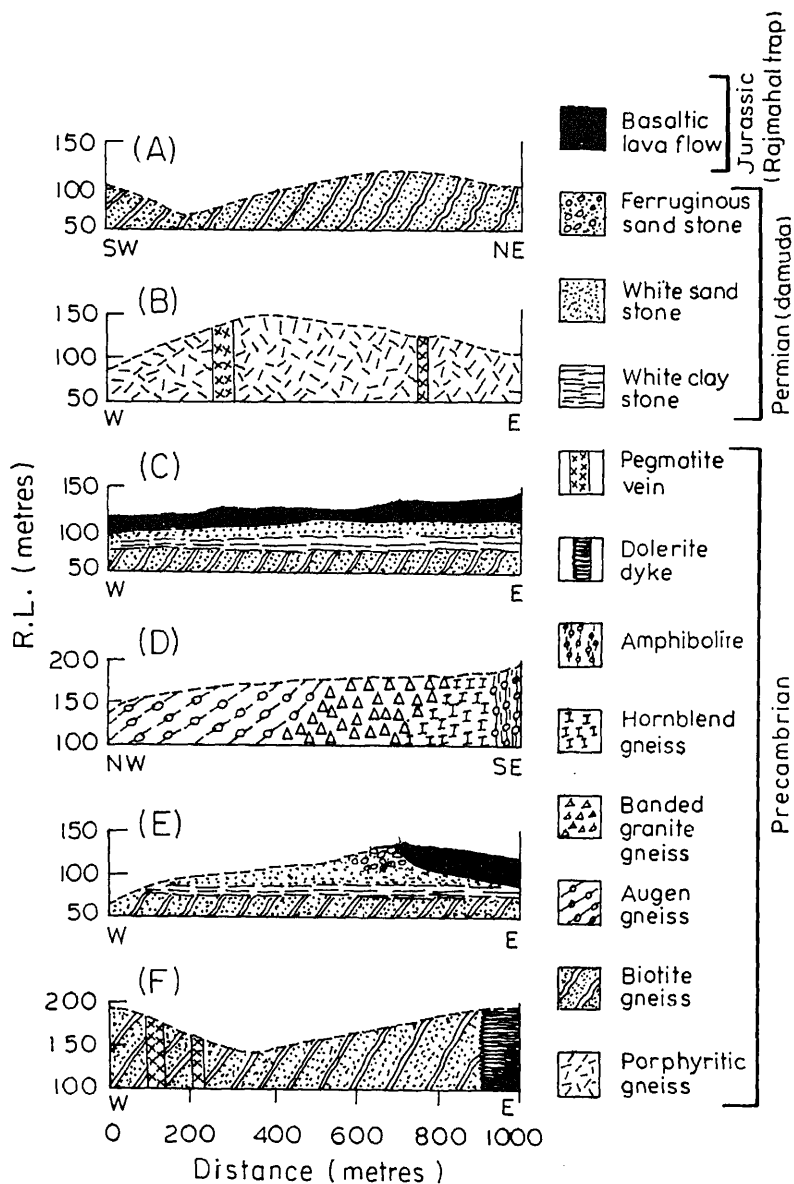


Figure 2. Geological cross-sections of the different areas of sample collection, (A) Sultanganj—along SW-NE, (B) Mandar Hill—along W-E, (C) Mirzachoki—along W-E, (D) Kakwara—along NW-SE, (E) Patharghatta—along W-E and (F) Garura—along W-E

tables 2 and 3 were used. The porosities when plotted against the corresponding densities of the rock domain (i.e. UW to CW) indicate a linear variation according to the equation.

$$\%n = md + C,$$

type of the rock obtained by the slope and intercept respectively of the linear curve. The plots of all the rock types studied are shown in figure 3. The porosity of the residual soil shows considerable deviation from the linearity for each type of rock studied. The values of m and C obtained for various rocks investigated have been included in table 6. Based on the values of m which denotes the rate of change in porosity with respect to density, the rocks studied were found to show an increase in porosity for the same decrease in density in the order, white sandstone > ferruginous sandstone > white claystone > porphyritic gneiss > quartzite > pegmatite > amphibolite \approx biotite gneiss > basalt = dolerite.

With a view to quantitatively assess the weathering, a dimensionless expression representing a new weathering potential index (WPI) using density-porosity data, was defined by the equation,

$$\text{WPI} = [(d/n) - (d_{rs}/n_{rs})] / [(d_{uw}/n_{uw}) - (d_{rs}/n_{rs})], \quad (4)$$

where d is the density of a rock belonging to any weathering stage, n is the corresponding porosity, d_{uw} and n_{uw} are the density and porosity respectively of the corresponding unweathered sample and d_{rs} and n_{rs} are the density and porosity respectively of the corresponding residual soil. The values of WPI for samples showing different stages of weathering viz UW, SW, MW, HW, CW and RS for various lithological types were calculated and recorded in table 6. As implied in (4) the value of WPI for residual soil is zero and the same for unweathered type is 1 in each case. Thus this is a measure of the available capability left for weathering and decreases (Reiche 1943) as the sample approaches a stable and completely

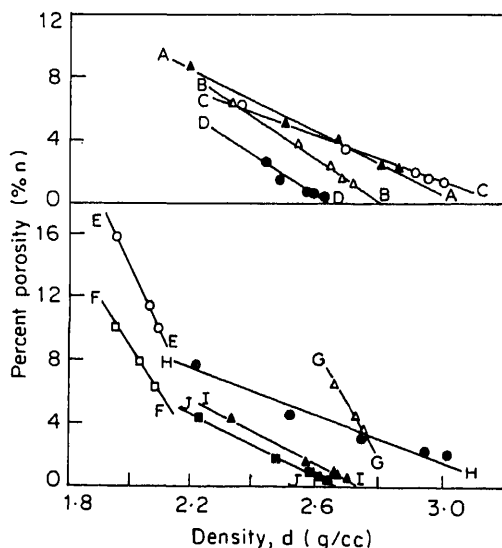


Figure 3. Variation of percent porosity % n with density d , g/cc for different rocks, (A-A) amphibolite, (B-B) porphyritic gneiss, (C-C) basalt, (D-D) quartzite, (E-E) white sandstone, (F-F) white claystone, (G-G) ferruginous sandstone, (H-H) dolerite, (I-I) pegmatite and (J-J) biotite gneiss

Table 6. Values of m and C as well as weathering potential index for various rocks studied

Lithological types	m	C	Values of WPI for various rocks under different stages of weathering					
			UW	SW	MW	HW	CW	RS
Dolerite	– 7.48	24.05	1.00	0.80	0.56	0.33	0.17	0.00
Basalt	– 7.76	24.10	1.00	0.78	0.63	0.34	0.16	0.00
Biotite gneiss	– 9.46	25.46	1.00	0.76	0.59	0.27	0.10	0.00
Amphibolite	– 9.79	30.15	1.00	0.87	0.51	0.37	0.18	0.00
Pegmatite	– 10.31	28.35	1.00	0.76	0.53	0.28	0.10	0.00
Quartzite	– 12.50	33.12	1.00	0.77	0.57	0.28	0.16	0.00
Porphyritic gneiss	– 13.42	37.85	1.00	0.76	0.52	0.31	0.16	0.00
White claystone	– 29.67	68.23	1.00	0.76	0.57	*	*	0.00
Ferruginous sandstone	– 34.78	99.12	1.00	0.79	0.51	*	*	0.00
White sandstone	– 40.51	94.80	1.00	0.84	0.55	*	*	0.00

* The samples disintegrates

Table 7. Classification proposed on the basis of weathering potential index (WPI)

WPI-range	Class
0.00	Residual soil
0.00–0.25	Completely weathered
0.25–0.50	Highly weathered
0.50–0.75	Moderately weathered
0.75–1.00	Slightly weathered
1.00	Unweathered

weathered end state. It is interesting to note that the WPI values of CW, HW, MW and SW samples of each lithological type studied fall in the same range 0–0.25, 0.25–0.50, 0.50–0.75, and 0.75–1.00 respectively. As such, instead of classifying the weathered rocks qualitatively in terms of SW, MW, HW and CW based on rough visual observations (GSL 1970). It is preferable to have a quantitative classification in terms of WPI as defined by (4) and given in table 7.

The WPI proposed here is expected to be useful in the foundation and construction design in the field of civil engineering, geomechanics and mining engineering projects, where it may be utilized in obtaining quantitative correlations of strength properties for different types of weathered rocks, it can also be used to correlate and predict petrophysical and petrochemical properties of a particular rock.

5. Conclusions

(i) The rocks studied were found to show an increase in porosity for the same decrease in density as a result of weathering in the order, white sandstone >

ferruginous sandstone > white claystone > porphyritic gneiss > quartzite > pegmatite > amphibolite \approx biotite gneiss > basalt \approx dolerite. (ii) A weathering potential index (WPI) based on the density-porosity data was defined with a view to have a quantitative assessment of different weathering stages. The calculated WPI values for a particular stage of weathering of all the lithological types studied were found to fall in the same range.

Acknowledgement

The authors thank Sri B Prasad, Research Officer, Soil Survey Scheme, Sabour for making available standard sieves for size analysis.

References

- Branner G C 1937 Sandstone porosities in palaeozoic region in Arkansas; *Bull. Am. Assoc. Petr. Geol.* **31** 67–79
- Chatterjee S R and Sengupta D K 1980 Structural and petrological evolution of the rocks around Jamua-Kakwara of Satpura orogeny Bhagalpur district, Bihar; *J. Geol. Soc. India*, **21** 171–182
- Daly R A, Manger G E and Clark S R 1966 in *Physical constants* (ed.) S P Clark *Geol. Soc. Am. Mem.* **97** 19–27
- Davis D H 1954 Estimating porosity of sedimentary rocks from bulk density; *J. Geol.* **62** 102–107
- Fairbairn H W 1943 Packing in ionic minerals; *Bull. Geol. Soc. Am.* **54** 1305–1374
- GSL 1970 Geological Society London, Engg Group Working Party; *Q. J. Geol.* **3** 1–24
- Grant W H 1969 Abrasion pH—an index of weathering; *Clays Clay. Miner.* **17** 151–155
- ISI 1952 Indian Standard Institution specifications for coarse and fine aggregates from natural sources for concrete, IS-383
- ISI 1974 Indian Standard Institution Methods of tests for determination of water absorption, apparent specific gravity and porosity of natural building stones, IS-383
- Krishnan M S 1968 *Geology of India and Burma* (Madras: Higginbothams) pp 81–82
- Legget R F and Karrow P F 1983 *Handbook of geology in civil engineering* (New York: McGraw Hill Co) pp 5–9
- Patton F D and Deere D U 1970 in *Handbook on mechanical properties of rocks* (eds) R D Lama and V S Vutukuri (Clausthal, Germany: Trans Tech Publishers) pp 271–272
- Punmia B C 1977 *Soil mechanics and foundations* (Delhi: Standard Book House) pp 12–17
- Ramana Y V and Venkat Narayana 1971 An air porosimeter for porosity of rocks; *Int. J. Rock. Mech. Min. Sci.* **8** 2953
- Reiche P 1943 Graphic representation of the chemical weathering; *J. Sed. Petrol.* **13** 58–63
- Roychoudhary P C 1962 *Bihar district gazetteer (Bhagalpur)* (Patna: Secretariat Press) pp 6–10
- US Task Committee 1972 Foundation Design Manual, Am. Soc. Civ. Eng.; *J. Soil. Mech. Found. Eng.* **98** 557

Seasonal variation of the salinity in the Zuari estuary, Goa, India

S R SHETYE and C S MURTY

Physical Oceanography Division, National Institute of Oceanography,
Dona Paula 403 004, India

MS received 13 April 1987; revised 24 August 1987

Abstract. The annual salt budget of the Zuari is examined. The characteristics of the estuary differ markedly from the low run off season during November–May to the heavy run off period of the southwest monsoon from June to October. During November–May the estuary is vertically mixed and the two processes controlling the transport of salt are run off induced advective transport out of the estuary, and tidally induced diffusive transport into the estuary. The magnitude of the latter is about 20% larger, leading to a salinity rise in the estuary. The diffusion coefficient has been estimated to be $233 \pm 101 \text{ m}^2/\text{sec}$. With the onset of the southwest monsoon, the run off increases dramatically, and the estuary loses about 75% of its salt during the first two months of the season. About 2/3 of this loss is recovered in the next two months when the run off decreases. Because the estuary is partially stratified during June–October, gravitational circulation is expected to play a role in addition to tidal diffusion and run off. The magnitude of its contribution has, however, not yet been determined.

Keywords. Estuary; salt budget; seasonal variation; vertically mixed; monsoon region; west coast of India.

1. Introduction

The Zuari estuary is located on the west coast of India and joins the Arabian Sea near the port city of Marmagao (figure 1). The salinity distribution in this estuary shows that during May, just before the onset of the southwest monsoon, tidally averaged salinities well in excess of 1 ppt are observed upto 40 km from the mouth. By July the salinity drops dramatically, and is generally < 1 ppt upstream of 20 km from the mouth of the estuary. The salinity throughout the length of the estuary increases continuously from October to May.

This seasonal cycle is typical of the shallow and narrow estuaries on the west coast of India, which comes under the influence of the atmospheric monsoon circulation and experiences a spell of heavy precipitation of the order of 250 cm during June–October. During November–May, the dry season, total precipitation is < 10 cm. These estuaries have not been studied much, and virtually nothing is known about the transport processes that control their seasonal salinity cycle. In the present paper we have attempted to synthesize the available data from the Zuari estuary to determine the principal constituents of the seasonal salt budget of the estuary.

2. Zuari — a physical description

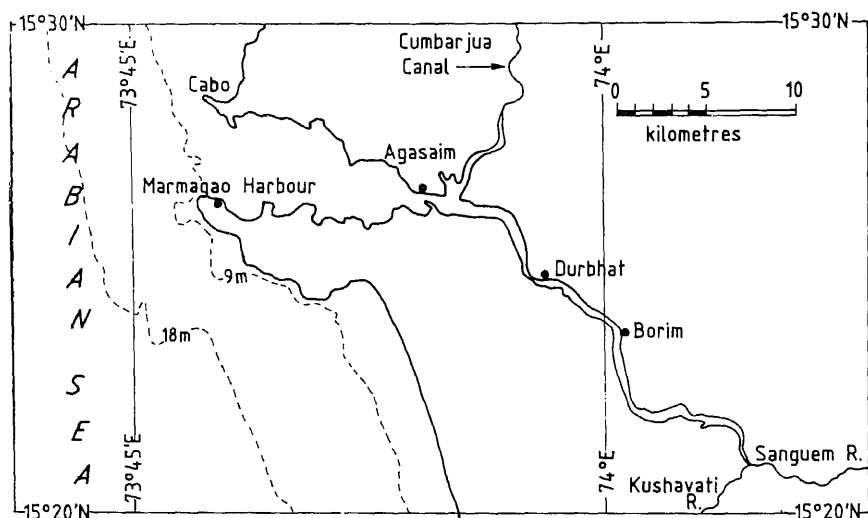


Figure 1. The Zuari estuary.

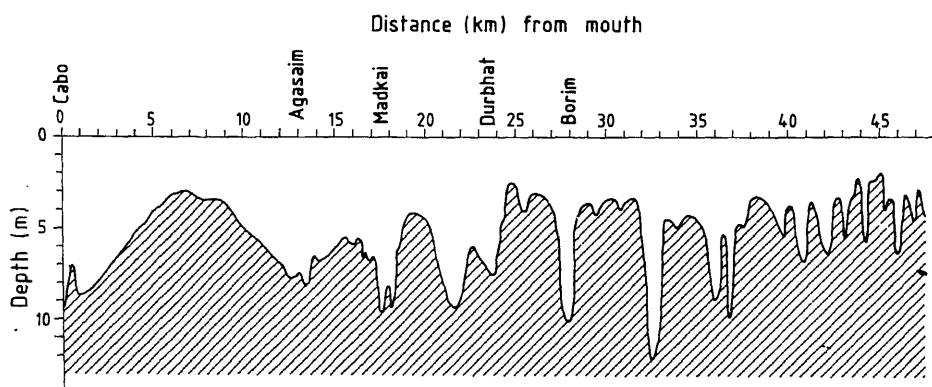


Figure 2a. Centreline mean depth (m) profile of the Zuari.

area is given in figure 2b. The average depth upto 40 km from the mouth is approximately 5 m. The bottom topography is marked by a few trenches as deep as 10 m. The cross-sectional area of the estuary decreases exponentially. The decrease is more rapid in the first 20 km from the mouth.

Joining the estuary at about 15 km from the mouth is the Cumbarjua Canal which connects the Zuari to another estuary, the Mandovi. The width of the canal varies between 100 and 320 m and its cross-sectional area decreases from 820 m² near the Zuari to 370 m² at the Mandovi (Mehta *et al* 1983). Since the cross-sectional area of the canal is small compared to the area of the Zuari at the

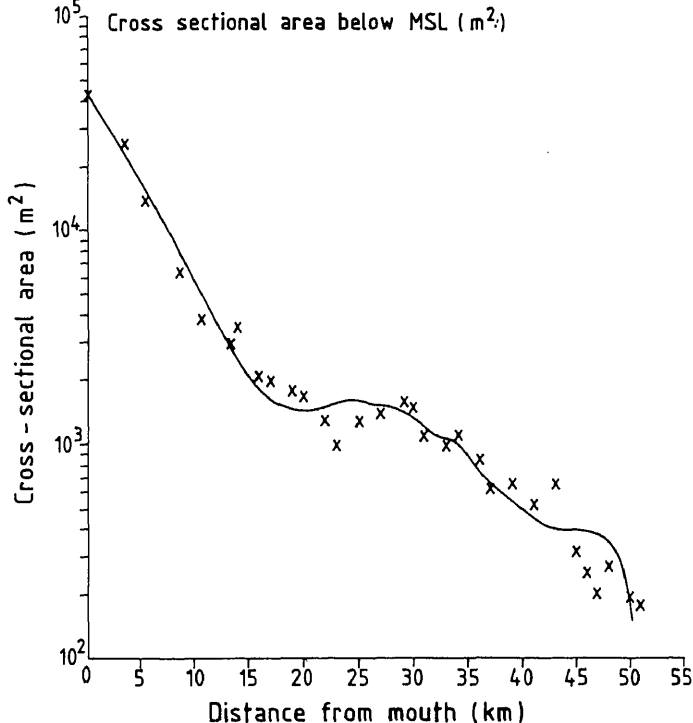


Figure 2b. Variation of mean cross-sectional area (m^2) in the Zuari. Horizontal axes give distance (km) from the mouth of the estuary.

high as 2.3 m. The nature of variation in the phase and range of the tide along the estuary is not known.

The two main rivers Kushavati and Sanguem, contributing freshwater run off to the Zuari were gauged during the southwest monsoon seasons of 1963, 1964 and 1966. The run off in the Zuari inferred from these data is given in figure 3 (Das *et al* 1972). Virtually all the rainfall in the catchment area of the Zuari occurs during June–October. The rainfall shows marked time variability corresponding to the break and active phases of the southwest monsoon. Consequently, the run off in the estuary can fluctuate from $100 \text{ m}^3/\text{sec}$ to $400 \text{ m}^3/\text{sec}$ over a period of few days. The Zuari has not been gauged during the dry spell from November to May, the period during which the catchment area receives $< 10 \text{ cm}$ of rainfall. The run off in the river is believed to decrease monotonically from November till the onset of the next southwest monsoon.

The vertical variation in salinity undergoes marked changes from season to season. At Agacaim, for example, Cherian *et al* (1975) report < 0.5 ppt salinity variation from surface to bottom during April, the vertically averaged salinity being 34.5 ppt. Towards the end of September the surface to bottom difference in salinity is almost 7 ppt, and the average salinity of the water column is 26 ppt. Cherian *et al* (1975) further report that the surface to bottom change in salinity at Borim is around 1 ppt in January and over 5 ppt in September, the vertically averaged salinities in January and September being 23 ppt and 10 ppt respectively. These

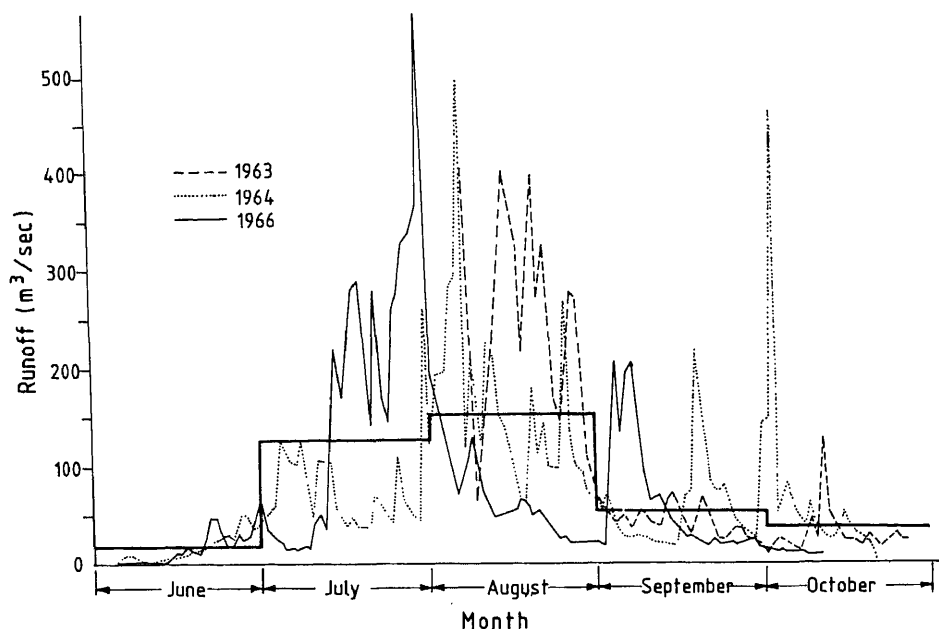


Figure 3. Run off (m^3/sec) in the Zuari estuary during the southwest monsoon seasons of 1963 (----), 1964 (.....) and 1966 (—). The monthly-mean run off, computed by averaging the run off for these three years, is shown by (—).

figures suggest that the character of the estuary changes from the dry season (November to May) to the wet season (June to October). This point is highlighted from the following consideration. The intertidal volume of the Zuari is around $90 \times 10^6 \text{ m}^3$. The fresh water contribution to the intertidal volume is thus $< 0.5\%$ during the dry season when the run off is $< 10 \text{ m}^3/\text{sec}$. The mean run off during August is $150 \text{ m}^3/\text{sec}$. Hence the run off contribution is $> 7\%$ of the intertidal volume. When, during an active phase of the monsoon, the run off exceeds $400 \text{ m}^3/\text{sec}$, the same contribution would exceed 20% . Such high rainfall episodes generally last only a few days and are distributed at random over a season. During such an episode, a rapid variation with time in the behaviour of the estuary is expected.

In summary, the Zuari shows two distinct conditions. It is vertically mixed with little time variability during the dry period of November–May. The estuary is partially stratified with large time variation due to fluctuations in run off during the southwest monsoon season.

3. Seasonal salt budget and horizontal diffusion coefficient

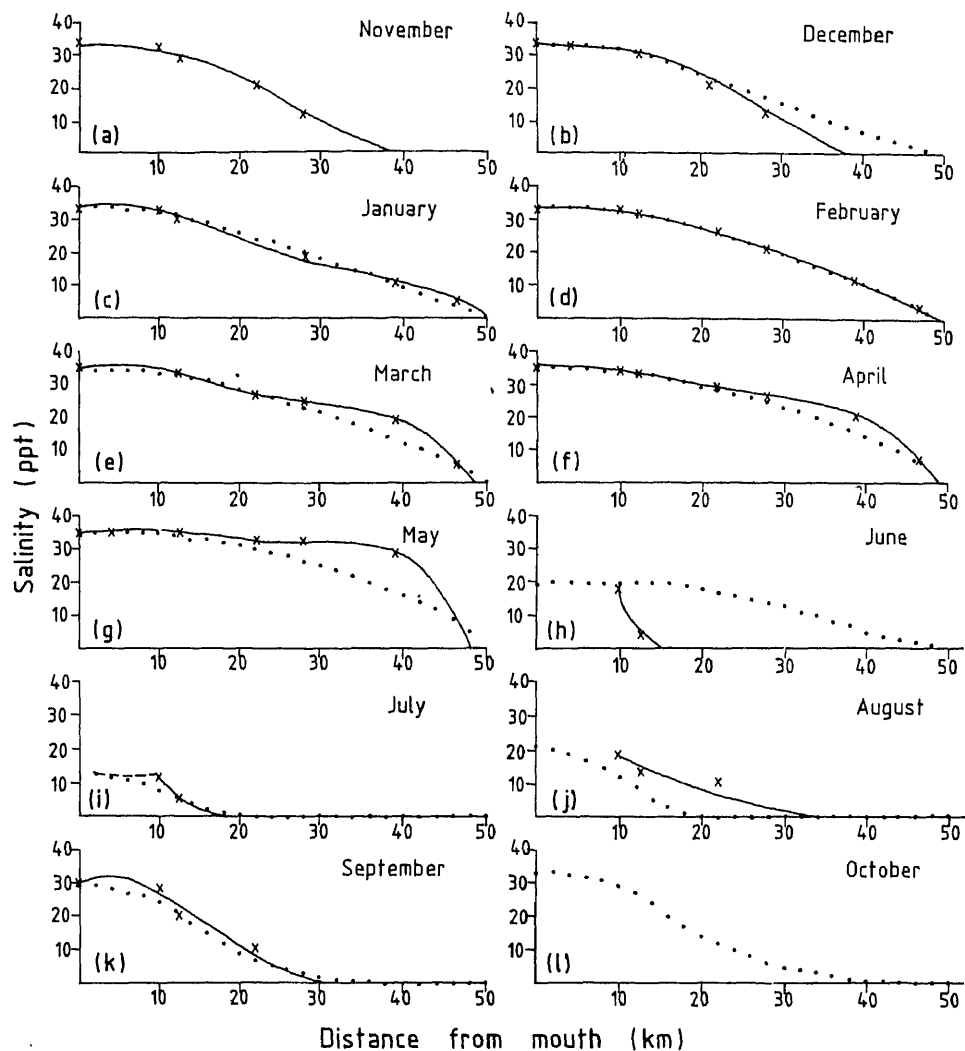


Figure 4. Annual cycle of salinity distribution in the Zuari. The horizontal axes give distance from the mouth. The observed values are denoted by crosses (x). Thin line gives a polynomial fit $S(x)$ to the observations (.....) gives the salinity simulated by the model described in §4.

the axial salinity distribution. As day-to-day or week-to-week variations in the Zuari are small during November–May, we can look at each one of the figures 4 a–g as representative for that month. The same, however, cannot be said about figures 4 h–k. For reasons discussed earlier, large variations in the characteristics of the estuary are expected from week to week during June–September. Hence significant scatter around the data plotted in figures 4 h–k is expected if observations are repeated.

In figure 4 we have also plotted curves which are polynomial least square fits to the observations. These curves give, for each month, salinity S as a continuous

function of x , the upstream distance from the mouth of the Zuari. The total salt in the estuary, S_{tot} , is given by

$$S_{\text{tot}} = \int_0^{\infty} S(x) A(x) dx, \quad (1)$$

where A is the cross-sectional area. The upper limit of the integral is the far upstream end of the estuary where S vanishes. In figure 5 we have plotted the annual variation in S_{tot} together with the average monthly-mean run off in the Zuari. The run off values for June–October are based on the data in figure 3. During November–May the monthly-mean run off has been assumed to decrease linearly with time from $15 \text{ m}^3/\text{sec}$ in October to $3 \text{ m}^3/\text{sec}$ in May.

As seen from figure 5, S_{tot} increases continuously from November to May, the rate of increase being approximately $70 \text{ (ppt m}^3\text{)}/\text{sec}$. The mean run off and the salinity at the mouth of the estuary during the same period are $9 \text{ m}^3/\text{sec}$ and 34.2 ppt respectively. Hence the average advective transport of salt out of the estuary due to run off during the period is about $300 \text{ (ppt m}^3\text{)}/\text{sec}$. As the estuary is well mixed in the vertical during the dry season, we expect the contribution of gravitational circulation to the salt transport into the estuary to be negligible. Hence, to explain the observed increase in S_{tot} , there has to be a tidally-induced diffusive transport of about $370 \text{ (ppt m}^3\text{)}/\text{sec}$ into the estuary. Thus the magnitude of the advective and that of the diffusive transport is about 5 times the rate of change of S_{tot} . The variation of S_{tot} during the southwest monsoon is far more rapid. The estuary loses about 75% of its salt in the first two months of the wet spell. During the next two months when the run off decreases, about 2/3 of this loss is recovered.

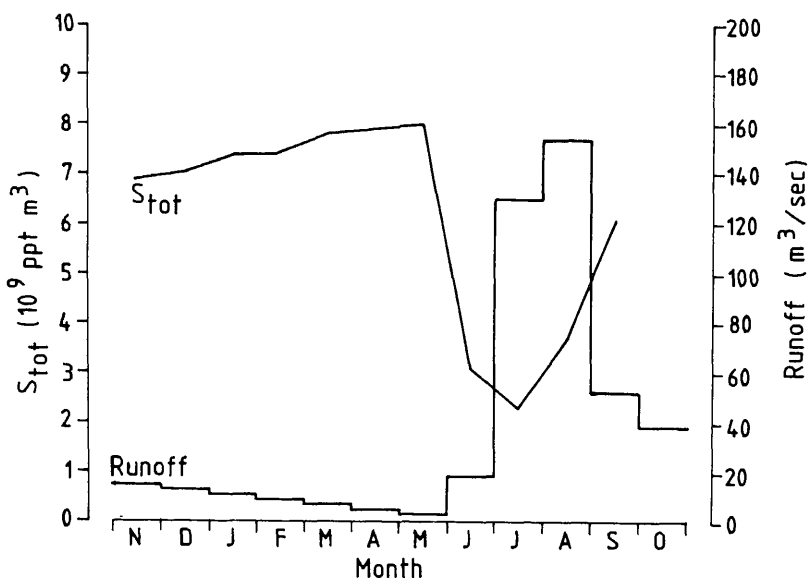


Figure 5. Annual cycles of S_{tot} (see equation (1)) and monthly-mean run off (m^3/sec)

point x along the estuary, the following one-dimensional advection-diffusion equation holds

$$\frac{\partial}{\partial t} \int_x^{\infty} S(x') A(x') dx' = KA \frac{\partial S}{\partial x} + RS. \quad (2)$$

Here K , R and t are the axial diffusion coefficient, run off and time respectively. Each of the terms, except K , in the above equation can be estimated by using the data in figures 2b, 4 and 5. Hence the relation can be used to compute K . A steady state version of this procedure has been used in Stommel (1953). We have computed K every 5 km up to 40 km upstream of the mouth. The left side of the equation was estimated using $S(x)$ for two consecutive months. The averages of $\partial S / \partial x$, S and R for these two months were used on the right side. The results are plotted in figure 6. As seen from the figure, K does not show any systematic variation with distance nor with time. The average and the standard deviation of all the values of K were found to be $233 \text{ m}^2/\text{sec}$ and $101 \text{ m}^2/\text{sec}$ respectively. A linear regression, $K = K_0 + K'x$, gave K_0 and K' equal to $244 \text{ m}^2/\text{sec}$ and $0.88 (\text{m}^2/\text{sec})/\text{km}$ respectively.

4. A one-dimensional advection-diffusion model study

To examine the extent to which the above one-dimensional advective-diffusive balance applies to the annual salinity cycle in the Zuari, we modelled S using the equation obtained by differentiating (2) w.r.t. x . The second order PDE was solved using an implicit alternating direction finite difference method with increments in t and x set equal to 0.1 day and 2 km respectively. The simulation was started on November 16 with $S(x)$ given in figure 4a. The observed salinities at the mouth

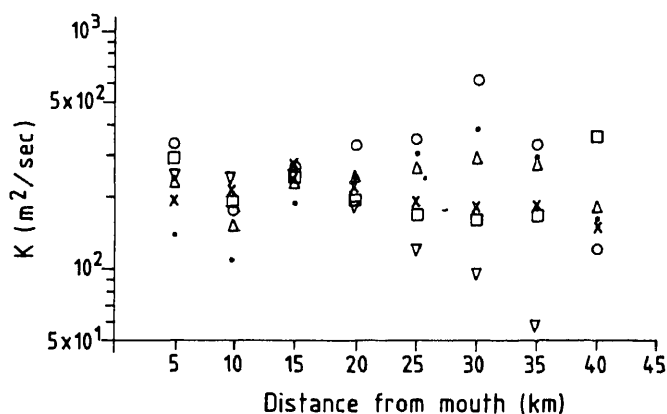


Figure 6. Horizontal diffusion coefficient K (m^2/sec), computed by using equation (2). Data for two consecutive months were used to estimate terms in the equation November-December (∇), December-January (\square), January-February (\times), February-March (\triangle), March-April (\bullet), and April-May (\circ).

$x = 0$ km, were used as one boundary condition. At the other boundary, $x = 50$ km, the salinity was set equal to zero. The diffusion coefficient was taken to be $240 \text{ m}^2/\text{sec}$, and the run off in figure 5 was used.

The result of the simulation on the 15th of each month (every month was assumed to be of 30 days) is plotted in figure 4. The simulation shows that the overall pattern of salinity variation is fairly well reproduced during the dry season. This result justifies the assumption in the model that the estuary is of a vertically and laterally mixed-type during this season. The model did not fare well during the southwest monsoon. The likely reasons are that during the southwest monsoon, because the estuary is partially stratified, gravitational circulation will be contributing to the salt transport. This has not been taken into account in the model. Secondly, the model has not considered the contribution of the wind driven circulation in the estuary. This contribution is expected to be important during the southwest monsoon when strong westerlies exert stress directed upstream of the estuary. Lastly, it is worth noting that the observed salinity field for a month given in figure 4 really represents the condition that existed on a particular day. During the southwest monsoon, when run off, windstress, etc. are highly variable, it is unrealistic to expect that the climatic model used here would be able to simulate conditions for a particular day.

5. Conclusions

The Zuari estuary, a typical shallow, narrow estuary on the west coast of India shows distinct characteristics in the wet season (June-September) of the southwest monsoon and the dry season during October-May.

During the dry season the estuary is well mixed vertically and experiences a temporal increase in salinity throughout its length. The two transport processes controlling the salt budget of the estuary during this season are the run off induced advection of salt out of the estuary, and the tidally induced diffusion into the estuary. The latter is about 20% larger of the two processes and leads to a net upstream movement of salt. The diffusion coefficient has been estimated to be $233 \pm 101 \text{ m}^2/\text{sec}$.

During the wet spell of the southwest monsoon, the run off in the estuary increases rapidly. As a result the estuary loses about 75% of its salt in approximately two months. During the following two months, when the run off decreases, about 2/3 of the lost salt is recovered. The transport of salt into the estuary is partly due to tidal diffusion, and partly due to gravitational circulation. The magnitude of the latter is not known, but is expected to be significant because the estuary is partially stratified during this season.

References

- Cherian T, Rao L V G and Varma K K 1975 Variations in physical characteristics of waters of the Zuari estuary; *Indian J. Mar. Sci.* **4** 5-10
- Das P K, Murty C S and Varadachari V V R 1972 Flow characteristics of Cumbarjua canal connecting the two estuaries Mandovi and Zuari; *Indian J. Mar. Sci.* **1** 95-101
- Indian Tide Tables 1985 Geodetic and Research Branch, Survey of India, Dehra Dun, India, Part 1

- Mehta A J, Naik B U and Hayter E G 1983 A preliminary investigation of fine sediment dynamics in Cumbarjua canal, Goa; *Mahasagar – Bull. Natl. Inst. Oceanogr.* **16** 95–108
- Qasim S Z and Sen Gupta R 1981 Environmental characteristics of the Mandovi-Zuari estuarine system in Goa; *Estuarine. Coastal Shelf Sci.* **13** 557–578
- Stommel H 1953 Computation of pollution in a vertically-mixed estuary; *Sewage Ind. Wastes* **25** 1065–1071

Selection of optimum frequency of a wind scatterometer

ABHIJIT SARKAR, RAJ KUMAR and MANNIL MOHAN

Meteorology and Oceanography Division, Space Applications Centre,
Ahmedabad 380 053, India

MS received 19 June 1987.

Abstract. The problem of selecting the optimum operating frequency of a scatterometer, used for remote sensing of sea surface wind speed has been addressed by applying the criteria of maximum sensitivity of backscattering coefficient to wind speed as well as its correlation with wind speed. The backscattering coefficient values for sea surface were computed by the two-scale scattering theory. To compute the atmospheric transmittance, 753 clear sky atmospheres over Indian Ocean were used. While the correlation coefficient was uniform (0.94) throughout the frequency range of 1 to 30 GHz, only frequencies above 5 GHz were found sensitive enough to yield a wind speed accuracy of $\pm 2 \text{ msec}^{-1}$ and better, the accuracy improving with frequency.

Keywords. Scatterometer; sea surface wind speed; optimum frequency; atmospheric transmittance.

1. Introduction

In order to achieve maximum accuracy and resolution of the remotely-sensed parameter, it is desirable to have remote sensing sensors with optimum operating characteristics. A number of studies on optimum system parameters of remote sensing instruments have been reported (Macdonald and Waite 1971; Ulaby and Batlivala 1976; Kondratyev and Pokrovsky 1979; Matzler *et al* 1982; Pandey and Kakar 1983; Peckham *et al* 1983). However, remote sensing instruments appear to have been developed by and large through the evolution of a new technology or the retrieval technique.

The present work evolves an optimum frequency of a wind scatterometer and it is hoped the results would be useful for defining a scatterometer system for remote sensing of oceanic winds in tropical regions like the Indian waters.

Satellite-borne radar scatterometer operating in microwave frequency band is emerging as a prime sensor for mapping global ocean wind. The earlier satellite-borne scatterometer SASS (Seasat A scatterometer system) provided surface wind speed to $\pm 2 \text{ msec}^{-1}$ and direction $\pm 20^\circ$ accuracy (Jones *et al* 1982). A number of satellite-borne scatterometer systems are being planned in the next few years e.g. ERS-1, NROSS, RADARSAT etc. Scatterometer systems are also being considered for future Indian remote sensing satellites.

To select an optimum frequency of a wind scatterometer, the sensitivity spectrum (sensitivity of backscattering coefficient to surfacial oceanic wind) and the correlation coefficient (correlation between the surface wind speed and the backscattering coefficient) were studied. The sensitivity spectrum was used to

identify the range of frequencies for which the backscattered signal has higher wind detectability. The backscattered signal however gets attenuated as it passes through the atmospheric column before it is sensed by the sensor onboard the satellite. As the attenuation is different for different frequencies, the value of correlation coefficient for any frequency is an indicator of the accuracy of the retrieved wind speed.

2. Sensitivity of backscattering coefficient to wind

To study the sensitivity of the backscattering coefficient (σ°) to ocean surface wind W over a range of frequencies (1 to 30 GHz), σ° was simulated through the well-known two-scale scattering model (Moore and Fung 1979; Fung and Lee 1982, 1983). Utilizing the common procedures of curve fitting and the above mentioned scattering theory, the sensitivity of σ° to W was derived for four specific values of frequency viz 1, 5, 9 and 13 GHz (representing L-, C-, X-, and Ku-bands) for the incidence angles ranging from 30 to 60° (Sarkar and Kumar 1985). The angle of incidence of 45° which was found to be optimum from the sensitivity point of view was chosen for this study while the frequency was varied from 1 to 30 GHz. A linear representation of backscattering coefficient in decibels is

$$\sigma^\circ(\text{dB}) = A + B \log(W).$$

The coefficient B indicates the sensitivity of scattering coefficient to wind speed. Figure 1 represents the variation of B over the frequency range from 1 to 30 GHz. As is seen from the figure, the value of B almost doubles when the frequency is changed from 5 to 25 GHz. The curve steadily rises with increasing frequency. Hence, from the sensitivity point of view, higher the frequency, greater will be the wind detectability. For most of the present-day meteorological and oceanographic

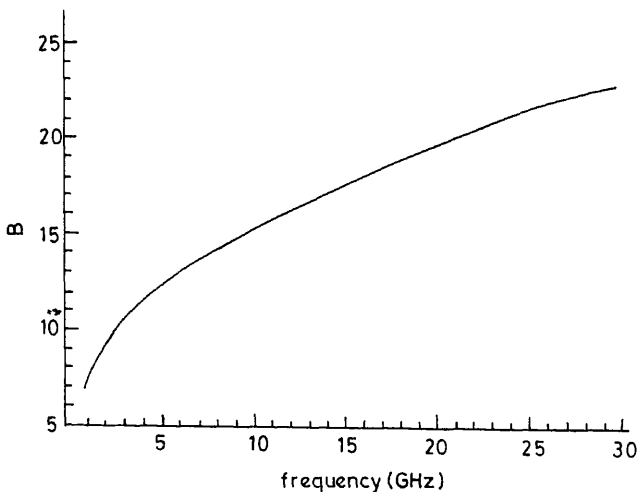


Figure 1. Variation of B with frequency.

applications, an accuracy of $\pm 2 \text{ msec}^{-1}$ in wind speed is acceptable. For low wind speed conditions this is achievable over the entire frequency range considered in this paper; but for higher wind speed conditions (i.e. more than 10 msec^{-1}), it may not be possible to achieve the wind accuracy of $\pm 2 \text{ msec}^{-1}$ by scatterometers operating at 5 GHz or lower (this can be verified in figure 1, assuming a 1 dB measurement precision).

3. Correlation between scattering coefficient and wind speed

In order to derive the realistic values of correlation coefficient, level III b data as generated by ECMWF over the selected test site (-13.125 to $+5.625^\circ$ latitude; 50°E to 90°E longitude) were used. The temperature, relative humidity and geopotential height values corresponding to the pressure levels of 1000, 850, 700, 600, 500, 400, 300, 200, 150 and 100 mb were utilized to compute the atmospheric transmittance τ . The equations used to obtain τ are given in Appendix I and the variation of τ for a typical cloudless atmosphere over the frequency range of 1 to 30 GHz is shown in figure 2. A rather big dip in τ occurs around 22 GHz, the water vapour resonance absorption frequency.

The values thus calculated were used to simulate the scattering coefficient that a spaceborne scatterometer placed above the atmospheric column would measure

$$\sigma_m^\circ = \sigma_s^\circ \tau^2,$$

where σ_m° is the measured scattering coefficient, and σ_s° the surface scattering coefficient (Moore and Fung 1979; Fung and Lee 1982, 1983; Sarkar and Kumar 1985). The surface (1000 mb) wind speed values as given in level III b data set, corresponding to the τ values for which σ_m° was computed were used for deriving the correlation coefficient. Figures 3–6 represent the scatter plots of simulated values of measured scattering coefficient vs surface wind speed for frequencies

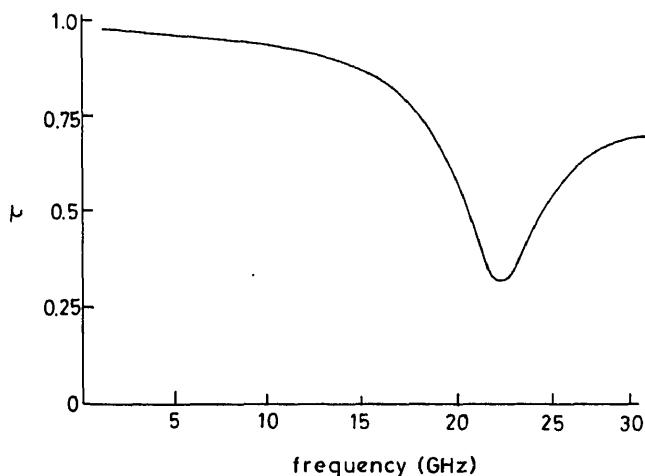


Figure 2. Variation of τ with frequency.

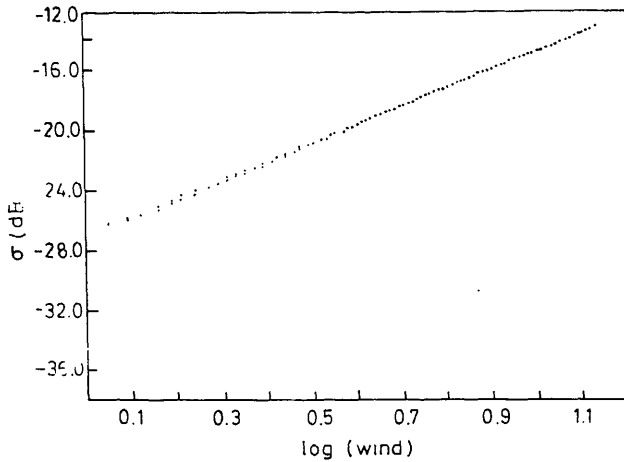


Figure 3. Scatter plot of σ^o (dB) vs $\log W$ for 5 GHz.

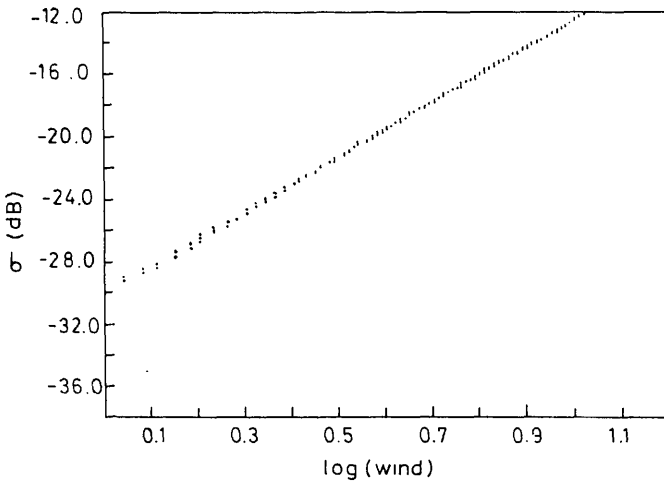


Figure 4. Scatter plot of σ^o (dB) vs $\log W$ for 15 GHz.

5 GHz, 15 GHz, 22 GHz and 30 GHz representing C, Ku and K_u bands respectively. The angle of incidence was fixed at 45° as this angle lies well within the peak portion of the wind sensitivity curve (Sarkar and Kumar 1985). Only the upwind case ($\phi = 0^\circ$) is studied in this paper. Any other value of wind azimuth angle ϕ does not alter the trend in the results and hence has not been reproduced here. Since polarization also has been found inconsequential, only HH polarization is considered here. Although τ changes substantially around 22 GHz, the spread of points is not significant. As a result, there is no significant variation in correlation coefficient for the frequencies considered here. For the 753 data sets considered here, the coefficient of determination (square of coefficient of correlation) was 0.89.

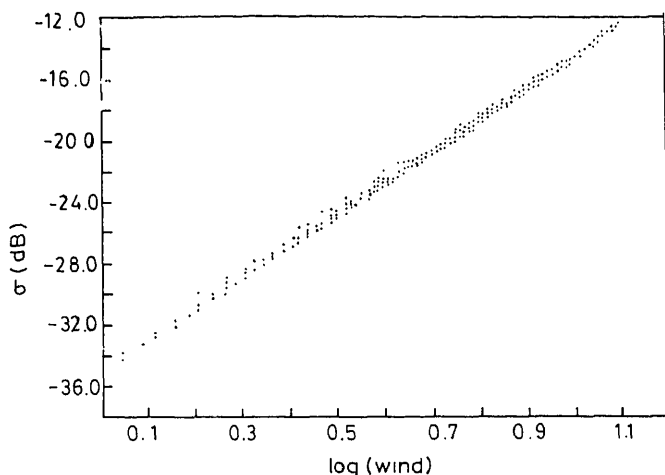


Figure 5. Scatter plot of σ^0 (dB) vs $\log W$ for 22 GHz.

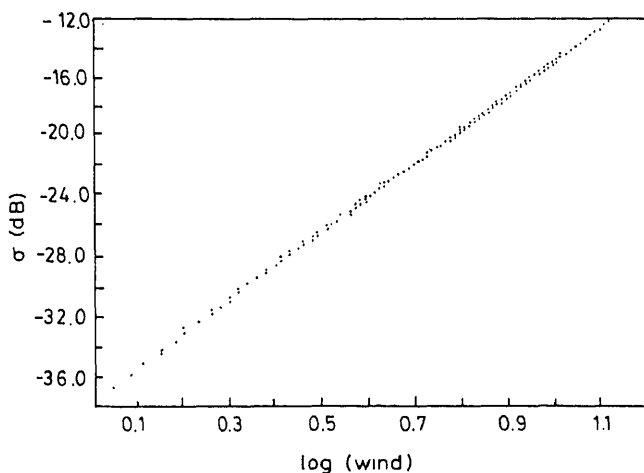


Figure 6. Scatter plot of σ^0 (dB) vs $\log W$ for 30 GHz.

4. Results and discussions

The 753 data sets used in this study represent cloud-free atmosphere in May, June and July 1979. The cloudy data were separated by discarding the data having relative humidity values higher than 80% at any level other than 1000 mb. The total water vapour content in the data varied between 1.5 g cm^{-2} and 4.7 g cm^{-2} and the surface wind speed varied from calm to 13.4 msec^{-1} . It is seen that the transmittance for these atmosphere makes only a small difference to the scattering coefficient values and hence the scatter of points for any frequency band is not large (the largest among them being 22 GHz). This results in an almost uniform correlation coefficient (correlation between the scattering coefficient and the

frequency is sensitivity. The relative sensitivity between C- and Ku-bands as seen from figure 1 agrees with the results of ESA's airborne scatterometer campaign 'PROMESS' (Freeman *et al* 1986).

The values of transmittance and the resultant scattering coefficient for cloudy atmosphere for the microwave frequency range are expected to vary considerably. This study is in progress and will be reported separately. As far as cloud-free atmospheres are concerned, frequencies higher than 5 GHz yield the required windspeed accuracy, the accuracy improving with frequency.

Acknowledgements

The authors are grateful to Dr P S Desai and Mr B Simon for explaining their work on evaporation estimates. Thanks are due to Dr M S Narayanan, who suggested the use of ECMWF data for this study and to Dr P C Joshi for assistance in data retrieval. The authors also thank Dr M M Ali and other colleagues for helpful discussions.

Appendix 1. Computation of atmospheric transmittance

$$\tau = \int K(Z) dZ, \text{ (dB)} \quad (\text{A.1})$$

where

$$K(Z), \text{ the total absorption coefficient} = K_{\text{H}_2\text{O}}(Z) + K_{\text{O}_2}(Z) \quad (\text{A.2})$$

$$\begin{aligned} K_{\text{H}_2\text{O}} &= 2f^2 \rho (300/T)^{3/2} \gamma_1 \\ &\times \left(\frac{300}{T} \right) \exp(-644/T) \frac{1}{(494.4 - f^2)^2 + 4f^2 \gamma_1} \\ &+ 1.2 \times 10^{-6}, \text{ dB km}^{-1} \end{aligned} \quad (\text{A.3})$$

where f is the frequency (GHz), ρ is the water vapour density (gm^{-3}), P is the pressure (mb) and T is the average temperature of the layer (K). γ_1 and K_{O_2} are given as

$$\gamma_1 = 2.85 \left(\frac{P}{1013} \right) \left(\frac{300}{T} \right)^{0.626} \left[1 + 0.018 \frac{\rho T}{P} \right] \text{ GHz}, \quad (\text{A.4})$$

$$\begin{aligned} K_{\text{O}_2} &= 1.1 \times 10^{-2} f^2 \left(\frac{P}{1013} \right) \left(\frac{300}{T} \right)^2 \gamma \\ &\times \left[\frac{1}{(f - f_0)^2 + \gamma^2} + \frac{1}{f^2 + \gamma^2} \right] \text{ dB km}^{-1} \end{aligned} \quad (\text{A.5})$$

where

$$f_0 = 60 \text{ GHz},$$

$$\gamma = \text{linewidth parameter}$$

$$= \gamma_0 \left(\frac{P}{1013} \right) \left(\frac{300}{T} \right)^{0.85} \text{ GHz, with}$$

$$\gamma_0 = \begin{cases} 0.59 & P \geq 333 \text{ mb}, \\ 0.59 [1 + 3.1 \times 10^{-3} (333 - P)], & 25 \leq P \leq 333 \text{ mb}, \\ 1.18 & P \leq 25 \text{ mb}. \end{cases} \quad (\text{A.6})$$

Equations (1) to (6) are from Ulaby *et al* (1981). The water vapour density ρ was computed as follows:

$$\rho = eM/RT,$$

where the vapour pressure is

$$e = R_h e_s / 100, \quad (\text{A.7})$$

M is the molecular weight of water vapour, R the universal gas constant, R_h the Relative humidity in % and the saturated vapour pressure (mb) is

$$e_s = T^A \times 10^{[(B+C)/T]}, \quad (\text{A.8})$$

where $A = 4.928$, $B = 23.55$ and $C = -2937.0$. The empirical equation (8) was first introduced into a radiative convective model by Manabe and Wetherald (1967). The above formulation was also used by Simon and Desai (1986) to obtain ocean evaporation estimates from satellite data.

References

- Freeman N G, Gray A L, Hawkins R K and Livingstone C E 1986 CCRS convair 580 results relevant to ERS-1 wind and wave calibration; *Proc. ESA workshop, Schliërsee, ESA SP-262*, (ed) J J Hunt (Noordwijk, Netherlands: ESA Pub.)
- Fung A K and Lee K K 1982 A semi empirical sea spectrum model for scattering coefficient estimation; *IEEE J. Oceanic Eng.* **OE-7** 166–176
- Fung A K and Lee K K 1983 Variation of sea wave spectrum with wind speed. In: *Digest of international geoscience and remote sensing Sym.* (ed.) M Buettner (New York: IEEE Pub.) Vol. II TP-2
- Jones W L, Schroeder L C, Boggs D H, Bracalente E M, Brown R A, Dome G J, Pierson W J and Wentz F J 1982 The Seasat-A satellite scatterometer: Geophysical evaluation of remotely-sensed wind vector over the ocean; *J. Geophys. Res.* **87** 3297–3317
- Kondratyev K Y and Pokrovsky O M 1979 A factor analysis approach to optimal selection of spectral intervals for multipurpose experiments in remote sensing of the environment and earth resources; *Remote Sensing Environ.* **8** 3–10
- Macdonald H C and Waite W P 1971 Optimum radar depression angles for geological analysis; *Mod. Geol.* **2** 179–193
- Manabe S and Wetherald R T 1967 Thermal equilibrium of the atmosphere with a given distribution of relative humidity; *J. Atmos. Sci.* **24** 241–259
- Matzler C, Schanda E and Good W 1982 Towards the definition of optimum sensor specifications for microwave remote sensing of snow; *IEEE Trans. Geosci. Electron.* **GE-20** 57–66
- Moore P K and Fung A K 1979 Radar determination of winds at sea; *Proc. IEEE* **67** 1504–1521

- Pandey P C and Kakar R K 1983 Selection of optimum frequencies for atmospheric electric path length measurements by satellite borne microwave radiometers; *IEEE Trans. Antennas Propag.* **AP-31** 136–140
- Peckham G E, Gatley C and Flower D A 1983 Optimizing a remote sensing instrument to measure atmospheric surface pressure; *Int. J. Remote Sensing* **4** 465–478
- Sarkar A and Kumar R 1985 A study on the sensitivity of the radar scattering coefficient to oceanic winds; *Proc. Indian Acad. Sci. (Earth Planet Sci.)* **94** 249–259
- Simon B and Desai P S 1986 Equatorial Indian Ocean evaporation estimates from operational meteorological satellites and some inferences in the context of monsoon and activity; *Boundary-Layer Meteorol.* **37** 37–52
- Ulaby F T and Batlivala P P 1976 Optimum radar parameters for mapping soil moisture; *IEEE Trans. Geosci. Electron.* **GE-14** 81–93

Longshore grain size trends in the Kakinada-Mulapeta Beach, east coast of India

D SATYA PRASAD, G V S SARMA and M SUBBA RAO

Department of Geology, Andhra University, Waltair 530 003, India

MS received 22 June 1987; revised 31 October 1987

Abstract. Shore-normal and shore-parallel variations in grain size statistics of beach sand have been studied over a period of one year along the Kakinada-Mulapeta coast. The southern beaches of this coast have been accretionary while the northern ones erosional since 125 years. The grain size gradings, beach and nearshore processes help in identifying (i) the Groins-fishing harbour beach influenced predominantly by the tidal regime, (ii) the Mulapeta-Vakalapudi beach influenced by refracted wave regime and (iii) the Vakalapudi-fishing harbour beach affected by both wave and tidal regimes at relatively subdued levels.

Keywords. Grain size trends; beach dynamics; nearshore dynamics; Kakinada-Mulapeta coast.

1. Introduction

The Kakinada Bay is located on the east coast of India at the mouths of the north-flowing distributaries of the Godavari river. On the east a sand spit separates it from the open sea (the Bay of Bengal). A navigational canal extends for a considerable distance into the bay on its western margin, maintained by groins erected on either side (figure 1). That part of the western coast of the bay south of the canal groins is practically devoid of sandy beaches. The coast to the north of the groins is characterized by the well-developed beaches backed by dune ridges and blown sand further inland. The 21 km long beach stretching from the groins to Mulapeta may be divided into two distinct geomorphic units viz (i) the southern 8 km stretch from the groins to Vakalapudi lighthouse has prograded considerably during the last 125 years and (ii) the northern 13 km segment from Vakalapudi lighthouse to Mulapeta has eroded, the erosion intensity varying from place to place. A few studies have been conducted to relate the recent morphological changes in the bay and along its margins to the nearshore hydrodynamics (Hemingway 1915; La Fond and Prasada Rao 1956; Sastry 1958; Subba Rao 1958, 1967; Reddy 1975; Reddy and Prasad 1982; Satyaprasad 1986). The Kakinada Port Authority maintains a record of the gross changes in the environs of the bay. A preliminary study of the beach morphodynamics of the groins-Mulapeta beach stretch has been made and this paper presents the spatial and temporal variations in grain size statistics in relation to the beach and nearshore dynamics.

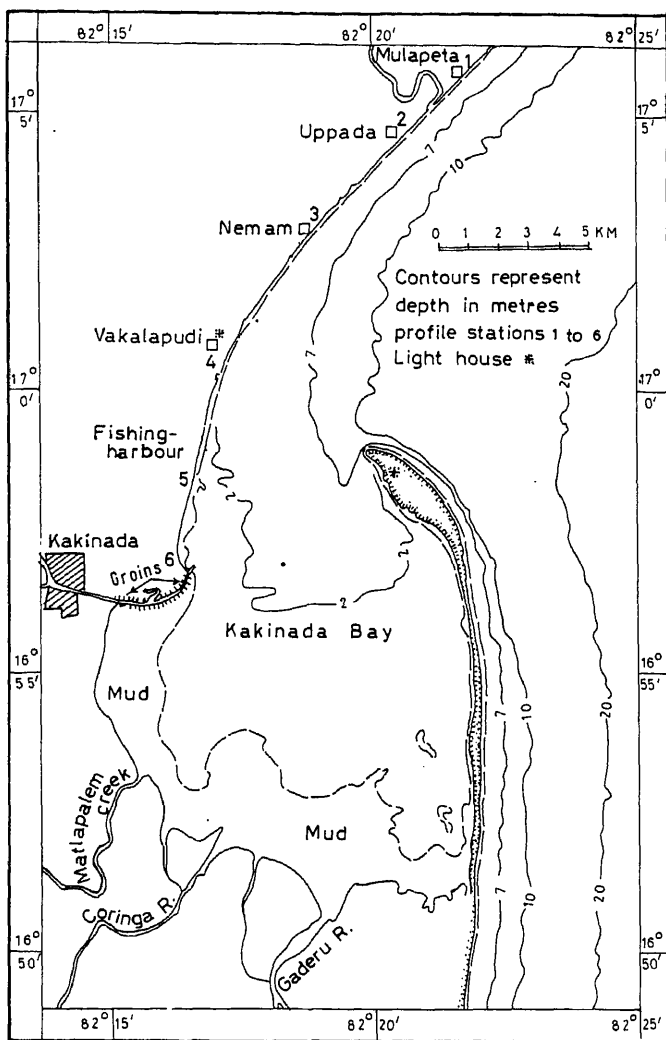


Figure 1. Kakinada Bay—general setting and station locations.

2. Oceanography

Winds in the Kakinada area are predominantly from the SW during May–September (SW monsoon season), from the NE during October–February (NE monsoon season) and from the SW/SE during March–April. Relatively high speed winds are associated with the SW and NE monsoons. In the open sea outside the bay, waves approach from the NE during November–February and from the SW during April–September. In March and October, the transitional months between the monsoon seasons, waves propagate in all directions. Wave heights are < 1.2 m in the NE monsoon and range from 1.2 – 2.0 m in the SW monsoon. Abnormal wave heights occur during cyclonic storms which frequently cross the east coast of India.

During the SW monsoon, waves enter the bay from east through south and are refracted because of the sand spit. This wave refraction results in the formation of a nodal zone around Uppada on the western margin of the bay and littoral currents are directed up and down the coast from this nodal zone. Also, littoral currents produced by NE monsoon waves are southerly. Thus, both in the SW and NE monsoon seasons, the sediment is transported down the coast towards the groins which prevent its movement further southward. The sediment is deposited in the area north of the groins and the beaches here have prograded bayward. The beaches north of the Vakalapudi lighthouse have been eroded rather abnormally because the northerly littoral drift is small and the beaches are undernourished. The tidal range in the bay nowhere exceeds 2 m and the bay may be described as low mesotidal, according to the classification of coastal types based on tidal range (Hayes 1979). The tidal currents are stronger on the western side of the sand spit than on the Kakinada-Mulapeta coast and never exceed 1.2 knots (Reddy 1975).

3. Field and laboratory procedures

Six stations were monitored along the 21 km long stretch of the coast from the groins to Mulapeta, one each at Mulapeta, Uppada, Nemam, Vakalapudi, just south of Fishing Harbour and just north of the groins (figure 1). At each station three to four sand samples were collected orthogonal to the beach trend to represent the low water line, midforeshore and backshore segments of the beach. The samples were collected over a period of 12 months (July-July 1984-85) at monthly intervals at spring low water level when the maximum beach emerged above the water line. In order to link the station to station grain size variations, additional samples were obtained at 1 km interval from low water line, midforeshore and backshore segments all along the Mulapeta-groins beach in July and October 1984 and in January and April 1985. Totally, 380 samples were collected and used in the present study. All the samples represent the top 5 cm deposition as on the day of sample collection.

The samples were washed free of salt and dried and sieved using $1/2 \phi$ interval ASTM sieves on a rotap for 15 min each. The mean grain size, standard deviation (sorting), inclusive graphic skewness and graphic kurtosis were computed according to the method of Folk and Ward (1957).

4. Results

Sediments from the Mulapeta, Uppada, Nemam, Vakalapudi, Fishing Harbour and groins beaches are classified adopting the verbal limits of Folk and Ward (1957) (table 1). The Mulapeta beach consists of fine to medium sand which are generally moderately well-sorted to well-sorted, near symmetrical to positive skewed and platykurtic to leptokurtic. The Uppada beach consists of fine sand which is moderately well-sorted, near-symmetrical to negative skewed and platykurtic to mesokurtic. The Nemam beach is composed of fine sand with frequent occurrence of medium sand and occasional occurrence of very fine sand. The sands of the

Table 1. Classification of samples according to grain size statistics.

(' Total number of samples under each class.

+ Total number of samples collected from the beach during the year.)

Statistics	Class	Samples from			Total Samples*	Total Samples+
		LWL	MFS	BS		
Mulapeta beach						
Mean size	Medium sand	2	5	2	9	25
	Fine sand	10	8	9	27	75
	Very fine sand	-	-	-	-	-
Sorting	Well sorted	3	2	5	10	28
	Moderately well sorted	8	10	6	24	67
	Moderately sorted	1	1	-	2	5
Skewness	Very positive skewed	2	3	2	7	19
	Positive skewed	4	3	2	9	23
	Near symmetrical	4	6	2	12	34
	Negative skewed	-	1	5	6	18
	Very negative skewed	2	-	-	2	6
Kurtosis	Platykurtic	7	6	4	17	47
	Mesokurtic	2	6	1	9	25
	Leptokurtic	2	1	6	9	25
	Very leptokurtic	1	-	-	1	3
Uppada beach (No backshore exists here)						
Mean size	Medium sand	2	-	-	2	8
	Fine sand	11	11	-	22	84
	Very fine sand	-	2	-	2	8
Sorting	Well sorted	1	3	-	4	15
	Moderately well sorted	11	10	-	21	81
	Moderately sorted	1	-	-	1	4
Skewness	Very positive skewed	2	-	-	2	8
	Positive skewed	1	3	-	4	16
	Near symmetrical	5	5	-	10	38
	Negative skewed	5	5	-	10	38
	Very negative skewed	-	-	-	-	-
Kurtosis	Platykurtic	5	8	-	13	50
	Mesokurtic	4	4	-	8	31
	Leptokurtic	3	1	-	4	15
	Very leptokurtic	1	-	-	1	4
Nemam beach						
Mean size	Medium sand	-	3	4	7	19
	Fine sand	11	9	7	27	73
	Very fine sand	1	-	2	3	8
Sorting	Well sorted	1	-	5	6	16
	Moderately well sorted	7	9	8	24	65
	Moderately sorted	4	3	-	7	19
Skewness	Very positive skewed	2	1	3	6	16
	Positive skewed	-	3	4	7	19
	Near symmetrical	2	3	3	8	21.5
	Very negative skewed	4	4	1	8	21.5
	Negative skewed	4	1	3	8	21.5
Kurtosis	Platykurtic	5	5	6	16	43
	Mesokurtic	4	4	6	14	38
	Leptokurtic	2	2	1	5	14
	Very leptokurtic	1	1	-	2	5

Table 1. *continued.*

Statistics	Class	Samples from			Total Samples*	Total Samples+
		LWL	MFS	BS		
Vakalapudi lighthouse beach						
Mean size	Medium sand	2	1	1	4	10
	Fine sand	11	11	11	33	90
	Very fine sand	—	—	—	—	—
Sorting	Well sorted	5	5	2	12	33
	Moderately well sorted	7	6	10	23	62
	Moderately sorted	1	1	—	2	5
Skewness	Very positive skewed	1	1	3	5	13.5
	Positive skewed	1	—	1	2	5
	Near symmetrical	4	2	5	11	30
	Negative skewed	5	8	3	16	43
	Very negative skewed	2	1	—	3	8.5
Kurtosis	Platykurtic	5	3	5	13	35
	Mesokurtic	3	4	6	13	35
	Leptokurtic	2	3	—	5	13.5
	Very leptokurtic	3	2	1	6	16.5
Fishing Harbour beach						
Mean size	Medium sand	—	—	—	—	—
	Fine sand	13	11	12	36	100
	Very fine sand	—	—	—	—	—
Sorting	Well sorted	9	2	6	17	47
	Moderately well sorted	4	9	5	18	50
	Moderately sorted	—	—	1	1	3
Skewness	Very positive skewed	—	—	—	—	—
	Positive skewed	—	—	—	—	—
	Near symmetrical	2	—	3	5	13
	Negative skewed	9	8	8	25	70
	Very negative skewed	2	3	1	6	17
Kurtosis	Platykurtic	3	2	2	7	19
	Mesokurtic	2	2	3	7	19
	Leptokurtic	7	7	6	20	56
	Very leptokurtic	1	—	1	2	6
Groins beach						
Mean size	Medium sand	—	—	—	—	—
	Fine sand	—	—	—	—	—
	Very fine sand	13	13	12	38	100
Sorting	Very well sorted	3	1	1	5	13
	Well sorted	9	12	11	32	84
	Moderately well sorted	1	—	—	1	3
Skewness	Very positive skewed	—	—	—	—	—
	Positive skewed	—	—	—	—	—
	Near symmetrical	—	2	2	4	10
	Negative skewed	5	10	10	25	66
	Very negative skewed	8	1	—	9	24
Kurtosis	Platykurtic	2	1	—	3	8
	Mesokurtic	5	3	5	13	34
	Leptokurtic	6	9	7	22	58
	Very leptokurtic	—	—	—	—	—

LWL, low water line; MFS, midforeshore; BS, backshore.

medium sand. Sand of this beach is usually moderately well-sorted but well-sorted sand is also observed. They are either symmetrical or negative skewed, the latter being more frequent. Platy, meso, and leptokurtic sand occurs in about equal frequency in this beach. The Fishing Harbour beach is exclusively made of fine sand which is well-sorted to moderately well-sorted, negative skewed and usually leptokurtic. The groins beach is exclusively composed of very fine sand which is essentially well-sorted and negative skewed. It is either leptokurtic or mesokurtic.

5. Comparison of sediments from the six beaches

5.1 *Mean size*

The groins and the Fishing Harbour beaches are unique. The former consists of very fine sand and the latter of fine sand. Although the other four beaches consist predominantly of fine sand, medium sand appears in these beaches. However, medium sand occurs at a greater frequency in the Uppada and Vakalapudi beaches; very fine sand occurs occasionally in the Uppada and Nemam beaches and is altogether absent from the Mulapeta and Vakalapudi beaches (table 1).

Monthly mean grain size values of low water line, midforeshore and backshore are compared in figure 2. In every segment of the beach there is a gradual increase in the mean grain size from $>3.0 \phi$ in the groins beach to about 2.1ϕ in the Mulapeta beach. Along the entire beach stretch, the mean grain size ranges from $2.41\text{--}2.83 \phi$ in low water line area, $2.41\text{--}2.74 \phi$ in midforeshore area and $2.32\text{--}2.75 \phi$ in backshore area. It is $< 2.5 \phi$ during January–February in low water line area, during January–May in midforeshore area and during April–August and November–January in backshore area. Generally the backshore beach sediments are coarser than those of the foreshore.

5.2 *Standard deviation (sorting)*

Although occasional, very well-sorted sand occurs only in the groins beach. This is the only beach where sediments are most predominantly well-sorted. Well-sorted to moderately well-sorted sand occurs in equal frequency in the Fishing Harbour beach. Moderately well-sorted sand is most predominant in the Uppada beach and more predominant in the Mulapeta, Nemam and Vakalapudi beaches than the other types of sediments. Relatively ill-sorted sediments (mean grain size $> 0.71 \phi$) occur rather frequently only in the Nemam beach.

Monthly mean standard deviation ranges from $0.45\text{--}0.56 \phi$ in low water line area, $0.45\text{--}0.62 \phi$ in midforeshore area and $0.45\text{--}0.56 \phi$ in backshore area (figure 2). In every segment of the beach, sorting worsens from the groins beach to the Fishing Harbour beach and further worsens from Nemam northwards. The sediments are least sorted in the Nemam and Vakalapudi beaches and best sorted in the groins beach. When the groins–Mulapeta beach is considered in its entirety, mean standard deviation ranges from $0.49\text{--}0.60 \phi$ but temporal variations are not

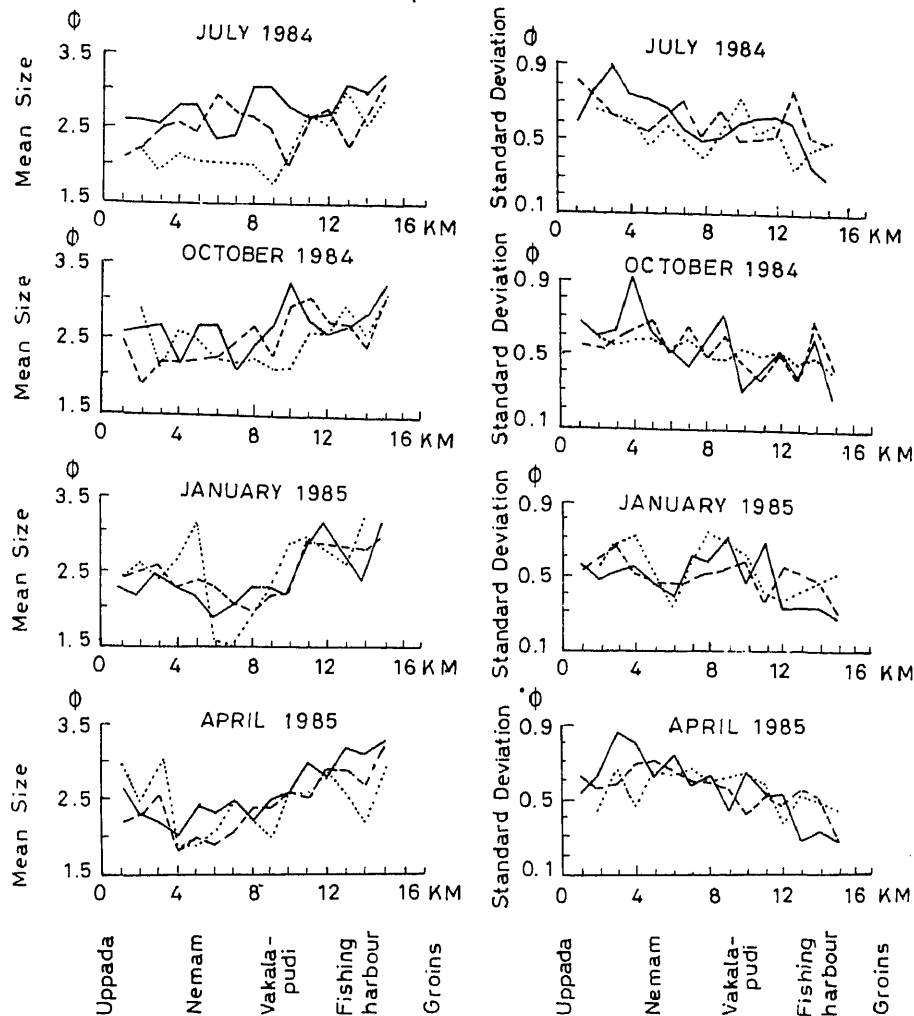


Figure 2. Longshore variations in mean size and standard deviation from Uppada to the groins.

significant. The backshore sand seems to be slightly better sorted than the foreshore sand.

5.3 Skewness

The Mulapeta beach sand is usually positive skewed to near-symmetrical, the Uppada beach sand near-symmetrical to negative skewed, the Vakalapudi beach sand negative skewed to near-symmetrical (the former type being more frequent) and the Fishing Harbour and groins beach sands negatively skewed. Very negative

skewed sand is more frequent in the groins beach than in the Fishing Harbour beach. The Nemam beach is unique in this respect. Its sands are variously skewed and no particular type is ever predominant. Positive skewed to near-symmetrical sand of the Mulapeta beach is replaced by near-symmetrical to negative skewed sand in the Uppada and Vakalapudi beaches. The latter in turn is replaced by negative to very negative skewed sand in the Fishing Harbour and groins beaches (figure 3).

Monthly mean skewness values in the three segments of the six beaches indicate that sand of the southern two beaches is negatively skewed and that of the northern two beaches symmetrical while that of the central two beaches is either symmetrical or negative skewed. Temporal variations in mean skewness value along the entire Mulapeta-groins beach do show certain seasonal trends: The low water line sand is symmetrical during October-January and negative skewed during the rest of the year. The midforeshore sediments are negative skewed during March-June and usually symmetrical during the rest of the year. The backshore sediments are negative skewed during February-March and usually symmetrical during the rest of the year. Thus, backshore sediments are usually symmetrical while foreshore sediments either symmetrical or negative skewed.

5.4 Kurtosis

The Mulapeta beach sand is platy, meso and leptokurtic, platykurtic sand being more frequent than either of the other two types. The Uppada beach sand is platykurtic and mesokurtic, the former type being more frequent. Platykurtic and mesokurtic sand is dominant and of equal frequency in the Nemam and Vakalapudi beaches. Leptokurtic sand is far more predominant in the Fishing Harbour beach than either platykurtic or mesokurtic sand. Leptokurtic sand continues its predominance in the groins beach also but here the platykurtic sediments are of rare occurrence. Very leptokurtic sand is significant only in the Vakalapudi beach. Thus, platykurtic sand gradually changes to leptokurtic type as kurtosis is traced from Mulapeta to the groins beach (figure 3).

Monthly mean kurtosis values of the three segments of the six beaches ranges from 1.02-1.17 in the low water line area, 0.91-1.15 in the midforeshore area and 0.92-1.13 in the backshore area. Mean kurtosis is > 1.11 in the foreshore south of Nemam and ranges from 0.90 - 1.11 between Nemam and Mulapeta. The dividing point between these two types of sand is located at Vakalapudi in the case of the backshore. Considering the Mulapeta-groins beach as a continuum, mean kurtosis is virtually in the mesokurtic range in midforeshore and backshore areas except during September-October in the midforeshore area and in August, October and December in the backshore area and during these months it is in the leptokurtic range. In respect of low water line area, temporal variations in mean kurtosis are erratic. It is in the mesokurtic range during July-September, November and March and in the leptokurtic range in October, January and April-June.

6. Longshore trends in grain size characteristics

Only 36 (9%) of the 380 sediment samples studied have their mean grain size in the 1.7-2.0 ϕ range. Such relatively coarse sand is found only in the beaches of

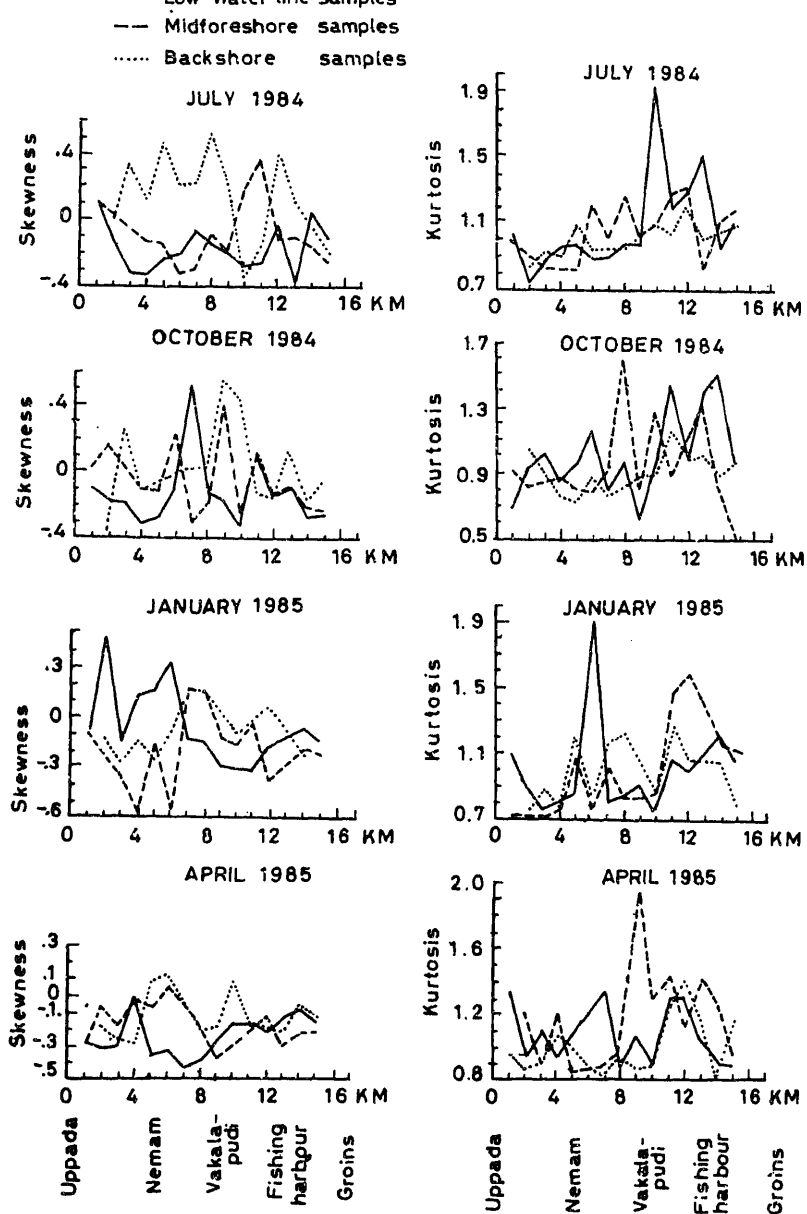


Figure 3. Longshore variations in skewness and kurtosis from Uppada to the groins.

Vakalapudi-Mulapeta coast, mostly in July, April and January. It is generally associated with the accretional periods of the beaches and is by and large relatively ill-sorted. Sediments finer than 3.0ϕ are confined to the groins beach. Thus, in the beach continuum from Fishing Harbour to Mulapeta, mean grain size fluctuates in a narrow range from 2.0 to 3.0ϕ (figure 2). The standard deviation ranges from 0.33 to $> 0.80 \phi$ but in many samples, it fluctuates between 0.4 and 0.7ϕ . Kurtosis

skewness value assumes a negative trend in the direction of the groins beach. Low water line, midforeshore and backshore segments register similar longshore trends.

7. Discussion

After being eroded by a storm, a beach restores itself to a fully accretive state over a period of a few weeks. Coarse material is deposited in the early phase of beach recovery and fine material in the final phase of recovery. Thus, an accretive subaerial beach exhibits variations in size distribution ranging from unimodal coarse through bimodal intermediate to unimodal fine (Sonu 1972). Bimodal sediments are rare in the beaches covered by the present study. Accretive cycles are often interrupted by erosional cycles in these beaches. However, whenever a beach accretes continuously for more than a month, sediments of the foreshore tend to become finer with the progress of beach build-up.

Changes in grain size along beach foreshores are common worldwide on such diverse beaches as boulder beaches, pebble beaches, mixed sand and gravel beaches and sand beaches. Such changes are known from both high energy and low energy beaches. Grain size changes are even generated along beaches < 10 cm in length in wave tanks by waves as low as 4 cm in height (Bryant 1982).

Variations in the four grain size statistics in the Mulapeta-groins beach continuum may be resolved into shore-parallel variations and temporal trends in these variations, and shore-normal changes and temporal trends in such changes. Any interpretation of these changes should be based on the nearshore hydrodynamics controlling sedimentation on the beaches: (1) wave energy levels decrease from the northern beaches towards the groins beach, (2) longshore currents weaken from the northern beaches towards the groins beach, and since there is net deposition in the southern beaches, the effective longshore drift is predominantly southerly, (3) tidal currents dominate the hydrodynamic regime along the southern beaches, and (4) because of extensive refraction and shoaling effects, waves have very little energy left before reaching the inshore zone of the Fishing Harbour-groins beach stretch at low tide. Wave energy levels are insufficient to generate significant inshore circulation or sediment entrainment at low tide but are effective in moving sediment on the foreshore at high tide. The Fishing Harbour-groins beach segment is thus a high-tide reflective and low-tide dissipative beach (Satyaprasad 1986).

Various mechanisms have been proposed to explain the origin of sediment size gradings along beach foreshores: (i) variation in wave energy alongshore (Bascom 1951; Goldsmith 1976), (ii) selective sorting of sediment in the direction of longshore transport (Pettijohn and Ridge 1932; Martens 1935), (iii) progressive loss of fine grains offshore in a downdrift direction (McCave 1978), and (iv) distance from coarse sediment sources (Judge 1971). Sonu (1973) reported that the dual linkage between morphology and wave-current characteristics can be expanded to include sediment attributes such as grain size variation alongshore and sediment sorting processes. Bryant (1982) showed that the strength of grain size variations along beach foreshores is dependent on whether the foreshore is reflective or dissipative, and that the temporal variation in grain size changes alongshore is linked to the degree of dissipation or reflectance of the whole beach

function of the vector of sediment movement and reflects both orthogonal and shore-parallel transport processes.

The energy postulate states that the mean grain size and sorting increase as shore-normal wave power increases. The drift postulate states that mean grain size increases downdrift. The energy postulate is more frequently applicable on reflective bay than dissipative ocean foreshores and the drift postulate is much more effective in accounting for mean size changes alongshore than the energy postulate except for the sheltered and exposed headland ends of beaches (Bryant 1982). In the present study area southerly longshore currents aided by flood tide currents provide the necessary mechanism to transport the selectively fine grained sediments towards the groins beach. A slight improvement in sorting is achieved in this process. Absence of significant temporal variations in grain size or sorting in the groins and Fishing Harbour beaches indicates that this beach segment is generally in a reflective beach morphologic state. Such stable reflective stages are not attained by the other beaches to the north.

The postulate that progressive loss of finer sediment offshore, leading to coarsening of sediment down drift on beach foreshores (McCave 1978) is not applicable to the present beach. Such a mechanism works when the longshore current strength is maintained undiminished.

Shore-normal variations in grain size attributes do not follow a specific trend, i.e. they do not increase or decrease systematically from the low water line through midforeshore to backshore. The general coarsening in grain size in the backshore area may be attributed to either transport of coarser grains by swash and their retention there or the lag effects.

8. Conclusion

The present study has revealed the existence of alongshore grain size gradings with respect to the grain size statistics: mean size, standard deviation, skewness and kurtosis. The size gradings and beach and nearshore dynamics permit recognition of three distinct types of beaches along the Mulapeta-groins beach continuum: (i) the groins-Fishing Harbour beaches: Three kinds of processes operate here. Longshore currents transport here only fine to very fine sands with which some coarse tails are entrained. Flood tide currents bring in silt and clay in suspension and a part of this suspended load is shed at the turn of tide. Although locally generated wind-waves are strong enough to winnow away this fine material, a tail is left over. These beaches are a product of tide-dominated hydrodynamic regime. (ii) Beaches between Mulapeta and Vakalapudi are a product of refracted wave-dominated hydrodynamic regime. (iii) Beaches between Vakalapudi and Fishing Harbour are shaped by a combination of wave and tidal processes acting at relatively subdued levels.

Acknowledgements

Thanks are due to Prof. A Sriramadas for a critical reading of the manuscript. DSP is thankful to UGC, New Delhi, and GVSS to the Department of Environment, Government of India, for financial support.

References

- Bascom W N 1951 The relationship between sand size and beachface slope; *Trans. Am. Geophys. U.* **32** 866–874
- Bryant E A 1982 Behaviour of grain size characteristics on reflective and dissipative foreshores, Br Bay, Australia; *J. Sediment. Petrol.* **52** 431–450
- Folk R L and Ward W V 1957 Brazos river bar: A study in the significance of grain size parameters; *Sediment. Petrol.* **27** 3–26
- Goldsmith W 1976 Continental shelf wave climate models: Critical links between shelf hydraulic and shoreline processes. In: *Beach and nearshore sedimentation* (eds) R A Davis Jr and R L Ethridge (Soc Econ Paleontologists and Mineralogists) **24** 24–47
- Greenwood B 1978 Spatial variability of texture over a beach-dune complex, North Devon, England; *Sediment. Geol.* **21** 27–44
- Hayes M O 1979 Barrier island morphology as a function of tidal and wave regime. In: *Barrier Islands* (Ed) S P Letherman (New York: Academic Press) pp. 1–29
- Hemingway F R 1915 Report on Godavari District; Madras District Gazetteer pp. 1–15
- Judge C W 1971 Heavy minerals in beach and stream sediments as indicators of shore processes between Monterey and Los Angeles, California; U S Army Corps Engineers, Tech. Memo **33** 44
- La Fond E C and Prasad Rao R 1956 On the erosion of the beach at Uppada; *The Port Engineer* **5** 1–10
- Martens J H C 1935 Beach sands between Charleston, South Carolina and Miami, Florida; *Am. Soc. Bull.* **46** 1563–1596
- McCave I N 1978 Grain size trends and transport along beaches: Examples from eastern England; *Geol.* **23** M43–M52
- Pettijohn F J and Ridge J D 1932 A textural variation series of beach sands from Edar point, Ohio; *Sediment. Petrol.* **2** 76–88
- Reddy B S R 1975 *Oceanographic studies in the neighbourhood of a barrier beach near Kakinada* Ph D thesis, Andhra University, Waltair 142 p (unpublished)
- Reddy B S R and Prasad K V S R 1982 The sand spit near Kakinada—further studies; *Indian J. Earth Sci.* **2** 167–173
- Sastry J S 1958 *Some aspects of shoreline processes and physical oceanography*; D Sc thesis, Andhra University, Waltair 255 p (unpublished)
- Satyaprasad D 1986 *Morphodynamics of the beaches and sand spit: Kakinada Bay, east coast of India* Ph D thesis, Andhra University, Waltair 255 p (unpublished)
- Sonu C J 1972 Bimodal composition and cyclic characteristics of beach sediment in continuous changing profiles; *J. Sediment. Petrol.* **42** 852–857
- Sonu C J 1973 Three-dimensional beach changes; *J. Geol.* **81** 42–64
- Subba Rao M 1958 *Some aspects of continental shelf sediments off the east coast of India*; D Sc thesis, Andhra University, Waltair 259 p (unpublished)
- Subba Rao M 1967 Studies on the Kakinada Bay on the east coast of India; *Q. J. Geol. Min. Metall. India* **39** 75–91

A steady state model of the Somali current

P K DAS, S K DUBE and G S RAO

Centre for Atmospheric Sciences, Indian Institute of Technology, New Delhi 110 016, India

MS received 30 November 1987

Abstract. A steady state model of the Somali current including forcing by both the curl and the divergence of the wind stress is discussed. The model equations are linear, but the results presented are for the one nonlinear case. The grid resolution was 12 km in the zonal and 24 km in the meridional direction. The streamfunction and velocity potential of the current are presented for forcing by divergence and compared with a situation when only the curl is present. The results indicate that a two-gyre system appears in July, a representative month for the summer monsoon, only when divergence is included. Computations with available data indicate that the divergence is comparable in magnitude to the curl near the location of the Somali current. The model produces three other important features: (i) strong upwelling off the east coast of Africa, (ii) downwelling over central Arabian sea and (iii) a strong eastward current in the upper layer towards the interior of the Arabian sea near 12°N.

Keywords. Somali current; curl; divergence; wind stress; upwelling; downwelling.

1. Introduction

A comprehensive investigation by Luther and O'Brien (1985) was able to simulate many features of the Somali current by a time-dependent model. Of particular interest was a two-gyre configuration beginning in June which ultimately coalesced towards the end of the summer monsoon. This result is interesting because Dube *et al* (1986) found that the southern gyre of the Somali current is prominent in a year of good monsoon, but is absent in a poor monsoon year.

The present paper suggests that an additional forcing by the divergence of the wind stress, in addition to the curl, leads to the formation of the second gyre.

2. Basic equations

We consider a two-layer ocean with an upper mixed layer and a deeper lower layer in which there is no motion. Turbulent mixing in the upper layer is sufficiently strong so that the wind stress acts as a body force throughout the depth of the mixed layer.

The wind induced current in the mixed layer is the sum of a rotational and a divergent part. Thus

$$\mathbf{V} = \hat{k} \times \nabla \psi + \nabla \chi, \quad (1)$$

where \mathbf{V} is a depth-averaged current, \hat{k} the unit vector along the vertical axis Z pointing upwards. ψ represents a streamfunction and x is a velocity potential for the wind-driven current. ψ and x will be determined by linearized equations for the conservation of vorticity and divergence.

Assuming a steady state and using the β -plane approximation for meridional variations of the Coriolis force f we have

$$-\beta yv = -\alpha \frac{\partial p}{\partial x} + \alpha \frac{\partial \tau_x}{\partial Z}, \quad (2)$$

$$\beta yu = -\alpha \frac{\partial p}{\partial y} + \alpha \frac{\partial \tau_y}{\partial Z}, \quad (3)$$

where α stands for the specific volume of water and $\beta = (df/dy)$. In cartesian coordinates ($oxyz$) u and v represent the zonal and meridional components of V and τ_x and τ_y are the components of the wind stress towards the east and north. The pressure p is related to the depth of the mixed layer h by

$$p = g'(h - H)\rho, \quad (4)$$

where $Z = -H$ is the mean undisturbed depth of the mixed layer. For a two-layer ocean, g' stands for the reduced gravity [$g(\Delta\rho/\rho)$] in which $\Delta\rho$ is the difference in densities of the upper and lower layer and ρ is the density of the upper layer.

Integrating (2) and (3) from the surface ($Z = 0$) to the base of the mixed layer ($Z = -H$) we find

$$kU - \beta yV = -\alpha \frac{\partial p}{\partial X} + \frac{\alpha}{H} (\tau_x)_0 \quad (5)$$

$$kV + \beta yU = -\alpha \frac{\partial p}{\partial y} + \frac{\alpha}{H} (\tau_y)_0, \quad (6)$$

where the suffix 0 denotes the values of τ_x and τ_y at the surface. The depth-averaged components of the current are

$$U = \frac{1}{H} \int_{-H}^0 u dZ, \quad (7)$$

$$V = \frac{1}{H} \int_{-H}^0 v dZ. \quad (8)$$

Following Stommel (1948), we have assumed that the frictional stress at the interface between the mixed layer and the deeper ocean below is proportional to U, V . We have put

$$\alpha\tau_x = \sigma U, \quad (9)$$

$$\alpha\tau_y = \sigma V. \quad (10)$$

at $Z = -H$. k represents the ratio σ/H . Its value is not known with much precision,

Table 1. Orders of magnitude (s^{-2})

kD	βV	$\beta y \zeta$	$-\alpha \nabla_\rho^2$	$\frac{\alpha}{H} (\nabla \cdot \tau)_0$
10^{-12}	10^{-12}	$10^{-12} - 10^{-11}$	10^{-11}	10^{-11}

computations. An experiment was performed with $k = 2 \times 10^{-6} s^{-1}$, but the results did not show any significant change.

From (2) and (3), the vorticity ζ and the divergence D is given by

$$k\zeta + \beta V + \beta y D = \frac{\alpha}{H} \hat{k} \cdot (\nabla \times \tau)_0, \quad (11)$$

$$kD + \underline{\beta u} - \underline{\beta y \zeta} = -\alpha \nabla^2 p + \frac{\alpha}{H} (\nabla \cdot \tau)_0. \quad (12)$$

The underlined terms in (12) represent a geostrophic balance. Considering the representative values of vorticity and divergence to be $10^{-6} s^{-1}$, we find that the different terms of (12) have the orders of magnitude shown in table 1.

The third term ($\beta y \zeta$) has the magnitude shown in table 1 in the region within $\pm 10^\circ$ on either side of the equator. As shown subsequently, the available wind data suggest that the divergence is of comparable magnitude to the curl. Moreover, as we can see, the geostrophic balance is unlikely in the near equatorial regions where the Somali current is located. Consequently, it is necessary to include the effect of divergence in the model.

Equations (11) and (12) form a coupled system of two equations. As a first approximation, the barotropic response to the wind stress curl was computed without the stretching term ($\beta y D$) in (11). The resulting streamfunction ψ is determined by the equation

$$\nabla^2 \psi + \left(\frac{\beta}{k} \right) \frac{\partial \psi}{\partial X} = \left(\frac{\alpha}{kH} \right) \hat{k} \cdot (\nabla \times \tau)_0. \quad (13)$$

with appropriate boundary conditions. This is Stommel's (1948) classical equation.

Similarly, a first approximation to the divergent part of the current is found by solving (12) without the second and third terms ($\beta u, \beta y \zeta$). We have

$$\nabla^2 \phi = \frac{1}{H} (\nabla \cdot \tau)_0, \quad (14)$$

where

$$\phi = (k\rho x + p). \quad (15)$$

As $\nabla^2(k\rho x) > \nabla^2 p$ the solution of (14) provides a reasonably good estimate of the velocity potential x .

The velocity potential may be used to estimate the intensity of upwelling. Variations in h at the interface between the upper mixed layer and the

ocean usually exceed similar variations at the surface ($Z = 0$). This is expressed by putting

$$W(-H) = \frac{\overline{\partial h}}{\partial t} = -H \nabla^2 x,$$

where an overbar indicates a mean value.

An estimate of vertical motion at the base of the mixed layer [$W(-H)$] is provided by $\nabla^2 x$.

3. Successive approximations and boundary conditions

Equation (13) was first solved by relaxation over the region shown in figure 1. This was the first approximation to the streamfunction which will be referred to as ψ_0 .

Similarly, solving (14) by relaxation provides the first approximation to the velocity potential. This is x_0 .

Computing the Laplacian of x_0 provides a first estimate of divergence. Inserting this in the stretching term ($\beta y D$) of (11) gives us a second approximation to the streamfunction, which is ψ_1 . Similarly, the Laplacian of ψ_0 will provide a first estimate of $\beta y \zeta$ in (12) and the solution of this equation gives us x_1 .

A staircase pattern was adopted for land boundaries. Finite difference coordinates are defined by

$$X = (m-1)\Delta X, \quad (m = 1, 2, \dots, M)$$

$$Y = (n-1)\Delta Y, \quad (n = 1, 2, \dots, N),$$

where $\Delta X = 12$ km and $\Delta Y = 24$ km. The land boundaries are at $m = 1, M$ and $n = 1, N$. An over-relaxation factor of 1.2 was found to be suitable for this purpose.

The boundary conditions are

$$\psi = \partial\psi/\partial n = 0$$

$$x = \partial x/\partial n = 0$$

which provide no flux normal to the land boundaries. These conditions are realistic along the open sea boundary to the south, but the currents measured by Cutler and Swallow (1984) during the monsoon indicate that along 10°S the flow is largely zonal and directed westwards. Thus, the absence of normal flux on the southern boundary is not likely to influence the pattern of ψ and x in the interior region.

Results will be presented to indicate the streamline and velocity potential for the second approximation. Computations for the third approximation were made but are not reproduced here because it was found that, apart from intensification of the gyres, there was no significant difference between the

additional vorticity by the stretching term in (11). This becomes clear even as we proceed from the first ψ_0 to the second approximation ψ_1 of the streamfunction.

It is possible, in principle, to eliminate divergence D from (11) and (12) and obtain a single equation for vorticity ζ . But this would have meant solving a higher order equation with mixed derivatives and more cumbersome boundary conditions. The use of successive approximations is simpler.

Nonlinear terms were not considered in the vorticity and divergence equations, but their effect may be inferred qualitatively. Here, it is convenient to express (13) in the form

$$J(\psi, \nabla^2 \psi) + \beta V + \beta y D = \frac{\alpha}{H} \hat{k} \cdot (\nabla \times \tau)_0 - k \zeta, \quad (19)$$

where J stands for the Jacobian operator. Terms on the left of (19) represent (i) nonlinear advection of vorticity, (ii) meridional transport of planetary vorticity and (iii) vorticity generated by the stretching of vortex tubes, while on the right we express forcing by the curl and dissipation by interfacial friction. When additional vorticity is inserted by nonlinear advection, an increase in dissipation will occur when the advection is positive. This leads to an increase in northward transport of planetary vorticity, and leads to an intensification of the coastal current and an asymmetry in the gyre. As shown shortly, this is borne out by the output from one of the model runs. The model outputs are similar to those of Cox (1981).

4. Results

Wind data over the Arabian sea have been published by Hastenrath and Lamb (1979). Similar data have been published by Cadet and Diehl (1984) for the period 1954–1976. Variations of wind stress off the Somali coast have been described by Bruce (1978), Wylie and Hinton (1982) and by Luther *et al* (1985). Computations of the curl and divergence have been made by Okumu (1985) with a limited data set for the coastal region off east Africa. These data sources were utilized to prepare maps of the curl and divergence for our region of interest. They are shown in figures 1 and 2.

The wind stress was computed from the bulk aerodynamic formula

$$\tau = \rho_a C_D |V_a| V_a, \quad (20)$$

where ρ_a is the density of air and V_a the wind velocity. We put $\rho_a = 1.2 \text{ kg m}^{-3}$ and $C_D = 1.25 \times 10^{-3}$. The variation of C_D with wind speed was ignored in the present work. Values of the stress computed by us agreed fairly well with the publications cited earlier. From these values of the wind stress, its divergence was computed (figure 2) numerically by using centred differences.

We chose mean conditions for July because it was a representative month of the monsoon. There is little difference in the monthly mean maps of the wind stress

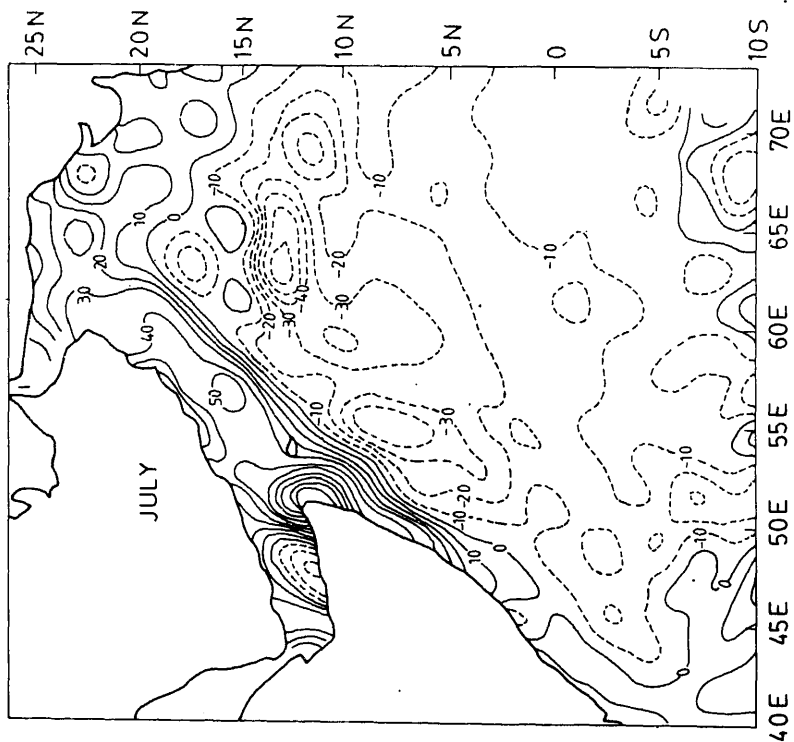


Figure 1. Mean wind stress curl in July (10^{-8} N/m³).

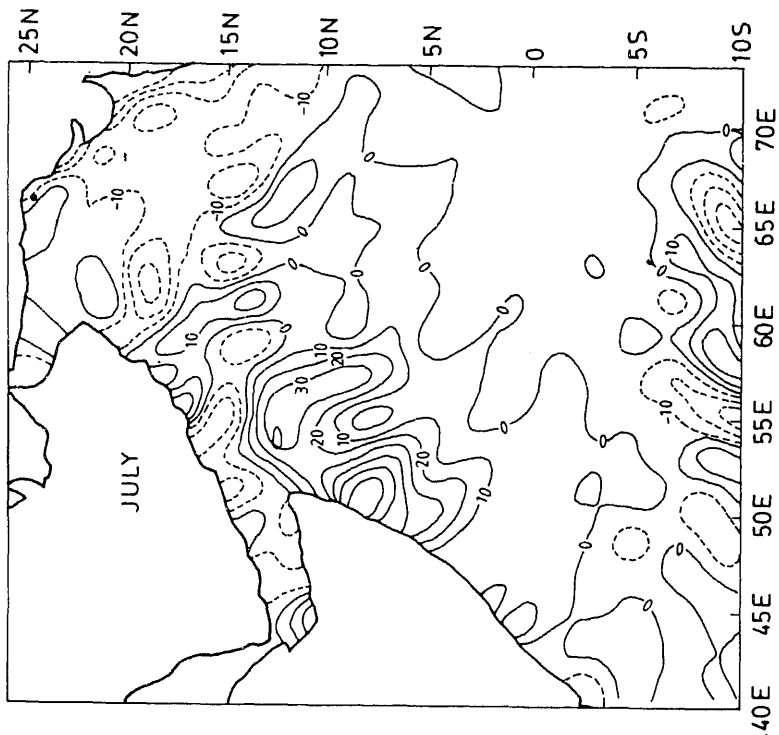


Figure 2. Mean wind stress divergence in July (10^{-8} N/m³).

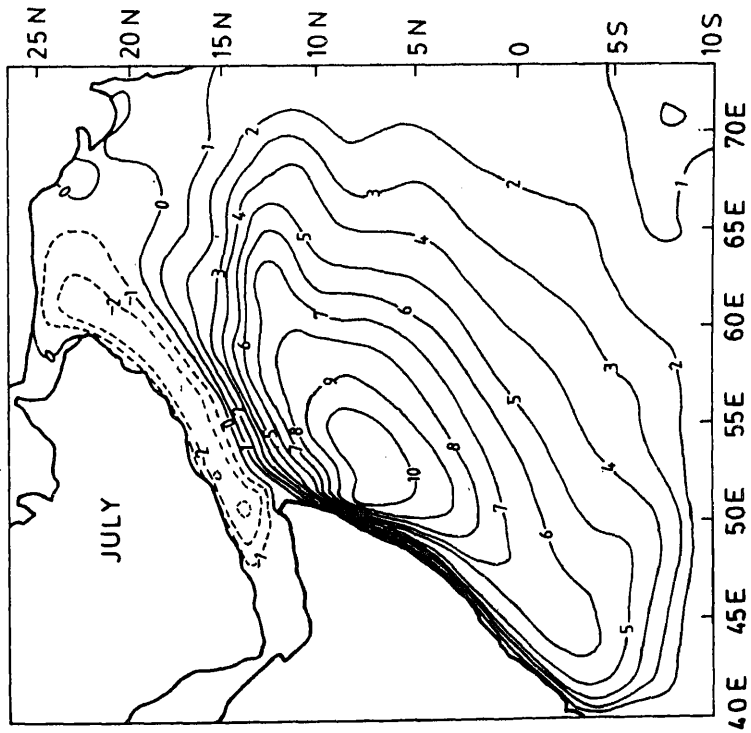


Figure 3. Field of ψ_0 ($10^4 \text{ m}^2/\text{s}$).

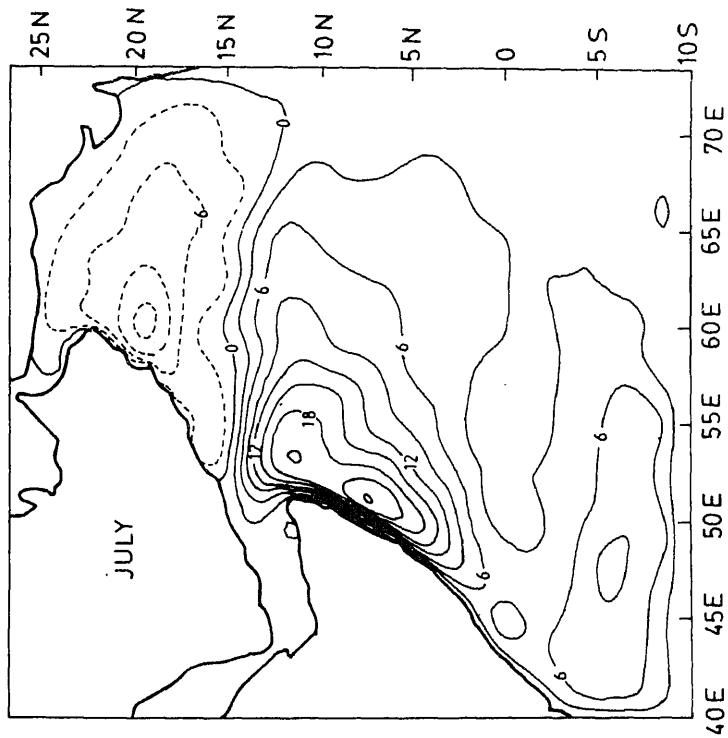


Figure 4. Field of ψ_1 ($10^4 \text{ m}^2/\text{s}$).

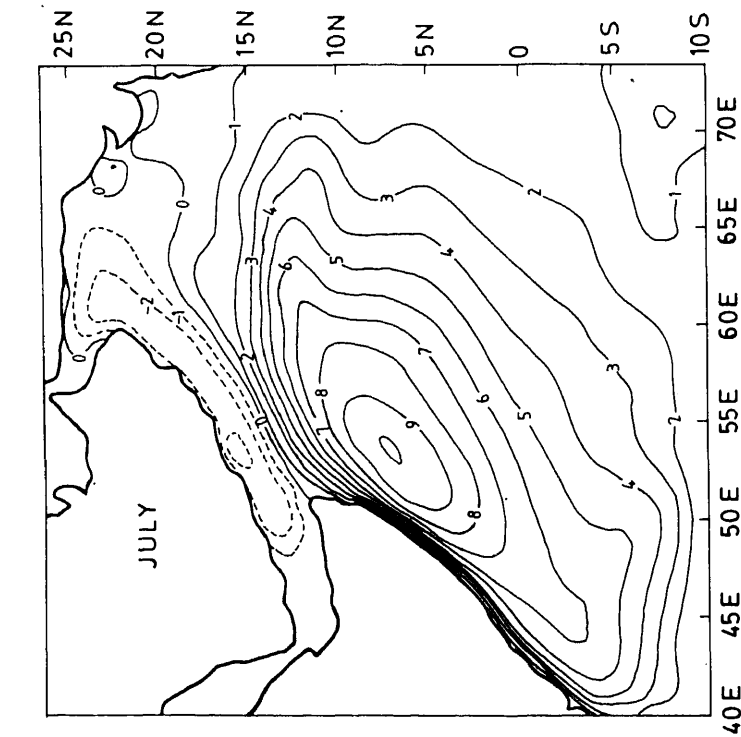


Figure 5. ψ_0 field with nonlinear terms ($10^4 \text{ m}^2/\text{s}$).

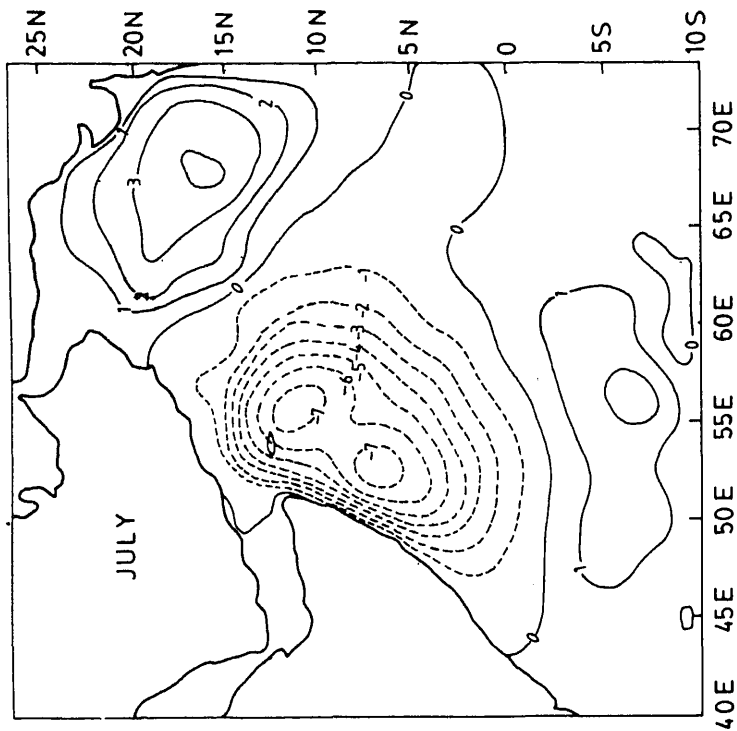


Figure 6. Velocity potential χ_0 ($10^4 \text{ m}^2/\text{s}$).

5–15°N and 55–70°E in the interior. Strong upwelling is associated with positive curl, while downwelling occurs over regions of negative curl. Dube *et al* (1986) find that the interior downwelling becomes weak in years of poor monsoon.

The divergence of the wind stress (figure 2) has high positive values in the region between 0–15°N and 50–60°E. Negative divergence prevails between 12–20°N and 60–70°E.

It is interesting to see that the narrow coastal region between 5–12°N is a zone of both positive curl and divergence. This is, therefore, a zone of marked coastal upwelling.

Figures 3 and 4 show the first and second approximations to the streamfunction (ψ_0, ψ_1). As we can see, the inclusion of divergence in the vorticity equation leads to the formation of a second gyre between the equator and 8°S. The second gyre is absent in the first approximation (figure 3), which only shows a big whirl between 5–12°N. The big whirl and the southern gyre is separated by a small eddy.

In figure 5 the streamfunction ψ_0 is shown with the inclusion of the nonlinear term as in (19). The stretching term was not present in this case; consequently, only

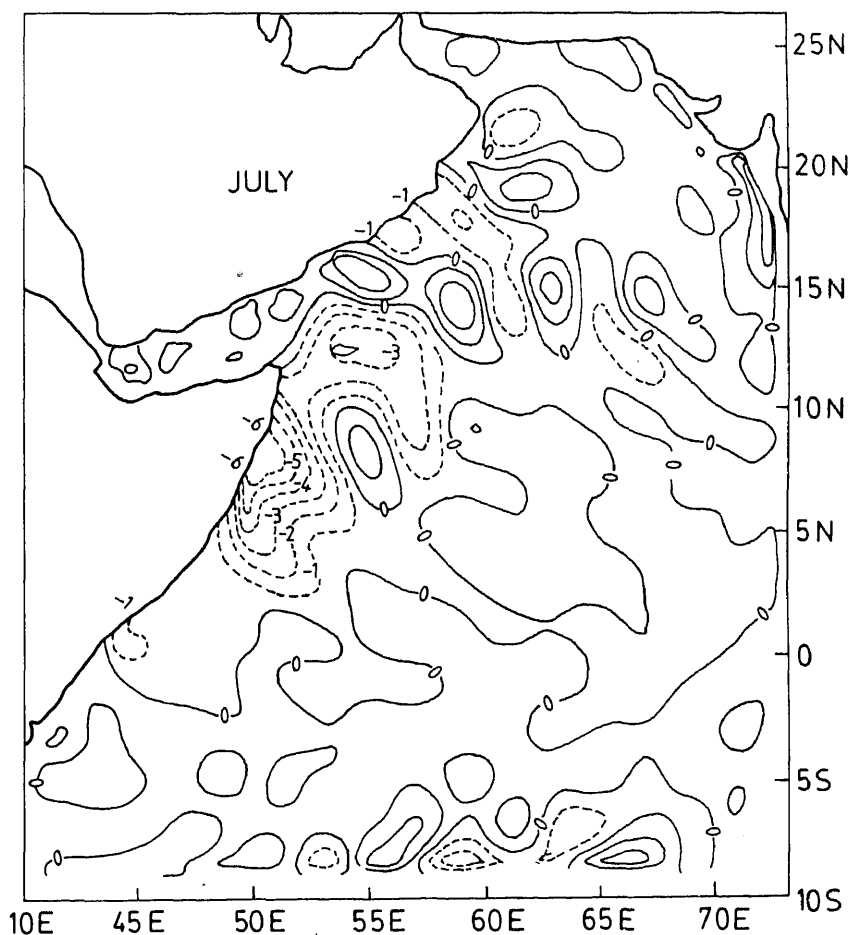


Figure 7. Vertical velocity (10^{-5} m/s).

UPPER LAYER VELOCITY

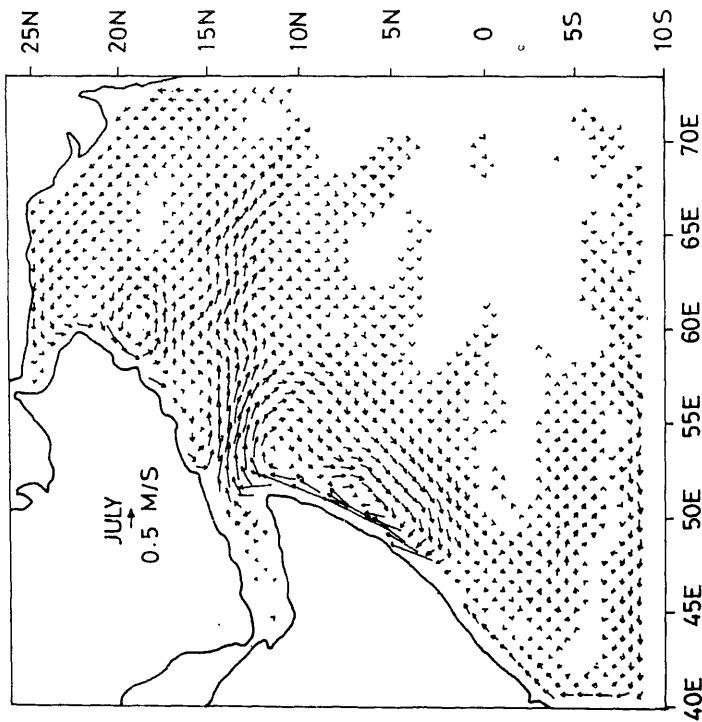


Figure 8. Upper layer velocity (0.5 m/s) computed from gradients of χ_1 .

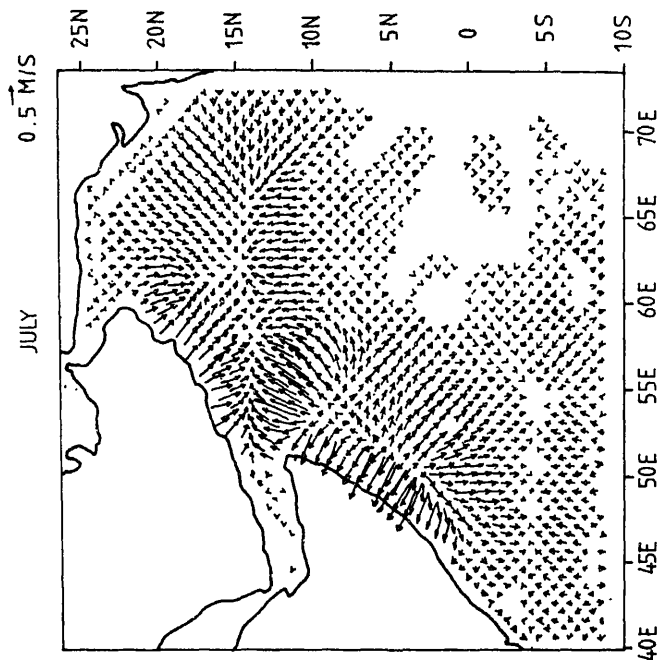


Figure 9. Upper layer velocity (0.5 m/s) from gradients of χ_1 .

a single gyre resembling the 'great whirl' appears. On the other hand, the coastal current is more intense and the central portion of the whirl near 8°N is considerably distorted. This agrees with our earlier inferences and the results of Cox (1981).

Figure 6 shows the first approximation to the velocity potential X_0 . To save space the second approximation X_1 is not shown because there was not much difference between X_0 and X_1 . The vertical velocity is shown in figure 7. Strong upwelling off the eastern coast of Africa is the main feature. The intensity of upwelling exceeds the value derived by Luther and O'Brien (1985) by a factor of 3, but there is good agreement on the location of the upwelling zone. Downwelling over the central parts of the Arabian sea is not so prominent.

Figures 8 and 9 show the upper layer velocity on account of rotation ψ_1 and divergence χ_1 . It is interesting to note that the strong eastward jet near 12°N is an outcome of the rotational part of the current. This jet carries much of the cooler upwelled waters from the coast to the interior of the Arabian sea. As we see in figure 9, the χ_1 field leads to weak divergent motion over the central Arabian sea.

These figures of the Somali current are interesting because Dube *et al* (1986) suggest that the southern gyre is prominent in a year of good monsoon rain. Our model suggests that the southern gyre is an outcome of the stretching term in the vorticity equation. This, in turn, is related to the divergence of the wind stress.

5. Conclusions

- (i) The divergence of the wind stress is comparable to the wind stress curl over equatorial regions of the Arabian sea and the north Indian ocean.
- (ii) The southern gyre of the Somali current is an outcome of forcing by the divergence of the wind stress.
- (iii) Nonlinear terms in the vorticity equation strengthen the coastal current and introduce an asymmetry in the main gyre.
- (iv) A strong eastward jet near 12°N is due to the rotational component of the upper layer velocity. This carries much of the cold upwelled waters from the coast to the interior.
- (v) The central parts of the Arabian sea are regions of weak downwelling.

Acknowledgement

The authors thank Dr Brian Johns, University of Reading, U.K. for reading the manuscript and offering valuable suggestions.

References

- Bruce J G 1978 Spatial and temporal variation of the wind stress off the Somali coast; *J. Geophys. Res.* **83** 963-967
- Cadet D L and Diehl B C 1984 Interannual variability of surface fields over the Indian ocean during recent decades; *Mon. Weather Rev.* **112** 1921-1935
- Cox M D 1981 A numerical study of surface cooling processes during summer in the Arabian sea in: *Monsoon dynamics* (eds) M J Lighthill and R P Pearce (Cambridge: University Press) pp. 529-540.

- Cutler A N and Swallow J C 1984 Surface currents of the Indian ocean; Rep. No. 187, Institute of Oceanographic Sciences, U.K.
- Dube S K, Luther M E and O'Brien J J 1986 Relationship between the interannual variability of ocean fields and the wind stress curl over the central Arabian sea and the Indian summer monsoon rainfall (unpublished)
- Hastenrath S and Lamb P J 1979 Climatic atlas of the Indian ocean—Part 1: Surface circulation and climate; (Wisconsin: University Press) p. 109
- Luther M E and O'Brien J J 1985 A model of the seasonal circulation in the Arabian sea forced by observed winds; *Prog. Oceanogr.* **14** 353–358
- Luther M E, O'Brien J J and Meng A H 1985 Morphology of Somali current system during the southwest monsoon in: *Coupled ocean atmosphere models* (ed) J C J Nihoul (Amsterdam: Elsevier) pp. 405–537
- Okumu M A 1985 Upwelling and the Somali current, M.S. thesis, University of Nairobi, Kenya
- Stommel H 1948 The westward intensification of wind driven ocean currents; *Trans. Am. Geophys. Union* **29** 202–206
- Wylie D P and Hinton B B 1982 The wind stress pattern over the Indian ocean during the summer monsoon of 1979; *J. Phys. Oceanogr.* **12** 186–199

SUBJECT INDEX

- Active break monsoon cycle
 - Some aspects of the 30–50 day oscillation 49
- Amplitude
 - Auxiliary functions of the Hilbert transform in the study of gravity anomalies 211
- Arid soils
 - Relationship between pedogenetic manifestations in some arid soil and age of the landforms 203
- Asymmetry
 - North-south asymmetry in response of geomagnetic activity to different solar events 195
- Atmospheric transmittance
 - Selection of optimum frequency of a wind scatterometer 259
- Auxiliary functions
 - Auxiliary functions of the Hilbert transform in the study of gravity anomalies 211
- Bay of Bengal
 - Distribution of particulate organic carbon in the central Bay of Bengal 189
- Beach dynamics
 - Longshore grain size trends in the Kakinada-Mulapeta Beach, east coast of India 267
- Break
 - On global summer monsoonal drought mechanics 147
- Charnockite
 - Gneiss-charnockite relation around Ponmudi, southern Kerala; evidences and implications of prograde charnockite formation in southern India 1
- Chlorophyll *a*
 - Distribution of particulate organic carbon in the central Bay of Bengal 189
- Coastal currents
 - Seasonal and diurnal variability of thermal structure in the coastal waters off Visakhapatnam 69
- Crescent-shaped upwelled region
 - Satellite-observed upwelled region and prime eddy off Somali coast during Monex-79 41
- Curl
 - A steady state model of the Somali current 279
- Dipping interfaces
 - Estimation of hypocentral parameters of local earthquakes when crustal layers have constant *P*-velocities and dipping interfaces 229
- Divergence
 - A steady state model of the Somali current 279
- Downwelling
 - A steady state model of the Somali current 279
- Earthquakes
 - Estimation of hypocentral parameters of local earthquakes when crustal layers have constant *P*-velocities and dipping interfaces 229
- Energy dispersive X-ray fluorescence
 - Geochemical studies on Kashmir loess profiles 135
- Estuary
 - Seasonal variation of the salinity in the Zuari estuary, Goa, India 249
- Flare index
 - 146-day signal in the geomagnetic field—probable association with the periodicity of the solar flare index 119
- Geochemistry
 - Gold-bearing rocks of Mangalur greenstone belt, Gulbarga District, Karnataka 103
- Geomagnetic activity
 - North-south asymmetry in response of geomagnetic activity to different solar events 195
- Geomagnetic field
 - 146-day signal in the geomagnetic field—probable association with the periodicity of the solar flare index 119
- Geomagnetic planetary index
 - 146-day signal in the geomagnetic field—probable association with the periodicity of the solar flare index 119
- Gold-quartz veins
 - Gold-bearing rocks of Mangalur greenstone belt, Gulbarga District, Karnataka 103
- Gradients
 - Analysis of gravity gradients over a thin infinite sheet 11
- Grain size trends
 - Longshore grain size trends in the Kakinada-Mulapeta Beach, east coast of India 267
- Granitoid pluton
 - Petrographic criteria for establishing the copper potential in granitoid plutons 221
- Gravity waves
 - Variability in the surface wind direction at a coastal site of complex terrain 59

- Hilbert transform
 Analysis of gravity gradients over a thin infinite sheet 11
 Auxiliary functions of the Hilbert transform in the study of gravity anomalies 211
- Hypocentral parameters
 Estimation of hypocentral parameters of local earthquakes when crustal layers have constant *P*-velocities and dipping interfaces 229
- Instantaneous frequency
 Auxiliary functions of the Hilbert transform in the study of gravity anomalies 211
- Interannual variability
 Some aspects of the 30–50 day oscillation 49
 Variability in the surface wind direction at a coastal site of complex terrain 59
- Intercomparison
 Results from the Indo-USSR ozonesonde intercomparison experiment 25
- Iron meteorites
 Variable $^{190}\text{Os}/^{184}\text{Os}$ ratio in acid residues of iron meteorites 81
- Isotopic anomalies
 Variable $^{190}\text{Os}/^{184}\text{Os}$ ratio in acid residues of iron meteorites 81
- Kakinada-Mulapeta coast
 Longshore grain size trends in the Kakinada-Mulapeta Beach, east coast of India 267
- Kerala
 Gneiss-charnockite relation around Ponmudi, southern Kerala; evidences and implications of prograde charnockite formation in southern India 1
- Khondalite
 Gneiss-charnockite relation around Ponmudi, southern Kerala; evidences and implications of prograde charnockite formation in southern India 1
- Landforms
 Relationship between pedogenetic manifestations in some arid soil and age of the landforms 203
- Loess
 Geochemical studies on Kashmir loess profiles 135
- Mangalur greenstone belt
 Gold-bearing rocks of Mangalur greenstone belt, Gulbarga District, Karnataka 103
- Mesoscale eddies
 Variability in the surface wind direction at a coastal site of complex terrain 59
- Meso scale island circulation
 Characteristics of air flow over Andaman Islands including precipitation 169
- Metavolcanic rocks
 Gold-bearing rocks of Mangalur greenstone belt, Gulbarga District, Karnataka 103
- Middle latitudes
 On global summer monsoonal drought mechanics 147
- Mineral chemistry
 Gneiss-charnockite relation around Ponmudi, southern Kerala; evidences and implications of prograde charnockite formation in southern India 1
- Monex
 Satellite-observed upwelled region and prime eddy off Somali coast during Monex-79 41
- MONEX
 Turbulent fluxes over east-central Arabian sea during MONEX 123
- Monsoon
 On global summer monsoonal drought mechanics 147
- Monsoon region
 Seasonal variation of the salinity in the Zuari estuary, Goa, India 249
- Nearshore dynamics
 Longshore grain size trends in the Kakinada-Mulapeta Beach, east coast of India 267
- Numerical simulation
 Characteristics of air flow over Andaman Islands including precipitation 169
- 146-day period
 146-day signal in the geomagnetic field—a probable association with the periodicity of the solar flare index 119
- Onset vortex
 Turbulent fluxes over east-central Arabian sea during MONEX 123
- Optimum frequency
 Selection of optimum frequency of a wind scatterometer 259
- Origin of iron meteorites
 Variable $^{190}\text{Os}/^{184}\text{Os}$ ratio in acid residues of iron meteorites 81
- Oscillation
 Some aspects of the 30–50 day oscillation 49
- Osmium isotopes
 Variable $^{190}\text{Os}/^{184}\text{Os}$ ratio in acid residues of iron meteorites 81
- Ozone
 Results from the Indo-USSR ozonesonde intercomparison experiment 25
- P-T conditions
 Gneiss-charnockite relation around Ponmudi, southern Kerala; evidences and implications of prograde charnockite formation in southern India 1

Palaeosol	
Geochemical studies on Kashmir loess profiles	135
Particulate organic carbon	
Distribution of particulate organic carbon in the central Bay of Bengal	189
Pasquill stability	
Variability in the surface wind direction at a coastal site of complex terrain	59
Pedogenetic manifestations	
Relationship between pedogenetic manifestations in some arid soil and age of the landforms	203
Penalty function approach	
Estimation of hypocentral parameters of local earthquakes when crustal layers have constant <i>P</i> -velocities and dipping interfaces	229
Petrogenesis	
Gold-bearing rocks of Mangalur greenstone belt, Gulbarga District, Karnataka	103
Petrographic features	
Petrographic criteria for establishing the copper potential in granitoid plutons	221
Petrographic score	
Petrographic criteria for establishing the copper potential in granitoid plutons	221
Petrological record	
Petrographic criteria for establishing the copper potential in granitoid plutons	221
Phase and envelope	
Auxiliary functions of the Hilbert transform in the study of gravity anomalies	211
Precursory gap	
Precursory swarm and its application for long range earthquake forecasting in Taiwan region	15
Precursory swarm	
Precursory swarm and its application for long range earthquake forecasting in Taiwan region	15
Pre-solar grains	
Variable $^{190}\text{Os}/^{184}\text{Os}$ ratio in acid residues of iron meteorites	81
Prime eddy	
Satellite-observed upwelled region and prime eddy off Somali coast during Monex-79	41
Principal component analysis	
Geochemical studies on Kashmir loess profiles	135
Regression equation	
Precursory swarm and its application for long range earthquake forecasting in Taiwan region	15
Rock density	
Weathering potential index for rocks based on density and porosity measurements	239
Rock porosity	
Weathering potential index for rocks based on density and porosity measurements	239
Rosby waves	
On global summer monsoonal drought mechanics	147
Salt budget	
Seasonal variation of the salinity in the Zuari estuary, Goa, India	249
Satellite-derived low-level winds	
Satellite-observed upwelled region and prime eddy off Somali coast during Monex-79	41
Scatterometer	
Selection of optimum frequency of a wind scatterometer	259
Sea/land breeze studies	
Characteristics of air flow over Andaman Islands including precipitation	169
Seasonal variation	
Seasonal variation of the salinity in the Zuari estuary, Goa, India	249
Sea surface wind speed	
Selection of optimum frequency of a wind scatterometer	259
Sector boundary	
North-south asymmetry in response of geomagnetic activity to different solar events	195
Seismicity fluctuation	
Precursory swarm and its application for long range earthquake forecasting in Taiwan region	15
Sequential unconstrained optimization	
Estimation of hypocentral parameters of local earthquakes when crustal layers have constant <i>P</i> -velocities and dipping interfaces	229
Sinking	
Seasonal and diurnal variability of thermal structure in the coastal waters off Visakhapatnam	69
Solar proton events	
North-south asymmetry in response of geomagnetic activity to different solar events	195
Solar wind streams	
North-south asymmetry in response of geomagnetic activity to different solar events	195
Somali current	
A steady state model of the Somali current	279
Satellite-observed upwelled region and prime eddy off Somali coast during Monex-79	41
Subseasonal oscillation	
Some aspects of the 30–50 day oscillation	49
Teleconnections	
On global summer monsoonal drought mechanics	147

Thermal structure		estuary, Goa, India	249
Seasonal and diurnal variability of thermal structure in the coastal waters off Visakhapatnam	69	Visakhapatnam coast	
Tholeiites		Seasonal and diurnal variability of thermal structure in the coastal waters off Visakhapatnam	69
Gold-bearing rocks of Mangalur greenstone belt, Gulbarga District, Karnataka	103	Weather forecast	
Turbulence		Characteristics of air flow over Andaman Islands including precipitation	169
Variability in the surface wind direction at a coastal site of complex terrain	59	Weathering classification	
Turbulent fluxes		Weathering potential index for rocks based on density and porosity measurements	239
Turbulent fluxes over east-central Arabian sea during MONEX	123	Weathering potential index	
Upwelling		Weathering potential index for rocks based on density and porosity measurements	239
A steady state model of the Somali current	279	West coast of India	
Seasonal and diurnal variability of thermal structure in the coastal waters off Visakhapatnam	69	Seasonal variation of the salinity in the Zuari estuary, Goa, India	249
Variability		Whole rock chemistry	
Results from the Indo-USSR ozonesonde inter-comparison experiment	25	Gneiss-charnockite relation around Ponmudi, southern Kerala; evidences and implications of prograde charnockite formation in southern India	1
Vertical distribution		Wind direction fluctuation	
Results from the Indo-USSR ozonesonde inter-comparison experiment	25	Variability in the surface wind direction at a coastal site of complex terrain	59
Vertically mixed		Wind stress	
Seasonal variation of the salinity in the Zuari		A steady state model of the Somali current	279

AUTHOR INDEX

Agrawal D P		Kar C Sarat	
<i>see</i> Lodha G S	135	Characteristics of air flow over Andaman Islands including precipitation	169
Appu K S		Kasture S V	
<i>see</i> Subbaraya B H	25	Some aspects of the 30–50 day oscillation	49
Arunkumar I		Keshavamurty R N	
<i>see</i> Ramadass G	211	<i>see</i> Kasture S V	49
Babu V Ramesh		Khatttri K N	
<i>see</i> Rao B Prabhakara	69	<i>see</i> Irene Sarkar	229
Bhosle N B		Khokin G A	
<i>see</i> Nandakumar K	189	<i>see</i> Subbaraya B H	25
Chander R		Kononkov V A	
<i>see</i> Irene Sarkar	229	<i>see</i> Subbaraya B H	25
Chandramohan P		Kumar G R Ravindra	
<i>see</i> Rao B Prabhakara	69	<i>see</i> Srikantappa C	1
Chatterjee K P		Kumar I Arun	
<i>see</i> Subbaraya B H	25	<i>see</i> Sundararajan N	11
Chizhov A F		Kumar Raj	
<i>see</i> Subbaraya B H	25	<i>see</i> Sarkar Abhijit	259
Choudhari J S		Lodha G S	
Relationship between pedogenetic manifestations in some arid soil and age of the landforms	203	Geochemical studies on Kashmir loess profiles	135
Das Asok		Mahajan P N	
<i>see</i> Singh R Pratap	239	Satellite-observed upwelled region and prime eddy off Somali coast during Monex-79	41
Das P K		Mohan Mannil	
A steady state model of the Somali current	279	<i>see</i> Sarkar Abhijit	259
Dube S K		Mohan N L	
<i>see</i> Das P K	279	<i>see</i> Sundararajan N	11
Gaur V K		<i>see</i> Ramadass G	211
<i>see</i> Irene Sarkar	229	Moshnikov I S	
Goel P S		<i>see</i> Subbaraya B H	25
Variable $^{190}\text{Os}/^{184}\text{Os}$ ratio in acid residues of iron meteorites	81	Murty C S	
Grinchinkov V D		<i>see</i> Shetye S R	249
<i>see</i> Subbaraya B H	25	Naik M S	
Irene Sarkar		Petrographic criteria for establishing the copper potential in granitoid plutons	221
Estimation of hypocentral parameters of local earthquakes when crustal layers have constant <i>P</i> -velocities and dipping interfaces	229	Nandakumar K	
Jayaraman A		Distribution of particulate organic carbon in the central Bay of Bengal	189
<i>see</i> Subbaraya B H	25	Narayanan V	
Juyal N		<i>see</i> Subbaraya B H	25
<i>see</i> Lodha G S	135	Perov S P	
Kadam B D		<i>see</i> Subbaraya B H	25
<i>see</i> Rao D R K	119	Prasad D Satya	
		Longshore grain size trends in the Kakinada-Mulapeta Beach, east coast of India	267

- | | | | |
|--|-----|---|-----|
| Ramadass G | | Singh J | |
| Auxiliary functions of the Hilbert transform in the study of gravity anomalies | 211 | <i>see</i> Singh V P | 15 |
| Ramanathan N | | Singh R Pratap | |
| <i>see</i> Kar C Sarat | 169 | Weathering potential index for rocks based on density and porosity measurements | 239 |
| Raman N N | | Singh V P | |
| <i>see</i> Varma K K | 123 | Precursory swarm and its application for long range earthquake forecasting in Taiwan region | 15 |
| Rangarajan G K | | Somayajulu Y V | |
| North-south asymmetry in response of geomagnetic activity to different solar events | 195 | <i>see</i> Subbaraya B H | 25 |
| Rao B Prabhakara | | Sreedharan C R | |
| Seasonal and diurnal variability of thermal structure in the coastal waters off Visakhapatnam | 69 | <i>see</i> Subbaraya B H | 25 |
| Rao D R K | | Srikantappa C | |
| 146-day signal in the geomagnetic field—a probable association with the periodicity of the solar flare index | 119 | Gneiss-charnockite relation around Ponmudi, southern Kerala; evidences and implications of prograde charnockite formation in southern India | 1 |
| Rao G S | | Subbaraya B H | |
| <i>see</i> Das P K | 279 | Results from the Indo-USSR ozonesonde inter-comparison experiment | 25 |
| Rao M Sankar | | Sundararajan N | |
| On global summer monsoonal drought mechanics | 147 | Analysis of gravity gradients over a thin infinite sheet | 11 |
| Rao M Subba | | Sundararajan N | |
| <i>see</i> Prasad D Satya | 267 | <i>see</i> Ramadass G | 211 |
| Rao S M Varaprasada | | | |
| <i>see</i> Ramadass G | 211 | Tenginkai S G | |
| Razdan H | | Gold-bearing rocks of Mangalur greenstone belt, Gulbarga District, Karnataka | 103 |
| <i>see</i> Lodha G S | 135 | Trivedi R K | |
| Sachidananda S V | | <i>see</i> Naik M S | 221 |
| <i>see</i> Rao M Sankar | 147 | Ugarkar A G | |
| Sadhuram Y | | <i>see</i> Tenginkai S G | 103 |
| Variability in the surface wind direction at a coastal site of complex terrain | 59 | Upadhyay Vijay Kumar | |
| Sarkar Abhijit | | <i>see</i> Singh R Pratap | 239 |
| Selection of optimum frequency of a wind scatterometer | 259 | | |
| Sarma G V S | | Varma K K | |
| <i>see</i> Prasad D Satya | 267 | Turbulent fluxes over east-central Arabian sea during MONEX | 123 |
| Sawhney K J S | | Venkat K | |
| <i>see</i> Lodha G S | 135 | <i>see</i> Nandakumar K | 189 |
| Shetye S R | | Zalpuri K S | |
| Seasonal variation of the salinity in the Zuari estuary, Goa, India | 249 | <i>see</i> Subbaraya B H | 25 |
| Shtrikov O V | | | |
| <i>see</i> Subbaraya B H | 25 | | |